

On Topology of Solar Coronal Magnetic Field

A thesis submitted in partial fulfilment of
the requirements for the degree of

Doctor of Philosophy

by

Yogesh Kumar Maurya

(Roll No. 19330022)

Under the guidance of

Dr. Ramitendranath Bhattacharyya

Professor

Udaipur Solar Observatory Division

Physical Research Laboratory, Ahmedabad, India.



Discipline of Physics

Indian Institute of Technology Gandhinagar

2024

To
my family
&
teachers

Declaration

I declare that this written submission represents my ideas in my own words and where others' ideas or words have been included, I have adequately cited and referenced the original sources. I also declare that I have adhered to all principles of academic honesty and integrity and have not misrepresented or fabricated or falsified any idea/data/fact/source in my submission. I understand that any violation of the above can cause disciplinary action by the Institute and can also evoke penal action from the sources which have thus not been properly cited or from whom proper permission has not been taken when needed.

(Signature)

(Name: Yogesh Kumar Maurya)

(Roll No: 19330022)

CERTIFICATE

This is to certify that this thesis titled “**On Topology of Solar Coronal Magnetic Field**” submitted by **Mr. Yogesh Kumar Maurya (Roll No. 19330022)** to the Indian Institute of Technology Gandhinagar, is a record of bona fide research work carried out under my supervision and has not been submitted elsewhere for a degree. I have read this dissertation and in my opinion, it is fully adequate, in scope and quality, for the degree of Doctor of Philosophy.

Dr. Ramitendranath Bhattacharyya

(Thesis Supervisor)

Professor

Udaipur Solar Observatory Division,

Physical Research Laboratory,

Ahmedabad, India.

Acknowledgments

Completing this thesis has been a journey made possible by the help and support of many people, and I want to express my deepest thanks to all of them.

First and foremost, I am deeply grateful to my PhD supervisor, Prof. Ramitendranath Bhattacharyya, for the opportunity to work with him. His patience, support, and guidance have been invaluable throughout my PhD journey. Working with such a considerate mentor, who allowed me the freedom to explore independently, has contributed significantly to my growth as a researcher.

I also want to thank my collaborators, Prof. David Ian Pontin and Dr. Sanjay Kumar, for their significant contributions and support. My gratitude extends to the members of my Doctoral Studies Committee, Dr. Brajesh Kumar, Dr. Girjesh R. Gupta, and Prof. Partha Konar, for their valuable feedback and evaluation of my work.

Special thanks go to Prof. Nandita Srivastava and Prof. Shibu K. Mathew for their support over the past four years and to Prof. Anil Bhardwaj, Director, Physical Research Laboratory (PRL), Ahmedabad, for providing the necessary facilities and organizing engaging activities. I am also grateful to IIT Gandhinagar for my PhD registration, Dr. Bhushit Vaishnav for help with academic matters, and the PRL computer center staff, especially Mr. Jigar Raval, for their assistance with computational issues.

I appreciate the administration and library staff at Udaipur Solar Observatory (USO) and Ahmedabad for their cooperation throughout my PhD. A special thanks to Mr. Abhishek, the administrative officer at USO, for his help with administrative matters.

I have enjoyed the company of my batchmates, seniors, and juniors at PRL. My sincere thanks go to Dr. Kuldeep Pandey, Dr. Avijeet Prasad, and Dr. Sushree Sangeeta Nayak for their support and help, especially during the initial stages of my research. I also want to thank my batchmates, seniors, and juniors at PRL for their support.

I want like to express my heartfelt gratitude to my friend, Ms. Vidya Sharma (Tanu), for her unwavering support, encouragement, and friendship throughout this journey.

Lastly, I want to express my heartfelt thanks to my family, especially my parents and elder brother, Mr. Nitesh Maurya, for their unwavering love, support, and encouragement. This thesis is dedicated to them, and despite the time spent away from home, their support has always been a source of strength for me.

Abstract

Magnetic topology involves the properties of magnetic field lines, such as their linkages and knottedness, which remain unchanged under ideal displacements such as bending and stretching. Understanding the magnetic topology of the solar corona is important as its change implies magnetic reconnection—a discontinuous process that re-structures the magnetic field lines and converts magnetic energy into heat and kinetic energy, resulting in various solar eruptive phenomena like solar flares, coronal jets, and coronal bright points. In two dimensions (2D), reconnection occurs at magnetic neutral or null points where the magnetic field is zero, and the configurations near these points can be either elliptic (O-type) or hyperbolic (X-type). In three dimensions (3D), reconnection occurs at topologies such as 3D magnetic nulls (where the magnetic field is zero) and separators—lines formed through the intersection of two fan planes. Contemporary research (theory, extrapolation, simulation, and observation) suggests that 3D nulls are abundant in the solar atmosphere and drive various solar transients such as flares, jets, and coronal bright points. However, the mechanism behind the generation of 3D nulls is not yet fully understood.

In the above background, the thesis explores how 3D magnetic nulls are created and annihilated by employing Implicit Large Eddy Simulations (ILESs) where magnetohydrodynamics (MHD) equations are solved in the absence of explicit magnetic diffusivity. The magnetofluid is idealized to be thermodynamically inactive and incompressible. Importantly, any simulation attempting to explore null generation (and annihilation) must satisfy the following two criteria,

1. identities of the nulls require to be maintained with high fidelity,
2. the net topological degree must be preserved.

Both these conditions are satisfied in the carried-out simulations and are discussed later in the thesis.

In its core chapters, the thesis explores three particular cases for the generation of nulls. In the first one, the dynamics are onset with a prescribed flow

in a magnetic configuration having an isolated, current-free, proper radial 3D null point. The flow renders the spine to bend toward the fan plane, resulting in magnetic reconnections along with the creation of a null pair having opposite topological degrees. Resultantly, the overall net topological degree remains preserved. The way these null pairs are generated is new, novel, and different from the usual pitchfork bifurcation. Importantly, the generated null pairs are created away from the central null, likely due to the interaction between the imposed flow and the reconnection outflow from the central current layer. Interestingly, as the simulation progresses, new null pairs develop spontaneously, which is a novel finding. These spontaneously generated null pairs also preserve the overall net topological degree, adding credibility to the simulation. The simulation also shows that nulls can annihilate in pairs. Tracing of magnetic field lines in time reveals that magnetic reconnections are the underlying cause for both the generation and annihilation of the nulls.

The second case study advances the first one by exploring the physics of autonomous null generations through a data-based simulation of a flaring region using photospheric magnetograms of a solar active regions instead of any predetermined magnetic structure or any prescribed flow—making it a unique exploration of spontaneous null generation in a realistic scenario. Additionally, solar active regions have complex magnetic topologies, suggesting that the 3D nulls have similar complexity. Understanding this process is crucial for insights into chromospheric and coronal heating. The active region is selected based on its proximity to the solar disk center, ensuring minimal errors in the observed photospheric magnetic field, the constancy of the photospheric magnetic flux across the active region during the flare, allowing for a line-tied boundary condition to simplify simulations and the availability of contemporary multiwavelength observations. The initial coronal magnetic field is obtained by extrapolating photospheric vector magnetogram data using the Non-Force-Free Field extrapolation technique. The resulting non-zero Lorentz force drives the plasma, generating initial dynamics, and the simulation focuses on the part of the flare’s reconnection-dominated impulsive phase, aligned with the objectives. The three

representative null generation/annihilation processes are chosen for a detailed analysis. One particularly interesting case involved a spontaneously generated radial null pair, not reported previously. Each null in this pair exhibited the typical dome-shaped structure of fan field lines expected in the solar atmosphere, accompanied by footpoint brightening in the 1600 Å channel of the Atmospheric Imaging Assembly (AIA), linked to slip reconnection. These brightenings may result from non-thermal particles impacting the lower solar atmosphere's plasma. Eventually, two such spontaneously generated nulls approach each other and get annihilated. Magnetic reconnection is identified as the underlying cause for both the generation and annihilation, preserving the net topological degree throughout the process. The other two null pairs exhibited similar characteristics, reinforcing the idea that magnetic reconnection is responsible for the spontaneous generation of 3D nulls in the solar atmosphere, and the observational signatures of these spontaneously generated nulls strongly support the findings.

Although null generation was ubiquitous in both above studies, nevertheless, the initial magnetic field contained magnetic nulls. It is then imperative to look for null generation in a scenario where no pre-existing nulls are present to establish the spontaneity of their generation. The plausibility of such a scenario has been explored in the third case study, where the initial magnetic field was chaotic and devoid of any 3D null. Toward the goal, the MHD simulations with varying levels of chaoticity have been carried out. The initial magnetic fields have been derived by superposing two ABC fields, each satisfying the linear force-force condition. For the computations, $C \in \{0.15, 0.20, 0.25, 0.30\}$ corresponds to initial fields with increasing chaoticity. A direct correlation has been found between chaoticity levels and the number of null generations, with higher chaoticity leading to earlier null creations and increased null count. Further, to explore null generation/annihilation in more detail, the chaoticity is set at $C = 0.3$. A spontaneously generated spiral null pair is selected as an exemplar of the null generation process. Interestingly, one of the nulls changes its nature from spiral to radial with evolution. Subsequently, this radial null reverts to a spiral null, which later annihilates with a different spiral null created in a distinct null pair

generation process. The relevant magnetic field lines are traced over time and advected with the plasma flow in the ideal region to illustrate the global impact of the creation and annihilation of nulls. It is found that the field lines change their connectivity from one domain to a different domain—demonstrating that the spontaneous generation (and annihilation) of 3D null point pairs leads to a change in the global field topology.

The results are found to be interesting and, more importantly, thought-provoking. In all three cases, magnetic reconnection is found to be the underlying cause of the generation and annihilation of nulls, and with nulls being preferential sites of reconnection—a novel possibility of reconnection-assisted spontaneous generation of nulls and subsequent reconnection at those nulls cannot be denied. Such a continuous process can explain the abundance of nulls in the solar atmosphere and contribute to solar chromospheric and coronal heating.

Keywords: Magnetic Topology; Magnetic Reconnection; Magnetohydrodynamics; Coronal Magnetic fields; Flares; Three-dimensional nulls; Genesis and Annihilation.

Contents

Acknowledgements	i
Abstract	iii
Contents	vii
List of Figures	xi
1 Introduction	1
1.1 A brief introduction to magnetic topology	1
1.1.1 Homeomorphism	2
1.2 Magnetic topology	3
1.2.1 Ideal limit ($R_M \gg 1$)	6
1.2.2 Non-ideal limit ($R_M \ll 1$)	10
1.2.3 Conservation of magnetic topology	11
1.3 Magnetic reconnection	13
1.3.1 Reconnection in two dimension	13
1.3.2 Sweet-parker model	15
1.3.3 Petschek model	18
1.3.4 Magnetic reconnection in three dimension	20
1.4 Objective and Outline of the Thesis	28
2 Observational manifestation of magnetic reconnection and theory of 3D magnetic null	31
2.1 Solar Flares	31
2.2 Jets	36

2.3	Coronal Bright Points	40
2.4	Theory of 3D magnetic null	45
2.4.1	Structure of 3D nulls	45
2.4.2	Radial and Spiral 3D null	48
2.4.3	Topological degree of 3D magnetic null	50
2.4.4	Conservation of net topological degree of 3D nulls	52
3	Methodology and necessary numerical tools	55
3.1	Data Acquisition	55
3.1.1	SDO	55
3.1.2	Geostationary Operational Environmental Satellite (GOES)	58
3.2	Non-Force Free Field (NFFF) extrapolation	59
3.3	Detection of 3D magnetic null	64
3.3.1	A trilinear method to detect the 3D null points	64
3.3.2	Algorithm for finding null point	66
3.4	Numerical Model	68
3.4.1	Advection solver MPDATA	69
3.4.2	EULAG-MHD	76
3.4.3	Implicit large eddy simulation	82
4	3D magnetic null generation and annihilation with an initial analytical magnetic field	85
4.1	Introduction	85
4.1.1	Initial magnetic field and flow	87
4.2	Results	89
4.3	Summary	118
5	Spontaneous generation and annihilation of 3D magnetic nulls in the solar atmosphere	121
5.1	Introduction	121
5.1.1	Non-Force Free Field Extrapolation of NOAA AR 11977 .	123
5.1.2	Governing Equations and Numerical Model	127

5.1.3	Numerical Setup	128
5.2	Results	129
5.2.1	Radial-radial-pair	130
5.2.2	Radial-spiral-pair-1	137
5.2.3	Radial-spiral-pair-2	145
5.3	Summary	152
6	Generation of 3D magnetic nulls in an initially chaotic magnetic field devoid of any nulls	155
6.1	Introduction	155
6.2	Results	157
6.3	Summary	166
7	Summary and Future Scopes	167
7.1	Summary	167
7.2	Future Scopes	169
	Bibliography	170
	List of Publications	189

List of Figures

1.1	Figure represents the continuous transformation of a coffee cup into a donut and vice versa. Hence, these two are topologically equivalent.	1
1.2	Schematic represents an example of Homeomorphism, the left field lines configuration represents the magnetic field \mathbf{B}_1 at time t_0 transformed into the field lines configurations shown on the right representing magnetic field \mathbf{B}_2 at the later time t ($t_0 < t$). Both field line configurations have similar magnetic topology. The image is adapted from Hornig & Schindler (1996)	6
1.3	Example of solar coronal loops observed by the Transition Region And Coronal Explorer (TRACE), 171Å filter. These loops have a temperature of approximately 10^6 K. These loops contrast greatly with the cool chromosphere below. (https://upload.wikimedia.org/wikipedia/commons/9/93/Traceimage.jpg) . . .	8
1.4	An example of reconnection near an X-type null point is shown through Schematic.	14
1.5	The Figure presents the example of a configuration in 2D near the null points. For $\alpha^2 > 1$, X-type null (panel (a)), $\alpha^2 = -1$, Circular-type (panel (b)), and $\alpha^2 < -1$, Elliptical-type (panel (c)).	15
1.6	Schematic represents the Sweet-Parker model of reconnection. . . .	16
1.7	Schematic represents the Petscheck model of reconnection.	19

1.8	The Figure depicts the concept of reconnection in 3D proposed by Axford. Magnetic connection: Two plasma elements, P and Q, are connected by a magnetic field line at time t_1 and remain connected by a magnetic field line at any later time t_2 under the plasma displacement. Slip-reconnection: the plasma elements P and Q are connected by a magnetic field line at time t_1 ; however, at a later time, t_2 , plasma elements exchange the magnetic field lines and do not remain connected by a magnetic field line.	22
1.9	An example of a 3D magnetic null point along with a spine-fan plane is shown in the Figure. The small yellow sphere represents the null point; the spine and fan plane are marked by arrows.	24
1.10	The Schematic represents an example of a magnetic separator. Blue and Red circles represent the negative and positive null points, whereas the separator is drawn in green; the picture adapted from (Pontin, 2011).	25
2.1	A schematic showing different phases indicated at the top; taken from (Benz, 2017).	33
2.2	The schematic shows a modified version of the CHSKP model for a solar flare, adapted from Shibata et al. (1995).	34
2.3	The figure depicts an example of flare onset by a 3D magnetic null; adapted from Nayak et al. (2021).	36
2.4	Two different types of jets, (a) an anemone jet, and (b) a two-sided jet; picture credit: (Shen, 2021). The arrow marks highlight the bright points near the base of both jets.	37
2.5	The Figure depicts two 3D magnetic nulls (in pink) and their associated field lines; picture taken from Nayak et al. (2019).	38
2.6	The sequence of field lines evolution, showing the magnetic reconnection and covering the duration of the jet; picture adapted from Nayak et al. (2019).	39

2.7	Identified coronal bright points in the quiet-Sun region; picture adapted from Zhang et al. (2001).	41
2.8	The schematic shows the several possible configurations leading to CBP, where (i) pre-interaction, (ii) interaction, (iii) cancellation, and (iv) final phases, for (a) equal and opposite, (b) unequal and opposite, (c) a large bipolar and a small unipolar, and a weak bipolar and a strong unipolar magnetic fragments. The schematic has been adapted from Priest et al. (1994).	42
2.9	Figure shows the identified CBPs in SXR and EUV channels at 01:01 UT. The picture adapted from Zhang et al. (2012).	43
2.10	Top view (left) and side view (right) of the coronal magnetic field feature around the two CBPs. The picture adapted from Zhang et al. (2012).	44
2.11	Figure depicts the association of 3D null point fan-dome structure with observed X-ray emissions from CBPS in CH regions. The picture has been taken from Galsgaard et al. (2017).	44
2.12	Figure depicts the potential 3D null point configuration for $p = 1$.	49
2.13	Figure depicts the example of non-potential 3D null point configuration for $J_{\perp} = 0$, $J_{thresh} = 2$ and $J_{\parallel} = 1$, i.e., $ J_{\parallel} < J_{thresh}$ (panel (a)), where $p = 1$, is used. Panel (b) depicts for $ J_{\parallel} = J_{thresh}$ and depicts the example of non-potential 3D null point configuration for Eigenvalues ($\lambda_1 = 1, \lambda_2 = 1, \lambda_3 = -2$).	49
2.14	Figure depicts the example of non-potential 3D null point configuration for $J_{\parallel} = 3, J_{\perp} = 0$ (panel (a)), $J_{\parallel} = 5, J_{\perp} = 0$ (panel(b)), and $J_{\parallel} = 5, J_{\perp} = 5$ (panel (c)).	50
2.15	Panel (a) depicts the example of the positive 3D null point where fan field lines are directed away from null whereas spine field lines are directed toward the null resulting in topological degree -1 , whereas fan field lines directed toward null point making topological degree $+1$ is shown in panel (b).	51

-
- 3.1 The different filters of AIA centered on specific wavelength and their corresponding observing solar atmosphere regions and different characteristic temperatures are listed in the table. The table has been adapted from Lemen et al. (2012). 58
- 3.2 The figure depicts the model of plasma β variation with height. The figure has been adapted from Gary (2001). 61
- 3.3 The flow chart of coronal magnetic field extrapolation algorithm to obtain extrapolated coronal magnetic field, using single-layer vector magnetogram. The figure has been taken from Hu et al. (2010). 63
- 4.1 Initial magnetic field configuration (left panel), which includes a potential (current free) 3D null located at the center of the box. The null point is shown by plotting the isosurface ψ (black surface) marked by an arrow. The two sets of field lines constituting the upper spine (in red color) and lower spine (in blue color) are fanning out in the fan plane (marked by arrows). For more details, the magnified view of the selected region (rectangular box) is shown in the right panel. The magnetic field lines in the upper and lower spine are directed toward the 3D potential null (null is shown by the black isosurface) and receding away from the null point in the fan plane, making the topological degree -1 89

- 4.2 Evolution of grid averaged magnetic (solid line) and kinetic (dashed line) energies normalized to their respective initial values. The magnetic energy increases as a consequence of the deformation of magnetic field lines due to the initial sinusoidal flow until $t \approx 10$ s. Afterward, it gets somewhat flattened in $t \in \{10, 15\}$ s. The total energy density (magnetic + kinetic) increases inside the volume. Consequently, the increment in kinetic energy is seen, and it gets arrested by the viscosity, showing a peak around $t \approx 3.2$ s. Subsequently, it starts increasing sharply as a result of magnetic reconnection in the current sheet near the central null showing another peak at $t \approx 15$ s. Within this span, the primary null pairs get generated. With time the spiral null (a constituent of a pair of nulls) gets more twisted—as shown in Figure 4.7. The increase in twist may result in the observed increase in magnetic energy. 91

- 4.3 The snapshots of the figure spanning time $t \in \{0, 3.2\}$ s represent the evolution total energy density (magnetic + kinetic) through Direct Volume Rendering (DVR). The color scale of the DVR represents the magnitude of the total energy density and is shown in the bottom right corner. At $t = 0$ s, the maximal energy density (pink) is at the top and bottom boundaries. With the evolution, maximal energy increases inside the volume (pink color) (c.f. panels (a)-(f)). Ultimately, an increase in the magnetic and kinetic energy is seen in the same time span. 92

- 4.4 The snapshots of the figure spanning $t \in \{0, 14.544\}$ s represent the evolution of the field lines. Here, the field lines are traced in time (the same field lines are traced by keeping the corresponding initial point of a field line invariant). At the $t = 0$ s, a current free radial null is located at the center of the box, and the red field lines are plotted near this central null. In panel (a), a set of auxiliary field lines (green and pink) in the first quadrant and (yellow and blue) are plotted in the third quadrant to demonstrate the null generation. The sinusoidal flow bends the spine towards the fan plane and consequently, pushes the auxiliary field lines to bend (panel (b)). Further evolution generates the elbow shape structure (panel (c)-(e)) and develops current intensity accordingly, as shown in panel (c) onward. The magnitude of current density $|\mathbf{J}| / |\mathbf{B}|$ is shown through DVR. Green (in the first quadrant) and blue (in the third quadrant) field lines are changing their connectivity see panel (e)—a sign of magnetic reconnection. Consequently, 3D null in the pairs has been generated at $t = 14.544$ s (panel (f)). Each pair consists of a radial and spiral null marked by arrows. 94

- 4.5 The snapshots of this Figure plot the selected magnetic field lines of the first quadrant and advected through plasma flow in $t \in \{14.496, 14.544\}$ s to illustrate the magnetic reconnection in null creation. Notably, here and hereafter, while advecting field lines, care has been taken to select seed points in the flow such that they always remain away from the reconnection region i.e., in the ideal region of the plasma, allowing identification of reconnection. For example, in this case the coordinates of seed points at $t = 14.544$ s are $(-0.003\pi, 0.630\pi, 0.322\pi)$, $(-0.002\pi, 0.625\pi, 0.328\pi)$, $(-0.001\pi, 0.586\pi, 0.316\pi)$ and $(-0.005\pi, 0.586\pi, 0.316\pi)$ for the four depicted field lines whereas the location of the current enhanced region is $\approx (-0.008\pi, 0.556\pi, 0.296\pi)$ in x , y and z directions. The development of the elbow shape is clearly visible in panels (a) and (b), which becomes most prominent in panel (c). Further, Across panels (c) and (d), one of the two green field lines changes its connectivity by moving from the right to the left of the elbow. Such changes in the connectivity of a single field line are suggestive of magnetic reconnection. Topological features such as the radial and spiral nulls along with their spine and fan plane of the radial null are marked by arrows in panel (d)—which are in concurrence with the same features depicted in panel (f) of Figure 4.5. Similarly, the pink field lines also change their connectivity through magnetic reconnection. 95

- 4.6 The plot shows the variation in average magnetic energy normalized to its corresponding value at $t = 14.0$ s. The average is taken over a subvolume of physical extent $\{(-0.143\pi, 0.111\pi); (0.396\pi, 0.650\pi); (0.111\pi, 0.365\pi)\}$ in x , y and z directions constituting the null pair at the first quadrant. The vertical axis represents the magnitude of average magnetic energy normalized to its corresponding value at 14.0s, and the horizontal axis represents time (in seconds). The monotonic decrease of magnetic energy in $t \in \{14.0, 14.544\}$ s corroborates the magnetic reconnection. 96
- 4.7 The snapshots of field lines spanning $t \in \{14.544, 18.128\}$ s represents the evolution of nulls. Here, the nulls are traced in time through the trilinear technique, and field lines are drawn to the locations of nulls. At $t = 14.544$ s, primary null pairs have been detected for the first time, and field lines are plotted near them, shown in panel (a). In subsequent panels, nulls are traced, and the twist of field lines of spiral null is increasing. Consequently, nulls of a particular pair are receding from each other (compare panels (a)-(j)). Simultaneously, the increase in the current density near the spiral null is also seen with the help of DVR of $|\mathbf{J}|/|\mathbf{B}|$. In each pair, one is radial null and another is spiral null (more details can be seen in Figure 4.8). Radial and spiral nulls are marked by arrows in panel (a) (the time instance when nulls have been generated in the system and in panel (j) (the time instance at which the first quadrant null pair is at maximum separation), only not in other panels so that the null structures can be seen clearly. . . . 97

- 4.8 Figure illustrates the detailed structure of nulls in a pair. The first quadrant null pair consists of a radial null and a spiral null (panel (a)). The field lines of radial null are plotted in (green), and that of a spiral null is plotted in (pink). The direction of spine field lines of radial null is towards the null point and away from the null point in the fan plane, making the topological degree -1 , whereas the direction of spine field lines of spiral null is away from the null point and towards the null point in the fan plane resulting the topological degree $+1$. Therefore, the net topological degree of this pair is zero, and the net topological degree of the system remains unaffected. Similarly, panel (b) illustrates details of the third quadrant null pair, which also consists of a radial null and a spiral null. The field lines of radial and spiral null are drawn in yellow and blue, respectively. The direction of spine field lines of radial null is towards the null point and receding away from the null point in the fan plane making the topological degree -1 whereas the direction of spine field lines of spiral null is away from the null point and towards the null point in the fan plane resulting the topological degree $+1$. The conservation of the topological degree is self-explanatory. 98

- 4.9 The snapshots of field lines spanning the $t \in \{0, 15.2\}$ s illustrate the evolution of central null marked by 3D null in the figure (the initial current free radial null located at the center of the box). The spine and fan field lines of the initial null are plotted in red and blue (panel(a)), with red field lines constituting the upper spine while field lines in blue belong to the lower spine. With the evolution, the current sheet (CS) near the central null develops which facilitates the magnetic reconnection in the current sheet. Panel (b) shows an intermediate field line structure in which the current sheet has been started to develop (identified with DVR of large $|\mathbf{J}| / |\mathbf{B}|$). The color scale of the DVR (right bottom corner) represents the magnitude of the current intensity. The blue and red field lines slip over the fan plane, and an intermediate structure is shown in panel(c) before the reconnection in the CS near the central null. The red and blue field lines are changing their connectivity (evident by panels (d)-(h)) and become part of the lower and upper spine, earlier at $t = 0$ s (panel (a)), red and blue field lines were only part of the upper and lower spine respectively. The corresponding magnetic energy decrease is shown in Fig. 4.10. 100

- 4.10 The plot shows the variation in average magnetic energy spanning time $t \in \{10.0, 15.2\}$ s. The vertical axis represents the normalized average magnetic energy, and the horizontal axis represents the time (in seconds). The plot shows the decrease in magnetic energy with time, which is averaged over the subvolume of physical extent $\{(-0.111\pi, 0.079\pi); (-0.111\pi, 0.079\pi); (-0.111\pi, 0.079\pi)\}$ in x , y and z directions constituting the central null and normalized to its initial value at $t = 10$ s (the approximate time when reconnection started in the current sheet near the central null). The decrease in magnetic energy corroborates the magnetic reconnection near the central null. In the same time span, the increase in the kinetic energy is seen (see Fig.. 4.2), the whereas magnetic energy of full volume remains somewhat flattened. 101

- 4.11 Figure illustrates the inflow and reconnection outflow at the central null using pink and blue arrows at a time $t = 10.56$ s. The red field lines are drawn to demonstrate the central null. The pink and blue arrows heading toward null represent the inflow, whereas those pointing away from central null represent the reconnection outflow. This outflow further confirms the reconnection at central null. The plotting of reconnection outflow is possible here because the central null is also a stagnation point. In contrast, in other reconnection locations, the flow is a superposition of evolved plasma flow and reconnection outflow (not separable). 102

4.12 The snapshots of the figure illustrate the evolution of the null first quadrant pair, which consists of a radial null and a spiral null. Here, nulls are traced in time, and field lines are plotted near them to show evolution. Radial (pink) and Spiral (green) null, along with its fan and spine, are marked by arrows. Panel (a) depicts radial and spiral null field line configurations at $t = 16.608$ s. The twist of the spiral null decreases, and consequently, nulls come closer to each other (the decrease in separation can be seen by comparing panels (a) and (b)) as they evolve in time. The decrease continues until the nulls in the pair is annihilated (panel (c)). The physical process behind annihilation is identified and is shown in Fig.4.13. A similar process is also seen in the case of the third quadrant null pair. 103

4.13 The snapshots of the figure spanning $t \in \{16.640, 16.992\}$ illustrate the physical process responsible for the annihilation of nulls of the first quadrant pair (shown in figure 4.12). The field lines are traced in time, and the time span of this figure is chosen for demonstration purposes of the physical process. Panel (a) illustrates the configuration at $t = 16.640$ s with the pink field lines mainly constituting the spiral null, fan plane, and the lower spine of the radial null, and the green field lines belonging to the radial null constituting the upper spine and fan plane (marked by arrows). The current intensity is shown with the help of DVR of $|\mathbf{J}| / |\mathbf{B}|$. In subsequent panels, the pink field lines change the connectivity through reconnection at the radial null, and simultaneously, the twist is reduced. The pink field lines become part of the upper spine and fan plane of radial null (panel (a)-(d)). Consequently, nulls will come close to each other as the twist decreases. This process continues till the nulls get annihilated. 105

- 4.14 The snapshots of the figure spanning $t \in \{18.5600, 18.624\}$ highlight the dynamics of selected magnetic field lines belonging to the first quadrant nulls and advected with the plasma flow velocity. The change in connectivity of field lines from panel (a) to (d) is a clear indication of reconnection. 106
- 4.15 The plot shows the variation in separation with time between nulls of the first quadrant null pair. The vertical axis represents the separation between the two nulls of a first quadrant pair, and the horizontal axis represents the time (in seconds). The separations of nulls start increasing with time and show a peak around $t = 18.2$ s, then decrease with time, and finally, nulls get annihilated around $t = 19.3$ s. A similar variation is also seen for the third quadrant null pair. 107
- 4.16 The plot illustrates the evolution of volume averaged $|\mathbf{B} \cdot \nabla \mathbf{B}|$ normalized to its initial value in the range $t \in \{14.54, 19.31\}$ s—covering the total duration in which the nulls (in the first quadrant) get generated and later, annihilated. The average is taken over a physical volume of extent $\{(-0.174\pi, 0.143\pi); (0.333\pi, 0.650\pi); (0.111\pi, 0.429\pi)\}$ in x, y and z coordinates, enclosing the null pair throughout their evolution. The plot shows an initial increase in magnetic tension along with the increase in separation between the nulls. Subsequently, as the nulls approach each other, the tension decreases. The vertical axis represents the modulus of normalized averaged magnetic tension, and the horizontal axis represents time (in seconds). 108

4.17 Panels ((a)-(f)) illustrate the locations of nulls with time. The location of nulls is traced through the trilinear null detection technique and located then in the 64^3 grid by using a Python 3D point plot. The red, blue, and green dots represent the locations of central, primary, and spontaneously generated nulls, respectively. At $t = 0$ s, only a central null is present (panel (a)). With evolution, the primary nulls are generated, and locations are shown in panel (b) along with central null at time $t = 14.72$ s. The nulls also get generated spontaneously with further evolution in time. The locations of spontaneously generated along with the central and primary nulls at time $t = 18.4, 18.88, 20.16$ and 20.32 s are shown in subsequent panels (c)-(f). The spontaneously generated null pair (shown in panel (d)) is considered for the detailed study based on the time tractability of the pair and can be confirmed by the estimating time from panels (d) and (f), which mark the approximate time of generation and annihilation, respectively. . . 109

4.18 The panels (a)-(c) illustrate the evolution of field lines by tracing in time, which leads to the spontaneous generation of null pairs. The field line configuration at $t = 18.400$ s (panel (a)) changes to another configuration at $t = 18.762$ s and develops the elbow-type structure (marked by an arrow in panel (b)). The enhancement in current intensity (identified by DVR of $|\mathbf{J}| / |\mathbf{B}|$) is seen accordingly. Further evolution makes the red and blue field lines helical through magnetic reconnection and, as a consequence, spontaneously generates a radial and a spiral null (marked by arrows in panel (c)). In subsequent panels (d)-(f), nulls are traced, and field lines are drawn at them. With evolution, the twist of the spiral null increases, and consequently, the nulls recede from each other. The increase in separation can be clearly seen by comparing panels (c)-(f). 110

- 4.19 The selected field lines (one blue, one red, and two green colors) are plotted and advected with plasma flow to illustrate the magnetic reconnection in spontaneous null generation. The field lines are moving with the plasma velocity (panels (a)-(c)). Later, across panels (c) and (d), one of the two green field lines is changes its connectivity and traverses through the left of the red and blue field lines. Such change in connectivity is through magnetic reconnection. To illustrate the developed structure clearly, the region marked by a rectangular box has been zoomed in and shown in the inset of panel (d), in which the spine and fan plane of radial and spiral null are marked by arrows. 111
- 4.20 Figure illustrates the details of a spontaneously generated null pair, which also consists of a radial and spiral null. The field lines are drawn near the radial (in green) and that of the spiral null (in red). The spine and fan plane of both nulls are marked in the figure. The direction of fan field lines of radial null is towards the null point and that of the spine field lines is directed away from the null point making topological degree +1 whereas the spine field lines of spiral null are directed towards the null point and directed away from the null point in the fan plane resulting the topological degree -1 . The net topological degree of this pair is zero and the conservation of net topological is self-explanatory. 112
- 4.21 This plot shows the variation in separation with time between nulls of a spontaneously generated pair. The vertical axis represents the separation between the two nulls, and the horizontal axis represents the time (in seconds). The nulls are being generated around $t \approx 18.688\text{s}$ with a separation. The separation initially increases, followed by a decrease, ultimately leading to the annihilation around $t \approx 20.35\text{s}$. The spontaneous null pair shows a similar behavior as seen in the case of primary null (see Fig.. 4.15).113

4.22 The snapshots of magnetic field lines illustrate the annihilation of spontaneously generated null pairs. To identify the physical process behind this phenomenon, field lines are traced (panels (a) to (b)) in time. The current density near the nulls is shown using DVR of $|\mathbf{J}|/|\mathbf{B}|$. In panel (a), the red field lines constitute the spine and fan plane of the spiral null, and the two green field lines constitute the lower spine of the radial null traverses through the right side of the spiral null. One of the two green field lines changes its connectivity, belongs to the upper spine of the radial null, and traverse the left of the spiral nulls (panel (b)). Such changes in connectivity are a telltale sign of magnetic reconnection. The twist of the spiral null decreases with time, and consequently, nulls come towards each other. This process continues until the nulls annihilate. Panels (c)-(f) illustrate the null annihilation in which nulls are traced in time, and the neighboring field lines are drawn near them. The nulls get annihilated at $t \approx 20.320$ s in pair as expected from the conservation of the topological degree (panel (f)). 114

4.23 The plot shows the variation in average magnetic tension spanning the time $t \in \{18.688, 20.304\}$ s and normalized to its corresponding initial value at $t = 18.688$ s. The average is over a subvolume of physical extent $\{(-0.047\pi, 0.016\pi); (0.396\pi, 0.555\pi); (0.396\pi, 0.429\pi)\}$ in x , y and z directions constituting the spontaneously generated null pair. The vertical axis represents the normalized average magnetic tension, and the horizontal axis represents the time (in seconds). The increase and decrease of magnetic tension is visibly compatible with the corresponding change in inter-null separation of spontaneously generated pair. 115

- 4.24 The figure illustrates the evolution of magnetic configuration enclosing a potential 3D null (panel (a)) in 128^3 resolution. Four sets of auxiliary field lines (in Blue, Pink, Cyan, and Green) are drawn to demonstrate the generation and annihilation of nulls. With the evolution, the auxiliary field lines develop an elbow shape (panel (b)), and subsequently, a pair of 3D nulls, which consists of radial and spiral 3D nulls, get generated (panel (c)) at $t = 14.96$ s. As they evolve, the separation between the nulls increases after their generation till around $t = 16.40$ s (panel (d)), and subsequently, starts decreasing (panel (e)) until their pairwise annihilation (panel (f)). The increase and decrease of magnetic tension is visibly compatible with the corresponding change in inter-null separation of spontaneously generated pair 117
- 5.1 Panel (a) depicts the Geostationary Operational Environmental Satellite (GOES) soft X-ray flux over the duration of the flare in the $1 - 8 \text{ \AA}$ channel. This graph illustrates a gradual increase in intensity starting around 02 : 45 UT (marked by the dashed vertical line), with the peak occurring at 03 : 04 UT (dash-dot vertical line). Our simulations cover the time range from 02:48 to 02:56 UT, as marked by two blue vertical solid lines during the rising phase of the flare. The photospheric flux variation for approximately 13 minutes, starting from 02 : 44 : 41 UT, is shown in panel (b), where the solid line represents positive flux and the dashed line represents negative flux. 124
- 5.2 The plot illustrates the variation in minimized deviation (E_n) with the number of iterations (k) for Non-Force Free Field extrapolation. This deviation decreases monotonically and saturates approximately at $\approx 36.3\%$ for 1500 iterations. 126

- 5.3 Panel (a) of the Figure depicts the direct volume rendering (DVR) of the magnitude of Lorentz force, showing the presence of the Lorentz force at lower heights. To further corroborate this observation, the logarithmic variation in the horizontally averaged strength of Lorentz force with height (z) is shown in panel (b). As expected, the logarithmic value of horizontally averaged Lorentz force decreases with height. Notably, the Lorentz force density is non-zero near the photosphere and nearly vanishes at coronal heights, similar to the typical description of the solar corona. . . . 127
- 5.4 The panel (a) illustrates the overall evolution of the number of nulls over time. The vertical axis represents the number of nulls, while the horizontal axis represents time (in seconds). As time progresses, the overall number of nulls decreases. At $t = 0s$, there are approximately 4000 nulls are present, which are distributed as depicted in panels (b) and (c) (panel (c) is from a different angle to show the distribution). The size of the box is 324.8Mm, 185.6Mm and 139.2Mm in x-, y- and z-direction respectively. The nulls are primarily located in the lower solar atmosphere, with some also found in the higher solar atmosphere (refer to panel (c)). 130
- 5.5 The figure illustrates the evolution of radial nulls over time. Nulls are traced in time, and field lines are drawn at their locations. The variation in magnitude of current intensity (identified by the Direct Volume Render (DVR) of $|\mathbf{J}| / |\mathbf{B}|$) is shown by the color bar. At $t = 120.032s$ (panel (a)), nulls are spontaneously created in pairs, and the trilinear null detection technique detects them simultaneously. The generated null pair consists of two radial nulls and are shown as radial null_1 and radial null_2 in the figure. It can be verified by collapsing them into 2D, where they appear to be akin to X-type nulls (shown in the inset of panel (a)). As the evolution continues, both radial nulls move away from each other after their generation (see panels (a)-(f)). 131

- 5.6 Magnetic field lines are traced in time and advected with plasma flow. The evolution shows the creation of nulls in pairs, consisting of two radial nulls marked as radial null_1 and radial null_2. The enhanced current intensity is overlaid using the DVR tool in VAPOR. At $t = 118.096\text{s}$, two green field lines connect from regions a to b and from e to d, while two pink field lines connect from regions c to d (panel (a)). During the evolution, one pink field line changes its connectivity from regions c to d and reconnects to regions c to a, and one green field line also changes its connectivity from regions b to a to regions b to d (panel (b)). Simultaneously, two radial nulls are created and marked by arrows in panel (b). Such changes in the connectivity of field lines represent magnetic reconnection. 133
- 5.7 The figure details the topological features of spontaneously generated radial nulls at time $t = 193.6\text{s}$. Two radial nulls are generated simultaneously and are marked by arrow as radial null_1 and radial null_2. Green and pink field lines are drawn near the radial null_1 and radial null_2, respectively. The fan field lines (in green) of radial null_1 are directed toward the null, making topological degree +1, while the fan field lines (in pink) of radial null_2 are directed away from the null, making topological degree -1. 134

- 5.8 The figure depicts the footpoint brightening in the AIA 1600Å channel associated with slip reconnection. The spine and the fan plane of the radial null (marked as ‘null’) are indicated by white arrows. Two sets of field lines drawn near the radial null.2 demonstrate the foot point brightening associated with slip reconnection. The plasma flow is plotted near the $z = 0$ plane and shown by blue arrows. Notably, the red field line, marked by the white arrow at $t = 197.47\text{s}$, is initially anchored to point ‘a’ (panel (a)) changes its connectivity from point ‘a’ to point ‘b’ through slip reconnection (plasma flow direction is different from the field line motion), resulting in the associated brightening seen in panel (b). Subsequently, the red field line changes its connectivity from point ‘b’ to point ‘c’ and then to point ‘d’ (refer to panels (c) and (d)). The overlaid AIA channel has dimension approximately $32.63\text{Mm} \times 63.80\text{Mm}$ in x and y , respectively. 136
- 5.9 In this figure, the evolution of radial nulls is shown by tracing and drawing field lines over time. The field lines (in green) are drawn near the radial null.1, and field lines (in pink) are drawn at radial null.2. The spine and fan plane of radial nulls are marked by arrows. With the evolution, radial nulls are approaching each other (panels (a)-(e)) and ultimately get annihilated at $t = 342.672\text{ s}$ (panel (f)). 137
- 5.10 Field lines are traced in time and advected with plasma flow. Five green and pink field lines are initially part of the spine and fan plane of radial null.1 and radial null.2, respectively (panel (a)). With the evolution, the green and pink field lines change their connectivity and get disconnected from the nulls. Consequently, the nulls are approaching each other and ultimately annihilate each other, as shown in Figure 5.9. 139

- 5.11 The figure depicts foot point brightening (marked by circles) in the AIA 1600 Å channel associated with magnetic reconnection, which annihilates the radial nulls. With the evolution (panels (a)-(d)), nulls are approaching each other with a change in connectivity of field lines, and the corresponding footpoint locations of field lines are co-spatial with the increased intensity in AIA 1600 Å filter, emulating the telltale signs of magnetic reconnection. The overlaid AIA channel has dimension approximately $32.63\text{Mm} \times 63.80\text{Mm}$ in x and y , respectively. 140
- 5.12 The panels of the figure illustrate the generation of nulls in a pair near a pre-existing 3D null. Magnetic field lines (in red) are drawn near the pre-existing null (a null already present at $t = 135.52\text{s}$), while sky-blue and green field lines are included to facilitate the generation of nulls at a later time (panel (a)). With the evolution, the sky-blue and green field lines develop an elbow shape at around $t = 160.69\text{ s}$, and an enhancement in current intensity (identified by the Direct Volume Render of $|\mathbf{J}| / |\mathbf{B}|$), marked as ‘cs’, is seen accordingly (panel (b)). In panel (c), a pair of nulls consisting of a radial and a spiral null is generated at $t = 164.56\text{ s}$. Panels (c)-(d), spanning $t \in 164.56, 178.11\text{ s}$, depict the tracing of nulls and the plotting of field lines. As the evolution progresses, the radial and spiral nulls move away from each other after their generation, whereas the spiral null of the generated pair approaches the pre-existing null 141

- 5.13 The figure illustrates the details of a pre-existing null along with a spontaneously generated null pair, which consists of a radial null and a spiral null at $t = 178.11$ s. The field lines (in red) are drawn near the location of the pre-existing null. The fan field lines are directed toward the null, resulting in a topological degree of +1. Field lines drawn near the radial null (in sky blue) and those of the spiral null (in green) are also shown. The spine and fan planes, along with the topological degrees of both nulls, are marked in the figure. The direction of the fan field lines of the radial null is toward the null point, and the spine field lines are directed away from the null point, resulting in a topological degree of +1. On the other hand, the spine field lines of the spiral null are directed toward the null point in the fan plane and away from the null point, resulting in a topological degree of -1. The net topological degree of this generated pair is zero, and the spiral null gets annihilated with the pre-existing null (in a pair). Therefore, the conservation of the net topological degree is self-explanatory. 142
- 5.14 Panels depict the footpoint brightening corresponding to the slip reconnection of fan field lines of the radial null of the spiral-radial null pair-1. The radial null is marked as “null” and the local plasma flow shown by blue arrows is plotted near the $z = 0$ plane. Initially, at $t = 164.35$ s, the green field line indicated by the white arrow is anchored to point a (panel (a)). With the evolution, the footpoints of the green field lines are changing their connectivity to points b and c (panel (b)) and subsequently to points d, e, f, and g due to slip reconnection. The overlaid AIA channel has dimension approximately $21.75\text{Mm} \times 21.75\text{Mm}$ in x and y , respectively. . . . 143

- 5.15 Nulls are traced over time, and field lines are drawn near the locations of the nulls. Panels (a)-(d) of this figure illustrate the annihilation of a spiral null and a pre-existing null. The spine and fan planes of the radial, spiral, and pre-existing nulls are indicated by the arrows. 144
- 5.16 The figure illustrates the details of the radial null $t = 203.28\text{s}$, left in the domain after the annihilation of the generated spiral null with the pre-existing null. The fan field lines of the radial null point toward the null point, while the spine field lines are directed away from the null point, resulting in a topological degree of $+1$. . 145
- 5.17 The snapshots of the field lines represent the evolution of nulls as they are traced over time. At $t = 180.05$ seconds, it is the first instance when nulls in a pair first appear using the trilinear detection technique, and field lines are drawn near their locations (panel (a)). These spontaneously generated nulls are named radial-spiral-pair-2 and consist of a spiral null (in yellow) and a radial null (in pink). As the evolution progresses, the spiral and radial nulls are moving away from each other (panels (a)-(d)). The spiral null loses its spirality and gets converted into a radial null; the conversion from spiral to radial null can be verified by collapsing the null's structure in 2D, where a spiral null will appear as an "O" type and a radial null will appear as an "X" type null. Panels (e) and (f) depict the 2D projections of the spiral null and converted radial null at $t = 199.41\text{s}$ and $t = 267.17\text{s}$, respectively. This illustration shows a similar conversion from "O" to "X" type. . . . 147

- 5.18 The figure illustrates the topological details of spontaneously generated radial-spiral-pair-2 nulls at $t = 199.41$ s. These nulls are generated in a pair and consist of a spiral null (in yellow) and a radial null (in pink). The spine field lines (in pink) of the radial null are directed toward the null point, resulting in a topological degree of -1 , while the fan field lines (in yellow) of the spiral null are directed toward the null point, making a topological degree $+1$. The net topological degree of this local system is zero, and hence, the overall topological degree of the system remains unaffected by the generation of these new nulls. 148
- 5.19 The figure illustrates the evolution of nulls over time. These nulls are tracked as they evolve, and field lines are drawn at their locations. Yellow, green, and red field lines are drawn near the radial null of the radial-spiral-pair-2 null pair, the spiral null, and the radial null of a spontaneously generated new null pair, respectively. The spontaneously generated new nulls are first detected by the trilinear null detection technique at $t = 267.17$ seconds, and the corresponding structure is shown in panel (a). As the evolution continues, the spiral and radial nulls of the newly generated pair move away from each other, while the radial null of the radial-spiral-pair-1 pair and the spiral null of the newly generated null approach each other simultaneously (panels (a)-(c)), ultimately resulting in annihilation around $t = 294.27$ s (marked by no null in panel (d)). The pairwise annihilation does not affect the net topological degree of the system. Consequently, one radial null, with a topological degree of $+1$, is left in the system. 149

- 5.20 The figure illustrates the topological details of spontaneously generated new nulls near the radial null of the radial-spiral-pair-2 pair at $t = 274.91s$. These new nulls are generated in pairs and are marked by the arrows. The fan field lines (in yellow) of the radial null of the radial-spiral-pair-1 pair are directed toward the null point, resulting in a topological degree of $+1$. Meanwhile, the fan field lines (in green) of the spiral null of the spontaneously generated new pair are directed away from the null point, resulting in a topological degree of -1 . Lastly, the fan field lines (in red) of the radial null of the spontaneously generated pair are directed toward the null point, making the topological degree $+1$. Hence, spontaneous generation occurs in a pair, and the annihilation of the radial null of the radial-spiral-pair-1 pair is with the spiral null of the generated pair. Therefore, the net topological degree of the system remains unaffected by the generation and annihilation of 3D nulls. 150

- 5.21 Magnetic field lines are traced over a time span of $t \in [274.912, 280.720]$ s and advected with plasma flow. This time span is selected to investigate the dynamics of field lines responsible for annihilation. Four selected field lines, two green and two yellow, are drawn to illustrate magnetic reconnection. At $t = 274.912$ seconds, the two green field lines are part of the spine and fan plane of the spiral null, connecting from region b to region a (panel (a)), while the two yellow field lines are part of the upper and lower spine along with the fan plane of the radial null, connecting regions c to d and b. As the evolution progresses, the green field lines change their connectivity from region b to region a to region b to e. Similarly, one yellow field line also changes its connectivity from region c to d to region c to b (panel (b)). With further evolution, one yellow field line changes its connectivity from region c to b to region e' (panel (c)), and then from region e' to region b to region a' to region b. These changes in connectivity occur through magnetic reconnection, ultimately resulting in the annihilation of nulls in a pair. 151
- 6.1 The plot shows an increase in the number of nulls at a given instant and its maximal value over the temporal range with an increase in chaoticity. The vertical axis represents the number of nulls, and the horizontal axis represents time. The plots in different colors (pink, blue, green, and red) represent the variation in number of nulls for a particular value of the chaoticity (0.15, 0.20, 0.25, 0.30, respectively). Generation of nulls occur earlier in time as the chaoticity C increases, i.e., $t = (31, 23, 9, 8)$ s for $C = (0.15, 0.20, 0.25, 0.30)$ 158

6.2 Panels depict a sudden increase in chaoticity near the second peaks in number of nulls, followed by its decrease. The figure shows a local flux surface traversed by a single field line for $C = 0.3$ in $t \in \{16.08, 16.29\}s$, spanning the second prominent peak at $t = 16.18$. Panel (a) depicts a flux surface structure drawn at $t = 16.08s$, and the traversing field line is almost perfectly tangential to the surface and becomes part of the chaotic region with the evolution (panel (b)). Subsequently, the surface loses its coherent structure as the field line becomes more volume filling and hence chaotic. At $t = 16.18s$ (Panel (c)), which marks the second peak, the local flux surface is almost destroyed but reorganized itself at later times (panels (d) to (f)). 160

6.3 Figure depicts the evolution of nulls with time after their generation. Nulls are traced in time, and field lines in green, pink, and red are drawn near the spiral null_1 ($SN1$), spiral null_2 ($SN2$), and spiral null_3 ($SN3$), respectively. The color bar in panels depicts the magnitude of the $|\mathbf{J}|/|\mathbf{B}|$, where \mathbf{J} and \mathbf{B} represent current density and magnetic field. Panel (a) depicts the field lines structure near the nulls at $t = 8.27s$ when two spiral nulls ($SN1, SN2$) first appear. With the evolution, $SN1$ and $SN2$ move away from each other (Panels (b)-(e)), and $SN1$ changes its nature from a spiral to a radial null (panel (e)). Subsequently, this radial null reverts back to a spiral null (panels (f)-(h)) and eventually annihilates with a different spiral null_3 ($SN3$) formed in a distinct null pair generation process (panel (j)). 161

- 6.4 The figure illustrates the magnetic reconnections leading to the generation of two spiral nulls. Two pink and one green magnetic field lines are traced in time from ideal plasma elements in the vicinity of the footpoint marked ‘a’. The colorbar represents the same quantity $|\mathbf{J}|/|\mathbf{B}|$ as mentioned in Fig. 6.3. At $t = 8.21\text{s}$, all field lines connect from region a to region b (panel (a)). Subsequently (panels (a)-(c)), the green field line develops a more prominent elbow shape, but connectivity remains unchanged. Across panels (c) and (d), a green and one pink field line change connectivity—a telltale sign of reconnection. Subsequently, the second pink field line also changes connectivity (panels (d)-(e)) and generates two spiral nulls at $t = 8.27\text{s}$ (panel (e)). The spontaneously generated two spiral nulls are elaborated in panel (f). 163
- 6.5 Figure depicts the topological details of the two spontaneously generated spiral nulls at $t = 8.46\text{s}$ (panel (a)) and the null pair at $t = 8.86\text{s}$ (panel (b)). The fan field lines (in green) of spiral null_1 ($SN1$) are directed away from the null, resulting in a topological degree of -1 (panels (a) and (b)), whereas the fan field lines (in pink) of spiral null_2 ($SN2$) are directed towards the null, making a topological degree $+1$. The fan plane field lines of spiral null_3 ($SN3$) (in red) are directed towards the null point making topological degree $+1$ (panel (b)). With time, these two nulls get annihilated. 164

Chapter 1

Introduction

1.1 A brief introduction to magnetic topology

Topology, a branch of mathematics, studies properties of spaces that are invariant under any continuous deformation, such as bending, stretching, and shrinking, while disallowing, closing, or opening holes, passing through itself, and tearing or gluing the parts. It is sometimes called “rubber-sheet geometry” because the objects can be stretched and contracted like rubber but cannot be broken. Such transformations which preserve the topology but change the geometry are called homeomorphisms. An example of homeomorphism is the transformation of a doughnut into a coffee cup and vice versa. The doughnut and coffee cup are topological equivalent because both have one hole (handle); they can be mathematically or topologically transformed into one another without cutting them in any way (Fig. 1.1).

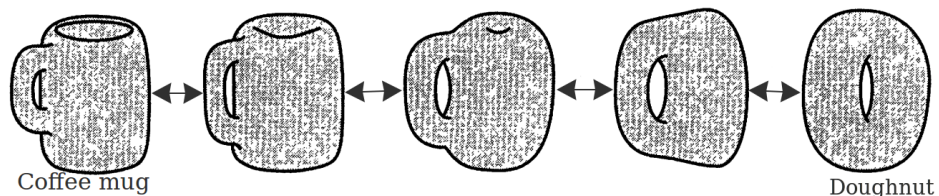


Figure 1.1: Figure represents the continuous transformation of a coffee cup into a donut and vice versa. Hence, these two are topologically equivalent.

Notably, both preservation and change in magnetic topology are important

contributing factors in deciding the terminal state of magnetized plasmas. For example, the theory of plasma relaxation is based on a comparative study of at least two physical quantities, one changing its topology, whereas for the other, the topology remains preserved for all practical purposes. The most celebrated among the relaxation theories is Taylor's theory of plasma relaxation (Taylor, 1974) where the magnetic topology represented by twists and writhes of magnetic field lines remains approximately conserved while the magnetic energy decays—leading to a state where the volume current density is parallel to the magnetic field: a force-free state. Such relaxations can also be envisaged to be occurring in solar flares; see Agarwal et al. (2024); Agarwal & Bhattacharyya (2024). In addition to twists and writhes, which are believed to be generated by photospheric dynamics, the generation of other magnetic configurations that contribute to the topology is not well understood and merits further attention—the focus of the thesis—built up after introducing the necessary concepts.

1.1.1 Homeomorphism

In mathematics, specifically in topology, homomorphism is a continuous bijective mapping function between topological spaces. It has a continuous inverse function that preserves all the topological properties of a given space. Two spaces with a homeomorphism between them are called homeomorphic, and are topological equivalent. Mathematically, A mapping function $f: X \rightarrow Y$ between two topological spaces (X and Y) is a homeomorphism if it has the following properties:

- f is a bijection (one-to-one and onto),
- f is continuous, and
- the inverse function f^{-1} is continuous.

The dynamics of solar coronal loops away from the reconnection regions can be an example of homeomorphism where the involved plasma flow transforms one morphology of any given magnetic field line into another one. The other

examples include slippage of magnetic field lines over a high squashing degree region—described later (Sect. 1.3.4) in the thesis.

1.2 Magnetic topology

Magnetic topology incorporates the properties of the magnetic field lines, such as the connectivities, linkages, and knottedness, which remains preserved under an ideal evolution (Parnell et al., 2015). Continuous transformations such as stretching and bending are examples of ideal evolution under which magnetic topology does not change. A change in magnetic topology implies a change in the connectivity of magnetic field lines—a non-ideal discontinuous process (Parnell et al., 2015). One such process in magnetized plasma is the magnetic reconnection: a process where field line connectivity changes along with the generation of heat and kinetic energy, can change magnetic topology (Parker, 1973; Hornig & Schindler, 1996) and is believed to be responsible for the solar transients. More details about magnetic reconnection can be found in Sect. 1.3. Magnetic reconnections are ubiquitous in space, astrophysical as well as laboratory plasmas, and their manifestations can be found in Earth’s magnetosphere, astrophysical jets, sawtooth crashes in tokamaks, and the accretion disks of astrophysical objects such as black holes, and neutron stars. Magnetic reconnection is one of the main mechanisms which can explain the million-degree Kelvin temperature of the solar corona (Parker, 1994).

Since favorable magnetic topology is required to initiate the magnetic reconnection, exploring it is crucial to understand the reconnection-driven various solar phenomena discussed in the following. Magnetic topology is immensely important because of its central role in onsetting various solar transients. Such transients can be solar flares (Aulanier et al., 2000; Masson et al., 2009; Edgar & Régnier, 2024), Coronal Mass Ejections (CMEs) (Ugarte-Urra et al., 2007), jets, and coronal bright points, can affect space weather.

Standardly, the astrophysical plasmas in general and solar plasmas in particular, can be approximated as a magnetized fluid governed by magnetohydro-

dynamics (MHD) description (Alfvén, 1942). The MHD description basically combines Navier-Stokes and Maxwell's equations, and are given by (in SI units)

- Momentum balance or force balance equation for incompressible fluid: Conservation of momentum

$$\rho \frac{d\mathbf{v}}{dt} = -\nabla p + \mathbf{J} \times \mathbf{B} + \rho\nu \nabla^2 \mathbf{v}, \quad (1.1)$$

where ρ , \mathbf{v} , p , \mathbf{J} , \mathbf{B} , and ν is the plasma density, flow velocity, kinetic pressure, current density, magnetic field, and the kinematic viscosity of the magnetofluid, respectively and $\frac{d}{dt}$ is total convective derivative or Lagrangian derivative, i.e., $\frac{d}{dt} = \frac{\partial}{\partial t} + \mathbf{v} \cdot \nabla$.

- Mass continuity equation: Conservation of mass

$$\frac{\partial \rho}{\partial t} + \nabla \cdot (\rho \mathbf{v}) = 0, \quad (1.2)$$

- Solenoidality condition

$$\nabla \cdot \mathbf{B} = 0, \quad (1.3)$$

- Ampere's law in pre-Maxwellian form

$$\nabla \times \mathbf{B} = \mu_0 \mathbf{J}, \quad (1.4)$$

- Faraday's Law

$$\nabla \times \mathbf{E} = -\frac{\partial \mathbf{B}}{\partial t}, \quad (1.5)$$

- Ohm's law

$$\mathbf{E} + \mathbf{v} \times \mathbf{B} = \mathbf{N}, \quad (1.6)$$

- Energy equation

$$\frac{d}{dt} \left(\frac{p}{\rho^\gamma} \right) = 0, \quad (1.7)$$

where \mathbf{N} in Eq. (1.6), is the non-ideal term and can be written as $\mathbf{N} = \eta \mathbf{J}$ for

resistive plasmas, where η is the electrical resistivity. In Eq. (1.7) γ is the ratio of the specific heat of the gas.

One of the fundamental MHD equations, namely, the induction equation for resistive plasma can be derived as follows: Taking curl of Eq. (1.6) and using $\mathbf{N} = \eta \mathbf{J}$,

$$\nabla \times \mathbf{E} + \nabla \times (\mathbf{v} \times \mathbf{B}) = \eta(\nabla \times \mathbf{J}), \quad (1.8)$$

from Eqs. (1.3) and the vector identity $\nabla \times (\nabla \times \mathbf{A}) = \nabla(\nabla \cdot \mathbf{A}) - \nabla^2 \mathbf{A}$, the Eq. (1.8) transforms to

$$-\frac{\partial \mathbf{B}}{\partial t} + \nabla \times (\mathbf{v} \times \mathbf{B}) = \frac{\eta}{\mu_0} (\nabla(\nabla \cdot \mathbf{B}) - \nabla^2 \mathbf{B}). \quad (1.9)$$

Using solenoidality condition i.e., Eq. (1.3), the Eq. (1.9) yields the Induction equation

$$\frac{\partial \mathbf{B}}{\partial t} = \nabla \times (\mathbf{v} \times \mathbf{B}) + \lambda \nabla^2 \mathbf{B}, \quad (1.10)$$

where $\lambda \equiv \eta/\mu_0$ is the magnetic diffusivity. This equation shows how the magnetic field \mathbf{B} evolves with time. The first term $\nabla \times (\mathbf{v} \times \mathbf{B})$ on the right-hand side of Eq.(1.10) is the advection term while the second term represents $(\lambda \nabla^2 \mathbf{B})$ is resistive diffusion. The ratio of advection to resistive diffusion is known as the magnetic Reynolds number, given by

$$R_M = \frac{L_0 v_0}{\lambda}, \quad (1.11)$$

where L_0 is length scale over which the magnetic field varies and v_0 is the characteristic speed. It is useful in determining whether the fluid flow will carry the magnetic field or the magnetic field will diffuse, which is essential for analyzing magnetohydrodynamic processes, e.g., if $R_M \gg 1$ (ideal limit) the advection processes dominate over diffusion, but if $R_M \ll 1$ (non-ideal limit) then the diffusive processes become dominant.

1.2.1 Ideal limit ($R_M \gg 1$)

Magnetic topology remains conserved in this limit as shown by [Hornig & Schindler \(1996\)](#). Conservation of topology means that the field lines of the vector field are deformed in a smooth manner so that their connections, knottedness, and linkage stay the same and no field lines are cut or reconnected. This is an example of a homeomorphism, i.e., a bijective transformation mapping, which maps a magnetic field configuration at time t_0 onto another magnetic field configuration at the later time t , as shown in Fig. 1.2. In addition to the conser-

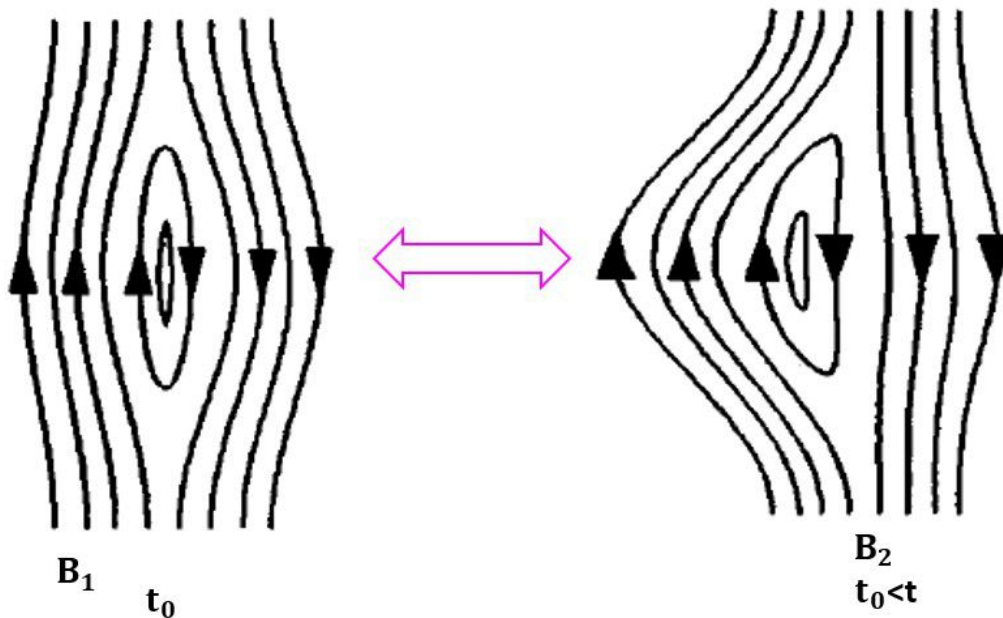


Figure 1.2: Schematic represents an example of Homeomorphism, the left field lines configuration represents the magnetic field \mathbf{B}_1 at time t_0 transformed into the field lines configurations shown on the right representing magnetic field \mathbf{B}_2 at the later time t ($t_0 < t$). Both field line configurations have similar magnetic topology. The image is adapted from [Hornig & Schindler \(1996\)](#)

vation of magnetic topology, the concepts of conservation of magnetic flux and magnetic field line are equally important to understand magnetic reconnection. In an ideal MHD limit, both the magnetic flux and magnetic field lines remain conserved, as discussed below:

Conservation of magnetic flux

In the limit of $R_M \gg 1$, Alfvén theorem (Alfvén, 1942) states that magnetic flux through any closed curve remains conserved—the flux-freezing condition, implying that the magnetic field lines are frozen-in or tied to the plasma, i.e., field lines move with the plasma parcels (Priest, 2014). For example, magnetic field lines trace the plasma loops observed in the corona, shown in Fig. 1.3. In this limit, the Induction equation reduces to

$$\frac{\partial \mathbf{B}}{\partial t} - \nabla \times (\mathbf{v} \times \mathbf{B}) = \mathbf{0}. \quad (1.12)$$

To prove the theorem, one needs to show that the rate of change of magnetic flux in a closed contour moving with a local plasma velocity remains constant with time. Consider a surface S bounded by a closed contour C , which moves with a plasma velocity. Then an elementary magnetic flux Φ , for a constant magnetic field, through an infinitesimal area dS is

$$d\Phi = \mathbf{B} \cdot \hat{n} dS, \quad (1.13)$$

where \mathbf{B} is a constant magnetic field and \hat{n} is the unit vector normal to dS . The change in the flux will be achieved by change in magnetic field strength crossing at a fixed location with time $\partial \mathbf{B} / \partial t \cdot \hat{n} dS$, and the change in the magnetic field at two points separated by an infinitesimal length dl moving with velocity \mathbf{v} with respect to time $\mathbf{B} \cdot (\mathbf{v} \times dl)$. Combining these, the total flux change through the contour C can be written as

$$\frac{d}{dt} \int_s \mathbf{B} \cdot \hat{n} dS = \int_s \frac{\partial \mathbf{B}}{\partial t} \cdot \hat{n} dS + \int_C \mathbf{B} \cdot (\mathbf{v} \times dl). \quad (1.14)$$

Using the vector identity $\mathbf{a} \cdot (\mathbf{b} \times \mathbf{c}) = (\mathbf{a} \times \mathbf{b}) \cdot \mathbf{c}$, the second term on the RHS of Eq. (1.14) can transform to

$$\mathbf{B} \cdot (\mathbf{v} \times dl) = -(\mathbf{v} \times \mathbf{B}) \cdot dl. \quad (1.15)$$

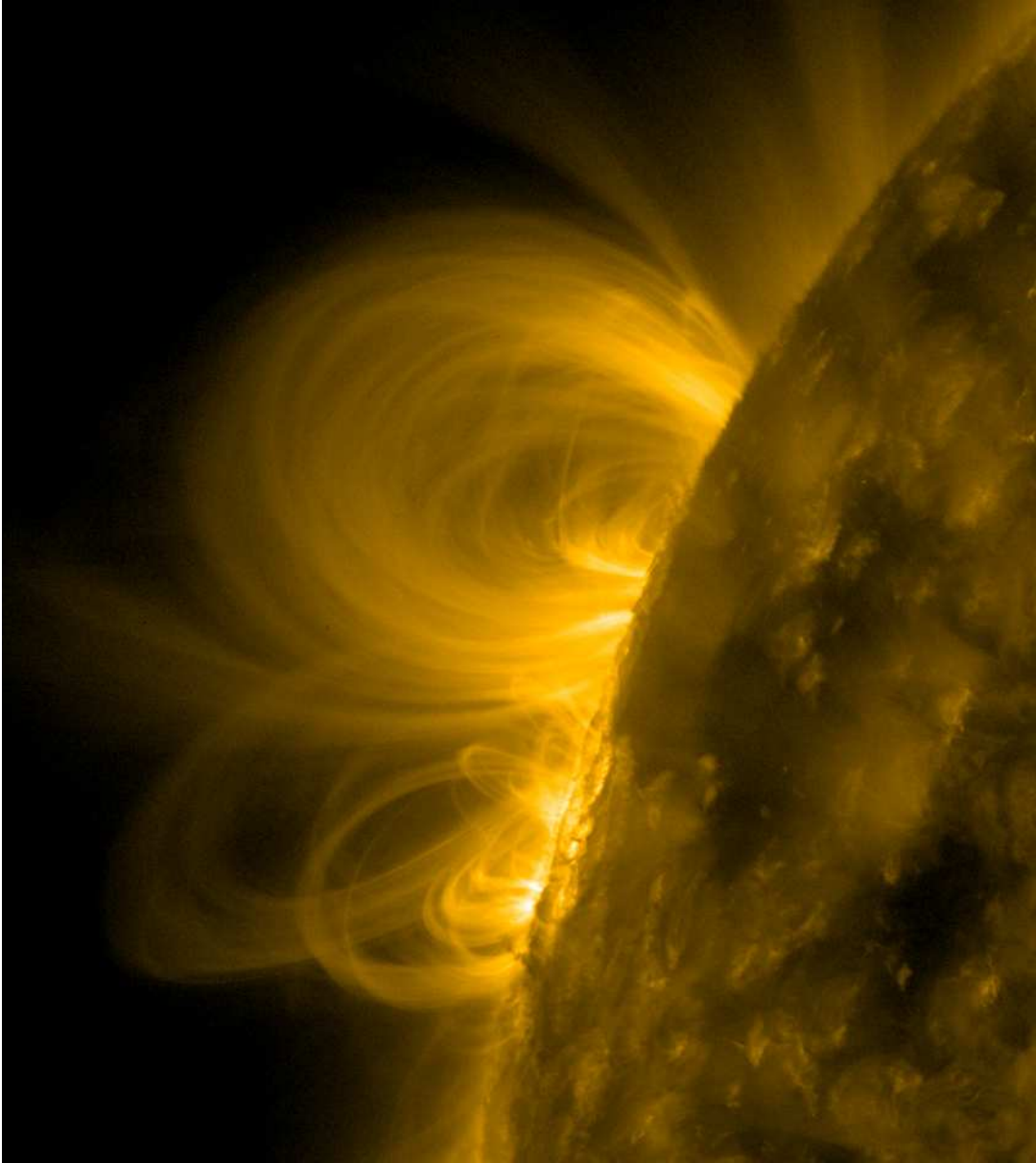


Figure 1.3: Example of solar coronal loops observed by the Transition Region And Coronal Explorer (TRACE), 171Å filter. These loops have a temperature of approximately 10^6 K. These loops contrast greatly with the cool chromosphere below. (<https://upload.wikimedia.org/wikipedia/commons/9/93/Traceimage.jpg>)

Now, Eq. (1.14) will be

$$\frac{d}{dt} \int_s \mathbf{B} \cdot \hat{n} dS = \int_s \frac{\partial \mathbf{B}}{\partial t} \cdot \hat{n} dS - \int_C (\mathbf{v} \times \mathbf{B}) \cdot d\mathbf{l}. \quad (1.16)$$

Using the Stoke's theorem

$$\int_C (\mathbf{v} \times \mathbf{B}) \cdot d\mathbf{l} = \int_s (\nabla \times (\mathbf{v} \times \mathbf{B})) \cdot \hat{\mathbf{n}} dS. \quad (1.17)$$

Eq. (1.16) becomes

$$\frac{d}{dt} \int_s \mathbf{B} \cdot \hat{\mathbf{n}} dS = \int_s \left(\frac{\partial \mathbf{B}}{\partial t} - (\mathbf{v} \times \mathbf{B}) \right) \cdot \hat{\mathbf{n}} dS. \quad (1.18)$$

From Induction Eq. (1.12), the above Eq. (1.18) turns out to be

$$\frac{d}{dt} \int_s \mathbf{B} \cdot \hat{\mathbf{n}} dS = 0, \quad (1.19)$$

and hence, the magnetic flux remains conserved.

Conservation of magnetic field lines

In ideal plasmas, the conservation of magnetic field lines follows from the conservation of magnetic flux. The concept of magnetic field lines can be illustrated by writing the ideal Induction equation in the following convenient form

$$\frac{\partial \mathbf{B}}{\partial t} + (\mathbf{v} \cdot \nabla) \mathbf{B} = (\mathbf{B} \cdot \nabla) \mathbf{v} - \mathbf{B} (\nabla \cdot \mathbf{v}). \quad (1.20)$$

The first term on the RHS of Eq. (1.20) represents that the magnetic field strength increases due to either acceleration of plasma parcel along the field or the shearing motion normal to the field, resulting in the change of direction of the field by increasing the field component along the flow direction. The second term on the right-hand side suggests the decrease and increase in the field strength depending upon the expansion ($\nabla \cdot \mathbf{v} > 0$) and compression ($\nabla \cdot \mathbf{v} < 0$) of plasma, respectively. The mass continuity equation (Eq. (1.2)) can be written as.

$$\frac{\partial \rho}{\partial t} + \mathbf{v} \cdot \nabla \rho = -\rho (\nabla \cdot \mathbf{v}), \quad (1.21)$$

the rearrangement of Induction equation (Eq. (1.20)) and use of Eq. (1.21) gives

$$\frac{d}{dt} \left(\frac{\mathbf{B}}{\rho} \right) = \left(\frac{\mathbf{B}}{\rho} \cdot \nabla \right) \mathbf{v}. \quad (1.22)$$

The Eq. (1.22) suggests that field lines are moving with plasma. To visualize this, let us consider a length element $\delta\mathbf{X}$ along the magnetic field line moving with plasma. Consider the plasma velocity at one end of the length segment is \mathbf{v} and $\mathbf{v} + \delta\mathbf{v}$ at another end. Differential velocity between both ends is $\delta\mathbf{v} = (\delta\mathbf{X} \cdot \nabla)\mathbf{v}$. Then, the rate of change of the length element ($\delta\mathbf{X}$) within time interval dt can be expressed as

$$\frac{d\delta\mathbf{X}}{dt} = \delta\mathbf{v} = (\delta\mathbf{X} \cdot \nabla)\mathbf{v}, \quad (1.23)$$

which has the same form as Eq. (1.22), implies that if the magnetic field (\mathbf{B}) and length element ($\delta\mathbf{X}$) are initially parallel, both will remain parallel at all time. Hence, this implies that any two plasma parcels connected by the magnetic field line will remain connected for all the time in ideal plasmas—conservation of magnetic field lines.

1.2.2 Non-ideal limit ($R_M \ll 1$)

The frozen-in field lines can be deformed to generate currents through sheared plasma flow, and this current increases with a local decrease in L , effectively decreasing the R_M . In this non-ideal limit $R_M \ll 1$, the Induction equation reduces to the form:

$$\frac{\partial\mathbf{B}}{\partial t} = \lambda\nabla^2\mathbf{B}. \quad (1.24)$$

The Eq. (1.24) represents the diffusive limit of the Induction equation, and the solution can be written as which describes how magnetic fields evolve under this condition,

$$B = B_0 \exp\left(-\frac{t}{\tau_d}\right), \quad (1.25)$$

where $\tau_d = L^2/\lambda$ is called the diffusion time scale, the time scale over which magnetic field lines diffuse out from the plasma parcels. If the configurations of these diffused field lines are favorable, the field lines can reconnect and generate

solar transients.

1.2.3 Conservation of magnetic topology

The ideal plasma evolution governed by the Induction equation given in Eq. (1.12) conserves the magnetic field lines and, therefore, magnetic topology. The condition for conservation of magnetic topology derived by [Hornig & Schindler \(1996\)](#), for a smooth magnetic field and field line transport velocity (\mathbf{w}) can be written as follows.

$$\frac{\partial \mathbf{B}}{\partial t} + \mathbf{w} \cdot \nabla \mathbf{B} - \mathbf{B} \cdot \nabla \mathbf{w} = \Lambda \mathbf{B}, \quad (1.26)$$

provided that a scalar function $\Lambda(\mathbf{x}, t)$ exist and defined as $\Lambda = -\partial^2 r' / \partial r \partial t$, for parameters r and r' are the parameters with which magnetic field varies as defined by [Hornig & Schindler \(1996\)](#). The expansion of the second terms in Eq. (1.12) gives,

$$\frac{\partial \mathbf{B}}{\partial t} + \mathbf{v} \cdot \nabla \mathbf{B} - \mathbf{B} \cdot \nabla \mathbf{v} + (\nabla \cdot \mathbf{v}) \mathbf{B} = 0, \quad (1.27)$$

for which the Ohm's is

$$\mathbf{E} + \mathbf{v} \times \mathbf{B} = 0. \quad (1.28)$$

From Eqs. (1.26) and (1.27), it is clear that the ideal plasmas conserve the magnetic topology, where $\Lambda = -\nabla \cdot \mathbf{v}$ and $\mathbf{w} = \mathbf{v}$, i.e. field lines transport velocity is the ideal plasma velocity. Therefore, magnetic topology is well-preserved in ideal MHD. However, magnetic topology is a property of the magnetic field alone and it can also be preserved in a non-ideal plasma, where field lines are not preserved by the plasma flow. The corresponding Ohm's law associated with Eq. (1.26) can be derived by using the divergence-free condition of the magnetic field, resulting in $\mathbf{B} \cdot \nabla(\Lambda + \nabla \cdot \mathbf{w}) = 0$, and is given by

$$\mathbf{E} + \mathbf{w} \times \mathbf{B} = \mathbf{A}_\mu, \quad (1.29)$$

where $\nabla \times \mathbf{A}_\mu = \mu \mathbf{B} = -(\Lambda + \nabla \cdot \mathbf{w}) \mathbf{B}$ and $\mu \mathbf{B}$ has a vector potential \mathbf{A}_μ . Therefore, non-ideal Ohm's law governed by Eq. (1.29) can also preserve the magnetic topology. For example, Ohm's law using Hall term, which preserves

the magnetic topology, is written as

$$\mathbf{E} + \mathbf{v} \times \mathbf{B} = \frac{1}{en}(\mathbf{J} \times \mathbf{B}) + \nabla\psi. \quad (1.30)$$

The Ohm's law given in Eq. (1.30) has similar form (for $\mu = 0$) given in Eq. (1.29), the field lines are frozen-in the electron fluid and do not move at the plasma velocity \mathbf{v} . The transporting velocity \mathbf{w} can be given as

$$\mathbf{w} = \mathbf{v} - \frac{\mathbf{J}}{en}. \quad (1.31)$$

Consequently, the topology of the field remains preserved. However, the plasma parcel slips across the field lines, and the connection between the plasma elements and a magnetic field line breaks. Overall, topology being the property of magnetic field alone and can be conceptualized if there is no plasma. The topology can remain frozen in a transporting velocity \mathbf{w} , which does not represent a realistic velocity. For example, the resistive Ohm's law is given as follows.

$$\mathbf{E} + \mathbf{v} \times \mathbf{B} = \lambda\mathbf{J}, \quad (1.32)$$

where λ is the magnetic diffusivity. This form of Ohm's law, governed by Eq. (1.32), does not provide a general transporting velocity. However, it can satisfy the condition of conservation topology in certain cases. An example is,

$$\mathbf{B} = b_x\hat{e}_x + b_y(x, t)\hat{e}_y, \quad (1.33)$$

where b_x provides the constant background of the magnetic field and $\mathbf{v} = 0$. It can be shown, if $\Lambda = 0$, the magnetic topology is conserved, and the transporting velocity \mathbf{u} is,

$$\mathbf{u} = \frac{\lambda J_z(x, t)}{b_x}\hat{e}_y. \quad (1.34)$$

Notably, the velocity given by Eq. (1.34) neither represents the plasma velocity nor any other fluid velocity; however, it transports the field lines to conserve magnetic topology and flux. In the above backdrop, magnetic reconnection is

discussed in the following section.

1.3 Magnetic reconnection

1.3.1 Reconnection in two dimension

The original concept of reconnection was started from two-dimensional (2D) analyses and defines the process through which plasma flows across a surface that separates the distinct topologically connected magnetic field lines domains as magnetic field line merging or reconnection (Vasyliunas, 1975). In this scenario, two separatrices intersect at a neutral point where $|\mathbf{B}| = 0$. In 2D, reconnection can occur at these neutral or null points (Pontin, 2011), and an example is shown through schematic in Fig. 1.4. The configuration near the neutral point can be obtained from Eq. 1.36 by putting $\alpha > 1$ and using the field lines equation as follows.

$$\frac{dx_i}{ds} = \frac{B_{x_i}}{|\mathbf{B}|}, \quad (1.35)$$

where $i = 1, 2, 3$ represents the x, y, z , component of Cartesian coordinate system, respectively. The red and blue field lines are connected from a to b and c to d (panel (a)), and the black dashed lines distinguish different topological domains and are called separatrix surfaces. The neutral point where $|\mathbf{B}| = 0$ is situated at their intersection. The magnetic field expression for such a configuration can be obtained as follows.

$$\mathbf{B} = y\hat{\mathbf{e}}_x + \alpha^2 x\hat{\mathbf{e}}_y, \quad (1.36)$$

where $\hat{\mathbf{e}}_x$ and $\hat{\mathbf{e}}_y$ are unit vectors along x and y directions of a Cartesian coordinate system. The $\alpha^2 > 1$ gives the expression for X-type neutral points, as shown above. An unbalanced force generates inflow shown by two horizontal thick arrows (in green) and brings a pair of oppositely directed field lines, namely, ab and dc, near the neutral point where they diffuse out because of a violation of the flux-freezing condition. At the null point, the two field lines change their

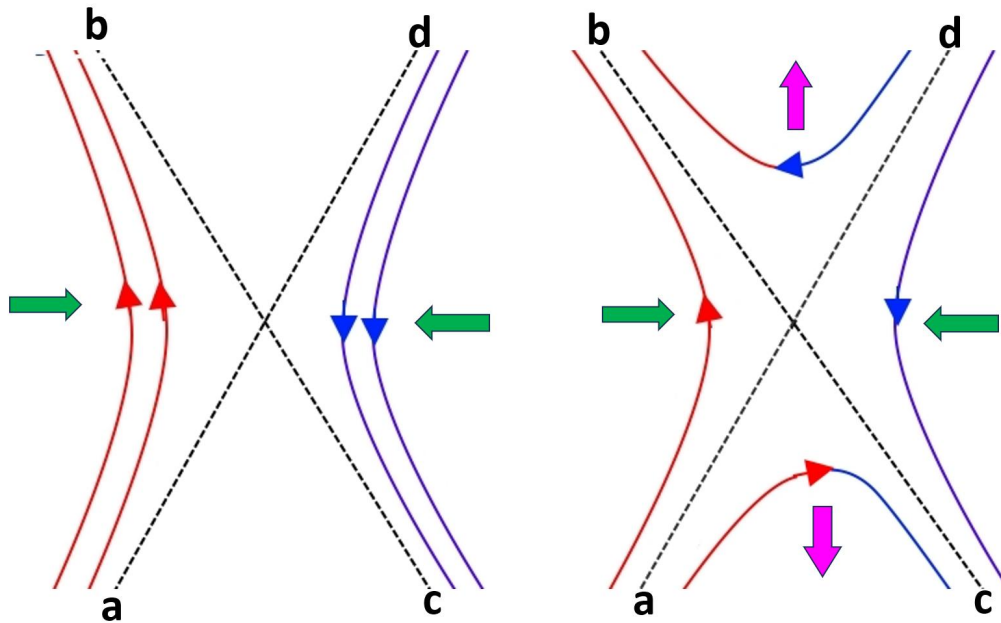


Figure 1.4: An example of reconnection near an X-type null point is shown through Schematic.

connection from a to b to a to c and from d to c to d to b, respectively. Subsequently, reconnected field lines leave the reconnection region with the outflow, shown by the two thick vertical arrows (in pink).

Topologies favorable for magnetic reconnection in 2D

Neutral points

As discussed above (sect. 1.3.1), the reconnection in 2D occurs only at null points. A location in a magnetic configuration where the magnetic field is zero is called a neutral point or null point. In 2D, they are of two types: (i) X-points and O-points, based on their field lines structures near the null points, i.e., hyperbolic and circular or elliptic, respectively. The X-points are ideal sites for magnetic reconnection because the oppositely directed field lines can break their connections and get reconnected, releasing energy. On the other hand, O-type nulls are the locations of flux annihilation or creations. Figure 1.5 presents the

examples of configuration in 2D near the null points obtained from Eq. (1.36), (i) X-type ($\alpha^2 > 1$), and (ii) O-type; Circular-type ($\alpha^2 = -1$), and Elliptical-type ($\alpha^2 < -1$). An asymmetric compression of the X-type null point will lead to

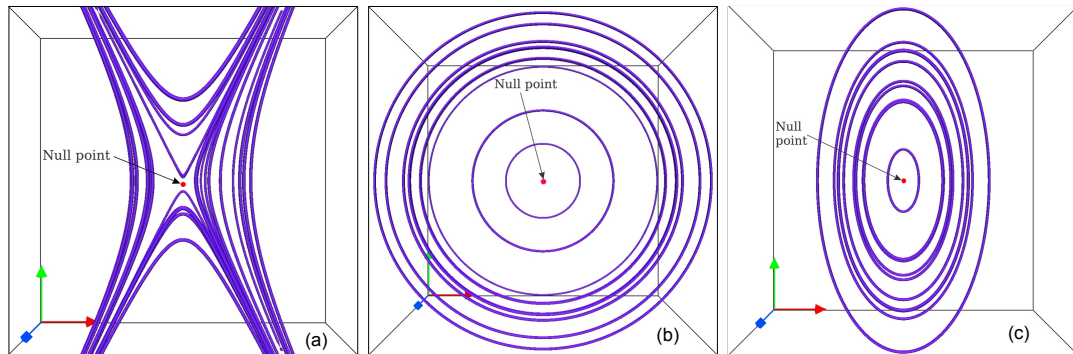


Figure 1.5: The Figure presents the example of a configuration in 2D near the null points. For $\alpha^2 > 1$, X-type null (panel (a)), $\alpha^2 = -1$, Circular-type (panel (b)), and $\alpha^2 < -1$, Elliptical-type (panel (c)).

the development of two Y-type nulls, characterized by strong current densities, or current sheets, localized on a plane across which the magnetic field flips sign. The first quantitative steady-state model of the reconnection process in a current sheet, which employed the MHD description of plasma, was proposed by Sweet and Parker (Sweet, 1958; Parker, 1957) is discussed in the following.

1.3.2 Sweet-parker model

This model utilizes the order of magnitude analysis approach to derive the reconnection rate of a solar flare. The plasma is assumed to be in steady-state ($\partial/\partial t = 0$), incompressible, and is a low plasma- β (where β is the ratio of kinetic pressure to magnetic pressure) (Choudhuri, 1998). These assumptions lead to the reduced set of MHD equations, which are given as follows.

$$\mathbf{v} \cdot \nabla \rho = 0, \quad (1.37)$$

$$\rho(\mathbf{v} \cdot \nabla) \mathbf{v} = \mathbf{J} \times \mathbf{B}, \quad (1.38)$$

$$0 = \mathbf{v} \times (\mathbf{J} \times \mathbf{B}) + \lambda \nabla^2 \mathbf{B}, \quad (1.39)$$

$$\nabla \cdot \mathbf{B} = 0, \quad (1.40)$$

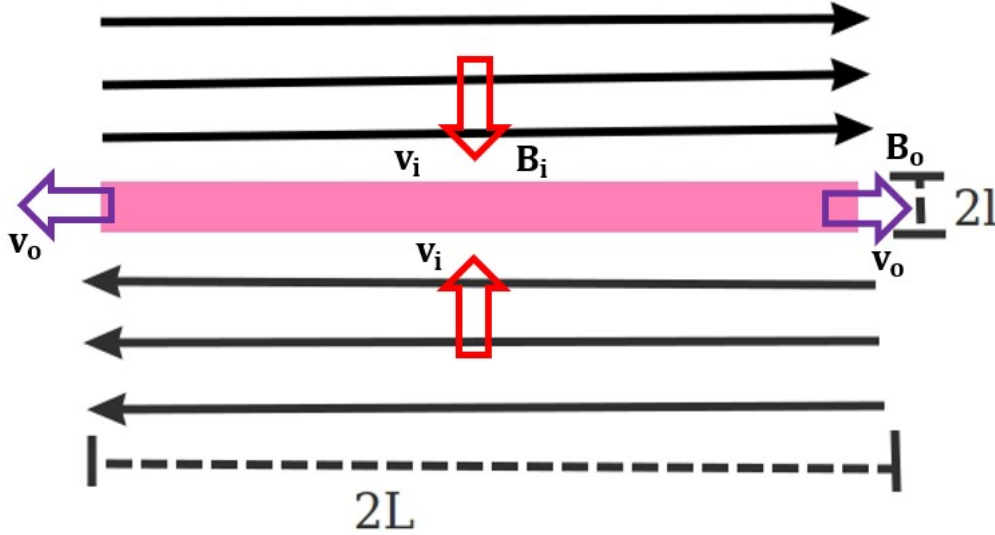


Figure 1.6: Schematic represents the Sweet-Parker model of reconnection.

In the model, the plasma inflow v_i is assumed in such a way that it pushes the oppositely directed magnetic field lines toward a diffusion region or current sheet of length $2L$ and width $2l$, sandwiched between the oppositely directed magnetic field (see Fig. 1.6). For a uniform mass density ρ , from the mass conservation (Eq.(1.37)) principle,

$$\rho(4L)v_i = \rho(4l)v_o, \quad (1.41)$$

where v_o is the outflow speed of plasma. Therefore,

$$Lv_i = lv_o. \quad (1.42)$$

From the flux balance,

$$v_i B_i = v_o B_o. \quad (1.43)$$

By order-of-magnitude analysis, the current density is $J \approx B_i/(\mu_0 l)$ and the Lorentz force along the diffusion region is $(\mathbf{J} \times \mathbf{B})_x \approx (B_o B_i)/(\mu_0 l)$. Lorentz

force accelerates the plasma from rest at the neutral point to v_0 over a distance L , and so, by Eq. (1.38) where the plasma pressure gradient is neglected, we have

$$\rho \frac{v_o^2}{L} \approx \frac{B_o B_i}{(\mu_0 l)}, \quad (1.44)$$

dividing Eq. (1.43) by Eq. (1.42), gives

$$\frac{B_i}{L} \approx \frac{B_o}{l}, \quad (1.45)$$

and Eq. (1.44) then gives

$$v_o = \frac{B_i}{\sqrt{\rho \mu_0}} \approx v_A, \quad (1.46)$$

where v_A is Alfvén speed. From Eq. (1.39),

$$\frac{v_i B_i}{L} = \frac{\lambda B_o}{l^2}, \quad (1.47)$$

using Eq. (1.45) leads to

$$v_i = \frac{\lambda}{l}. \quad (1.48)$$

From Eq. (1.42), (1.46), and (1.48), the reconnection rate, defined as the ratio of inflow speed to outflow speed, can be given as follows.

$$M_A = \frac{v_i}{v_A} = \frac{1}{\sqrt{S}}, \quad (1.49)$$

where M_A is known as the Alfvén-Mach number and S is a dimensionless number known as the Lundquist number, which compares the timescale (τ_A) of an Alfvén wave crossing to the timescale of resistive diffusion (τ_D). It is a special case of the magnetic Reynolds number when the Alfvén velocity is the typical velocity scale of the system and is given by

$$S = \frac{L v_A}{\lambda} = \frac{\tau_D}{\tau_A} \quad (1.50)$$

where L is the typical length scale of the system, λ is the magnetic diffusivity of the plasma. A large Lundquist number indicates plasma to be highly conducting

and has magnetic field lines frozen to the plasma parcels, while a small Lundquist number makes the plasma to be diffusive and allows for the field lines to diffuse through the plasma parcel, violating the flux freezing condition (Priest & Forbes, 2000).

For a solar flare the typical values can be $L \equiv 10^7\text{m}$, $v_A \equiv 10^5 \text{ms}^{-1}$, and $\lambda \equiv 1 \text{m}^2\text{s}^{-1}$, the Lundquist number $S = 10^{12}$ and the reconnection rate is 10^{-6} , which is smaller than its expected value in flares (Aschwanden, 2005). Consequently, a fast reconnection model, the Petschek model, was proposed and discussed below.

1.3.3 Petschek model

The speed at which magnetic flux enters the diffusion region can be significantly increased, proposed by Petschek (Petschek, 1964), if the size of the diffusion region, where oppositely directed magnetic fields meet, is much smaller than the overall system's length scale. He suggested that the four standing slow-mode MHD shock waves accelerate the plasma parallel to the shock front. The external plasma flow velocity v_e equals the shock speed v_s , where v_s is given as follows.

$$v_s = \sqrt{\frac{B_n^2}{\mu_0 \rho}}, \quad (1.51)$$

where B_n is the normal component of the magnetic field. He also suggested that $L \ll L_e$, where L is the length of the diffusion region and L_e is the system's length scale. Consider v_i and B_i represent the plasma inflow velocity and magnetic field strength in the inflow region, respectively, and v_e and B_e are the plasma flow velocity and the magnetic field strength in an external region surrounding the diffusion region. In the external region, the reconnection rate (M_e) and the Lundquist number (S_e) can be written as.

$$M_e = \frac{v_e}{v_{Ae}}, \quad (1.52)$$

and

$$S_e = \frac{L_e v_{Ae}}{\eta}. \quad (1.53)$$

From magnetic flux conservation and assuming a steady state,

$$v_i B_i = v_e B_e. \quad (1.54)$$

Therefore, the reconnection rates in the inflow and external regions are related as.

$$\frac{M_i}{M_e} = \frac{B_e^2}{B_i^2}. \quad (1.55)$$

Near the diffusion region, the magnetic field B_i is slightly curved compared to

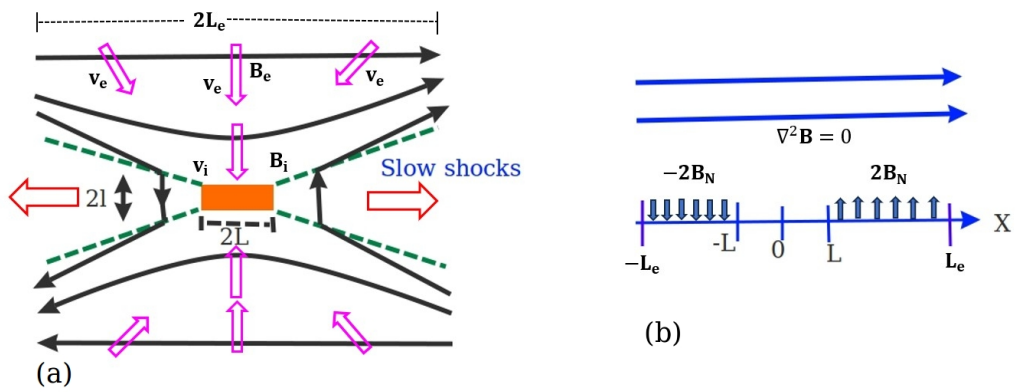


Figure 1.7: Schematic represents the Petschek model of reconnection.

the uniform external magnetic field B_e due to the normal component B_n of the shocks. The shock speed v_s causes B_y to be $2B_n$ on both sides of the diffusion region. In the diffusion region (between $-L$ and L), B_n vanishes. The total magnetic field in the inflow region is the sum of the external field B_e and the field B_i obtained by solving Laplace's equation in the upper half region.

$$B_i = B_e - \frac{4}{\pi} B_n \log \frac{L_e}{L}. \quad (1.56)$$

From Eq. (1.51), (1.52) and $v_s = v_e$, the Eq. (1.56) will be

$$B_i = B_e - \frac{4}{\pi} M_e \log \frac{L_e}{L}. \quad (1.57)$$

As the reconnection rate M_e increases, the shock angle increases while the diffusion region's size decreases. Petschek suggested that if M_e is large enough, the process will self-regulate and provide the expression for the reconnection rate

$$M_e^* \approx \frac{\pi}{8 \log S}, \quad (1.58)$$

where S is the Lundquist number defined in the Sweet-Parker model. For solar flare, the rate lies between 0.01 and 0.1; therefore, much faster than the rate given by the Sweet-Parker model (Priest, 2014). Hence, the Petschek model is also known as the fast reconnection model.

Although studying the reconnection process in 2D helps us understand the basics, real-life scenarios involve complex 3D magnetic structures, like those found in the solar atmosphere and other astrophysical systems. In 3D, reconnection is more complicated and generally may not involve anti-parallel magnetic field lines. Instead, there are possible sites for magnetic reconnection, such as 3D null points, where $|\mathbf{B}| = 0$, and non-null ($|\mathbf{B}| \neq 0$) locations like separators. In the following, a brief introduction to 3D reconnection is presented.

1.3.4 Magnetic reconnection in three dimension

In 3D, magnetic reconnection offers a more comprehensive understanding of solar flares compared to the traditional 2D framework like the model developed by Carmichael (Carmichael, 1964), Sturrock (Sturrock, 1966), Hirayama (Hirayama, 1974), and Kopp & Pneuman (Kopp & Pneuman, 1976), also known as CSHKP model. Unlike the 2D model, which heavily relies on the presence of a flux rope system (CSHKP model), 3D reconnection allows for dynamic magnetic interactions even in the absence of flux ropes. For example, the X3.1 class flare on October 24, 2014, was found to be onset by reconnection near a 3D magnetic

null, completed with well-recognizable fan and spine structures; for details of 3D nulls, refer to Sec. 1.3.4, that drives energy release and generates observable features like circular chromospheric ribbons. Further, recent observations from Solar Orbiter reveal persistent null-point reconnection in the corona (Cheng et al., 2023), emphasizing the necessity of studying reconnection in 3D. These findings strongly compel further to explore the reconnection in 3D to fully understand its role in dynamic coronal processes. There are several definitions of magnetic reconnection in 3D, found in the literature, for example, (i) the reconnection requires plasma flow across a separatrix surface proposed by Vasyliunas (1975), (ii) the electric field along the X-type neutral line or separator is necessary for reconnection in 3D proposed by Sonnerup (1979), and (iii) the reconnection is based on the change in the connection between the magnetic field line and plasma elements due to the localized breakdown of the frozen-in field proposed by Axford (1984). The connection used in this definition means that plasma elements initially linked by a single magnetic field line remain connected over time. Importantly, Vasyliunas's and Sonnerup's definitions require identifying separatrix surfaces in 3D, which involves tracing magnetic field lines back to their origin, which can be difficult, especially in realistic scenarios (Birn et al., 1997). At the same time, Axford's definition is more general because it doesn't rely on magnetic topology and doesn't need tracing field lines back to their origin. Instead, it focuses on the temporal evolution of magnetic field line connections between plasma elements over short times and possibly small distances. This definition highlights the exchange of magnetic field lines between plasma elements, i.e., the breakdown of magnetic connections, also known as the slippage of plasma elements from magnetic field lines (see Fig. 1.8). This concept led to the idea of General Magnetic Reconnection (GMR) proposed by Hesse & Schindler (1988); Schindler et al. (1988). According to GMR, 3D reconnection is classified into two categories: (i) Zero-B reconnection: Where reconnection occurs at location having the magnetic field strength ($|\mathbf{B}| = 0$) zero in the diffusion region; 3D null points reconnections are the examples of Zero-B reconnection, (ii) Finite-B Reconnection: Where the reconnection occurs at the location where magnetic

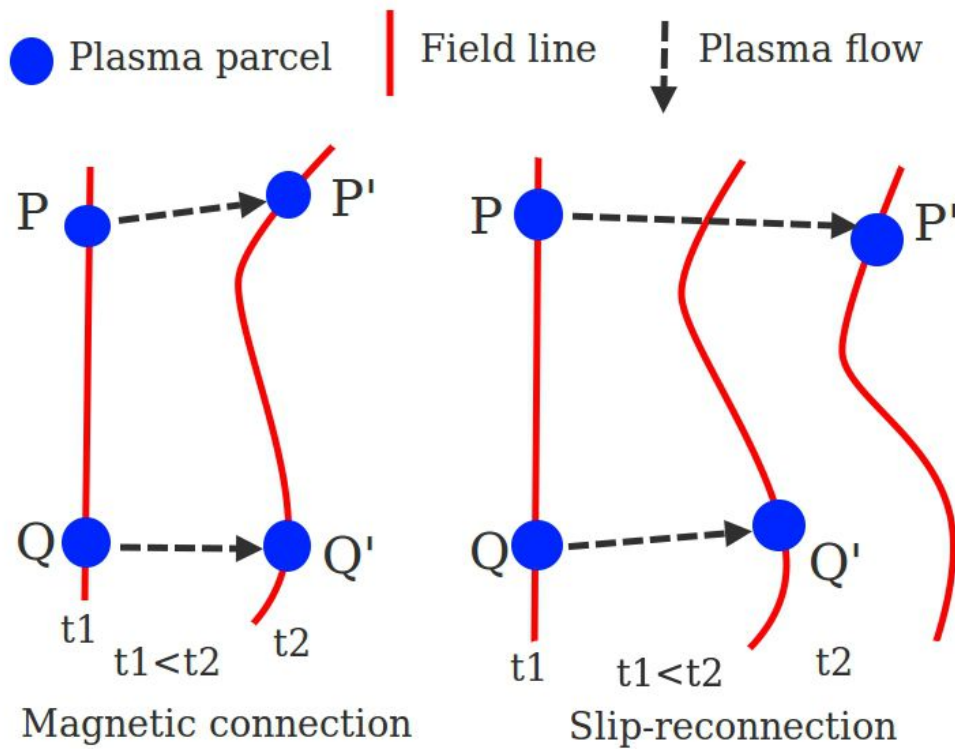


Figure 1.8: The Figure depicts the concept of reconnection in 3D proposed by Axford. Magnetic connection: Two plasma elements, P and Q, are connected by a magnetic field line at time t_1 and remain connected by a magnetic field line at any later time t_2 under the plasma displacement. Slip-reconnection: the plasma elements P and Q are connected by a magnetic field line at time t_1 ; however, at a later time, t_2 , plasma elements exchange the magnetic field lines and do not remain connected by a magnetic field line.

field is non-zero ($|\mathbf{B}| \neq 0$) in the diffusion region; The reconnection occurring at the separators, and Quasi-Separatrix Layers (QSLs) are the examples of Finite-B reconnections. Soft X-ray observations of fast bidirectional motions of coronal loops (Aulanier et al., 2007), observed by Hinode spacecraft, provide evidence supporting the existence of slipping magnetic reconnection in the Sun's corona. These motions, which involve rapid shifts of coronal loop footpoints, co-align with the brightening. The slip reconnection occurs at regions of steep magnetic field gradients, such as quasi-separatrix layers (QSLs), where magnetic field lines undergo continuous slippage rather than vanishing entirely. Notably, such slipping reconnections at quasi-separatrix layers (QSLs) are studied by Prasad et al. (2018) and suggested that they are co-located with post-flare circular brightening

at chromospheric heights. This dynamic process not only explains the observed chromospheric features but also highlights the critical role of reconnection in 3D in driving energy release and plasma motions in the solar atmosphere. These reconnections exemplify finite-B reconnection. The following briefly introduces the concept of 3D magnetic null and separator along with QSL, which are relevant to the thesis.

Null points in three dimensions

A point in space where the magnetic field ($|\mathbf{B}| = 0$) is zero is called a 3D magnetic null point. They are crucial in understanding the magnetic reconnections (Dungey, 1959; Schindler et al., 1988; Wyper & Jain, 2010; Pontin & Priest, 2022; Cheng et al., 2023) leading to various solar transients, wave mode conversion (Kumar et al., 2024) and coronal heating (Parnell & De Moortel, 2012) because of their unique structure. The magnetic field structure around the null point can be characterized by two distinct structures, namely the Spine and Fan plane. A set of field lines that diverge out from the null or converge into the null point in a plane is called a Fan plane. The fan planes are also known as separatrix surfaces, as this plane separates two topologically distinct regions of magnetic reconnectivity (Pontin, 2011). The same set of field lines is directed toward or away from the null along an axis known as the spine (see Fig. 1.9). For more details about the structure and properties associated with 3D magnetic nulls, see Sect. 2.4. The spines and separatrix surfaces are important topological features to quantify the solar coronal magnetic field. Due to the dynamic nature of the solar photosphere, i.e., the presence of the photospheric plasma flow, the current density accumulation can occur along the spines and separatrix surfaces, which may lead to magnetic reconnection and can contribute to the coronal heating (Priest et al., 2002). However, there is very little observational evidence to show what roles each of these mechanisms plays in the way in which the solar corona is heated. Another important magnetic topology known as a magnetic separator is introduced in the following.

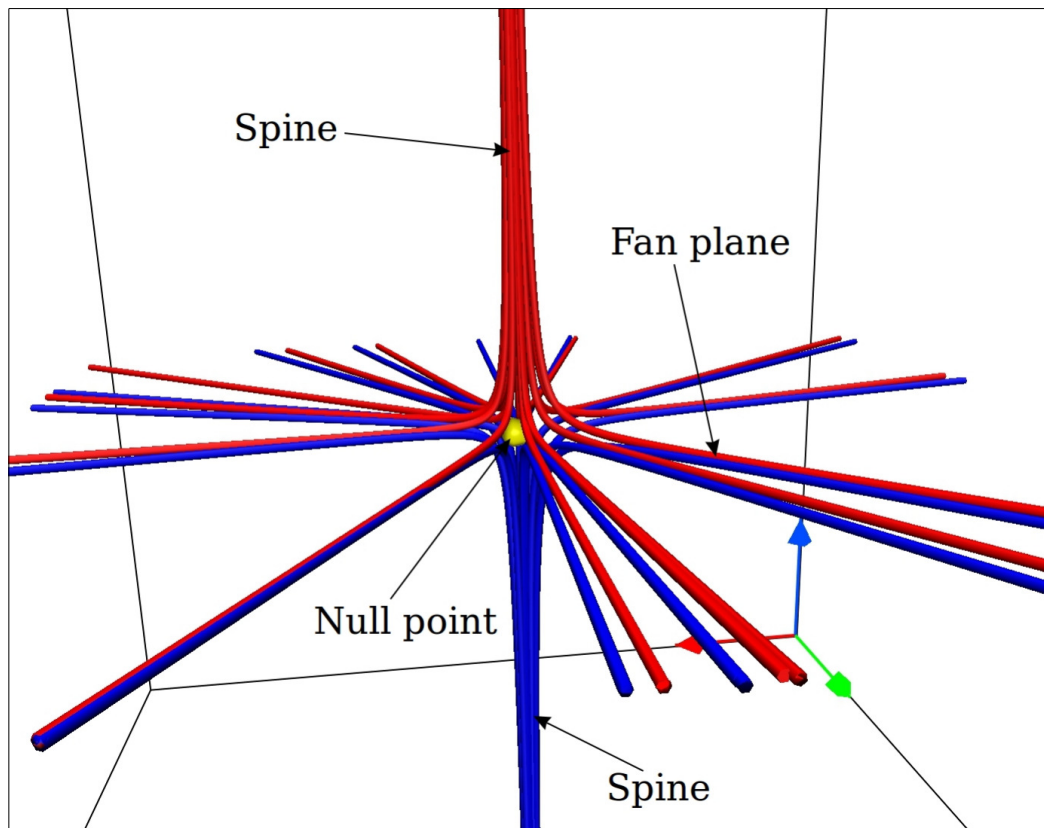


Figure 1.9: An example of a 3D magnetic null point along with a spine-fan plane is shown in the Figure. The small yellow sphere represents the null point; the spine and fan plane are marked by arrows.

Magnetic separator

The lines which are formed through the intersection of separatrix surfaces and connect two nulls are known as magnetic separators (Longcope, 1996) (see Fig. 1.10). The magnetic field strength varies along the separators, and reconnection at this topology is an example of the non-zero B reconnection. Suppose one projects the magnetic field onto any plane perpendicular to the separator line. In that case, then the projected field has an X-type null at the point where the separator crosses the plane, and the two associated separatrices correspond to the intersections of the separatrix surfaces with the plane. Separators enable the formation and accumulation of high current density at large scales (Lau & Finn, 1990; Haynes et al., 2007; Parnell et al., 2010a; Stevenson et al., 2015). They connect vast distances in the solar corona and facilitate reconnections across

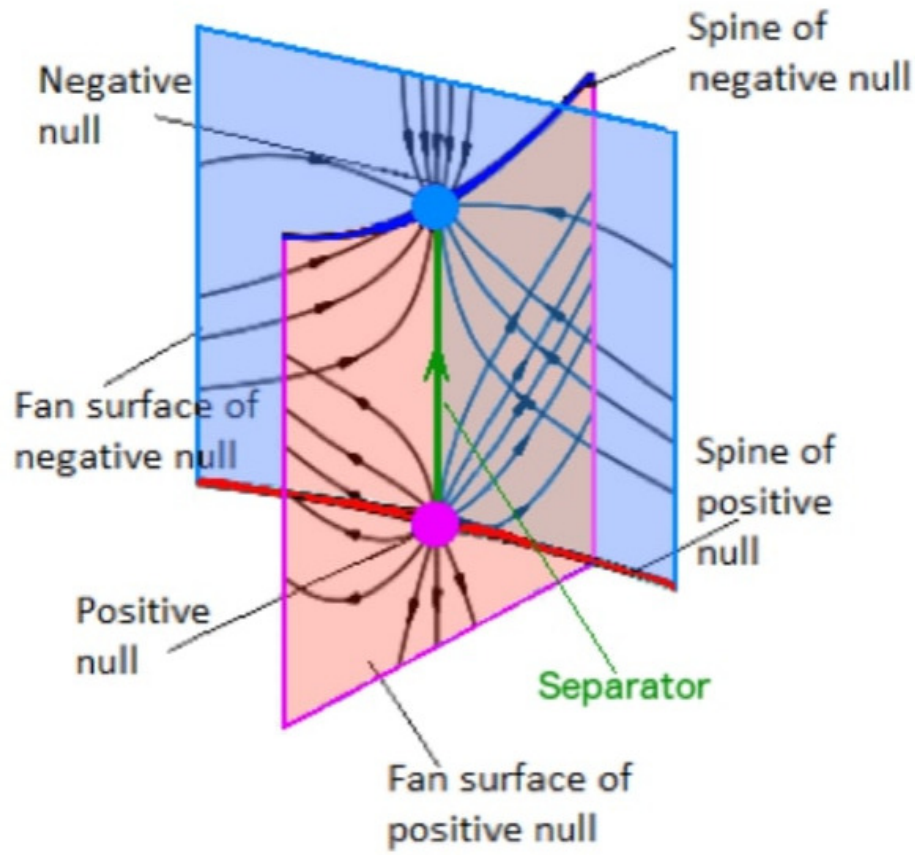


Figure 1.10: The Schematic represents an example of a magnetic separator. Blue and Red circles represent the negative and positive null points, whereas the separator is drawn in green; the picture adapted from (Pontin, 2011).

extended regions of the solar corona, unlike the highly localized reconnection at 3D null points (Close et al., 2004; Parnell et al., 2010b; Platten et al., 2014). Longcope et al. (2005) observes the separator reconnection in the solar corona and its presence has been confirmed within Earth's magnetosphere through in situ measurements from cluster satellites (Xiao et al., 2007; Guo et al., 2013) and through numerical models (Dorelli & Bhattacharjee, 2008; Komar et al., 2013). In the Earth's magnetosphere, separators can be found at Dayside magnetopause as well as magnetotail and serve as the magnetic reconnection in the Earth's magnetosphere (Wang & Bhattacharjee, 1996; Dorelli et al., 2007; Guo et al., 2022). Separator reconnections play a role in particle acceleration as suggested by Metcalf et al. (2003); Threlfall et al. (2016). Moreover, a recent study by Parnell (2024) has shown the importance of separators in 3D magnetic reconnection.

Quasi-Separatrix Layers (QSLs)

Quasi-separatrix Layers (QSLs) are the magnetic configuration having a large gradient in the mapping of the footpoints of field lines, and strong currents may arise and can serve as the preferential sites for the magnetic reconnection in 3D (Demoulin et al., 1996, 1997; Titov, 2007). The reconnections at the QSLs are also examples of finite or non-zero B reconnection, the idea floated by Schindler et al. (1988). In principle, the gradient in footpoint mapping is quantified by a Q-value known as the squashing factor and can be calculated as follows.

Consider two footpoints locations R1 (x_1, y_1) and R2 (x_2, y_2). The footpoints are mapped from locations R1 to R2; the associated Jacobian matrix is given by

$$D_{12} = \begin{bmatrix} \frac{\partial x_2}{\partial x_1} & \frac{\partial x_2}{\partial y_1} \\ \frac{\partial y_2}{\partial x_1} & \frac{\partial y_2}{\partial y_1} \end{bmatrix} = \begin{bmatrix} a & b \\ c & d \end{bmatrix} \quad (1.59)$$

The squashing factor (Q-value) is given by

$$Q = \frac{a^2 + b^2 + c^2 + d^2}{|B_{n,1}(x_1, y_1)/B_{n,2}(x_2, y_2)|} \quad (1.60)$$

where $B_{n,1}(x_1, y_1)$ and $B_{n,2}(x_2, y_2)$ are the components normal to the target planes. To represent the location of QSLs, the criterion on squashing degree is $Q > 2$ (Liu et al., 2016). The field lines are prone to slip in the regions having large Q-values, and the connectivity of different field lines change from one polarity to another same polarity at the bottom layers exhibiting the slip-running or slipping reconnection (Aulanier et al., 2006, 2007).

3D magnetic nulls play a key role in energy release through magnetic reconnection, although they are not the only locations where reconnection can occur in complex astrophysical plasmas. They are observed in the reconnection facilitating current layer of Earth's magnetotail through in situ experiments from the Cluster satellite (Xiao et al., 2006, 2007) and being inferred from fully 3D simulations of polar cusp regions (Dorelli et al., 2007). The reconnections in laboratory plasma have also shown the importance of 3D nulls (Gray et al., 2010). In the solar atmosphere, the existence of 3D nulls is almost guaranteed due to

the large number of mixed flux sources observed in the photospheric magnetograms. In quiet Sun conditions, the number of nulls is to be greatest near the photosphere with a drop with height between an exponential (Régnier et al., 2008) and power law (Longcope & Parnell, 2009). During an increased solar activity, reconnection onset by a 3D nulls plays an important role in solar flare in the higher solar atmosphere (Aulanier et al., 2000; Nayak et al., 2021). The other solar phenomena such as solar jets (Pariat et al., 2009; Liu et al., 2011), flare brightening (Fletcher et al., 2001; Masson et al., 2009), flux emergence (Török et al., 2009), and coronal mass ejections (Longcope, 1996; Lynch et al., 2008) are also linked to reconnections occurring at 3D nulls. The extrapolations and simulations (Prasad et al., 2018; Nayak et al., 2021) have also shown the existence of 3D nulls in the solar atmosphere (Fletcher et al., 2001), and are preferential sites for reconnections (Zweibel & Yamada, 2009; Yamada et al., 2010). Recent observations suggest that coronal rain is ubiquitous (Mason et al., 2019) in large-scale coronal magnetic topologies, particularly those associated with null points, spine lines, and fan surfaces. The frequent occurrence of rain formation in such regions indicates that these structures play a significant role in coronal cooling, with potential mechanisms including thermal nonequilibrium and interchange reconnection. Moreover, contemporary observations show the persistent null point reconnection resulted in supplying the mass in the corona (Cheng et al., 2023). Magnetic reconnections onset by 3D null topology are the proposed as underlying cause of these solar transients (for details, refer to Chapter 2). The 3D magnetic nulls are abundant in the solar atmosphere and play crucial role in onsetting the various coronal transients; the mechanism of their generation merits utmost attention. Additionally, the existence of 3D null can be counter-intuitive. To fix ideas, consider $(N-1)$ a number of magnetic dipoles in 3D, which produce a magnetic field \mathbf{B} at a point P . In principle, it is possible to position an additional dipole, say the N th one, in a way that its magnetic field contribution at P is $-\mathbf{B}$. Therefore, the net magnetic field at P is zero, and the point P is a 3D null point. However, this is a tailor-made arrangement and is not expected to be trivially achieved in a magnetically complex system like

the active region corona. It is then important to explore whether such a special arrangement is feasible in a magnetic system and, if it is, how the configuration is sustained. The straightforward expectation is the reliance on a mechanism fundamental to magnetohydrodynamics. Both theory and simulations (Parker, 1994; Kumar et al., 2017) suggest magnetic reconnection to be a fundamental process expected in a near-ideal fluid through a local reduction of the magnetic Reynolds number.

1.4 Objective and Outline of the Thesis

In the backdrop of Sections 1.3.4, it is imperative to explore various properties of 3D null topologies and, more importantly, their generation—the objective of the thesis. To achieve this objective, the necessity is to trace magnetic field line evolution and identify locations of newly generated nulls along with their dynamics. Incidentally, not much work has been done with this objective. Nayak et al. (2020) carried out a set of MHD simulations, in one of which spontaneous generation of magnetic nulls was obtained. Although magnetic reconnection seemed to be a plausible cause behind the generations, but was not established rigorously. Another thrust area is the exploration of null bifurcation where a null bifurcates into three nulls (including the original one) within a null current sheet—a region having a steep gradient of the magnetic field (Wyper & Pontin, 2014). Nevertheless, identifying the mechanism to generate nulls still remains elusive. Toward this goal, aptly devised numerical simulation is employed. Three sets of simulations are carried out. Two are with analytical initial conditions to enforce more control on the field line evolution, whereas the first one also sets up the essential foundation for such studies. These computations are augmented with a data-based simulation where the initial magnetic field is constructed using the vector magnetogram data of an Active Region on the solar photosphere. The purpose here is to look at and study null generations and corresponding dynamics in a realistic scenario and, further, to compare the findings against observational features. On this general note, the thesis is further structured as,

In the first part of the Chapter 2 titled *Observational manifestation of magnetic reconnection and theory of 3D magnetic null*, the overview and examples of the solar flare, jets, and coronal bright point onset by 3D magnetic null are presented. The second part discusses the structure and properties associated with 3D magnetic null.

Chapter 3 *Methodology and necessary numerical tools* introduces the EULAG-MHD model, used extensively for the simulations and trilinear null detection tools required for detection, tracing, calculation of the topological degree of nulls and in the determination of the nature of the nulls.

Chapter 4 *3D magnetic null generation and annihilation with an initial analytical magnetic field* explores the mechanism of 3D magnetic null generation and annihilation through MHD simulation of an initial analytical magnetic field having an isolated current-free 3D null. The simulation is initiated through a prescribed sinusoidal flow, which deforms the spine of the existing null and leads to reconnections, resulting in null pair generation having a complimentary topological degree. Interestingly, subsequent evolution shows reconnection-assisted spontaneous null pairs generation—preserves net topological degree—increasing the tenability of the simulation. The pairwise annihilation of nulls is also seen. This chapter establishes reconnection-assisted null pair generation and annihilation in two scenarios: initial flow-assisted and autonomous.

Chapter 5 *Spontaneous generation and annihilation of 3D magnetic nulls in the solar atmosphere* explores the plausibility of the spontaneous generation of nulls in naturally occurring plasmas, i.e., solar atmosphere, identify the mechanism behind it and its observation implications. A data-based simulation of a C6.6 class flare associated with the photospheric active region NOAA 11977 is carried out for the goal. The simulation confirms the spontaneous pairwise generation of 3D nulls with magnetic reconnections as the underlying cause. Importantly, magnetic field lines associated with the spontaneously generated nulls are found to trace observed chromospheric bright points—highlighting their observational relevance.

Chapter 6 *Generation of 3D magnetic nulls in an initially chaotic magnetic*

field devoid of any nulls explores 3D magnetic null generation through the MHD simulation with an initial analytical chaotic magnetic field devoid of any null while precisely identifying the locations, topological degrees, and natures (spiral or radial) of nulls, along with the tracing of field lines in light of recent advancements and tools. This chapter also explores the influence of the chaoticity on 3D null generation.

The first part of Chapter 7 *Summary and Future Scopes* summarizes the results of the thesis work. In the second part, the future scopes are discussed.

Chapter 2

Observational manifestation of magnetic reconnection and theory of 3D magnetic null

In the frozen-in limit, magnetic topology remains preserved while plasma parcels trace the magnetic field lines. Whereas change in magnetic topology—magnetic reconnection occurs in the diffusive limit of the plasma achieved through an increase in gradients of the current density, which can initiate the solar transients. Thus, understanding the topology of the solar coronal magnetic field is crucial for comprehending the solar transients. The following presents a brief overview of the relevant solar transients, highlighting their key aspects.

2.1 Solar Flares

Solar flares are the sudden and intense release of electromagnetic (EM) radiation from the solar atmosphere, emanating from the release of stored magnetic energy in the active region's magnetic field lines. These events profoundly affect space weather, including Earth's lower ionosphere. Various studies have revealed their origin, associated magnetic configuration, and impact using ground and space observations. Flares cover the whole EM spectrum and have different temporal scales. In the following, the distinct phases of Solar flares are discussed.

- **Pre-flare phase:** This phase is characterized by gradual energy buildup with heating of the plasma and soft X-ray (SXR) emission.
- **Impulsive phase:** This phase is marked by the rapid energy release and acceleration of particles; the signature is the X-ray footpoint sources appearing at the chromospheric height.
- **Flash phase:** this phase is characterized by rapid increase in intensity in H_{α} .
- **Decay phase:** where the coronal plasma relaxes (Benz, 2017).

The stages of a flare in multi-wavelengths are depicted in Fig.2.1. The solar flares are believed to be driven by magnetic reconnection, a process that releases stored magnetic energy in twisted field lines. For a length scale (L) and magnetic field (B) of a typical sunspot, the stored magnetic energy (E_{mag}) can be

$$E_{mag} \approx \left(\frac{B^2}{8\pi}\right) L^3 \approx \left(\frac{B}{10^3 G}\right)^2 \left(\frac{L}{3 \times 10^9 cm}\right)^3 10^{33} ergs, \quad (2.1)$$

which is sufficient enough to produce a large flare (Shibata & Magara, 2011). Giovanelli (1947, 1948), Hoyle (1950) have first proposed that the hyperbolic X-type neutral points ($\mathbf{B} = 0$) play a role in the excitation of particles during flares and auroras. Later, Dungey (1953) proved that the X-type neutral point is likely a site for releasing charged particles in astrophysical plasmas. The indirect evidences of similar reconnection-assisted events in other astrophysical plasmas have further supported this proposal (Verbunt, 1982; Mullan, 1986; Romanova & Lovelace, 1992; Drenkhahn & Spruit, 2002; Giannios, 2010). Based on magnetic reconnection, the standard flare model by Carmichael (1964); Sturrock (1966); Hirayama (1974); Kopp & Pneuman (1976); Svestka & Cliver (1992) (CHSKP model) has been developed and is explained through schematic in Figure 2.2. Essential to the standard flare model is the presence of a magnetic flux rope, a set of twisted magnetic field lines anchored on the photosphere and confining the cooler plasma material. The rope is quantified by the winding number or twist (T_w) parameter, which measures the number of turns the field lines make

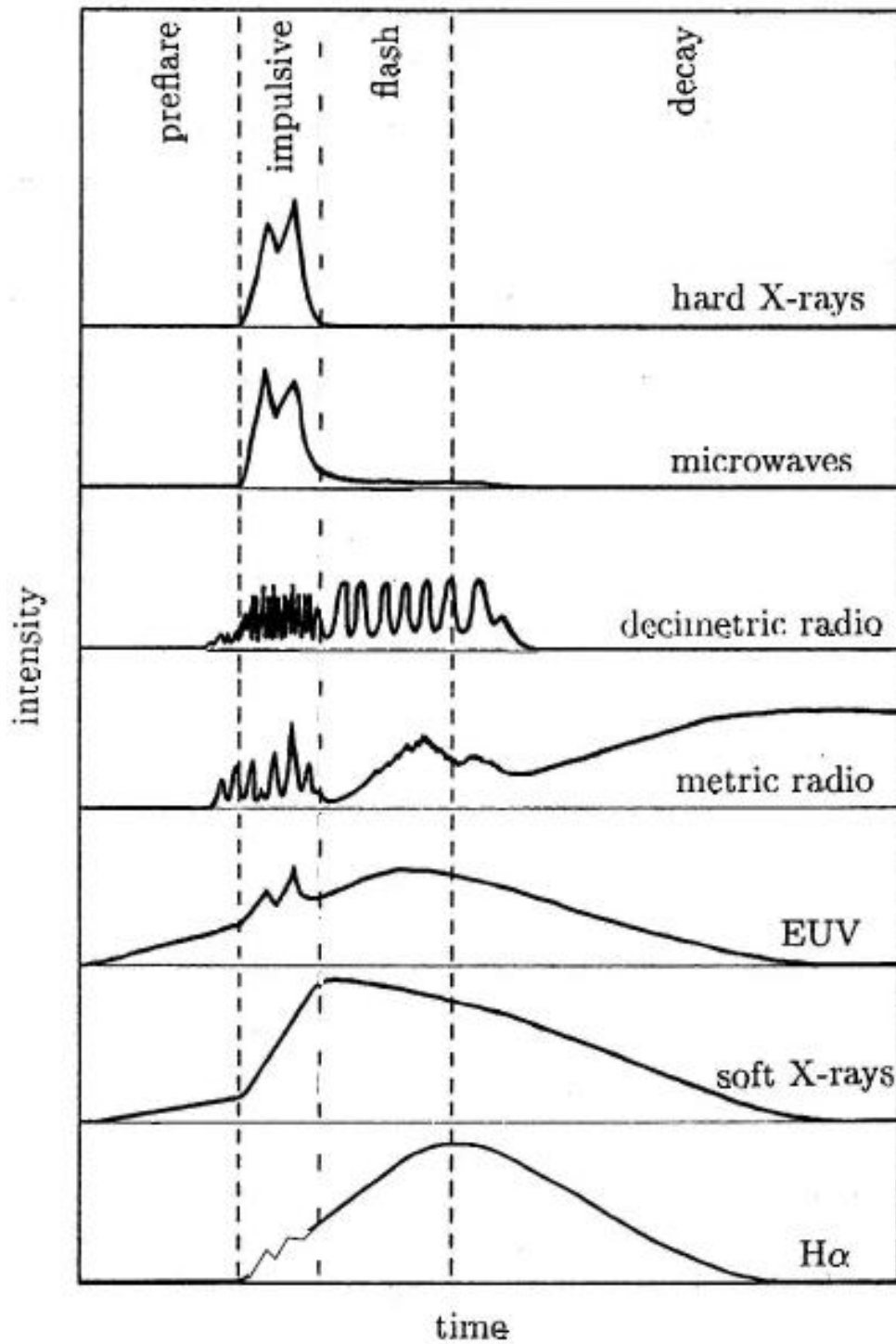


Figure 2.1: A schematic showing different phases indicated at the top; taken from (Benz, 2017).

about the axis while going from positive to negative polarity across the polarity inversion line (PIL). Some studies for example Yan et al. (2001); Roussev

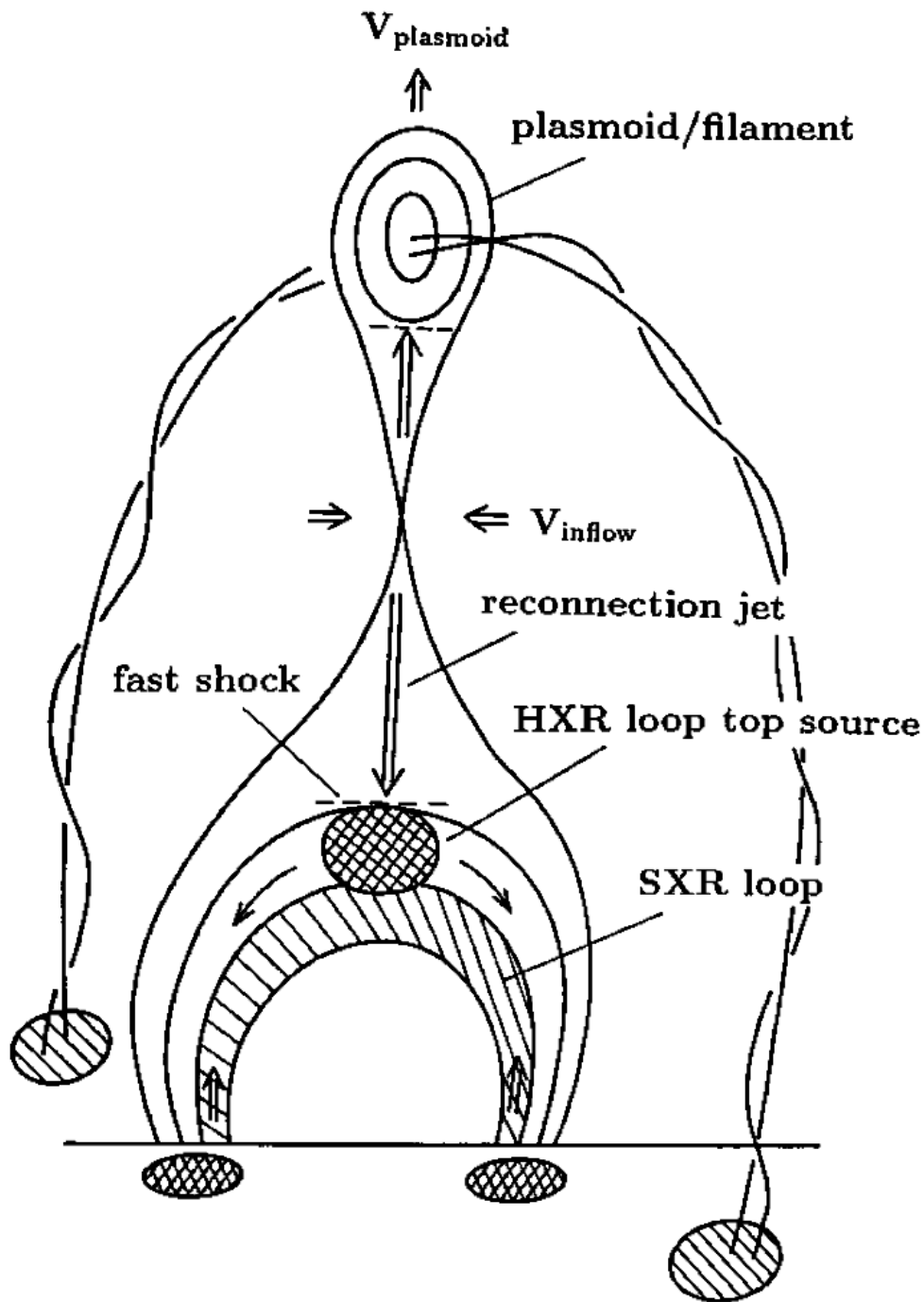


Figure 2.2: The schematic shows a modified version of the CHSKP model for a solar flare, adapted from [Shibata et al. \(1995\)](#).

[et al. \(2003\)](#) showed that the optimal winding number is > 2 whereas, [Amari & Luciani \(1999\)](#); [Aulanier & Demoulin \(1998\)](#); [Régnier & Amari \(2004\)](#); [van Ballegooijen \(2004\)](#); [Su \(2007\)](#); [Savcheva & van Ballegooijen \(2009\)](#) suggest that the number is < 2 . [Antiochos et al. \(1994\)](#) proposed that the winding num-

ber or twist parameter be even less than 0.5. Importantly, if the rope begins to rise after its activation, it stretches the overlying field lines and creates a magnetic vacuum below it. The local decrease in magnetic pressure brings oppositely directed field lines toward each other, developing an extended current sheet (CS) that onsets magnetic reconnection, which manifests itself as the flare. The reconnection also accelerates charged particles, which move along the post-reconnection magnetic field lines and ultimately impact the lower atmosphere. Consequently, the ambient plasma is heated, and the corresponding pressure imbalance causes the plasma to flow up. This flow gradually fills up the magnetic loops with plasma. The process is known as chromospheric evaporation, and the field lines visible in the soft X-ray are called the soft X-ray loops. The more details can be found in (Benz, 2017; Shibata & Magara, 2011). Recent numerical simulation proposed that the magnetic reconnection onset by a 3D magnetic null can contribute to the solar flare (Nayak et al., 2021). The initial magnetic field was constructed by extrapolating the photospheric magnetogram of active region NOAA 12017 at 17:48 on March 29, 2014, hosting an X-class flare by employing the Non-Force Free Field extrapolation technique. The initial field contains the important topology, a 3D magnetic null (see panel (a) of Fig. 2.3). With the evolution, magnetic reconnections occur at the 3D null and can potentially explain the observed chromospheric brightenings during the flare. Panel (c) depicts the co-spatiality of the footpoints of field lines constituting the fan surface with the observed chromospheric brightenings where the AIA 304 Å channel is overlaid with the co-temporal field line structure of null. Consequently, it is expected that magnetic reconnection at the null accelerates the charged particles, which travel along the field lines and dissipate their energy while entering into the denser chromosphere, resulting in brightenings. The magnetic reconnection (marked by the green arrow in panel (b)) at null restructure the corresponding spine and fan field lines and the change in connectivity of lower spine and fan field lines (in pink) to the upper spine and fan field lines (in sky blue) (c.f. panels (b) and (d) of Fig. 2.3). The post-reconnections field lines marked by black arrows (panel (d)) are comparable with the observed post-flare loops.

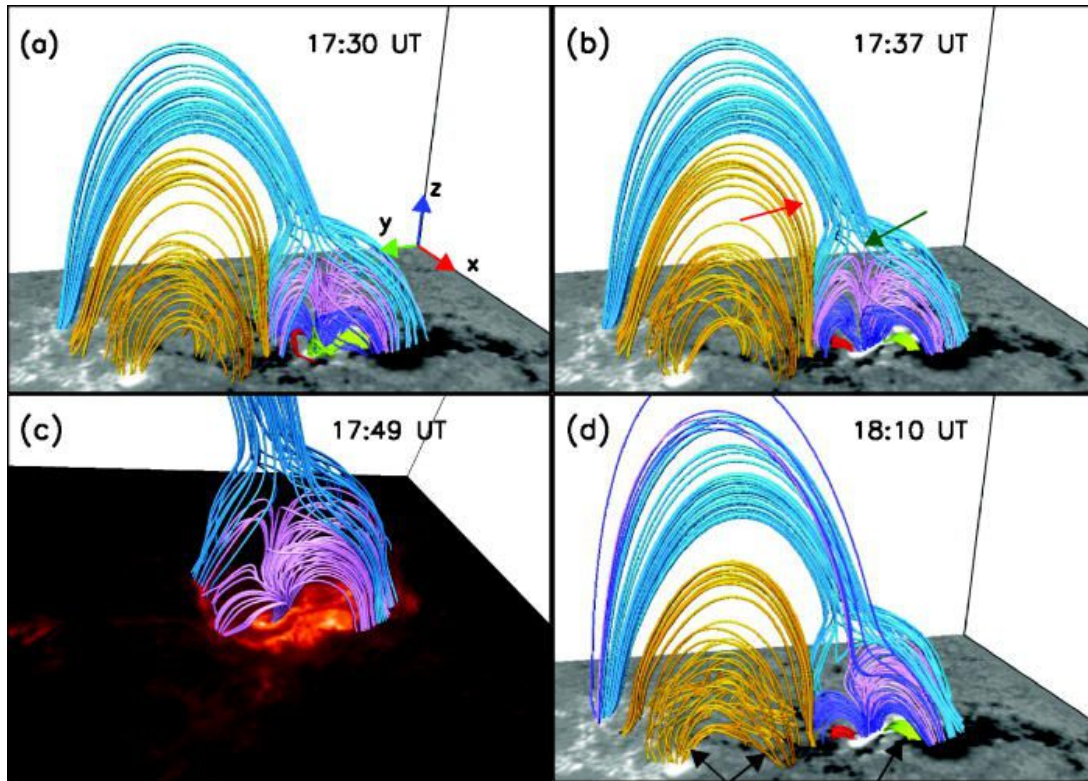


Figure 2.3: The figure depicts an example of flare onset by a 3D magnetic null; adapted from [Nayak et al. \(2021\)](#).

2.2 Jets

Jets are the collimated eruptions from the solar atmosphere. These are energetically 10^4 - 10^5 orders less than the flares ([Pucci et al., 2013](#); [Raouafi et al., 2016](#)) and can be of many varieties—like chromospheric jets, surges, spicules, microspicules, and large coronal jets. The nomenclature is based on their observational traits. They differ in length scales and formation heights in the solar atmosphere. The jets are reckoned as smaller versions of the large filament eruptions like in CMEs. They are ubiquitous and are visible in the active regions, coronal holes, quiet the Sun, and preferably in boundaries with open coronal field lines. Jets are seen in different wavelengths, like in $H\alpha$, extreme UV, and X-rays, and can have different temperatures. Several instruments such as Solar and Heliospheric Observatory (SOHO; ([Domingo et al., 1995](#))), the Transition Region and Coronal Explorer (TRACE; ([Handy et al., 1999](#))), the Reuven Ramaty High Energy Solar Spectroscopic Imager (RHESSI; ([Lin et al., 2002](#))), the Hinode ([Ko-](#)

sugi et al., 2007), the Solar Terrestrial Relations Observatory (STEREO; (Kaiser et al., 2008)), the Solar Dynamics Observatory (SDO; (Pesnell et al., 2012)), and the Interface Region Imaging Spectrograph (IRIS; (De Pontieu et al., 2014)) have recorded jets in the past and still are doing so. Some ground-based observatories have also contributed to the study of the jets. Shibata et al. (1994) arranged the jets into two types. One is the straight anemone jet, and the other is the two-sided jet. In the case of an anemone jet, a collimated plasma erupts (the spire part) with a bright point (at the base part) behind it or in the inverted Y-shape (also referred to as lambda or Eiffel tower shape). In contrast, the two-sided jet has bipolar plasma columns spreading out from the central bright point. Panel-(a) in Fig.2.4 shows an anemone jet, and panel-(b) shows a two-sided jet. The anemone jets are again divided into two sub-types: (1) standard jets and (2)

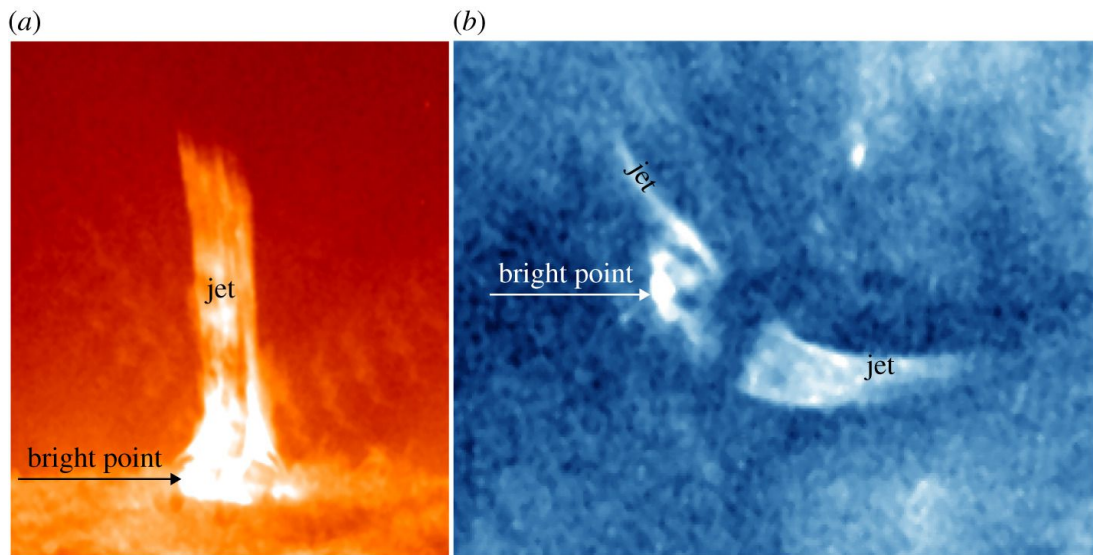


Figure 2.4: Two different types of jets, (a) an anemone jet, and (b) a two-sided jet; picture credit: (Shen, 2021). The arrow marks highlight the bright points near the base of both jets.

blowout jets based on their observational appearances (Moore et al., 2010). An additional X-ray brightening inside the base arc, blowout eruption of the core field of the base arc, often made of cool filament ($T \sim 10^4 - 10^5 \text{K}$) plasma, and extra jet-spire strand anchored near to the bright point makes blowout jet different from the standard jets (for details see Moore et al. (2010)). The standard jets are driven by reconnection as proposed by (Yokoyama & Shibata, 1995; Shi-

mojo et al., 1996; Canfield et al., 1996; Shimojo & Shibata, 2000), and Shimojo et al. (1998) provided the model of the standard jets driven by reconnection. A universal model for the eruption of CME and jet is proposed by Wyper et al. (2017) and claimed that the eruptions follow the breakout model. Various studies proposed that the jets can also be due to flux cancellation (Panesar et al., 2016, 2017, 2018), and flux emergence (Mulay et al., 2016). The details of the different eruption mechanisms and origins of jets can be found in Raouafi et al. (2016); Shen (2021). Recent data-constrained MHD simulation proposed that the magnetic reconnections onset by a set of two 3D nulls (shown in Fig. 2.5) initiated the jet (Nayak et al., 2019) and claimed that the evolution agrees with the breakout model of blowout jets. In Fig. 2.5, two 3D magnetic nulls (in pink) and the open magnetic field lines (in red) constitute the outer spines of the null pairs, whereas the anchored field lines (in blue and yellow) making the inner spines of the nulls are shown at 05 : 48 UT. Figure 2.6 depicts the sequence

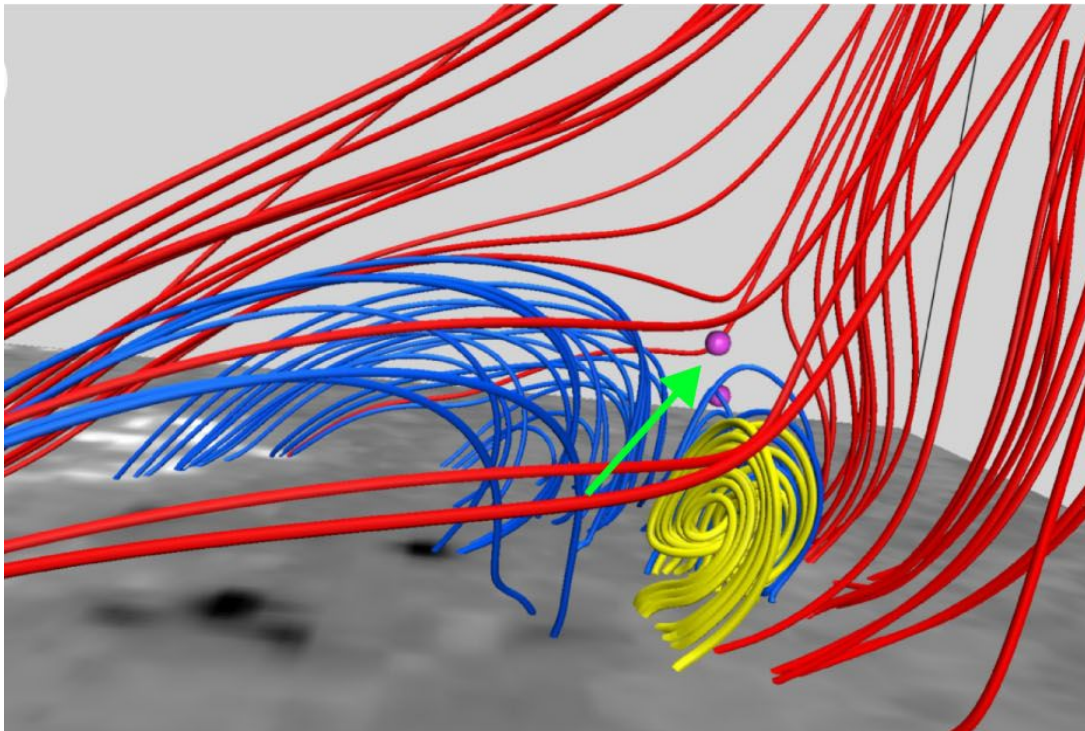


Figure 2.5: The Figure depicts two 3D magnetic nulls (in pink) and their associated field lines; picture taken from Nayak et al. (2019).

of the field lines evolution starting (panel (a)) from the field lines configuration shown in Fig. 2.5 spanning $t \in \{05 : 48, 06 : 05\}$ UT, covering the duration of the

jet. Importantly, with the evolution, anchored field lines (in yellow and blue) changed their connectivity and became part of the outer spine (panels (b)-(f)). Consequently, the entrapped cold plasma can get channeled along the open field lines of the outer spine and make the spire. Noticeably, the plasma flow vectors shown in green become more field-aligned with the evolution.

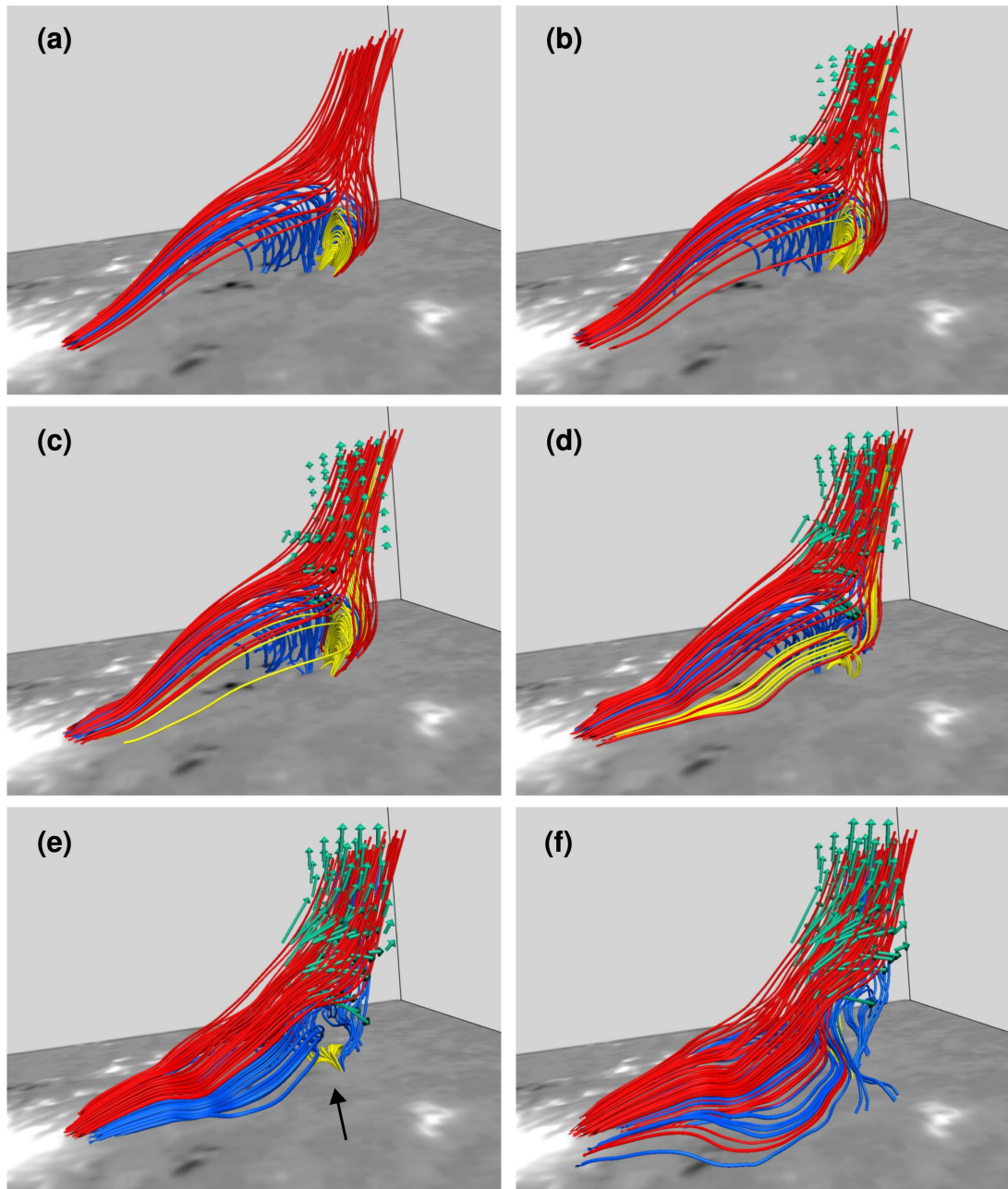


Figure 2.6: The sequence of field lines evolution, showing the magnetic reconnection and covering the duration of the jet; picture adapted from [Nayak et al. \(2019\)](#).

2.3 Coronal Bright Points

The Coronal Bright Points (CBPs) are the phenomenon that appears as bright structures in extreme-ultraviolet (EUV) and X-ray wavelengths ubiquitously found in the solar atmosphere. They are small-scale (on average 20''-30''), short-lived (from a few minutes to a few tens of hours) structures (Golub et al., 1977; Webb et al., 1993; Brown et al., 2001; Mou et al., 2016) and are believed to be the signature of a direct energy deposition in the upper solar atmosphere (McIntosh, 2007). The CBPs are first imaged in Soft X-Ray (SXR) during rocket missions in 1968-1973 (Vaiana et al., 1973) and analyzed later through the Skylab mission (Golub et al., 1976a,b; Habbal, 1992). Fig. 2.7 shows the example of identified CBPs in the quiet Sun region. Various studies (Parnell et al., 1994a,b) proposed that CBPs are often linked with the cancellation of opposite polarity magnetic fragments in the photosphere (i.e., so-called canceling magnetic features) and have been considered as evidence of magnetic reconnection occurring in CBPs (Pérez-Suárez et al., 2008; Alexander et al., 2011; Zhang et al., 2012). (Presé & Phillips, 1999) suggested that all the energy losses of a CBP are, in fact, replenished by magnetic energy. Additionally, (Zhang et al., 2014) has proposed that the interchange reconnection might occur between two close chambers of a CBP. A model has been proposed by (Priest et al., 1994; Parnell et al., 1994b) where the reconnection results from the converging motion of magnetic polarities in different scenarios as shown in Figure 2.8 and the interaction distance has to be less than a certain value in order to trigger the appearance of a CBP. This cancellation, driven by converging motions of two magnetic bipolar sources, can heat the solar corona as proposed by (von Rekowski et al., 2006a,b; von Rekowski & Hood, 2008). Figure 2.9 shows the images in SXR of Hinode/XRT (top left) and three EUV channels (171 Å, 195 Å, and 284 Å) of STEREO/EUVI. (Zhang et al., 2012) has identified around 13 CBPs and labeled them as BP1-BP13. The dashed box (59.8'' × 59.8'') on the top left of each panel drawn in the dark area is considered as the background, and a careful inspection of the 5 hr SXR images reveals that the quiet background region does not contain any CBP. To study

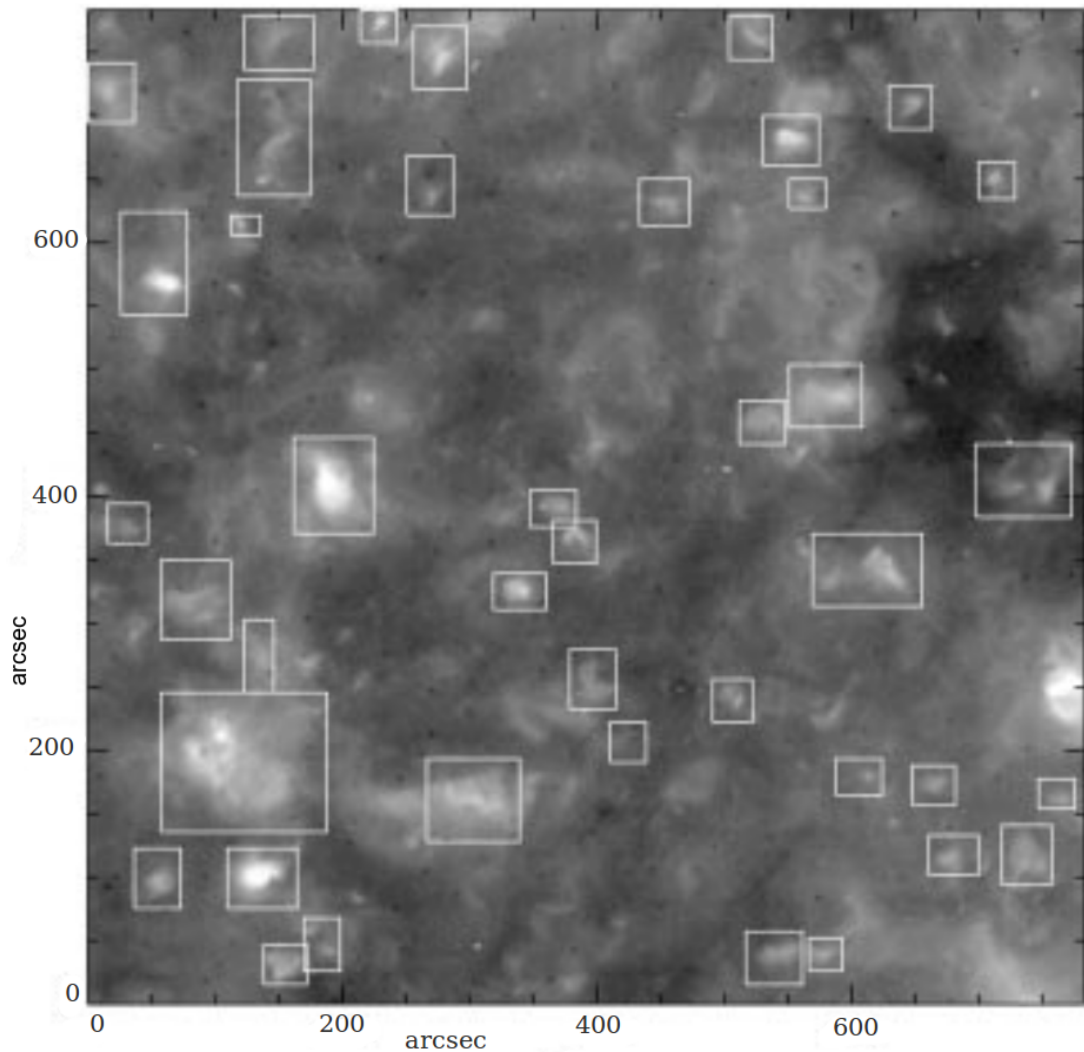


Figure 2.7: Identified coronal bright points in the quiet-Sun region; picture adapted from [Zhang et al. \(2001\)](#).

the dynamics and the associated magnetic configuration of CBPs, they picked two major CBPs, i.e., BP1 and BP2. Their study suggested that CBPs are covered by a dome-like separatrix surface, with the 3D magnetic null point structure above it, as shown in Fig. 2.10 from two view angles. Top view (left) and side view (right) of the coronal magnetic field configuration, including the 3D nulls around the two CBPs at 01:01 UT. The magnetic field lines near the spines are plotted in blue, and those below the dome-shaped separatrix are in green. The background color image depicts the SXR map at 01:00 UT, with the photospheric magnetogram superposed; black solid lines correspond to the positive polarity, and the dashed lines correspond to the negative polarity. They proposed that

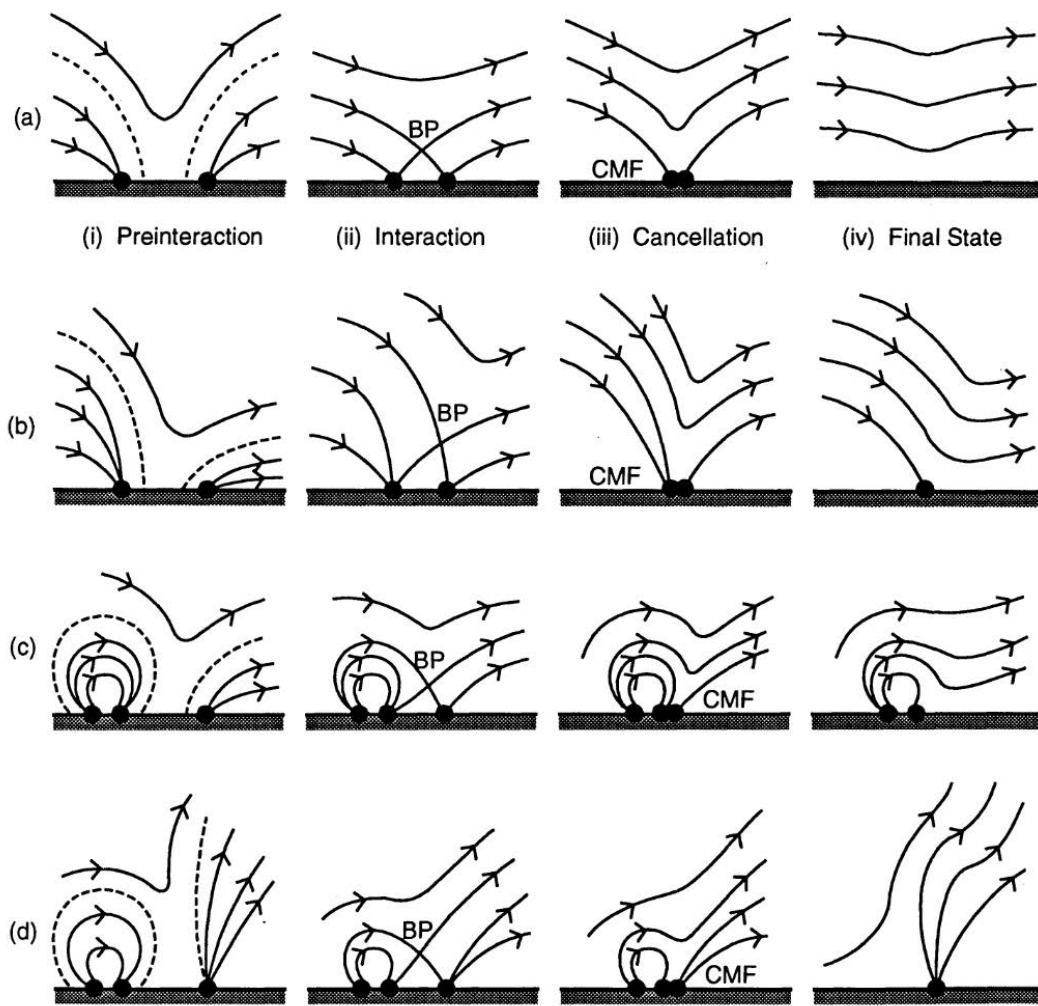


Figure 2.8: The schematic shows the several possible configurations leading to CBP, where (i) pre-interaction, (ii) interaction, (iii) cancellation, and (iv) final phases, for (a) equal and opposite, (b) unequal and opposite, (c) a large bipolar and a small unipolar, and a weak bipolar and a strong unipolar magnetic fragments. The schematic has been adapted from [Priest et al. \(1994\)](#).

the repetitive CBP flashes and the recurrent SXR jets result from the impulsive null-point reconnection. At the same time, the long-lived brightenings are due to the interchange reconnection along the separatrix surface. The CBPs in coronal holes (CH) and quiet Sun regions are seen to reside in regions on the Sun where coronal magnetic nulls are present and proposed by ([Galsgaard et al., 2017](#)). Using null point location and topology, the relation between the magnetic field structure and the projected location of the X-ray emission for the 10 selected BP regions is established. They showed that the X-ray emissions are associated with

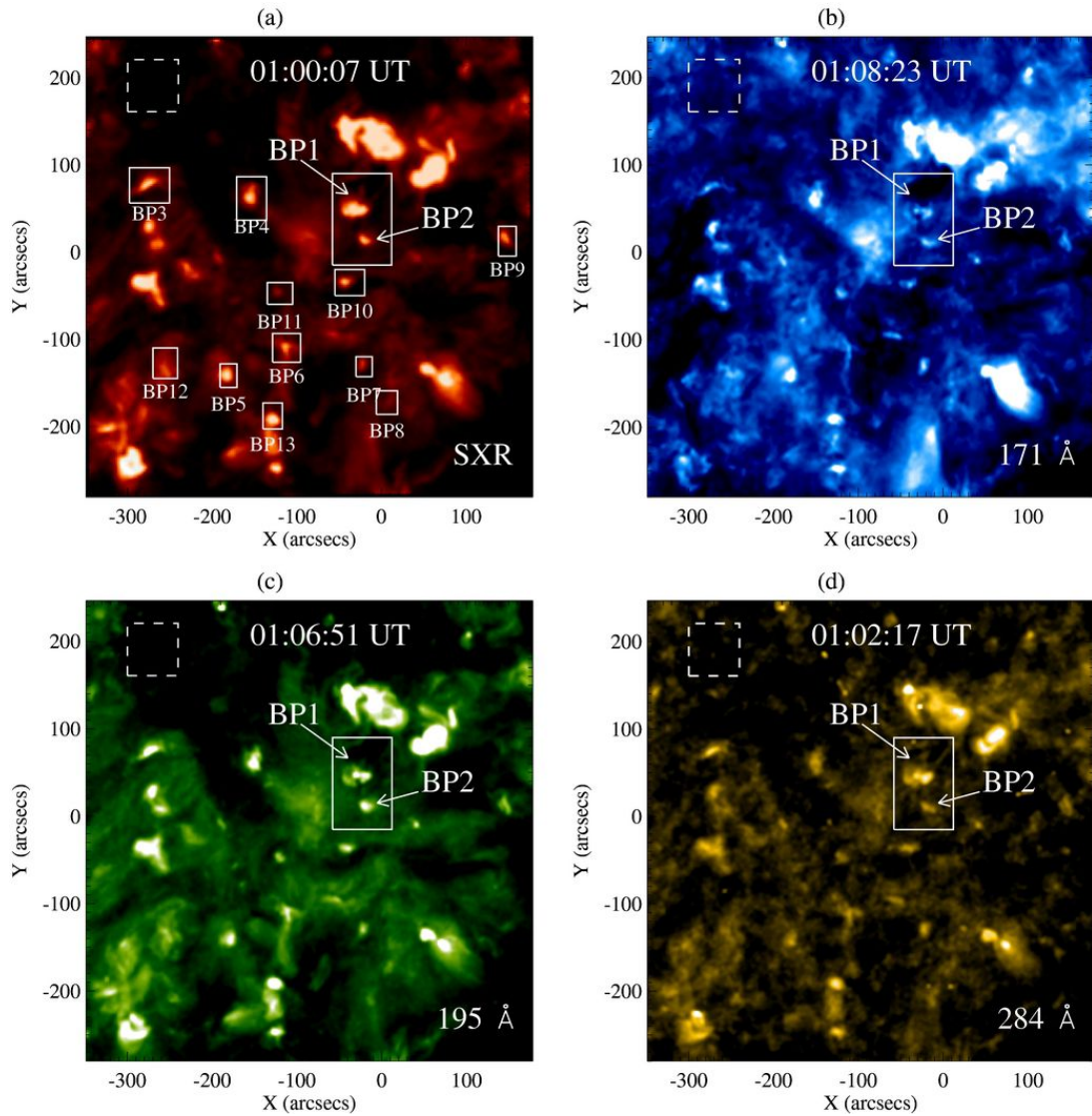


Figure 2.9: Figure shows the identified CBPs in SXR and EUV channels at 01:01 UT. The picture adapted from [Zhang et al. \(2012\)](#).

the 3D null points fan-dome structure for all observed CBPs in CH regions. One such example using the time evolution of the BP1 case is shown in Fig. 2.11. The magnetogram is shown in the top row and scaled to $\pm 200\text{G}$, and the magnetic field configurations using potential field extrapolation. The negative and positive polarity are represented by blue and red color, respectively. The isosurface (in grey) renders the location of the null point, with the field lines drawn near the null. The color of the field line depicts the magnetic field strength, strongest field (in red), and weak field (in green-blue). The bottom boundary depicts the XRT observations scaled linearly, shown in lower rows, where red represents low

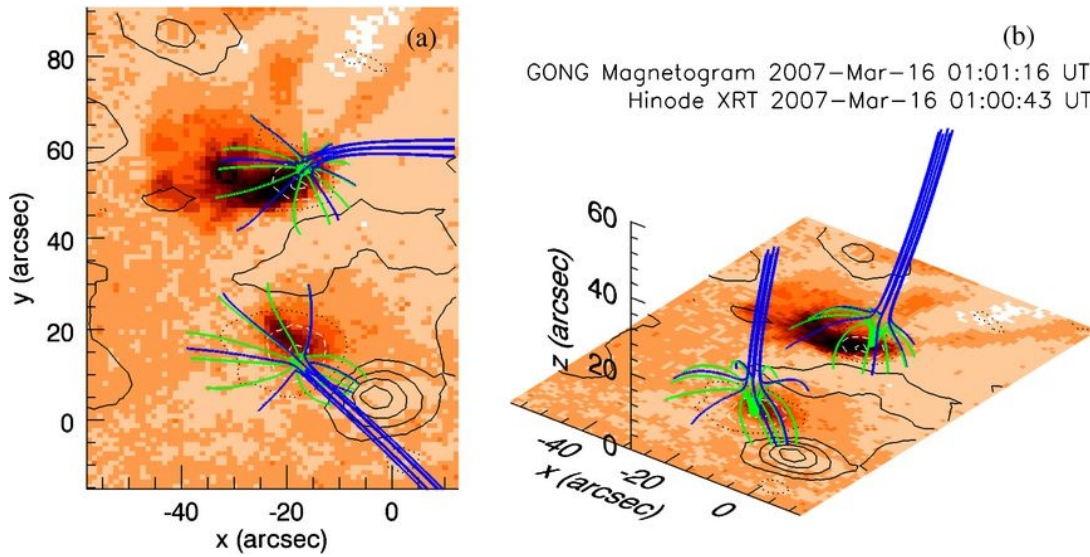


Figure 2.10: Top view (left) and side view (right) of the coronal magnetic field feature around the two CBPs. The picture adapted from [Zhang et al. \(2012\)](#).

values and purple shows the peak values. The left to right pictures correspond to the time at 06:38:13 UT, 08:38:05 UT, 10:38:08 UT, and 11:59:35 UT on 09 November 2007. They strongly suggested that the presence of a null point is important to release the energy from CBPs.

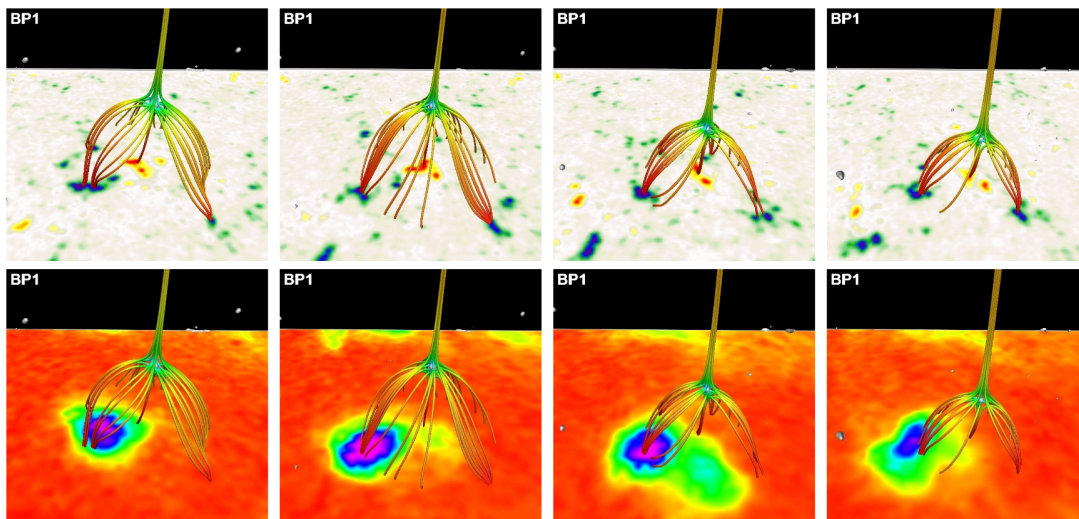


Figure 2.11: Figure depicts the association of 3D null point fan-dome structure with observed X-ray emissions from CBPs in CH regions. The picture has been taken from [Galsgaard et al. \(2017\)](#).

Overall, it is important to emphasize that the topology of 3D magnetic null has a crucial role in hosting the magnetic reconnection and shaping the various

reconnection-driven solar transients, as presented above. Therefore, it is crucial to understand the topology of 3D magnetic null. The following discusses the structure and properties associated with 3D magnetic nulls.

2.4 Theory of 3D magnetic null

2.4.1 Structure of 3D nulls

The local magnetic structure in the vicinity of magnetic null (where $\mathbf{B} = 0$) can be obtained by assuming that the field varies linearly (Lau & Finn, 1990; Parnell et al., 1996). Using Taylor's first-order expansion and considering the null point is situated at the origin, the magnetic field \mathbf{B} near a null point can be expressed as follows:-

$$\mathbf{B} = \mathbf{B}(\mathbf{x}_0) + \nabla \mathbf{B}|_{\mathbf{x}_0} \cdot (\mathbf{x} - \mathbf{x}_0) = \mathbf{M} \cdot \mathbf{r} \quad (2.2)$$

where \mathbf{x}_0 is location of magnetic null, \mathbf{r} is a position vector $(x,y,z)^T$, and \mathbf{M} is a jacobian matrix with its elements $(\partial B_i / \partial x_j)$ given as follows.

$$\mathbf{M} = \begin{bmatrix} \frac{\partial B_x}{\partial x} & \frac{\partial B_x}{\partial y} & \frac{\partial B_x}{\partial z} \\ \frac{\partial B_y}{\partial x} & \frac{\partial B_y}{\partial y} & \frac{\partial B_y}{\partial z} \\ \frac{\partial B_z}{\partial x} & \frac{\partial B_z}{\partial y} & \frac{\partial B_z}{\partial z} \end{bmatrix} \quad (2.3)$$

The divergence-free condition ($\nabla \cdot \mathbf{B} = 0$) of the magnetic field provides,

$$\frac{\partial B_x}{\partial x} + \frac{\partial B_y}{\partial y} + \frac{\partial B_z}{\partial z} = 0. \quad (2.4)$$

The trace of matrix \mathbf{M} is given by

$$\text{Tr}(\mathbf{M}) = \frac{\partial B_x}{\partial x} + \frac{\partial B_y}{\partial y} + \frac{\partial B_z}{\partial z} \quad (2.5)$$

Combining Eq. (2.4) and (2.5), we get

$$\text{Tr}(\mathbf{M}) = 0 \quad (2.6)$$

If λ_i i.e. $(\lambda_1, \lambda_2, \lambda_3)$ are the Eigenvalues of the matrix \mathbf{M} . Then from Eq. (2.6), we get

$$\text{Tr}(\mathbf{M}) = \lambda_1 + \lambda_2 + \lambda_3 = 0, \quad (2.7)$$

and by solving the Eigenvalue equation $|\mathbf{M} - \lambda\mathbf{I}| = 0$, we get the three Eigenvectors $(\mathbf{x}_1, \mathbf{x}_2, \mathbf{x}_3)$ corresponding to the three eigenvalues $(\lambda_1, \lambda_2, \lambda_3)$. The Eq. (2.7) restricts that there exists a single Eigenvalue whose sign will always be opposite to the sign of the real part of the remaining two Eigenvalues. The spine is the field lines parallel to the Eigenvector related to that single Eigenvalue. In contrast, the field lines tangential to the plane formed by the Eigenvectors of the remaining two Eigenvalues are called Fan plane (Parnell et al., 1996). It is sometimes known as the Separatrix surface as it differentiates the two magnetic flux domains. One such example of 3D magnetic null is shown in Fig. 1.9. From Maxwell's Eq. (1.4), we have $\mu_0(J_x, J_y, J_z) = ((\partial B_z/\partial y - \partial B_y/\partial z), (\partial B_x/\partial z - \partial B_z/\partial x), (\partial B_y/\partial x - \partial B_x/\partial y))$. Therefore, off-diagonal elements of the matrix \mathbf{M} given by Eq. (2.4) are related to the current density, and the diagonal elements are associated with the potential part of the magnetic field (Parnell et al., 1996). To study all possible configurations of the localized field of the 3D null point, the matrix \mathbf{M} can be reduced to the least number of free parameters without losing the generality. For that, if we choose the local orthogonal coordinate system such that the Eigenvector associated with the single Eigenvalue, which makes the spine of the null is in the z-direction, i.e., the spine is directed along the z-axis and the Eigenvectors of the remaining Eigenvalues forming a plane, i.e., fan plane is in x,y-plane. Further, the matrix may be reduced by rotating the xy-plane about the z-axis so that the new x-axis can be aligned toward the net resultant current in the xy-plane. Finally, by dividing by a scale factor, the matrix is further reduced to the following (Parnell et al., 1996).

$$\mathbf{M} = \begin{bmatrix} 1 & \frac{1}{2}(q - J_{\parallel}) & 0 \\ \frac{1}{2}(q + J_{\parallel}) & p & 0 \\ 0 & J_{\perp} & -(p + 1) \end{bmatrix} \quad (2.8)$$

, where $p \geq -1$, $q^2 \leq J_{\parallel}^2 + 4p$, with p and q defined as the potential part of the field and the current density \mathbf{J} can be written as

$$\mathbf{J} = \frac{1}{\mu_0}(J_{\perp}, 0, J_{\parallel}). \quad (2.9)$$

where J_{\parallel} represents the component of current parallel to the spine and J_{\perp} represents the component of current perpendicular to the spine. Where the parameters and elements of \mathbf{M} can be written in terms of magnetic field as follows, $p = \partial B_y / \partial y$, $q = 2\partial B_y / \partial x$, $J_{\parallel} = (\partial B_y / \partial x) - (\partial B_x / \partial y)$, $J_{\perp} = \partial B_z / \partial y$, $\partial B_x / \partial x = 1$, $\partial B_x / \partial y = (1/2)(q - J_{\parallel})$, $\partial B_y / \partial x = (1/2)(q + J_{\parallel})$, $\partial B_z / \partial x = \partial B_x / \partial z = \partial B_y / \partial z = 0$. The condition $\det(\mathbf{M}) = 0$ gives the case of degenerate nulls where two or more nulls are overlapped on each other and the configuration near the nulls can be obtained by considering the higher order terms in the expansion of field near the null (Yang, 2017). Therefore, to avoid the degeneracy the condition $\det(\mathbf{M}) \neq 0$ must hold. Further, the threshold current J_{thresh} can be obtained by putting the discriminant of the matrix (shown in Eq. (2.8)) equal to zero and is given in terms of p and q .

$$J_{thresh} = \sqrt{(p-1)^2 + q^2}. \quad (2.10)$$

The Eigenvalues ($\lambda_1, \lambda_2, \lambda_3$) associated with matrix given in Eq. (2.8) can given as

$$\lambda_1 = \frac{p+1 + \sqrt{J_{thresh}^2 - J_{\parallel}^2}}{2}, \quad (2.11)$$

$$\lambda_2 = \frac{p+1 - \sqrt{J_{thresh}^2 - J_{\parallel}^2}}{2}, \quad (2.12)$$

and

$$\lambda_3 = -(p+1). \quad (2.13)$$

The relative values of J_{thresh} and J_{\parallel} will decide whether the (λ_1, λ_2) will be real or complex Eigenvalues. The complex Eigenvalues arise due to the non-zero values and the differences of the off-diagonal elements. Consequently, they are

associated with the current density. Therefore, the presence of current in the field structure makes the Eigenvalues complex. They will exist in complex conjugate pairs because of the condition mentioned in Eq. (2.7). In the following, the nulls can be classified into two types based on the value of current density (\mathbf{J}).

2.4.2 Radial and Spiral 3D null

If the current density (\mathbf{J}) is zero, i.e., $J_{\parallel} = 0$, $J_{\perp} = 0$, the 3D null is potential (current-free) 3D magnetic null. Further, if $q = 0$, then the matrix \mathbf{M} given in Eq. (2.8) reduces to the following.

$$\mathbf{M} = \begin{bmatrix} 1 & 0 & 0 \\ 0 & p & 0 \\ 0 & 0 & -(p+1) \end{bmatrix} \quad (2.14)$$

The Eigenvalues of the above matrix are $\lambda_1 = 1$, $\lambda_2 = p$, $\lambda_3 = -(p+1)$ and the magnetic can be written as

$$\mathbf{B} = (x, py, -(p+1)z) \quad (2.15)$$

The example of a 3D potential null for $p = 1$ is shown in Fig. 2.12 and they are also called as radial null. The field lines in the fan plane are emanating radially outward. If the current density is non-zero in the null configuration, it is called a non-potential or current-carrying null. For this scenario, the matrix in Eq. (2.8) can be utilized to construct the magnetic field, and the corresponding Eigenvalues are mentioned in Eq. (2.11)-(2.13). For $q = 0$, the magnetic field can be written as follows.

$$\mathbf{B} = (x - \frac{1}{2}J_{\parallel}y, \frac{1}{2}J_{\parallel}x + py, J_{\perp}y - (p+1)z) \quad (2.16)$$

In the following, examples of non-potential nulls are shown. Fig. 2.13 shows the field lines configuration near the null for $J_{\perp} = 0$, $J_{thresh} = 2$ and $J_{\parallel} = 1$, i.e., $|J_{\parallel}| < J_{thresh}$, where $p = 1$, is used. Therefore, all three Eigenvalues ($\lambda_1 =$

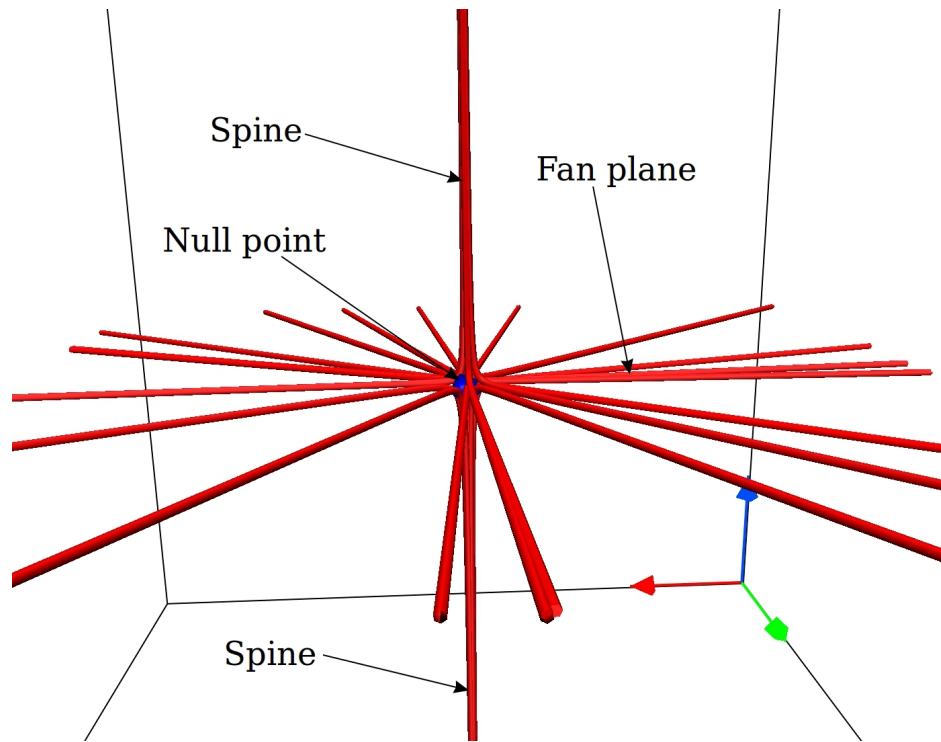


Figure 2.12: Figure depicts the potential 3D null point configuration for $p = 1$.

$1 + \sqrt{3}/2, \lambda_2 = 1 - \sqrt{3}/2, \lambda_3 = -2$) are real and distinct. For $|J_{\parallel}| = J_{thresh}$,

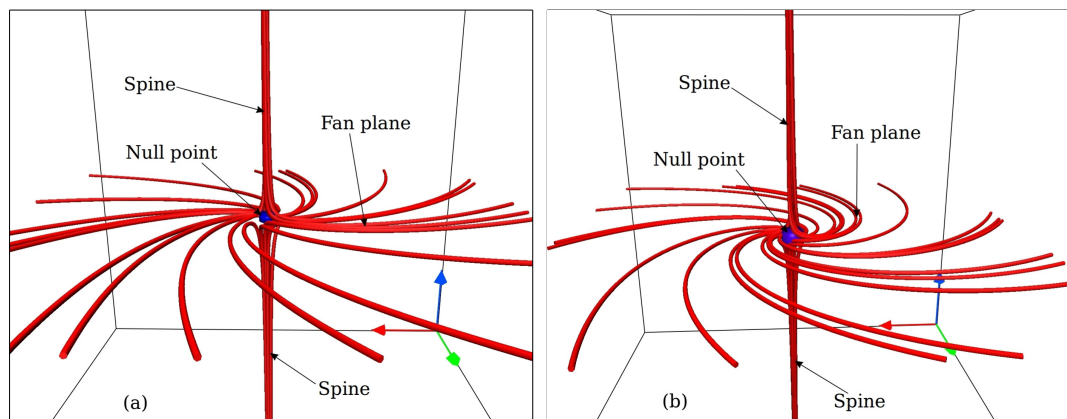


Figure 2.13: Figure depicts the example of non-potential 3D null point configuration for $J_{\perp} = 0$, $J_{thresh} = 2$ and $J_{\parallel} = 1$, i.e., $|J_{\parallel}| < J_{thresh}$ (panel (a)), where $p = 1$, is used. Panel (b) depicts for $|J_{\parallel}| = J_{thresh}$ and depicts the example of non-potential 3D null point configuration for Eigenvalues $(\lambda_1 = 1, \lambda_2 = 1, \lambda_3 = -2)$.

i.e., two out of three Eigenvalues will be the same, and an example is shown in Fig. 2.13. Here, $J_{\parallel} = 2$ is used. Therefore, the all three Eigenvalues $(\lambda_1 = 1, \lambda_2 = 1, \lambda_3 = -2)$ are real and two are repeated. For $|J_{\parallel}| > J_{thresh}$, i.e., the

two Eigenvalues will be complex numbers. The examples are shown in Fig. 2.14, having $J_{\parallel} = 3$, $J_{\perp} = 5$ with $J_{\perp} = 0$ (panels (a), (b)), and $J_{\parallel} = 5$, with $J_{\perp} = 5$ (panel (c)), respectively. It is noted that the J_{\parallel} (current along the spine) plays

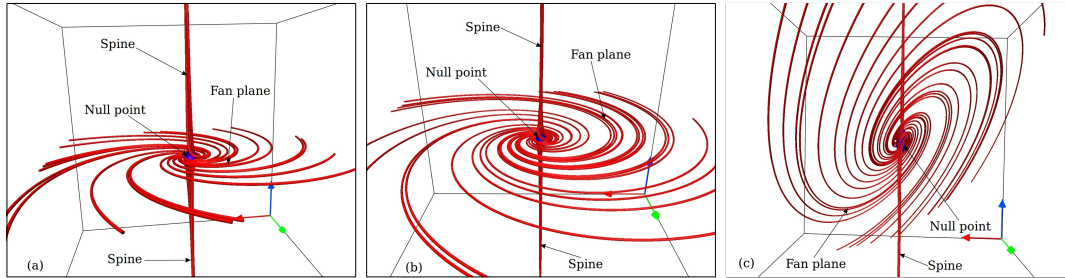


Figure 2.14: Figure depicts the example of non-potential 3D null point configuration for $J_{\parallel} = 3$, $J_{\perp} = 0$ (panel (a)), $J_{\parallel} = 5$, $J_{\perp} = 0$ (panel(b)), and $J_{\parallel} = 5$, $J_{\perp} = 5$ (panel (c)).

a role in spiraling the field lines in the fan plane near the null (c. f. panels (a)-(b)) and with $J_{\perp} = 0$, the spine and fan plane are at a right angle. However, the $J_{\perp} \neq 0$ makes the spine and fan plane field lines inclined as shown in panel (c) of Fig. 2.14. All these three nulls are known as spiral nulls, and their two Eigenvalues are complex conjugate pairs. In conclusion, the 3D nulls with current J_{\parallel} along the spine are spiral nulls whose Eigenvalues contain imaginary parts. By changing the parameters p , q , J_{\parallel} , and J_{\perp} , the different field line structures of the null can be obtained. However, the magnetic field is a vector quantity, and the field line direction in those structures defines the topological degree (TD) discussed in the next Section.

2.4.3 Topological degree of 3D magnetic null

Two cases are possible depending on the direction of the magnetic field near the null in the spine-fan topology. (i) The field lines in the spine directed toward null and emanating out from the null in the fan plane are called Positive null, and (ii) Negative type null; the fan field lines are directed toward the null and directed away from the null along the spine (Lau & Finn, 1990). From Eq. (2.2)

and at magnetic nulls ($\mathbf{B}(\mathbf{x}_0) = 0$), the equation reduces to

$$\mathbf{B} = \nabla\mathbf{B}|_{x_0} \cdot (\mathbf{x} - \mathbf{x}_0) \quad (2.17)$$

The direction of magnetic field \mathbf{B} can be obtained by calculating the $\det\nabla\mathbf{B}|_{x_0}$, which defines the topological degree of the null as follows (Lau & Finn, 1990).

$$\text{TD} = \text{sign}(\det(\nabla\mathbf{B}|_{\mathbf{x}_0})) = \pm 1. \quad (2.18)$$

Therefore, if the fan field lines are directed toward the null, then the topological degree of the 3D null is “+1” and vice-versa. The examples of 3D null having TD +1, and -1 are shown in Fig. 2.15. To locate, trace, and determine their

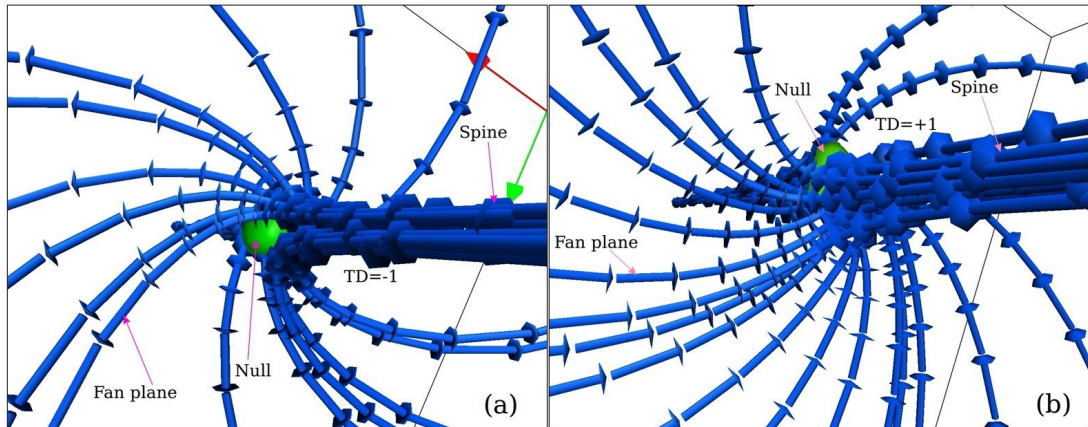


Figure 2.15: Panel (a) depicts the example of the positive 3D null point where fan field lines are directed away from null whereas spine field lines are directed toward the null resulting in topological degree -1, whereas fan field lines directed toward null point making topological degree +1 is shown in panel (b).

type (spiral or radial) based on the nature (complex or real) of Eigenvalues of $\nabla\mathbf{B}|_{\text{null}}$, and topological degrees, the modified trilinear null detection technique (see Sect. 3.3) has been employed. If a system initially consists of i number of 3D nulls and uses Taylor’s first order expansion near each null, the magnetic field can be written as (Greene, 1992; Murphy et al., 2015).

$$\mathbf{B} = \mathbf{B}(\mathbf{x}_i) + \sum_i \nabla\mathbf{B}|_{\mathbf{x}_i} \cdot (\mathbf{x} - \mathbf{x}_i), \quad (2.19)$$

where \mathbf{x}_i are the locations of the null points, where $\mathbf{B}(\mathbf{x}_i) = 0$. Therefore, the net topological degree (D) is defined as follows.

$$D = \sum_i \text{sign}(\det(\nabla \mathbf{B}|_{\mathbf{x}_i})) \quad (2.20)$$

If that system evolves with time and the number of nulls varies with time, then it should satisfy the conservation of net topological degree proven in the next Section.

2.4.4 Conservation of net topological degree of 3D nulls

An interesting fundamental property of 3D nulls is the conservation of the net topological degree, denoted by D, which is proven mathematically in the following. From ideal Ohm's law

$$\mathbf{E} + \mathbf{v} \times \mathbf{B} = 0 \quad (2.21)$$

Taking curl on both sides, we get

$$\nabla \times \mathbf{E} + \nabla \times (\mathbf{v} \times \mathbf{B}) = 0, \quad (2.22)$$

Using Maxwell's Eq. (1.4), we have

$$\frac{\partial \mathbf{B}}{\partial t} = \nabla \times (\mathbf{v} \times \mathbf{B}) \quad (2.23)$$

$$\frac{\partial \mathbf{B}}{\partial t} = \mathbf{v}(\nabla \cdot \mathbf{B}) - \mathbf{B}(\nabla \cdot \mathbf{v}) + (\mathbf{B} \cdot \nabla)\mathbf{v} - (\mathbf{v} \cdot \nabla)\mathbf{B}, \quad (2.24)$$

using $\nabla \cdot \mathbf{B} = 0$

$$\frac{\partial \mathbf{B}}{\partial t} = \mathbf{B} \cdot \nabla \mathbf{v} - \mathbf{v} \cdot \nabla \mathbf{B} - \mathbf{B}(\nabla \cdot \mathbf{v}), \quad (2.25)$$

and at magnetic null ($\mathbf{B}=0$)

$$\frac{\partial \mathbf{B}}{\partial t} = -\mathbf{v} \cdot \nabla \mathbf{B}, \quad (2.26)$$

$$\frac{\partial \mathbf{B}}{\partial t} + \mathbf{v} \cdot \nabla \mathbf{B} = 0 \quad (2.27)$$

$$\frac{d\mathbf{B}}{dt} = 0, \quad (2.28)$$

Therefore, 3D magnetic nulls will preserve their identity during the ideal plasma evolution. However, the resistive Ohm's law, which allows the magnetic reconnection in the system, is given as follows.

$$\mathbf{E} + \mathbf{v} \times \mathbf{B} = \eta \mathbf{J} \quad (2.29)$$

where η represents the magnetic diffusivity. Taking curl on both side of Eq. (2.29),

$$\nabla \times \mathbf{E} + \nabla \times (\mathbf{v} \times \mathbf{B} - \eta \mathbf{J}) = 0, \quad (2.30)$$

using Maxwell's Eq. (1.4), we have

$$\frac{\partial \mathbf{B}}{\partial t} = \nabla \times (\mathbf{w} \times \mathbf{B}), \quad (2.31)$$

where $\mathbf{w} \times \mathbf{B} = \mathbf{v} \times \mathbf{B} - \eta \mathbf{J}$ and \mathbf{w} is a velocity which has two contributions one from plasma velocity and other from diffusion velocity. On expanding the right-hand side of Eq. (2.31),

$$\frac{\partial \mathbf{B}}{\partial t} = \mathbf{w}(\nabla \cdot \mathbf{B}) - \mathbf{B}(\nabla \cdot \mathbf{w}) + (\mathbf{B} \cdot \nabla)\mathbf{w} - (\mathbf{w} \cdot \nabla)\mathbf{B}, \quad (2.32)$$

using $\nabla \cdot \mathbf{B} = 0$,

$$\frac{\partial \mathbf{B}}{\partial t} = (\mathbf{B} \cdot \nabla)\mathbf{w} - (\mathbf{w} \cdot \nabla)\mathbf{B} - \mathbf{B}(\nabla \cdot \mathbf{w}), \quad (2.33)$$

and at magnetic null ($\mathbf{B} = 0$),

$$\frac{\partial \mathbf{B}}{\partial t} = -(\mathbf{w} \cdot \nabla)\mathbf{B}, \quad (2.34)$$

or

$$\frac{d\mathbf{B}}{dt} = 0, \quad (2.35)$$

The above Eq. (2.35) tells that even in the presence of magnetic reconnections, the 3D magnetic null will preserve its identity in the reference frame moving with velocity \mathbf{w} (Hornig & Schindler, 1996). Therefore, the identity of 3D null is preserved in both the cases, ideal and in resistive plasma, which implies that 3D nulls can be traced in time. If a system initially consists of i number of 3D nulls and uses Taylor's first order expansion near each null, the magnetic field can be written as (Greene, 1992; Murphy et al., 2015).

$$\mathbf{B} = \mathbf{B}(\mathbf{x}_i) + \sum_i \nabla \mathbf{B}|_{\mathbf{x}_i} \cdot (\mathbf{x} - \mathbf{x}_i), \quad (2.36)$$

where \mathbf{x}_i are the locations of the null points. From Eq. (2.35) and (2.36), we get \mathbf{B} is constant. Therefore,

$$\sum_i \nabla \mathbf{B}|_{\mathbf{x}_i} = \text{constant}. \quad (2.37)$$

From Eq. (2.20) and (2.37), the net topological degree is

$$D = \sum_i \text{sign}(\det(\nabla \mathbf{B}|_{\mathbf{x}_i})) = \text{constant} \quad (2.38)$$

Therefore, D is constant in time, i.e., the net topological degree remains conserved with the evolution and puts stringent constraints on the change in a number of null in time. Hence, in a system having one or more nulls, the net topological degree of nulls is invariant (Hornig & Schindler, 1996). Consequently, the plasma evolution, which generates and annihilates the 3D nulls, must satisfy this fundamental constraint and is also explored in the thesis work along with the core objective described in Sec. 1.4 through numerical simulations. For the purpose, the employed numerical tools are described in the next chapter.

Chapter 3

Methodology and necessary numerical tools

3.1 Data Acquisition

3.1.1 SDO

The Solar Dynamics Observatory (SDO) is the first space-weather mission in NASA's Living With a Star (LWS) program, launched on February 11, 2010, into a circular geosynchronous orbit inclined by 28° about the longitude of the SDO (Pesnell et al., 2012). It started providing science data on May 01, 2010. The science goal is to determine how the Sun's magnetic field is generated and structured, how this stored magnetic energy is released into the heliosphere and geospace as the solar wind, energetic particles, and variations in the solar irradiance, which will lead to an increased understanding of the role that solar variability plays in changes in Earth's atmospheric chemistry and climate. For the aim, the SDO mission includes three scientific instruments: Atmospheric Imaging Assembly (AIA), Extreme Ultraviolet Variability Experiment (EVE), and Helioseismic and Magnetic Imager (HMI). The data only from HMI and AIA instruments have been used in this Thesis, as discussed below.

Helioseismic and Magnetic Imager (HMI)

The Helioseismic and Magnetic Imager (HMI) instrument aims to study solar oscillations using helioseismic techniques and magnetic fields near the solar surface. The HMI instrument is designed to measure the vector magnetic field, solar surface velocity, and continuum intensity at the solar photosphere using the 6173Å Fe I absorption line (Schou et al., 2012). HMI gives the full disk photospheric velocity measurement (or Dopplergram) every 45 seconds with a resolution of 1 arcsec, a noise level $\approx 25\text{m s}^{-1}$, used to understand the Sun's interior. HMI uses the Zeeman effect (Zeeman, 1897) of the same spectral line to measure the Stokes parameters (I, Q, U, V, defined below) required to create full-disk photospheric Line-of-sight (LOS) and vector magnetic field maps (vector magnetogram). The LOS magnetograms have a cadence of 45 seconds with a resolution of 1 arcsec, a noise level of 17 G, and a dynamic range of ± 3 kG. The cadence of vector magnetograms is 12 minutes and has a polarization accuracy of no less than 0.3%. HMI thus provides the first rapid-cadence measurements of the strength and direction of the solar magnetic field over the visible disk of the Sun. As discussed above, the magnetic field on the Sun's photosphere is measured using Zeeman's effect, in which the splitting of spectral lines occurs in the presence of the magnetic field. The shift in the wavelength (Borrero et al., 2011) is given by

$$\Delta\lambda = \pm 4.67 \times 10^{-10} g_{eff} |\mathbf{B}| \lambda_0^2 = \pm 0.04464 |\mathbf{B}| (m\text{\AA}) \quad (3.1)$$

where $\Delta\lambda$, g_{eff} , λ_0 , and $|\mathbf{B}|$ is a shift in wavelength, Landè g-factor, central wavelength, and strength of the magnetic field, respectively. For HMI, the Fe I (6173 Å) line is used for which the Landè g-factor is 2.5 (Borrero et al., 2011). The polarization state of the radiation is measured in the form of a Stokes vector (I, Q, U, and V). Where I represents the total intensity of the radiation, Q represents the intensity difference between vertical and horizontal linear polarization, U is the intensity difference between linear polarization at $+45^\circ$ and -45° and V is the intensity difference between right and left-hand circular polarization. The

Stokes parameter can be written as (Venkatakrishnan & Gosain, 2008):

$$I = \langle E_x^2 \rangle + \langle E_y^2 \rangle, \quad (3.2)$$

$$Q = \langle E_x^2 \rangle - \langle E_y^2 \rangle, \quad (3.3)$$

$$U = \text{Re} \langle E_x E_y^* \rangle, \quad (3.4)$$

$$V = \text{Im} \langle E_x E_y^* \rangle \quad (3.5)$$

where, E_x and E_y are components of Electric field and $\langle \rangle$ represents the expectation value. Using Stokes vector and by employing the Very Fast Inversion of Stokes Vector (VFISV) (Borrero et al., 2011) code, the required vector magnetic field is obtained (Metcalf et al., 1991). Two types of datasets are available at the HMI pipeline first, the full disk of temporal cadence 720s and 135s and a cylindrical equal-area active region patch with temporal cadence of 720s, for details <http://jsoc.stanford.edu/jsocwiki/HARPDaDataSeries>. The components of the field are the radial (B_r), poloidal B_p , and toroidal B_t , which are B_r , B_p , and B_t equal to B_x , $-B_y$ and B_z , respectively, in cartesian coordinate system. The ‘hmi. sharpcea720s’ data series magnetogram from the HMI on board the SDO has been used in one of the studies of the Thesis. This data series provides the magnetic field on a Cartesian grid, which is initially remapped onto a Lambert cylindrical equal-area (CEA) projection and then transformed into heliographic coordinates (Bobra et al., 2014). For details of the data products, see http://jsoc.stanford.edu/HMI/Vector_products.html. The coronal magnetic field can be constructed from these photospheric magnetograms using extrapolation models. In Section 3.2, the NFFF extrapolation model, relevant to this Thesis, is discussed.

Atmospheric Imaging Assembly (AIA)

The AIA is an array of four telescopes that gives simultaneous high-resolution full disk images of the surface and atmosphere of the Sun with 1.5 arcsec spatial resolution and 12-second temporal resolution. Filters on the telescopes cover ten different wavelength bands. The seven narrow-band imaging in extreme ultraviolet (EUV) bands centered on specific lines: Fe XVIII (94 Å), Fe XVII, XXI (131 Å), Fe IX (171 Å), Fe XII, XXIV (193 Å), Fe XIV (211 Å), He II (304 Å), and Fe XVI (335 Å). Two observe in C IV (near 1600 Å) and the nearby continuum (1700 Å), and one filter observes in the visible to align the images from other filters. With these multiple simultaneous high-resolution full disk observations, the key aspects of the solar activity are to be revealed. The wavelength bands cover temperature diagnostics range from 6000 K to 3×10^6 K (Lemen et al., 2012). The primary ions for each band, their characteristic emission temperatures, and the types of solar features that may be observed are listed in the table 3.1.

Channel	Primary ion(s)	Region of atmosphere	Char. log(T)
4500 Å	continuum	photosphere	3.7
1700 Å	continuum	photosphere	3.7
304 Å	He II	chromosphere, transition region	4.7
1600 Å	C IV + continuum	transition region, upper photosphere	5.0
171 Å	Fe IX	quiet corona, upper transition region	5.8
193 Å	Fe XII, XXIV	corona and hot flare plasma	6.2, 7.3
211 Å	Fe XIV	active region corona	6.3
335 Å	Fe XVI	active region corona	6.4
94 Å	Fe XVIII	flaring corona	6.8
131 Å	Fe VIII, XXI	transition region, flaring corona	5.6,7.0

Figure 3.1: The different filters of AIA centered on specific wavelength and their corresponding observing solar atmosphere regions and different characteristic temperatures are listed in the table. The table has been adapted from Lemen et al. (2012).

3.1.2 Geostationary Operational Environmental Satellite (GOES)

The data from Geostationary Operational Environmental Satellite (GOES)-15, launched on 4 March 2010, has been used in this Thesis. GOES-15 was one of the

many GOES. The GOESs are the mission of the National Aeronautics and Space Administration (NASA) and are operated and managed by the National Oceanic and Atmospheric Administration (NOAA). In September 2010, it recorded its first data and the last data was recorded in March 2020. The class of solar flare is defined based on X-ray flux measured by X-ray sensors onboard GOES-15 (Antalova, 1996; Bowen et al., 2013). GOES-15 has two soft X-ray (SXR) channels, which measure fluxes in two bands, first in (0.5-4) Å and the second in (1-8) Å, which approximately corresponds to the energy ranges of (3-25) keV and (1.5-12) keV, respectively. The X-ray fluxes are measured in the physical unit of W m^{-2} . Classes A, B, C, M, and X are defined based on the peak fluxes. The most powerful flares in this classification are flares of the X class, corresponds to the absolute flux of more than 10^{-4} W m^{-2} in the SXR-range, X-ray flares of M1-M9 classes correspond to the flux from 10^{-5} to 10^{-4} W m^{-2} , X-ray flares of C1-C9 corresponds to the flux from 10^{-6} to 10^{-5} W m^{-2} , X-ray flares of B1-B9 corresponds to the flux from 10^{-7} to 10^{-6} W m^{-2} , and X-ray flares of class A correspond to the flux less than 10^{-7} W m^{-2} (Antalova, 1996; Bowen et al., 2013; Bruevich, 2020).

3.2 Non-Force Free Field (NFFF) extrapolation

The importance of magnetic topology in magnetic reconnection leading to various solar eruptions is discussed in Chapter 3. Therefore, it is important to determine the solar coronal field's magnetic topology to understand these phenomena. In the absence of a reliable direct measurement of the coronal magnetic field, the viable alternative is to use the solar coronal magnetic field extrapolation model. The photospheric plasma has high plasma- β and is not force-free, and plasma- β is negligible at the mid-corona as suggested by (Gary, 2001), see Fig. 3.2. A straightforward calculation gives the rationale for NFFF extrapolation (Mittra et al., 2018). The salient features are discussed for completeness. A dimensional analysis of the momentum balance equation of MHD will lead to the following

for the ratio of the Lorentz force to the rate of change of momentum

$$\frac{|\mathbf{J} \times \mathbf{B}|}{|\rho \frac{dv}{dt}|} \sim \frac{\mathbf{B}^2}{\rho |v|^2} \sim \frac{\mathbf{B}^2}{\rho |v_{th}|^2} \frac{|v_{th}|^2}{|v|^2} \sim \frac{1}{\beta} \frac{|v_{th}|^2}{|v|^2} \quad (3.6)$$

where v_{th} is the kinetic velocity. The above equation for the typical plasma flow velocity and thermal velocity at the photosphere is $\sim 1 \text{ Km s}^{-1}$ (Vekstein, 2016; Khlystova & Toriumi, 2017), leads to

$$\frac{|\mathbf{J} \times \mathbf{B}|}{|\rho \frac{dv}{dt}|} \sim \frac{1}{\beta}, \quad (3.7)$$

or

$$|\mathbf{J} \times \mathbf{B}| \sim \left| \rho \frac{dv}{dt} \right| \quad (3.8)$$

since $\beta \approx 1$ at the Photosphere. Therefore, Eq. (3.8) suggests that the Lorentz force is non-zero at the photosphere, which can act as a driver for corresponding plasma motions. Notably, the NFFF extrapolation model is different from more widely used Non-Linear Force Free Field (NLFFF) extrapolation as it supports a non-zero Lorentz force while such a force is zero in NLFFF.

The following briefly introduces the NFFF extrapolation model used in the Thesis. For the extrapolation purpose, the method developed by Hu & Dasgupta (2008); Hu et al. (2008) and uses the principle of minimum dissipation rate (MDR), which is applicable to open dissipative systems like the solar corona (Bhattacharyya et al., 2007). According to this principle, the terminal state of a relaxing magnetofluid is determined by minimizing the total (Ohmic+viscous) dissipation rate while keeping the generalized helicity dissipation rates invariant (Bhattacharyya et al., 2007). An inhomogeneous double-curl Beltrami equation for the magnetic field \mathbf{B} given by (Bhattacharyya & Janaki, 2004; Bhattacharyya et al., 2007) is being solved.

$$\nabla \times \nabla \times \mathbf{B} + a_1 \nabla \times \mathbf{B} + a_2 \mathbf{B} = \nabla \psi, \quad (3.9)$$

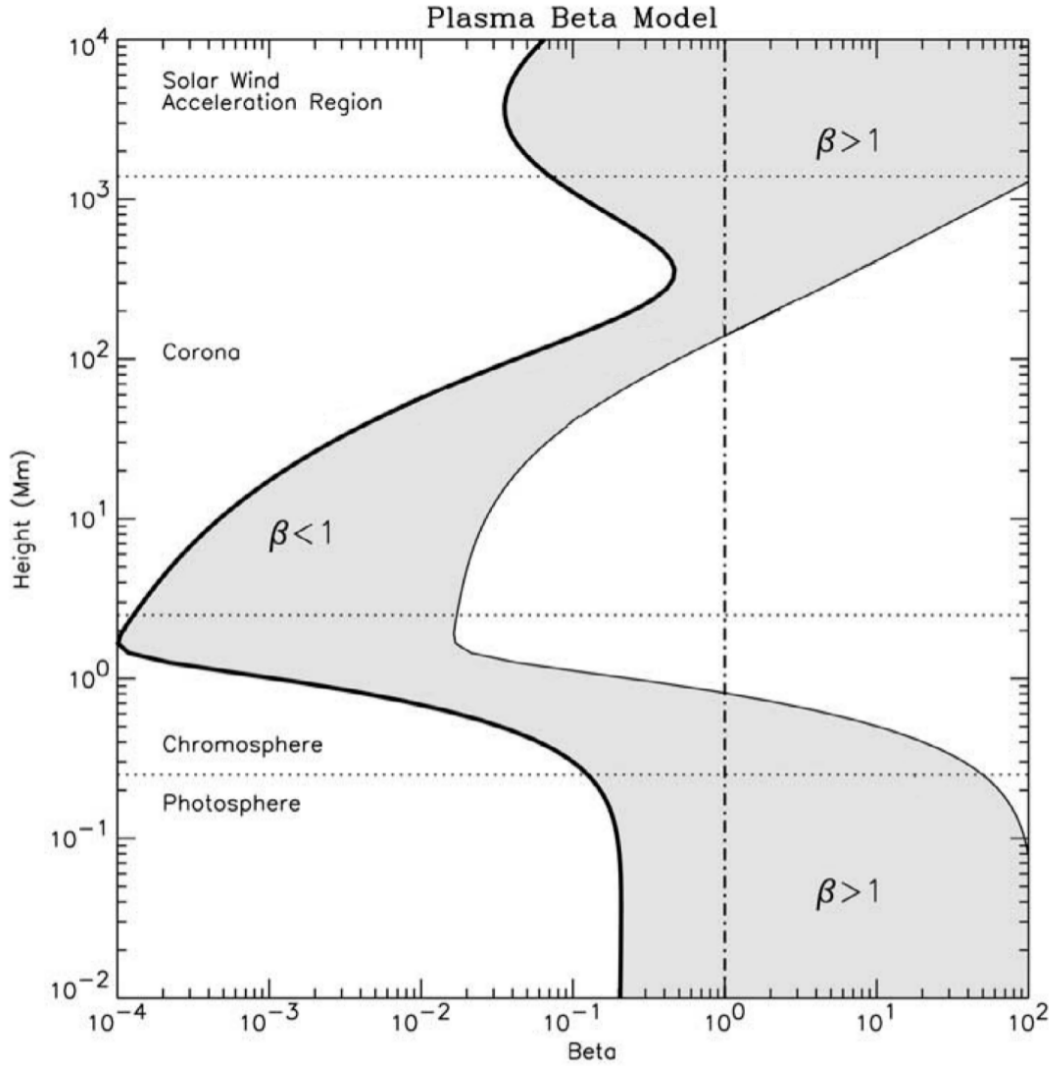


Figure 3.2: The figure depicts the model of plasma β variation with height. The figure has been adapted from Gary (2001).

where a_1 and a_2 are the constants. This equation can be written as

$$\nabla \times \nabla \times \mathbf{B}' + a_1 \nabla \times \mathbf{B}' + a_2 \mathbf{B}' = 0, \quad (3.10)$$

where $\mathbf{B}' = \mathbf{B} - \nabla\psi/a_2$. The solution to a double-curl Beltrami equation (Eq. 3.10) can be given by using Chandrasekhar-Kendall functions, forming a complete orthonormal basis.

$$\mathbf{B} = \mathbf{B}_1 + \mathbf{B}_2 + \mathbf{B}_3; \quad \nabla \times \mathbf{B}_i = \alpha_i \mathbf{B}_i, \quad (3.11)$$

where $i = 1, 2, 3$ and α_i are constant for a given \mathbf{B}_i (Hu & Dasgupta, 2008; Hu et al., 2008). Here, each sub-field \mathbf{B}_i represents a linear force-free field (LFFF) characterized by specific constants α_i . Without a loss of generality, a selection $\alpha_1 \neq \alpha_3$ and $\alpha_2 = 0$ can be made, implying \mathbf{B}_2 a potential field. By taking curl two times on both sides of Eq. (3.11), one can obtain the following,

$$\begin{pmatrix} \mathbf{B}_1 \\ \mathbf{B}_2 \\ \mathbf{B}_3 \end{pmatrix} = v^{-1} \begin{pmatrix} \mathbf{B} \\ \nabla \times \mathbf{B} \\ \nabla \times \nabla \times \mathbf{B} \end{pmatrix}, \quad (3.12)$$

where v^{-1} is the Vandermonde matrix and given below.

$$v^{-1} = \begin{pmatrix} 1 & 1 & 1 \\ \alpha_1 & \alpha_2 & \alpha_3 \\ \alpha_1^2 & \alpha_2^2 & \alpha_3^2 \end{pmatrix} \quad (3.13)$$

is non-singular if α s are distinct. According to Eq. (3.11), one can get the final extrapolated field by summing the three LFFFs. Subsequently, an iterative approach is employed to determine the optimal pair $\alpha = \alpha_1, \alpha_3$, which finds the pair by minimizing the average deviation between the observed (\mathbf{B}_t) and the calculated (\mathbf{b}_t) transverse field on the photospheric boundary. Effectively, the metric

$$E_n = \left(\sum_{i=1}^M |\mathbf{B}_{t,i} - \mathbf{b}_{t,i}| \times |\mathbf{B}_{t,i}| \right) / \left(\sum_{i=1}^M |\mathbf{B}_{t,i}|^2 \right), \quad (3.14)$$

where $M = n^2$ represents the total number of grid points on the transverse plane is iteratively minimized (Prasad et al., 2018).

The iteration starts with $k = 0$, i.e. $\mathbf{B}_2^{(k)} = c_{min} \mathbf{B}'$ in the extended series of potential field, $\mathbf{B}_2^{(k)}$, $k = 0, 1, 2, 3, \dots$, and devise an iteration procedure as depicted in Fig. 3.3. In the flow chart, Y and N represent the Yes and No satisfying criterion shown in the logic boxes, and k_{max} represents the maximum number of iterations. The E_n can be evaluated by Eq. 3.14, and if the value is small enough, the process ends. Otherwise, iteration goes to the next step ($k = k + 1$), in which the next sub-potential field in the series is obtained from

$\nabla \mathbf{b}_t = \mathbf{B}_t - \mathbf{b}_t$, add it to the existing series, and repeat the computation. To achieve an optimal value of E_n , a corrector potential field \mathbf{B}_2 is further derived from the difference transverse field, i.e., $\mathbf{B}_t - \mathbf{b}_t$, and added to the previous \mathbf{B}_2 in anticipation of an improved match between the transverse fields, as measured by the E_n . In the Eq. 3.14, the grid points are weighted with respect to the

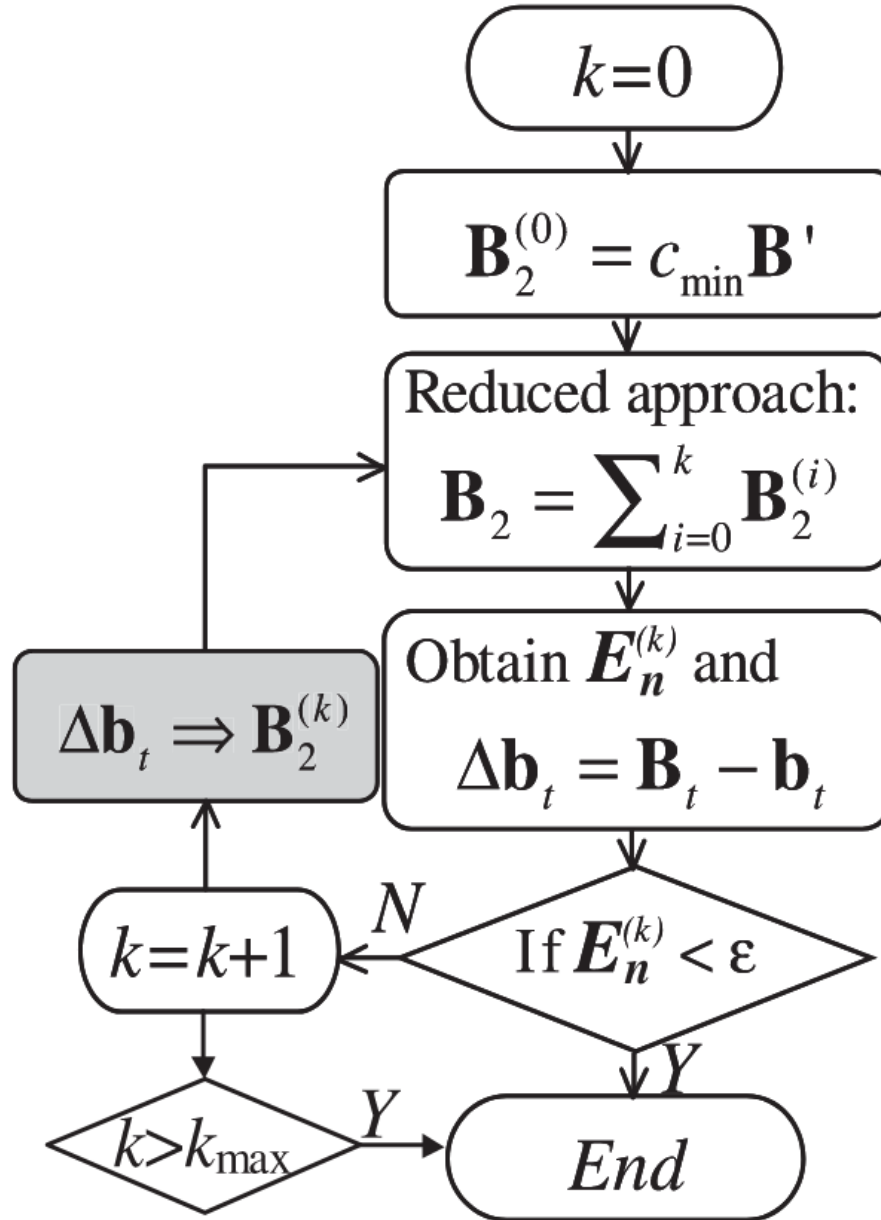


Figure 3.3: The flow chart of coronal magnetic field extrapolation algorithm to obtain extrapolated coronal magnetic field, using single-layer vector magnetogram. The figure has been taken from [Hu et al. \(2010\)](#).

strength of the observed transverse field to minimize the contribution from the

weaker fields (see [Hu & Dasgupta \(2008\)](#); [Hu et al. \(2010\)](#), for further details).

3.3 Detection of 3D magnetic null

3.3.1 A trilinear method to detect the 3D null points

3D null points are important locations in the magnetic field, as discussed in Chapter 3. A trilinear method is utilized to locate the 3D nulls in the data cube generated from the numerical simulations ([Haynes & Parnell, 2007](#)). These numerical experiments provide the data in a cube grid, which can divide the computational domains into a grid of cells. The knowledge of the field between the grid points is required to trace the field lines within the cells. The field is interpolated using the trilinear interpolation method to estimate the field between grid points. The linear, bilinear, and trilinear interpolation methods are discussed below.

Linear interpolation

The simplest form of interpolation between $\mathbf{B}(0)$ and $\mathbf{B}(1)$ in one-dimension (1D) is linear interpolation, which generates an equation of the form

$$\mathbf{B}(x) = \mathbf{B}(0) + [\mathbf{B}(1) - \mathbf{B}(0)]x \quad (3.15)$$

By rearranging the above equation, one gets

$$\mathbf{B}(x) = [1 - x]\mathbf{B}_0 + x\mathbf{B}_1, \quad (3.16)$$

where $\mathbf{B}_0 = \mathbf{B}(0)$ and $\mathbf{B}_1 = \mathbf{B}(1)$.

Bilinear interpolation

Similar to 1D interpolation, two-dimensional (2D) interpolation can be obtained by interpolating linearly along the horizontal sides of a square of unit length and then by linear interpolation between the two resulting points. Points along the

bottom of the square are given by $\mathbf{B}_0(x) = (1 - x)\mathbf{B}_{00} + x\mathbf{B}_{10}$ and along the top by $\mathbf{B}_1(x) = (1 - x)\mathbf{B}_{01} + x\mathbf{B}_{11}$, where $\mathbf{B}_{00} = \mathbf{B}(0, 0)$, $\mathbf{B}_{01} = \mathbf{B}(0, 1)$, and $\mathbf{B}_{11} = \mathbf{B}(1, 1)$ etc. Then the field at a point x, y is given by interpolating along the vertical line of constant x between points $\mathbf{B}_0(x)$ and $\mathbf{B}_1(x)$. Hence,

$$\mathbf{B}(x, y) = (1 - y)\mathbf{B}_0(x) + y\mathbf{B}_1(x) \quad (3.17)$$

$$= (1 - x)(1 - y)\mathbf{B}_{00} + x(1 - y)\mathbf{B}_{10} + (1 - x)y\mathbf{B}_{01} + xy\mathbf{B}_{11} \quad (3.18)$$

$$\mathbf{B}(x, y) = a + bx + cy + dxy \quad (3.19)$$

where $a = \mathbf{B}_{00}$, $b = \mathbf{B}_{10} - \mathbf{B}_{00}$, $c = \mathbf{B}_{01} - \mathbf{B}_{00}$, and $d = \mathbf{B}_{11} - \mathbf{B}_{10} - \mathbf{B}_{01} + \mathbf{B}_{00}$. A similar result can be obtained by doing the first vertical interpolation followed by the horizontal interpolation.

Trilinear interpolation

By expanding 2D interpolation to three-dimensional (3D), the trilinear interpolation for the field at a point (x, y, z) inside a cube of unit length can be obtained.

$$\mathbf{B}(x, y, z) = a + bx + cy + dxy + ez + fxz + gyz + hxyz. \quad (3.20)$$

where $a = \mathbf{B}_{000}$,

$b = \mathbf{B}_{100} - \mathbf{B}_{000}$,

$c = \mathbf{B}_{010} - \mathbf{B}_{000}$,

$d = \mathbf{B}_{110} - \mathbf{B}_{100} - \mathbf{B}_{010} + \mathbf{B}_{000}$,

$e = \mathbf{B}_{001} - \mathbf{B}_{000}$,

$f = \mathbf{B}_{101} - \mathbf{B}_{100} - \mathbf{B}_{001} + \mathbf{B}_{000}$,

$g = \mathbf{B}_{011} - \mathbf{B}_{010} - \mathbf{B}_{001} + \mathbf{B}_{000}$,

$h = \mathbf{B}_{111} - \mathbf{B}_{110} - \mathbf{B}_{101} - \mathbf{B}_{011} + \mathbf{B}_{100} + \mathbf{B}_{010} + \mathbf{B}_{001} - \mathbf{B}_{000}$,

and $\mathbf{B}_{000} = \mathbf{B}(0, 0, 0)$, $\mathbf{B}_{111} = \mathbf{B}(1, 1, 1)$ etc. The values of these constants are unique for each cube. These equations form a trilinear interpolation and give equal values on the shared surface of adjacent cubes (Haynes & Parnell, 2007).

Location of null point on the surface

If a 3D null is at a surface, it can be located as follows. From bilinear interpolation discussed in Sect.3.3.1.

$$\mathbf{B}_i(x, y, z) = a_i + b_i x + c_i y + d_i x y, \quad (3.21)$$

where $i \in (1, 2)$. At the null point, $\mathbf{B}_1(x, y, z) = \mathbf{B}_2(x, y, z) = 0$ should be satisfied. Therefore, for a given value of x , the resulting 2D coordinate is found using

$$y = \frac{-(a_i + b_i x)}{(c_i + d_i x)} \quad (3.22)$$

or for a given value of y

$$x = \frac{-(a_i + b_i y)}{(c_i + d_i y)} \quad (3.23)$$

3.3.2 Algorithm for finding null point

The trilinear null finding method can be divided into three distinct parts, namely, (i) reduction; in this part, every cell gets quickly scanned, and the cells that do not contain a null point are removed. (ii) This part confirms if a null point does or does not lie inside a flagged grid cell. (iii) The last (third) part then finds the position of the null point within the grid cell. The following briefly discusses these three parts of the trilinear null-finding method.

Reduction

This stage of the algorithm scans every grid cell and examines whether a null point can exist inside the grid cell by assuming that the field is linear or trilinear within each cell. This implicit assumption implies that there is sufficient resolution in the data. Consequently, it constrains the minimum and maximum values of B_x , B_y , and B_z at the corners of the cell. Therefore, if B_x is non-zero and has the same sign at each corner of the cell, it can not be zero. Similarly for B_y , and B_z . The sign of the B_x , B_y , and B_z should be opposite at each corner of the cell for the existence of the null. Failing of this condition, i.e., if any of

the three magnetic field components have the same sign at all eight corners of any cell. That cell is removed from the further analysis since it can not contain a null point.

Analysis

The analysis part of the method is based upon the fact that if a null point exists, it must lie on all three of the following curves: $B_x=B_y=0$, $B_x=B_z=0$, and $B_y=B_z=0$. These curves must be one of two types: (i) a loop inside a cell. In this scenario, there will be two nulls within the cell, which implies considerable subgrid structure and clearly shows insufficient grid resolution. (ii) a curve that extends through the boundary of the cell at each end. This case is the most important as the trilinear algorithm is designed to detect these types of null points. The lines $B_x=0$, $B_y=0$, and $B_z=0$ on the cell's surface are found, and the remaining magnetic field components change their sign respectively along the surface. Then, the null point exists on the surface and can be located using the method described in Sect. 3.3.1. For the corners, $B_x=B_y=0$, $B_x=B_z=0$, and $B_y=B_z=0$, and if B_z , B_y , and B_x change their sign along these corners, then the null point will exist and can be located using Eq. (3.16). Finally, if all three components, B_x , B_y , and B_z , change their sign inside the cell, then the null point exists inside the cell and can be located by the method described in Sect. 3.3.2.

Location of the null point

Once the existence of a null point has been confirmed within a given cell, then null gets located to subgrid resolution. There are many possible methods for locating the nulls at the subgrid scale. However, the following 3D Newton-Raphson method, which is fast and generally successful, is employed. A 3D version of the iterative Newton-Raphson method for finding roots of equations is given by

$$\vec{\mathbf{x}}_{i+1} = \vec{\mathbf{x}}_i - [\nabla \mathbf{B}|_{\vec{\mathbf{x}}_i}]^{-1} \vec{\mathbf{B}}_i(\vec{\mathbf{x}}_i), \quad (3.24)$$

where $[\nabla\mathbf{B}]_{ij} = \frac{\partial B_i}{\partial x_j}$ and $\vec{\mathbf{x}}_i$ is location of initial guess for the null. This calculation is repeated until $|\vec{\mathbf{x}}_{i+1} - \vec{\mathbf{x}}_i|$ or $\vec{\mathbf{B}}_i(\vec{\mathbf{x}}_i)$ is less than a given tolerance. The trilinear method chooses the initial guess \vec{x}_0 to be at either the center of the cell or a cell corner to locate the null. The distinct initial points are tried in this method until the iterative method succeeds at some point within the cell. If this method fails, the grid cell is split into eight subgrid cells using trilinear interpolation, and the trilinear method is used again on these eight new cells to locate the null. In general, the trilinear method is accurate for most nonlinear fields, and null points may be falsely created or destroyed, either in pairs or lost through the boundaries of the domain where the field within a cell is highly nonlinear. If we constrain the field to be trilinear within cells, the trilinear method is accurate with the exception when two null points exist within one cell, making it highly suitable for numerical magnetic fields (Haynes & Parnell, 2007).

Calculation of topological degree and nature of 3D nulls

The trilinear null detection technique has been employed to detect the 3D nulls studied in the Thesis, which is developed by (Chiti, 2020) based on the theory mentioned in Sect. 3.3. It gives the location (x, y, z) of the 3D nulls and the value of $|\mathbf{B}|$ at that position. The script is written in Python programming language and can be found at <https://zenodo.org/record/4308622#.YByPRS2w0wc>. However, the modified version of the code provides the topological degree (see Sect. 2.4.3) of each detected 3D null (Maurya et al., 2024). It also provides the eigenvalues as well as eigenvectors calculated at the detected nulls, which ultimately gives information about the nature (spiral or radial) (for theory, refer to Sect. 2.4.2) of nulls (Maurya et al., 2024).

3.4 Numerical Model

A successful numerical simulation of active region dynamics requires stringent satisfaction with the condition of flux-freezing away from the reconnection sites, while at the sites, the requirement is to break the flux-freezing and allow for

diffusion of magnetic field lines. In other words, the necessity is an intermittent diffusivity that appears only when and where the magnetic reconnections occur. For our computations, we utilize the well-established numerical model EULAG-MHD (Smolarkiewicz & Charbonneau, 2013), which is an extension of the hydrodynamic model EULAG predominantly used in atmospheric and climate research (Prusa et al., 2008). The EULAG-MHD is based on the spatio-temporally (at least) second-order accurate non-oscillatory forward-in-time (NFT) advection scheme multidimensional positive definite advection transport algorithm, MPDATA, (Smolarkiewicz & Margolin, 1998; Smolarkiewicz, 2006). The accuracy of MPDATA ensures the satisfaction of the flux-freezing with a high fidelity away from the reconnection region. Additionally, a feature unique to MPDATA and important in our calculations is its proven effectiveness in generating an intermittent and adaptive residual dissipation whenever the concerned advective field is under-resolved (Margolin et al., 2006). The magnetic nulls and QSLs, in the absence of magnetic diffusion, provide an unbound sharpening of the corresponding field gradient and inevitably generate under-resolved scales. The MPDATA then produces the residual dissipation to regularize these scales through the onset of simulated magnetic reconnections. In the following, we present salient features of the EULAG-MHD that are relevant to our simulations.

3.4.1 Advection solver MPDATA

MPDATA is a finite-difference algorithm invented by P. K. Smolarkiewicz in the early 1980s (Smolarkiewicz, 1983, 1984; Smolarkiewicz & Clark, 1986). The algorithm is at least second-order accurate, positive definite, conservative, and computationally efficient. The second-order accuracy in MPDATA is achieved by utilizing the first-order accurate donor cell (also known as upstream or upwind) scheme in an iterative manner. The first iteration is a simple donor cell differencing. With a donor cell solution obtained from the first iteration, MPDATA increases the accuracy of the calculation by estimating and compensating for (second-order) truncation error in the second iteration. Similarly, additional iterations can be performed to approximately compensate the residual error pro-

duced from the previous iteration, which further enhances the accuracy. Since its invention, MPDATA has been extended to curvilinear coordinates, full monotonicity preservation, third-order accuracy, and variable sign fields; details can be found in (Smolarkiewicz & Margolin, 1998; Smolarkiewicz, 2006). Here, we discuss basic concepts underlying the design of the MPDATA scheme in Cartesian coordinates.

Derivation of MPDATA

To fix ideas, we consider a simple one-dimensional advection equation,

$$\frac{\partial \phi}{\partial t} + \frac{\partial(k\phi)}{\partial x} = 0 \quad (3.25)$$

for a scalar variable ϕ . The velocity k may also be a function of space and time.

The donor cell discretization of the advection equation is given by,

$$\phi_i^{n+1} = \phi_i^n - \frac{\delta t}{\delta x} (k_{i+\frac{1}{2}} \phi_r^n - k_{i-\frac{1}{2}} \phi_l^n) \quad (3.26)$$

where ϕ_r^n and ϕ_l^n are chosen depending on the sign of $k_{i+\frac{1}{2}}$ and $k_{i-\frac{1}{2}}$:

$$\phi_{\mathbf{r}}^{\mathbf{n}} = \begin{cases} \phi_i^n, & k_{i+\frac{1}{2}} > 0, \\ \phi_{i+1}^n, & k_{i+\frac{1}{2}} < 0, \end{cases} \quad (3.27)$$

and

$$\phi_{\mathbf{r}}^{\mathbf{n}} = \begin{cases} \phi_{i-1}^n, & k_{i-\frac{1}{2}} > 0, \\ \phi_i^n, & k_{i-\frac{1}{2}} < 0, \end{cases} \quad (3.28)$$

with the integer and half-integer indices corresponding to cell centers and cell walls. In Eq. (3.26), ϕ_i^{n+1} on the LHS is the solution sought at the grid point (t^{n+1}, x_i) with $\delta t = t_{n+1} - t_n$ and $\delta x = x_{i+1} - x_i$ representing temporal and spatial increments respectively. The above case distinctions can be avoided by writing

the Eq. (3.26) in the following form,

$$\phi_i^{n+1} = \phi_i^n - \frac{\partial t}{2\partial x} (k_{i+\frac{1}{2}}(\phi_i^n + \phi_{i+1}^n) - k_{i-\frac{1}{2}}(\phi_{i-1}^n + \phi_i^n) + |k_{i+\frac{1}{2}}|(\phi_i^n - \phi_{i+1}^n) - |k_{i-\frac{1}{2}}|(\phi_{i-1}^n - \phi_i^n)) \quad (3.29)$$

Notably, if the sign of k determines the flow direction, this scheme always chooses the values of ϕ (for a given time), which lies in the upstream direction (Griebel et al., 1997). The donor cell approximation in flux form is expressed as,

$$\phi_i^{n+1} = \phi_i^n [F(\phi_i^n, \phi_{i+1}^n, U_{i+\frac{1}{2}}) - F(\phi_{i-1}^n, \phi_i^n, U_{i-\frac{1}{2}})], \quad (3.30)$$

where the flux function F is

$$F(\phi_L, \phi_R, U) = [U]^+ \phi_L + [U]^- \phi_R, \quad (3.31)$$

$U \equiv \frac{a\delta t}{\delta x}$ represents the dimensionless local Courant number while, $[U]^+ \equiv 0.5(U + |U|)$ and $[U]^- \equiv 0.5(U - |U|)$ denoting the nonnegative and nonpositive parts of the Courant number (Smolarkiewicz & Margolin, 1998; Smolarkiewicz, 2006).

The donor cell scheme is conditionally stable, and the corresponding stability condition, for every time step, has a form

$$\max \left(\frac{|k_{i+\frac{1}{2}}| \delta t}{\delta x} \right) \leq 0 \forall i. \quad (3.32)$$

Moreover, under the condition Eq. (3.32), the scheme is also positive definite, implying if $\phi_i^0 \geq 0, \forall i$ and n . These two properties, as well as low computational cost and low phase error, make the scheme (Eq. (3.30)) attractive for the numerical evaluation of the advection equation. However, the scheme being first-order accurate (both in space and time) produces large implicit numerical diffusion.

To quantify the diffusion in Eq. (3.30), we assume k to be constant and ϕ to be nonnegative for simplicity. A straightforward truncation analysis, expanding all dependent variables in a second-order Taylor series about the time level n and spatial point i , reveals that the scheme more accurately approximates the

advection-diffusion equation

$$\frac{\partial \phi}{\partial t} = \frac{\partial(k\phi)}{\partial x} + \frac{\partial}{\partial x} \left(K \frac{\partial \phi}{\partial x} \right) \quad (3.33)$$

where the diffusion coefficient

$$K = \frac{\delta x^2}{2\delta t} (|U| - U^2) \quad (3.34)$$

In other words, the scheme estimates the solution of the advection equation with a second-order truncation error. To enhance the accuracy, it is necessary to construct a numerical estimate of the error and subtract it from Eq. (3.30). The basic strategy, fundamental to all MPDATA schemes, is then to once again utilize a donor cell approximation to calculate the error term in order to preserve the properties of the donor cell scheme. To do so, the error term, the RHS term of Eq. (3.33), is rewritten as

$$e^1 \equiv \frac{\partial}{\partial x} \left(K \frac{\partial \phi}{\partial x} \right) \equiv \frac{\partial(k^1 \phi)}{\partial x} \quad (3.35)$$

where e^1 symbolizes error term and $k^1 \equiv \frac{K}{\phi} \frac{\partial \phi}{\partial x}$ is termed as pseudo velocity. The superscript (1) is used to mark the first iteration for subtracting the error. To compensate the error, we again use the donor cell scheme, but this time with the pseudo velocity k^1 and the ϕ^{n+1} already available from Eq. (3.30) in lieu of the physical velocity k and the ϕ^n . A first-order accurate estimate of the pseudo velocity is

$$k_{i+\frac{1}{2}}^1 \equiv \frac{2K}{\delta x} \frac{\phi_{i+1}^{(1)} - \phi_i^{(1)}}{\phi_{i+1}^{(1)} + \phi_i^{(1)}} \quad (3.36)$$

where $\phi^{(1)}$ represents the first-order accurate ϕ^{n+1} estimated from Eq. (3.30). The modified Courant number is $V_{i+\frac{1}{2}}^1 \equiv \frac{k_{i+\frac{1}{2}}^1 \delta t}{\delta x}$. In the second iteration, we subtract a donor cell estimate of the error to improve the accuracy. The equation of the second iteration is

$$\phi_i^2 = \phi_i^1 - \left[F \left(\phi_i^1, \phi_{i+1}^1, V_{i+\frac{1}{2}}^1 \right) - F \left(\phi_{i-1}^1, \phi_i^1, V_{i-\frac{1}{2}}^1 \right) \right] \quad (3.37)$$

which estimates ϕ^{n+1} which is the second-order accurate while preserving the sign of ϕ . It is an easy matter to show that, like the donor cell scheme, MPDATA is consistent and conditionally stable (Smolarkiewicz, 1983; Smolarkiewicz & Margolin, 1998; Smolarkiewicz, 2006). However, in contrast to the donor scheme, MPDATA does not contain strong numerical implicit diffusion because of the improved accuracy. The extension of MPDATA to multiple dimensions is straightforward. To demonstrate, we consider a simple two-dimensional advection equation,

$$\frac{\partial \phi}{\partial t} + \frac{\partial(k\phi)}{\partial x} + \frac{\partial(l\phi)}{\partial y} = 0, \quad (3.38)$$

where k and l are velocities in the x and y directions. The corresponding donor cell approximation is then

$$\begin{aligned} \phi_{i,j}^{n+1} = \phi_{i,j}^n &- \left[F\left(\phi_{i,j}^n, \phi_{i+1,j}^n, U_{i+\frac{1}{2},j}\right) - F\left(\phi_{i-1,j}^n, \phi_{i,j}^n, U_{i-\frac{1}{2},j}\right) \right] \\ &- \left[F\left(\phi_{i,j}^n, \phi_{i,j+1}^n, U_{i,j+\frac{1}{2}}\right) - F\left(\phi_{i,j-1}^n, \phi_{i,j}^n, U_{i,j-\frac{1}{2}}\right) \right] \end{aligned} \quad (3.39)$$

where the flux function is similar to Eq. (3.31) and, $U \equiv \frac{k\delta t}{\delta x}$ and $V \equiv \frac{l\delta t}{\delta y}$ are Courant numbers. Further, the Taylor's series expansion of Eq. (3.39) about the cell point (i, j) and the time level n with constant velocities yields the following advection-diffusion equation,

$$\frac{\partial \phi}{\partial t} + \frac{\partial(k\phi)}{\partial x} + \frac{\partial(l\phi)}{\partial y} = K \frac{\partial^2 \phi}{\partial x^2} + L \frac{\partial^2 \phi}{\partial y^2} - \frac{UV\delta x\delta y}{\delta t} \frac{\delta^2 \phi}{\delta x\delta y}, \quad (3.40)$$

with $K \equiv \frac{\delta x^2}{2\delta t}(|U| - U^2)$ and $L \equiv \frac{\delta y^2}{2\delta t}(|V| - V^2)$. To estimate the truncation error using the donor cell scheme, we rewrite the error terms, the RHS terms of Eq. (3.40), in the following form

$$K \frac{\partial^2 \phi}{\partial x^2} + L \frac{\partial^2 \phi}{\partial y^2} - \frac{UV\delta x\delta y}{\delta t} \frac{\delta^2 \phi}{\delta x\delta y} = \frac{\partial(k^1\phi)}{\partial x} + \frac{\partial(l^1\phi)}{\partial y} \quad (3.41)$$

where

$$k^1 \equiv \frac{K}{\phi} \frac{\partial \phi}{\partial x} - \frac{UV\delta x\delta y}{2\delta t} \frac{1}{\phi} \frac{\delta \phi}{\delta y} \quad (3.42)$$

and

$$l^1 \equiv \frac{L}{\phi} \frac{\partial \phi}{\partial y} - \frac{UV \delta x \delta y}{2 \delta t} \frac{1}{\phi} \frac{\delta \phi}{\delta x} \quad (3.43)$$

are pseudo velocities in the x and y directions. Utilizing these velocities and updated value of ϕ^{n+1} from Eq. (3.30), the donor cell scheme is used to estimate the error. In the second iteration, the error is subtracted to enhance the accuracy.

Extension to generalized transport equation

The general transport equation is

$$\frac{\partial \varphi}{\partial t} + \nabla \cdot (\mathbf{K} \varphi) = R, \quad (3.44)$$

where R combines all forcing and source terms. In general, both R and velocity \mathbf{k} depend on variable φ . The forward-in-time discretization of Eq. (3.44) is assumed as,

$$\frac{\varphi^{n+1} - \varphi^n}{\delta t} + \nabla \cdot (\mathbf{k}^{n+\frac{1}{2}} \varphi^n) = R^{n+\frac{1}{2}}. \quad (3.45)$$

Expansion of 3.45 into the second-order Taylor series about the time level n shows that the scheme 3.45 approximates to the equation

$$\frac{\partial \varphi}{\partial t} + \nabla \cdot (\mathbf{k} \varphi) = R - \nabla \cdot [0.5 \delta t \mathbf{k} (\mathbf{k} \cdot \nabla \varphi) + 0.5 \delta t \mathbf{k} \varphi (\nabla \cdot \mathbf{k})] + \nabla \cdot (0.5 \delta t \mathbf{k} R) + \mathcal{O}(\delta t^2). \quad (3.46)$$

In RHS of Eq. (3.46), all $\mathcal{O}(\delta t)$ truncation errors originated by uncentered time differencing in Eq. (3.45) are already expressed by spatial derivatives. Specification of the time levels of both the advective velocity and the forcing term as $n + \frac{1}{2}$ in Eq. (3.45) eliminates $\mathcal{O}(\delta t)$ truncation errors which are proportional to their temporal derivatives (Smolarkiewicz & Clark, 1986). From Eq. (3.46), it is clear that the formulation of second-order accurate forward-in-time scheme for Eq. (3.44) requires the compensation of $\mathcal{O}(\delta t)$ truncation errors to at least the second-order accuracy. For such a formulation, we note $\mathcal{O}(\delta t)$ error terms in Eq. (3.46) have two distinct components. The first component is merely due to advection and does not involve the forcing R . In contrast, the second component

depends on the forcing R . Toward compensating the first component, notable is the reduction of Eq. (3.44) to a homogeneous transport equation for $R = 0$. Then, MPDATA scheme retains the form of the basic scheme (subsection 3.4.3) where the first donor cell iteration utilizes the advective velocity k^{n+2} and φ^n , and subsequent iterations use pseudo velocities and φ calculated from the preceding iteration; for details cf. (Smolarkiewicz, 1991; Smolarkiewicz & Margolin, 1993, 1998; Smolarkiewicz, 2006). Compensation of the second component requires subtraction of a first-order accurate approximation of the error from the RHS of Eq. (3.45). A simple, efficient, and second-order accurate MPDATA for Eq. (3.44) can then be symbolically written as,

$$\varphi_i^{n+1} = A_i \left(\varphi^n + 0.5\delta t R^n, \mathbf{K}^{n+\frac{1}{2}} \right) + 0.5\delta t R_i^{n+1}, \quad (3.47)$$

where A denotes the basic MPDATA advection scheme (Smolarkiewicz, 1991; Smolarkiewicz & Margolin, 1993). In this equation, we assume $R^{n+2} = 0.5(R^n + R^{n+1})$ with R^{n+1} representing $\mathcal{O}(\delta t^2)$ accurate approximation of R at time level $(n + 1)$. Noticeably, the first donor cell iteration in the MPDATA scheme uses the auxiliary variable $\varphi^n + 0.5\delta t R^n$ in lieu of the physical variable φ^n with a physical advective velocity $k^{n+\frac{1}{2}}$. The advection of the auxiliary field is important for preserving the global accuracy and stability of the forward-in-time approximations (Smolarkiewicz, 1991; Smolarkiewicz & Margolin, 1993; Smolarkiewicz & Margolin, 1997).

The advective velocity at intermediate $n + \frac{1}{2}$ time level may be approximated by linear interpolation or extrapolation

$$\mathbf{k}^{n+\frac{1}{2}} = \frac{1}{2} (\mathbf{k}^{n+1} + \mathbf{k}^n), \quad (3.48)$$

$$\mathbf{k}^{n+\frac{1}{2}} = \frac{1}{2} (3\mathbf{k}^n - \mathbf{k}^{n-1}), \quad (3.49)$$

either of which is sufficient to maintain second-order accuracy in Eq. (3.47). For the subtleties involved in a particular choice of $\mathbf{k}^{n+\frac{1}{2}}$, readers are referred to (Smolarkiewicz & Clark, 1986).

Nonoscillatory MPDATA

The basic MPDATA scheme discussed above preserves sign¹ but not monotonicity of the advected variables (Smolarkiewicz, 1983, 1984; Smolarkiewicz & Clark, 1986) and, in general, the solutions are not free of spurious oscillations particularly in presence of steep gradients (Smolarkiewicz & Grabowski, 1990; Smolarkiewicz, 1991). However, MPDATA is made fully monotone (Smolarkiewicz, 1991) by adapting the flux-corrected-transport (FCT) methodology (Boris & Book, 1973; Book et al., 1975; Boris & Book, 1976). Actually, MPDATA is well suited for this kind of approach for a number of reasons. First, the initial MPDATA iteration is the donor cell scheme—a low-order monotone scheme which is commonly used as the reference in the FCT design. Second, assuring the monotonicity of subsequent iterations provides a higher-order accurate reference solution for the next iteration with the effect of improving the overall accuracy of the resulting FCT scheme. Third, since all MPDATA iterations have similar low phase errors characteristic of the donor cell scheme (Smolarkiewicz & Clark, 1986), the FCT procedure mixes solutions with consistent phase errors. This significantly improves the overall accuracy of the resulting FCT scheme (Smolarkiewicz & Grabowski, 1990).

3.4.2 EULAG-MHD

The numerical model EULAG is an established model for simulating fluid flows across a wide range of scales and physical scenarios (Prusa et al., 2008). The name EULAG alludes to the capability to solve fluid equations in either an Eulerian (Smolarkiewicz & Margolin, 1993) or a Lagrangian (Smolarkiewicz & Pudykiewicz, 1992) mode. The numerics of EULAG are unique, owing to a combination of MPDATA advection schemes, robust elliptic solver, and generalized coordinate formulation enabling grid adaptivity. The EULAG-MHD is a spin-off of the numerical model EULAG (Charbonneau & Smolarkiewicz, 2013). Here, we describe the numerical apparatus of EULAG-MHD utilized for our calculations.

¹For historical reasons, we refer to this property as positive-definiteness in the previous subsections.

Governing equations of EULAG-MHD

MHD equations for an incompressible magnetofluid with infinite electrical conductivity are cast in the following form

$$\frac{d\mathbf{v}}{dt} = -\nabla\pi + \frac{1}{4\pi\rho_0}\mathbf{B} \cdot \nabla\mathbf{B} + F_\nu, \quad (3.50)$$

$$\frac{d\mathbf{B}}{dt} = \mathbf{B} \cdot \nabla\mathbf{v} - \mathbf{B}\nabla \cdot \mathbf{v}, \quad (3.51)$$

$$\nabla \cdot \mathbf{v} = 0, \quad (3.52)$$

$$\nabla \cdot \mathbf{B} = 0, \quad (3.53)$$

in non-rotating Cartesian coordinates. The Lagrangian derivative is related to the Eulerian derivative in the usual manner

$$\frac{d}{dt} \equiv \frac{\partial}{\partial t} + (\mathbf{v} \cdot \nabla). \quad (3.54)$$

Importantly, by incompressibility we mean $\frac{d\rho}{dt} = 0$ and $\rho = \text{constant}$. Although incompressibility approximation is a restrictive approximation for the coronal plasma, it was also used in earlier works (Dahlburg et al., 1991; Aulanier et al., 2005). Moreover, the compressibility of the fluid is important for the thermodynamics of the coronal loops (Ruderman & Roberts, 2002), whereas the magnetic topology is not affected by viscosity. On the RHS of the momentum transport equation (3.50), π is a density normalized pressure in which thermodynamic pressure is subsumed to magnetic pressure. F_ν symbolizes the viscous drag force. All other symbols have their usual meaning. On a general note, EULAG's governing equations are formulated and solved in transformed time-dependent generalized curvilinear coordinates

$$(\bar{t}, \bar{x}) \equiv (t, F(t, x)), \quad (3.55)$$

The physical domain (t, x) , where the physical problem is posed, is assumed to be any stationary orthogonal coordinate system (i.e., Cartesian, spherical, and cylindrical). Moreover, the transformed horizontal coordinates (\bar{x}, \bar{y}) are as-

sumed to be independent of the vertical coordinate z (Prusa & Smolarkiewicz, 2003)(Prusa & Smolarkiewicz, 2003). The calculations carried out in this Thesis implement the physical domain to be Cartesian and, therefore, both the computational domain and the physical domain are identical, i.e., $(\bar{t}, \bar{x}) \equiv (t, x)$. Here, we present the details of the EULAG-MHD for the Cartesian domain. The generalized coordinate formulation of EULAG-MHD utilizes the rigorous tensorial exposition of MHD equations; cf. (Smolarkiewicz & Charbonneau, 2013).

Numerics

Utilizing equations (3.52) and (3.51), the momentum transport equation (3.50) and the induction equation (3.51) can be rewritten as,

$$\frac{\partial \Psi}{\partial t} + \nabla \cdot (\mathbf{v} \Psi) = \mathbf{R} \quad (3.56)$$

where

$$\Psi = \{\mathbf{v}, \mathbf{B}\}^T \quad (3.57)$$

represents the vector of dependent variables and

$$\mathbf{R} = \{\mathbf{R}_v, \mathbf{R}_B\}^T \quad (3.58)$$

denotes the RHS forcing terms in Eqs. (3.50) and (3.51). Notably, in Eq. (3.56), the Lorentz force term of the momentum transport equation and the convective term of the induction equation is cast in the conservative forms via relations,

$$\mathbf{B} \cdot \nabla \mathbf{B} = \nabla \cdot \mathbf{B} \mathbf{B}, \mathbf{B} \cdot \nabla \mathbf{v} = \nabla \cdot \mathbf{B} \mathbf{v}. \quad (3.59)$$

In addition, an ad hoc term $-\nabla \pi^*$ is added to the RHS of the induction equation, in the spirit of the pressure π in the momentum transport equation, to ensure $\nabla \cdot \mathbf{B} = 0$ in numerical integrations. The equation (3.56) is integrated using the non-oscillatory forward-in-time algorithm MPDATA. Following section (3.4.1), an EULAG template algorithm for integration of the (3.56) can be compactly

written as,

$$\Psi_i^{n+1} = \mathcal{A}_i \left(\Psi^n + 0.5\delta t \mathbf{R}^n, \mathbf{v}^{n+\frac{1}{2}} \right) + 0.5\delta t \mathbf{R}_i^{n+1} \equiv \hat{\Psi}_i + 0.5\delta t \mathbf{R}_i^{n+1}, \quad (3.60)$$

where Ψ_i^{n+1} is the solution sought at the grid point (t^{n+1}, x_i) . For an inviscid dynamics ($F_\nu = 0$), the model template algorithm (3.60) is implicit for all dependent variables in Eqs. (3.50) and (3.51) because all forcing terms are assumed to be unknown at time level $n + 1$. To retain the proven structure of Eq. (3.60) for the MHD system, the EULAG-MHD template can be viewed as

$$\Psi_i^{n+1,q} = \hat{\Psi}_i + \frac{\delta t}{2} \mathbf{L} \Psi_i^{n+1,q} + \frac{\delta t}{2} \mathbf{N}(\Psi)|_i^{n+1,q-1} - \frac{\delta t}{2} \nabla \Theta|_i^{n+1,q}, \quad (3.61)$$

where the RHS forcing \mathbf{R} is decomposed into linear term $\mathbf{L}\Psi$ with \mathbf{L} denoting a linear operator, non linear-term $\mathbf{N}(\Psi)$, and potential term $-\nabla\Theta$ with $\Theta = (\pi, \pi, \pi, \pi^*, \pi^*, \pi^*)$. In Eq. (3.61), $q = 1, \dots, m$ numbers fixed point iterations. The algorithm Eq. (3.61) is still implicit with respect to the forcing terms $\mathbf{L}\Psi$ and $-\nabla\Theta$. Using straightforward algebraic manipulations, the representation Eq. (3.61) can be cast into a closed form

$$\Psi_i^{n+1,q} = [\mathbf{I} - 0.5\delta t \mathbf{L}]^{-1} \left(\hat{\Psi} - 0.5\delta t \nabla \Theta^{n+1,q} \right)_i, \quad (3.62)$$

where the explicit element is modified to

$$\hat{\Psi} = \hat{\Psi} + 0.5\delta t \mathbf{N}(\Psi)|^{n+1,q-1}. \quad (3.63)$$

The viscous forcing within this algorithm framework is incorporated by integrating explicitly to the first-order accuracy in time and then adding to the auxiliary argument of MPDATA operator A. Now the argument modifies as $\tilde{\Psi} = \Psi^n + 0.5\delta t(\mathbf{R}^n + 2\tilde{\mathbf{R}})$ where $\tilde{\mathbf{R}}$ symbolizing the first-order time accurate viscous forcing. All the dependent variables being spatially co-located in Eq. (3.62), the time updated Ψ is obtained by solving two discrete elliptic equations for π and π^* generated by the solenoidality constraints Eqs. (3.52) and (3.53)

discretized consistently with the divergence operator implied by \mathbf{A} ; see (Prusa et al., 2008). Under appropriate boundary conditions, these elliptic equations are solved iteratively using a preconditioned generalized conjugate residual (GCR) algorithm (Eisenstat, 1983; Eisenstat et al., 1983; Smolarkiewicz & Margolin, 1997). Because the GCR is an iterative scheme, to distinguish the iterations appearing in Eq. (3.61) and in the GCR solver, the iteration in Eq. (3.61) is referred as “outer”, while the iteration corresponds to GCR is termed as “inner.” The convergence of the outer iteration is generally controlled by the time step of the model and monitored by the convergence of the inner iteration in the GCR solvers (Smolarkiewicz & Szmelter, 2009, 2011). With the completion of the outer iteration loop, the solution updates, and the total implicit forcing $\mathbf{RI} = \mathbf{L}\Psi - \nabla\Theta$ in Eq. (3.61) is returned as $\mathbf{RI}_i^n = \frac{2}{\delta t} (\Psi_i^n - \hat{\Psi}_i)$. While the total explicit forcing $\mathbf{RE} = \mathbf{N}(\Psi) + \tilde{\mathbf{R}}$ is calculated according to its definition using the updated solution, so $\mathbf{RE}_i^n = \mathbf{RE}_i(\Psi^n)$. The total forcing $\mathbf{R} = \mathbf{RI} + \mathbf{RE}$ is then stored for use in the subsequent time step in the auxiliary argument of the MPDATA operator in Eq. (3.60).

In the following, we briefly discuss the actual implementation of the iterative formulation of Eq. (3.60). The iterations progress stepwise such that the most current update of a dependent variable is used in the ongoing step, wherever possible. Each outer iteration has two distinct blocks. The first block involves the integration of the momentum transport equation where the magnetic field enters the Lorentz force and is taken as supplementary. Being at the half of a single outer iteration, it is denoted by the index $q - \frac{1}{2}$. This block ends with the final update of the velocity via the solution of the elliptic equation for π . Hence, this block actually mirrors the standard EULAG solution of hydrodynamic equations (Prusa et al., 2008), leading to the nomenclature “hydrodynamic block”. The second block, referred to as the “magnetic block,” uses the current updates of the velocities to integrate the induction equation. It ends with the final update of the magnetic field via the solution of the elliptic equation for π^* to clean the divergence of the magnetic field. In the following, we summarize the sequence of steps fulfilled at each outer iteration for integrating the MHD Eqs. (3.50)-(3.53).

For brevity, the superscripts n are dropped everywhere, as by now, there should be no ambiguity. Moreover, at $q = 1$ the initial guess for \mathbf{v} and \mathbf{B} is assumed as $\mathbf{v}^0 = 2\mathbf{v}^{n+1} - \mathbf{v}^n$, and $\mathbf{B}^0 = 2\mathbf{B}^{n+1} - \mathbf{B}^n$, respectively.

The first step of the hydrodynamic block starts with the estimation of the magnetic field $\mathbf{B}^{q-\frac{1}{2}}$ at time t^{n+1} by inverting the induction equation,

$$\mathbf{B}_i^{q-\frac{1}{2}} = \hat{\mathbf{B}}_i + 0.5\delta t \left[\mathbf{B}^{q-\frac{1}{2}} \cdot \nabla \mathbf{v}^{q-1} - \mathbf{B}^{q-\frac{1}{2}} \text{tr} \nabla \mathbf{v}^{q-1} \right]_i. \quad (3.64)$$

The subsequent step uses this latest magnetic field to obtain velocity following the standard EULAG procedure,

$$\mathbf{v}_i^q = \mathbf{v}^i + \frac{0.5\delta t}{\rho_0\mu_0} (\nabla \cdot (\mathbf{B}\mathbf{B})_i^{q-\frac{1}{2}} - 0.5\delta t (\nabla \pi)_i^q). \quad (3.65)$$

Plugging this velocity in the discrete form of the Eq. (3.52) produces the elliptic equation for the pressure π , the solution of which provides the updated solenoidal velocity \mathbf{v} . The first step of the magnetic block begins with the estimation of the magnetic field $\mathbf{B}^{q-\frac{1}{4}}$ at t^{n+1} using the update velocity, and the latest magnetic field is evaluated implicitly in analogy to Eq. (3.64):

$$\mathbf{B}_i^{q-\frac{1}{4}} = \hat{\mathbf{B}}_i + 0.5\delta t \left[\mathbf{B}^{q-\frac{1}{4}} \cdot \nabla \mathbf{v}^q - \mathbf{B}^{q-\frac{1}{4}} \text{tr} \{ \nabla \mathbf{v}^q \} \right]_i. \quad (3.66)$$

where the superscript $q - \frac{1}{4}$ is symbolized as such for being a quarter of iteration away from the accomplishment. The subsequent step follows in the spirit of the momentum transport equation, using the conservative form of the forcing terms in the induction equation:

$$\mathbf{B}_i^q = \hat{\mathbf{B}}_i + 0.5\delta t \left(\nabla \cdot \mathbf{B}^{q-\frac{1}{4}} \mathbf{v}^q \right)_i - 0.5\delta t (\nabla \pi^*)_i^q. \quad (3.67)$$

Implementing the magnetic field in the discrete form of the solenoidality condition Eq. (3.53) produces the elliptic equation for auxiliary pressure term π^* , the solution of which provides the updated solenoidal magnetic field \mathbf{B} .

EULAG-MHD is parallelized with MPI (Message Passing Interface), which

supports NetCDF for writing output data. For visualization of magnetic field lines, the VAPOR (Visualization and Analysis for Ocean, Atmosphere, and Solar Researchers) developed by the National Center for Atmospheric Research (NCAR) is utilized. VAPOR can easily handle data up to terabytes (Clyne et al., 2010). The magnetic field lines are traced by using VAPOR’s field line advection technique under the influence of flow vector (Clyne et al., 2010). The EULAG-MHD model is presently running on the High-Performance Computing Cluster: Param Vikram-1000, operational at the Physical Research Laboratory, which has 108 computing nodes dispensing 7296 CPU cores, 2,76,480 GPU Cores, 74 TB of RAM, and 1 PB of high-performance Lustre parallel filesystem (the details can be found at <https://www.prl.res.in/prl-eng/paramvikram1000>).

3.4.3 Implicit large eddy simulation

As discussed above, EULAG-MHD is based on the MPDATA advection scheme. Notably, the higher-order truncation terms of MPDATA provide an implicit turbulence model (Domaradzki et al., 2003; Margolin et al., 2006) and hence, allow to perform LESs without utilizing an explicit subgrid model (Smolarkiewicz & Prusa, 2002; Domaradzki et al., 2003; Domaradzki & Radhakrishnan, 2005; Rider, 2006; Prusa et al., 2008). In contrast to the standard LESs, which filter out the under-resolved scales by applying explicit subgrid-scale models, MPDATA filter-outs the under-resolved scales by utilizing the residual dissipation—intermittent and adaptive to the generation of under-resolved scales—produced via numerics which mimics the action of explicit subgrid-scale turbulence models. In literature, such calculations relying on the properties of non-oscillatory numerics are referred to as implicit large eddy simulations (ILESs). A detailed review along with numerous examples of ILES is given in a book edited by Grinstein & Drikakis (2007), which includes its applications to local and global solar/stellar convection. In a simulation with fixed grid resolution, under-resolved scales appear at the reconnection regions. MPDATA produces sufficient local effective residual dissipation, which sustains the monotonic nature of the solution and removes these under-resolved scales. Being intermittent and adaptive, the resid-

ual dissipation, as mentioned above, facilitates the model's ability to perform ILESs. The regular solar cycles have been simulated successfully by Ghizaru et al. (2010); Racine et al. (2011) while utilizing such ILESs with model and subsequently, the rotational torsional oscillations are characterized and analyzed by (Beaudoin et al., 2013). The simulations conducted with EULAG-MHD continue relying on the effectiveness of ILES in regularizing the onset of magnetic reconnections, concurrent and collocated with the reconnection sites (Kumar et al., 2013, 2015a) (Kumar et al., 2013, 2015; Kumar & Bhattacharyya, 2016).

The above delegation of the entire magnetic diffusivity to ILES has its own advantages and limitations. The residual dissipation being localized and intermittent minimizes computational cost in simulating magnetic reconnections and simultaneously maximizes the effective Reynolds number away from the reconnection sites (Waite & Smolarkiewicz, 2008; Smolarkiewicz & Szmelter, 2009). Contrarily, in the absence of physical diffusivity, a direct relation between electric field and current density does not exist—rendering estimation of magnetic Reynolds number difficult. Moreover, the residual dissipation being intermittent in time and space, its quantification is meaningful only in the spectral space where analogous to the eddy viscosity of explicit subgrid-scale models for turbulent flows, it only acts on the shortest modes admissible on the grid (Domaradzki et al., 2003), in particular, in the vicinity of steep gradients in simulated fields.

In summary, the Sect. 3.4 describes the numerical models EULAG-MHD used to explore the generation and annihilation of 3D null points. The numerical models are based on (at least) second-order accurate (both in space and time) non-oscillatory forward in-time advection scheme MPDATA. MPDATA utilizes the donor-cell scheme iteratively to improve the accuracy of the solution while preserving the properties of the donor-cell scheme. We have discussed the derivation of MPDATA and its salient features, which are relevant to our calculations, followed by the review of the numerics of the numerical model EULAG-MHD. The model employs the established framework of EULAG with an additional magnetic block to solve the induction equation. Notably, the proven property of MPDATA to produce locally adaptive residual dissipations in response to the

generation of under-resolved scales facilitates the numerical model to carry out computations in the spirit of implicit large eddy simulations.

Chapter 4

3D magnetic null generation and annihilation with an initial analytical magnetic field

4.1 Introduction

For the aim of this study described in Sect. 1.4, the magnetic field lines of a current-free null are deformed with a prescribed flow. The field lines constituting the fan and spine get deformed accordingly, resulting in the folding of a set of auxiliary field lines, which ultimately reconnects to generate null pairs. This process of null pair generation is distinctive in comparison to an earlier work done by [Wyper & Pontin \(2014\)](#) where fan-spine reconnection was invoked to generate nulls through pitchfork bifurcations within a tearing-unstable three-dimensional current sheet about an existing null. New nulls were also generated through internal reconnections and interactions of resulting flux ropes, which were localized within the ropes. Complimentary to those findings, here, further evolution shows the spontaneous generation of null pairs, which are located more sparsely in space. Indeed, a recent simulation by [Nayak et al. \(2020\)](#) established the spontaneous formation of 3D nulls from an initial chaotic magnetic field devoid of any nulls. Although not explicitly analyzed, the simulation was indicative of the probable role of reconnections in the autonomous generation of nulls. The

novelty of the present work is its considerably detailed focus on the reconnection dynamics leading to spontaneous generation and annihilation of magnetic nulls.

The important properties associated with 3D nulls are presented in Sect. 2.4 and are highlighted here. Firstly, a 3D null maintains its identity during evolution by satisfying the differential equation

$$\frac{d\mathbf{B}}{dt} = 0, \quad (4.1)$$

at the null point shown in Hornig & Schindler (1996), the d/dt being the Lagrangian derivative. As a consequence, tracking a null point during a simulated evolution is feasible. Second, in any evolution, the net topological degree defined in Greene (1992) and Longcope (2005) of a system consisting N number of nulls defined by

$$D = \sum_N \text{Sign} (\det(\nabla\mathbf{B}|_{x_N})), \quad (4.2)$$

remains conserved Hornig & Schindler (1996); Pontin & Priest (2022). The conservation law puts a stringent constraint on any simulation involving the generation/annihilation of nulls that must be satisfied to make the computation credible.

The generic structure of the field lines around a 3D null involves spine and fan structures (Fig. 4.1). The spine is made of two complementary sets of field lines approaching (or receding) from each other and fanning out on the plane containing the 3D null—constituting the fan plane. The topological degree of a null is assigned to be +1 or −1, defined by Lau & Finn (1990), depending upon the direction of the magnetic field lines of either the spine or fan relative to the null. For example, if field lines of the spine are directed away from the magnetic null point, the TD is +1 and vice-versa. The simulations presented here conserve the net topological degree by producing null pairs consisting of radial and spiral nulls of complementary topological degrees, which ascertains the computations to be reliable.

This chapter is organized as follows. Sec. 4.1.1 describes the construction of the initial magnetic field and the flow. The simulation results are presented in

Sec. 4.2 and Sect. 4.3 summarizes the important findings.

4.1.1 Initial magnetic field and flow

Toward constructing the initial state, Taylor's first-order expansion of the magnetic field in the vicinity of the null is given by Parnell et al. (1996):

$$\mathbf{B} = \mathbf{M} \cdot \mathbf{r} \quad (4.3)$$

where \mathbf{M} is a matrix with elements $M_{ij} = \begin{bmatrix} \frac{\partial B_x}{\partial x} & \frac{\partial B_x}{\partial y} & \frac{\partial B_x}{\partial z} \\ \frac{\partial B_y}{\partial x} & \frac{\partial B_y}{\partial y} & \frac{\partial B_y}{\partial z} \\ \frac{\partial B_z}{\partial x} & \frac{\partial B_z}{\partial y} & \frac{\partial B_z}{\partial z} \end{bmatrix}$ and \mathbf{r} is the position vector $(x, y, z)^T$.

The initial magnetic field is constructed to support an isolated linear null at the origin of the computational cube having physical extensions $\{(-\pi, \pi), (-\pi, \pi), (-\pi, \pi)\}$ in the three directions of a Cartesian coordinate system mapped on a $64 \times 64 \times 64$ computational grid. From Parnell et al. (1996), the components of a general magnetic field \mathbf{B} supporting such a null is

$$B_x = x + \frac{1}{2}(q - J_{\parallel})y, \quad (4.4)$$

$$B_y = \frac{1}{2}(q + J_{\parallel})x + py, \quad (4.5)$$

$$B_z = J_{\perp}y - (p + 1)z, \quad (4.6)$$

where the constants p and q are related to the potential part of the \mathbf{B} whereas J_{\parallel} and J_{\perp} are currents parallel and perpendicular to the spine. The initial field is constructed by selecting $p = 1$, $q = 0$, $J_{\parallel} = 0$ and $J_{\perp} = 0$. The null is located at the origin $\mathbf{x} = \mathbf{0}$. Notably, here and afterward, the well-established trilinear method described in Sect. 3.3 is used to locate the nulls. The parameters q and p are selected so that the constructed null is a positive proper radial null with the fan plane being constituted by field lines having rotational symmetry. The null is current free owing to the absence of J_{\parallel} and J_{\perp} , which makes the fan

and spine field lines perpendicular to each other. Categorically, the current free null is chosen to ensure the initial Lorentz force is zero and the only controlling parameter to initiate the dynamics is a prescribed flow which, can be tailored to initiate reconnection. Figure 4.1 depicts the initial field line topology. Notably, the isosurface (colored black in the figure) of the functional

$$\psi(\mathbf{x}) = \exp \left[- \frac{(\mathbf{B} - \mathbf{B}_0)^2}{d_0^2} \right], \quad (4.7)$$

aids to visualize the null. The chosen isovalue is $\psi_0 = 0.06563$, whereas the constants are $B_0 = 0.0075$, $d_0 = 0.036$. The rationale behind the technique is documented in the appendix of [Nayak et al. \(2020\)](#). Magnetic field lines in the neighborhood of the null are plotted in the inset with their directions indicated by arrows. With magnetic field lines constituting the fan plane being directed away from the null, its topological degree is -1 . The x , y , and z directions of the Cartesian coordinate system are indicated with red, green, and blue arrows, respectively.

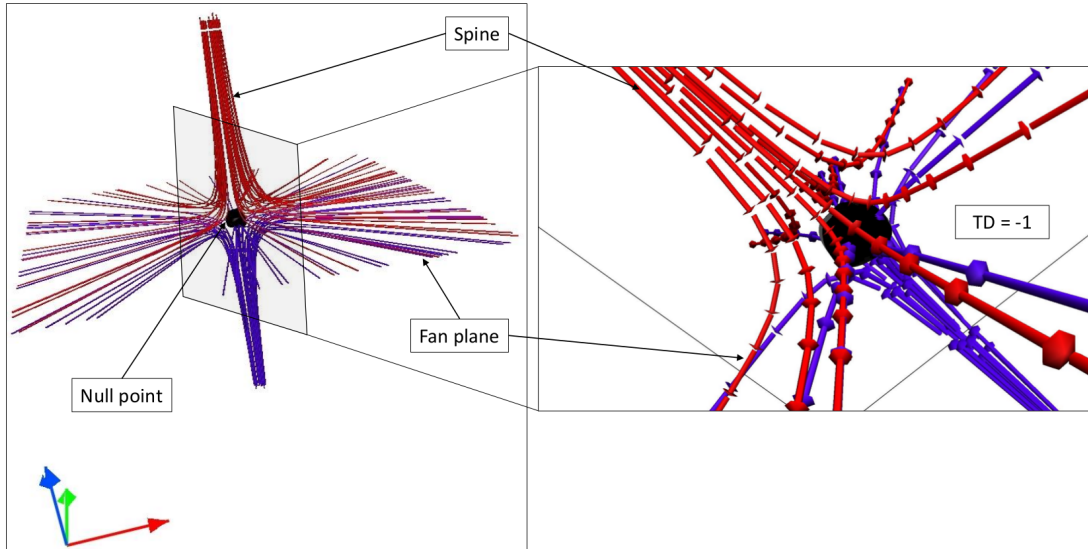


Figure 4.1: Initial magnetic field configuration (left panel), which includes a potential (current free) 3D null located at the center of the box. The null point is shown by plotting the isosurface ψ (black surface) marked by an arrow. The two sets of field lines constituting the upper spine (in red color) and lower spine (in blue color) are fanning out in the fan plane (marked by arrows). For more details, the magnified view of the selected region (rectangular box) is shown in the right panel. The magnetic field lines in the upper and lower spine are directed toward the 3D potential null (null is shown by the black isosurface) and receding away from the null point in the fan plane, making the topological degree -1 .

The initial flow is

$$\mathbf{v} = \{0, 0.5 \sin(z), 0\}, \quad (4.8)$$

as in [Nayak et al. \(2020\)](#), which is chosen to initiate reconnection while maintaining the null to be a stagnation point. The second requirement is to make sure that the null point remains more or less static during the evolution and, specifically, does not move outside the computation box—resulting in a seeming violation of the topological degree preservation. The amplitude is selected through a trial and error basis to achieve computationally effective optimal dynamics, highlighting crucial features of the evolution.

4.2 Results

The simulation is started with the aforementioned field, flow, and grid resolution. The kinematic viscosity is set as $\nu_0 = 0.010$ while the spatial and the tempo-

ral grid increments are $\Delta x = \Delta y = \Delta z = 0.09973$ and $\Delta t = 0.016$, in CGS units. The open boundary condition is applied for both magnetic and velocity fields. The grid resolution is retained to be $64 \times 64 \times 64$ to facilitate magnetic reconnection while optimizing the computation cost. A crude estimate of the Lundquist number ($S = \frac{LV_A}{\eta}$; $V_A \equiv$ Alfvén speed, $\eta \equiv$ magnetic diffusivity) at the reconnection sites can be obtained by approximating $\eta = \frac{(\Delta x)^2}{\Delta t}$ using dimensional analysis. Plugging in all parameters, the estimated value is $S = 0.665$ for the simulation—this is as expected since the local magnetic Reynolds number will always be of order 1 for structures on the grid scale. For reference, the solar coronal value is 10^7 (viz., Ref. (Bora et al., 2021)). Here, the Lundquist number based on the domain size is smaller due to the mismatch between the length scales of the computational box and the coronal scales, which are of the order of 10^6 m. However, this difference is inconsequential since the frozen-in condition is maintained with a high fidelity in locations away from the reconnection sites (Bhattacharyya et al., 2010)—see discussion in Sect. 3.4. The overall evolution of the magnetofluid is depicted in Figure 4.2 by tracing time variations of normalized magnetic (solid line) and kinetic (dashed line) energies averaged over the whole computational volume. The normalization parameters are the corresponding values at $t = 0$ s. An approximate monotonic increase of the magnetic energy is seen, which lasts for $t \approx 10$ s. Subsequently, the curve somewhat flattens out until just before $t \approx 15$ s. The increase can be attributed to the bending of spine field lines because of the initial flow. The normalized kinetic energy also shows an initial increase and reaches a peak value at $t \approx 3.2$ s after which, it presumably gets arrested by the viscosity. The initial increase in kinetic energy is suggestive of an energy flux entering the volume.

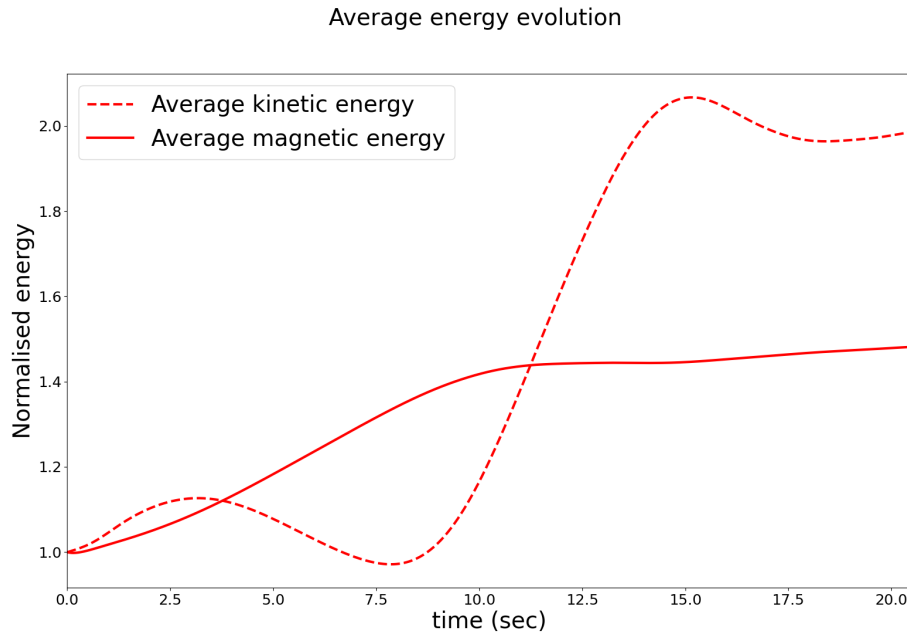


Figure 4.2: Evolution of grid averaged magnetic (solid line) and kinetic (dashed line) energies normalized to their respective initial values. The magnetic energy increases as a consequence of the deformation of magnetic field lines due to the initial sinusoidal flow until $t \approx 10$ s. Afterward, it gets somewhat flattened in $t \in \{10, 15\}$ s. The total energy density (magnetic + kinetic) increases inside the volume. Consequently, the increment in kinetic energy is seen, and it gets arrested by the viscosity, showing a peak around $t \approx 3.2$ s. Subsequently, it starts increasing sharply as a result of magnetic reconnection in the current sheet near the central null showing another peak at $t \approx 15$ s. Within this span, the primary null pairs get generated. With time the spiral null (a constituent of a pair of nulls) gets more twisted—as shown in Figure 4.7. The increase in twist may result in the observed increase in magnetic energy.

Figure 4.3 plots the Direct Volume Rendering (DVR) of the total (magnetic + kinetic) energy density and establishes the energy density to be initially maximal at the top and bottom surface. Subsequently, the energy density peaks up inside the volume and can contribute to the observed kinetic energy increase. Note that the increase of total energy in the domain is consistent with theoretical analyses of null collapse in 2D and 3D. Specifically, our applied flow causes the initial (unstable) equilibrium to be lost as the spine and fan approach one another. This “collapse” process was studied in the linear region (close to the null) and shown to approach a state with a current singularity at the null, with the energy being supplied from the external region—see, e.g., [Bulanov & Olshanetsky \(1984\)](#);

Bulanov & Sakai (1997). Due to the open boundaries in our simulation, the same energy inflow through the boundaries occurs.

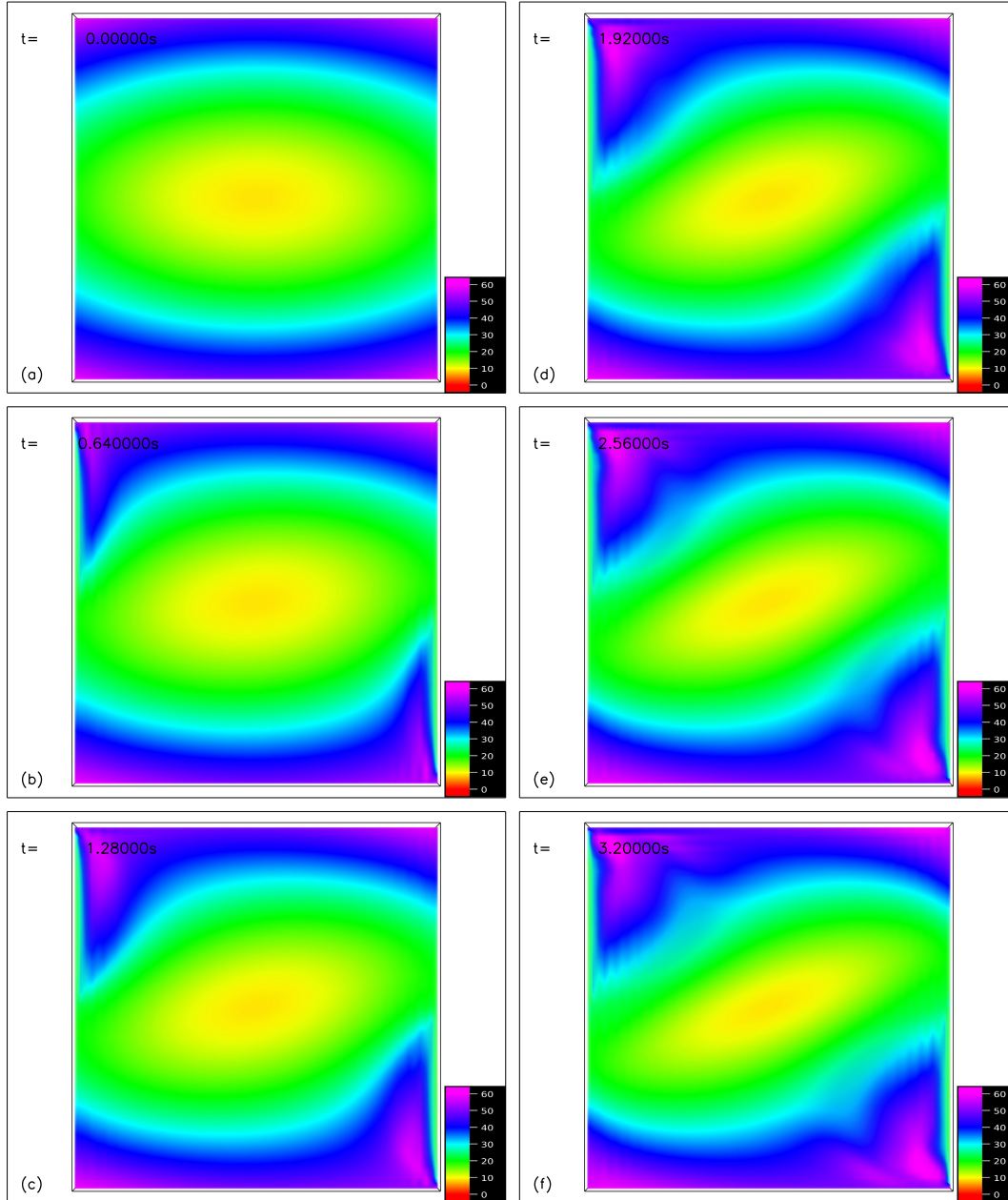


Figure 4.3: The snapshots of the figure spanning time $t \in \{0, 3.2\}$ s represent the evolution total energy density (magnetic + kinetic) through Direct Volume Rendering (DVR). The color scale of the DVR represents the magnitude of the total energy density and is shown in the bottom right corner. At $t = 0$ s, the maximal energy density (pink) is at the top and bottom boundaries. With the evolution, maximal energy increases inside the volume (pink color) (c.f. panels (a)-(f)). Ultimately, an increase in the magnetic and kinetic energy is seen in the same time span.

The details of magnetic field line dynamics overlaid with DVR of $|\mathbf{J}|/|\mathbf{B}|$, \mathbf{J} being the volume current density are plotted in Figure 4.4. The initial points of the field line integrals are kept fixed in time. The interval for the plot is $t \in \{0, 14.544\}$ s, covering the evolution from the initial field configuration to the detection of the first two additional null pairs detected by the trilinear method. The auxiliary field lines in pink and green color (in the first quadrant) along with blue and yellow field lines (in the third quadrant) are plotted to facilitate the demonstration of null generations. As the initial flow pushes the plasma, the upper and the lower spines along with the auxiliary field lines get deformed (panels (b) to (e)). Importantly, the auxiliary field lines get elbow-shaped, most prominently in panel (e). The current intensity also increases accordingly. Finally, the two complementary sides of the elbow seemingly reconnect and generate a pair of nulls (panel (f)), each pair consisting of a radial and a spiral null.

To further relate the magnetic reconnection with null pair generation, in Figure 4.5 field lines in the first quadrant are advected with the plasma flow velocity in $t \in \{14.496, 14.544\}$ s. Notably, here and hereafter, while advecting field lines, care has been taken to select seed points in the flow such that they always remain away from the reconnection region, i.e., in the ideal region of the plasma, allowing identification of reconnection (Knizhnik & Cabral-Pelletier, 2022). For example, in this case, the coordinates of seed points at $t = 14.544$ s are $(-0.003\pi, 0.630\pi, 0.322\pi)$, $(-0.002\pi, 0.625\pi, 0.328\pi)$, $(-0.001\pi, 0.586\pi, 0.316\pi)$ and $(-0.005\pi, 0.586\pi, 0.316\pi)$ for the four depicted field lines whereas the location of the current enhanced region is $\approx (-0.008\pi, 0.556\pi, 0.296\pi)$ in x , y and z directions. The development of the elbow shape is clearly visible in panels (a) and (b), which becomes most prominent in panel (c). Further, Across panels (c) and (d), one of the two green field lines changes its connectivity by moving from the right to the left of the elbow. Such changes in the connectivity of a single field line are suggestive of magnetic reconnection. Topological features such as the radial and spiral nulls along with their spine and fan plane of the radial null are marked by arrows in panel (d)—which are in concurrence with the same features depicted in panel (f) of Figure 4.5. Similarly, the pink field lines also

change their connectivity through magnetic reconnection.

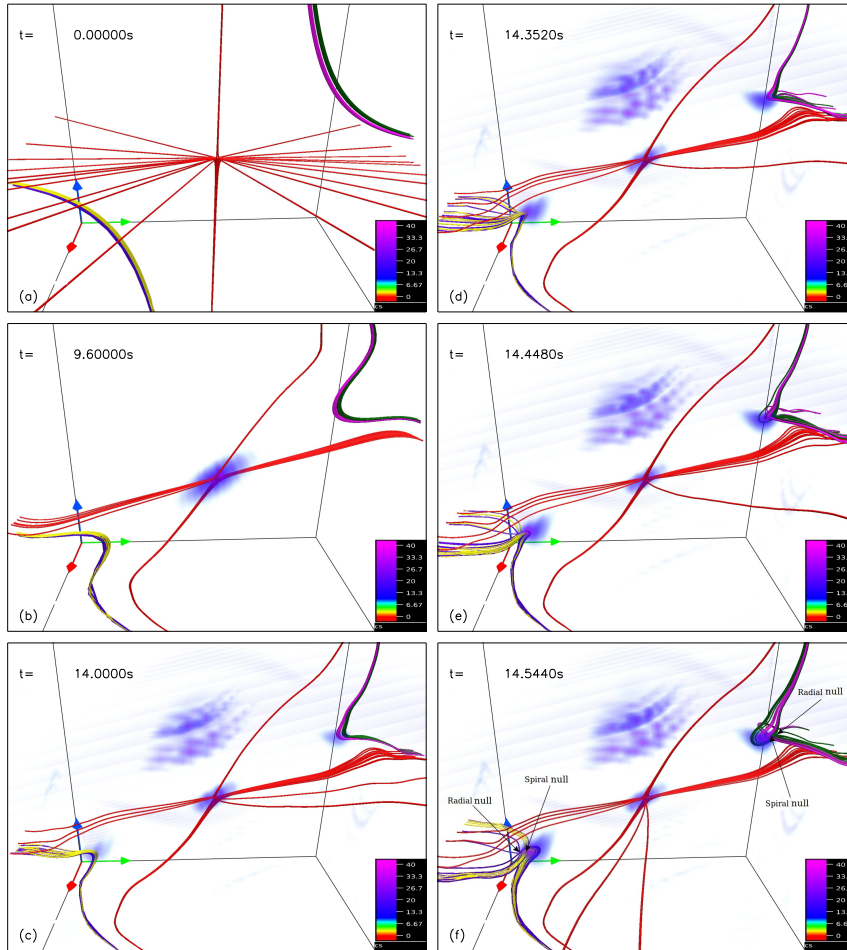


Figure 4.4: The snapshots of the figure spanning $t \in \{0, 14.544\}$ s represent the evolution of the field lines. Here, the field lines are traced in time (the same field lines are traced by keeping the corresponding initial point of a field line invariant). At the $t = 0$ s, a current free radial null is located at the center of the box, and the red field lines are plotted near this central null. In panel (a), a set of auxiliary field lines (green and pink) in the first quadrant and (yellow and blue) are plotted in the third quadrant to demonstrate the null generation. The sinusoidal flow bends the spine towards the fan plane and consequently, pushes the auxiliary field lines to bend (panel (b)). Further evolution generates the elbow shape structure (panel (c)-(e)) and develops current intensity accordingly, as shown in panel (c) onward. The magnitude of current density $|\mathbf{J}|/|\mathbf{B}|$ is shown through DVR. Green (in the first quadrant) and blue (in the third quadrant) field lines are changing their connectivity see panel (e)—a sign of magnetic reconnection. Consequently, 3D null in the pairs has been generated at $t = 14.544$ s (panel (f)). Each pair consists of a radial and spiral null marked by arrows.

Figure 4.6 depicts the magnetic energy, averaged over a subvolume of physical

extent $\{(-0.143\pi, 0.111\pi); (0.396\pi, 0.650\pi); (0.111\pi, 0.365\pi)\}$ in x , y and z directions constituting the null pair of the first quadrant, to decrease monotonically in $t \in \{14.0, 14.54\}$ s and further corroborates the magnetic reconnection.

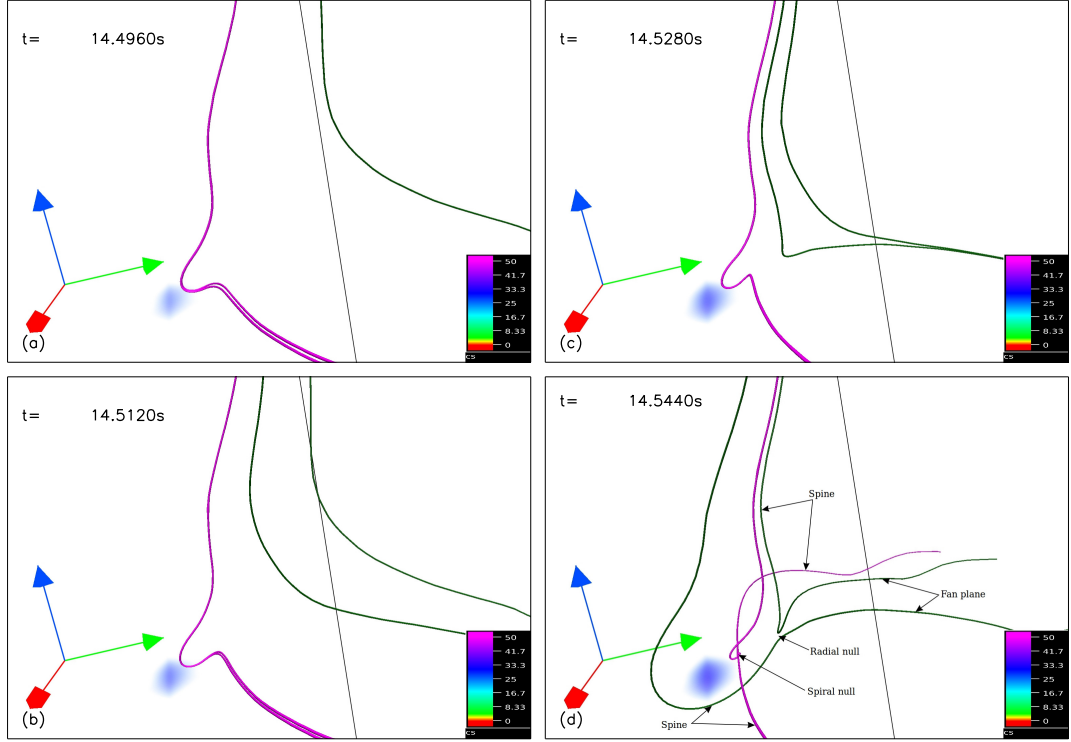


Figure 4.5: The snapshots of this Figure plot the selected magnetic field lines of the first quadrant and advected through plasma flow in $t \in \{14.496, 14.544\}$ s to illustrate the magnetic reconnection in null creation. Notably, here and hereafter, while advecting field lines, care has been taken to select seed points in the flow such that they always remain away from the reconnection region i.e., in the ideal region of the plasma, allowing identification of reconnection. For example, in this case the coordinates of seed points at $t = 14.544$ s are $(-0.003\pi, 0.630\pi, 0.322\pi)$, $(-0.002\pi, 0.625\pi, 0.328\pi)$, $(-0.001\pi, 0.586\pi, 0.316\pi)$ and $(-0.005\pi, 0.586\pi, 0.316\pi)$ for the four depicted field lines whereas the location of the current enhanced region is $\approx (-0.008\pi, 0.556\pi, 0.296\pi)$ in x , y and z directions. The development of the elbow shape is clearly visible in panels (a) and (b), which becomes most prominent in panel (c). Further, Across panels (c) and (d), one of the two green field lines changes its connectivity by moving from the right to the left of the elbow. Such changes in the connectivity of a single field line are suggestive of magnetic reconnection. Topological features such as the radial and spiral nulls along with their spine and fan plane of the radial null are marked by arrows in panel (d)—which are in concurrence with the same features depicted in panel (f) of Figure 4.5. Similarly, the pink field lines also change their connectivity through magnetic reconnection.

Figure 4.7 traces the evolution of the null pairs along with neighboring field lines from their first detection at $t = 14.5440$ s to $t = 18.1280$ s when the separation between the constituent nulls of a pair is maximum. The radial and spiral nulls are further marked with arrows in panels (a) and (j) for better identification. Notably, the field lines belonging to the spiral null get more twisted with time. This increased twist generates more magnetic tension, which pushes the two nulls of a given pair further apart, cf. panels (a) to (j) of the Figure 4.7.

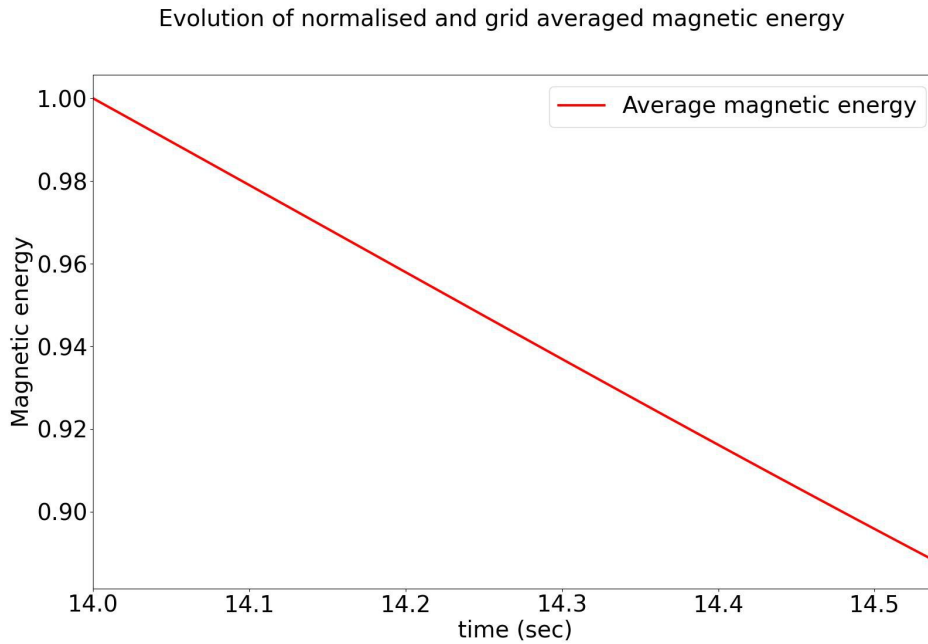


Figure 4.6: The plot shows the variation in average magnetic energy normalized to its corresponding value at $t = 14.0$ s. The average is taken over a subvolume of physical extent $\{(-0.143\pi, 0.111\pi); (0.396\pi, 0.650\pi); (0.111\pi, 0.365\pi)\}$ in x , y and z directions constituting the null pair at the first quadrant. The vertical axis represents the magnitude of average magnetic energy normalized to its corresponding value at 14.0s, and the horizontal axis represents time (in seconds). The monotonic decrease of magnetic energy in $t \in \{14.0, 14.544\}$ s corroborates the magnetic reconnection.

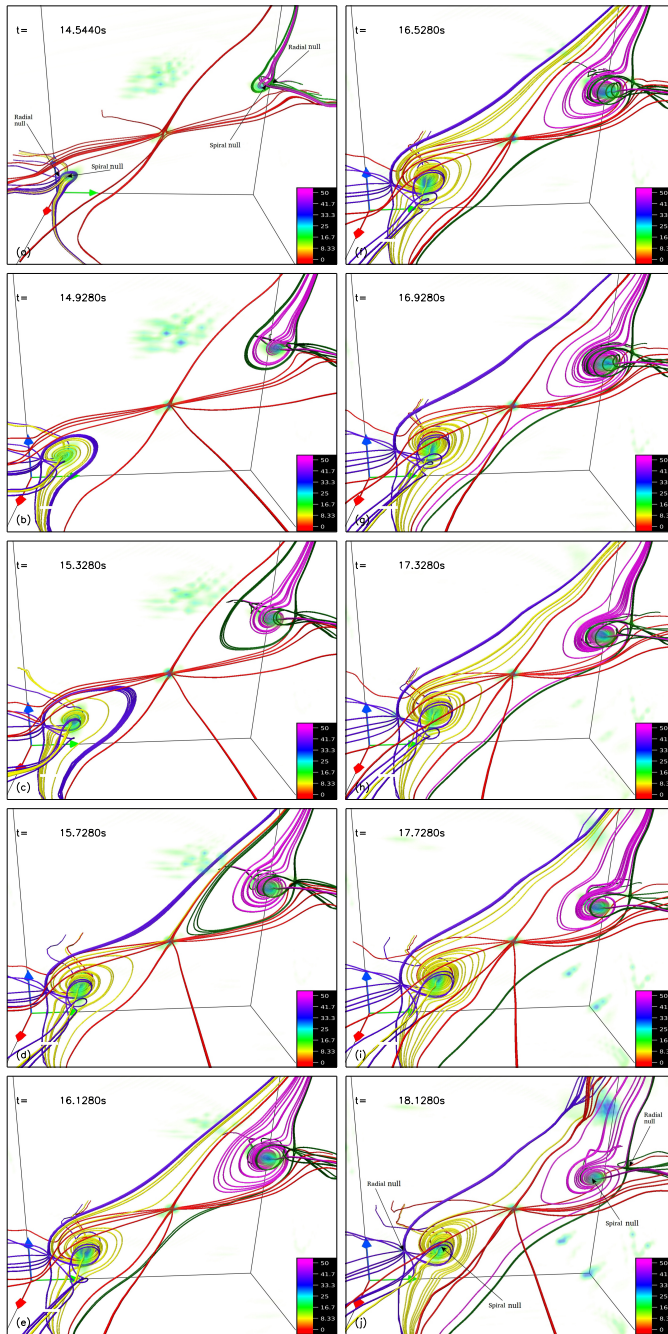


Figure 4.7: The snapshots of field lines spanning $t \in \{14.544, 18.128\}$ s represents the evolution of nulls. Here, the nulls are traced in time through the trilinear technique, and field lines are drawn to the locations of nulls. At $t = 14.544$ s, primary null pairs have been detected for the first time, and field lines are plotted near them, shown in panel (a). In subsequent panels, nulls are traced, and the twist of field lines of spiral null is increasing. Consequently, nulls of a particular pair are receding from each other (compare panels (a)-(j)). Simultaneously, the increase in the current density near the spiral null is also seen with the help of DVR of $|\mathbf{J}| / |\mathbf{B}|$. In each pair, one is radial null and another is spiral null (more details can be seen in Figure 4.8). Radial and spiral nulls are marked by arrows in panel (a) (the time instance when nulls have been generated in the system and in panel (j) (the time instance at which the first quadrant null pair is at maximum separation), only not in other panels so that the null structures can be seen clearly.

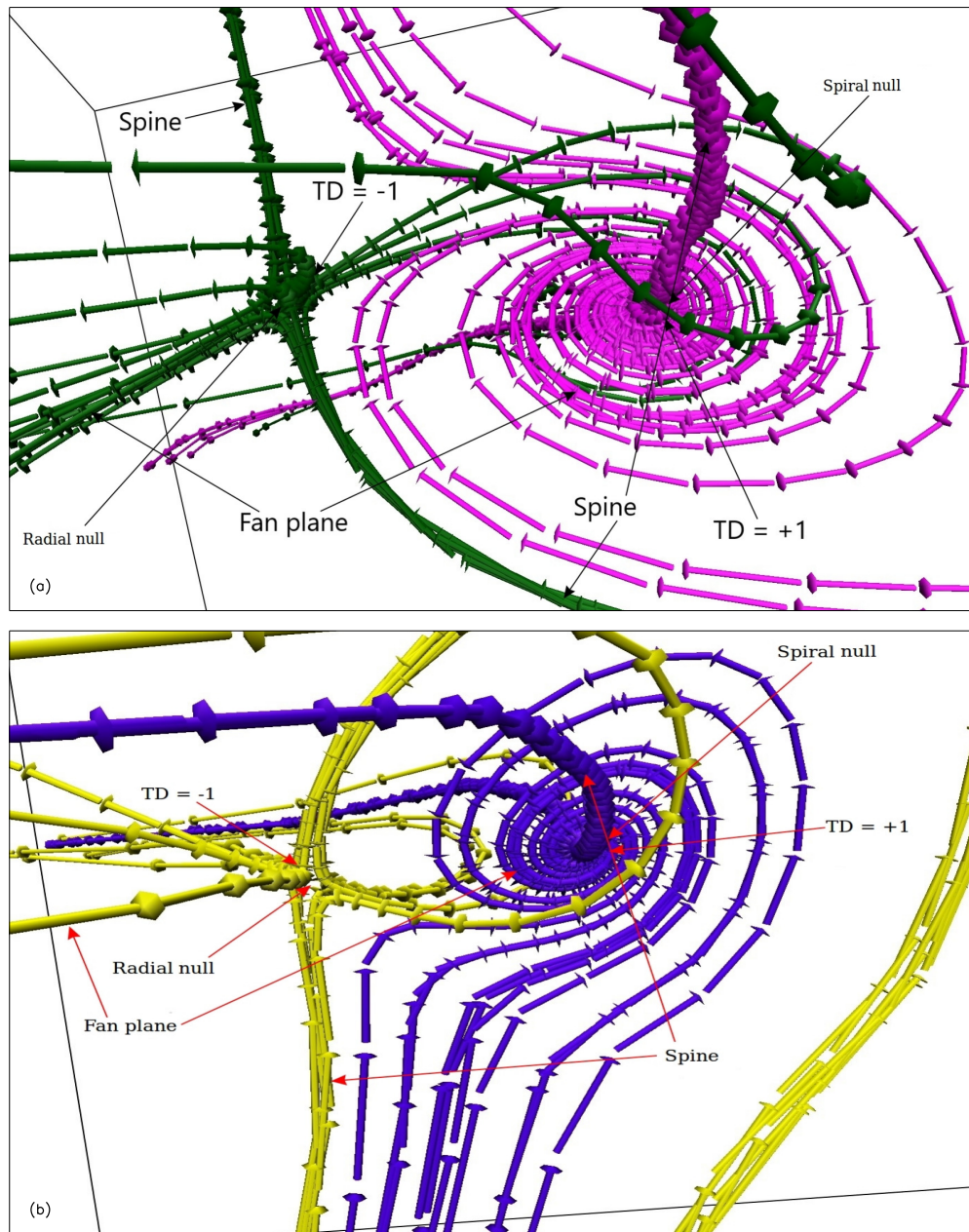


Figure 4.8: Figure illustrates the detailed structure of nulls in a pair. The first quadrant null pair consists of a radial null and a spiral null (panel (a)). The field lines of radial null are plotted in (green), and that of a spiral null is plotted in (pink). The direction of spine field lines of radial null is towards the null point and away from the null point in the fan plane, making the topological degree -1 , whereas the direction of spine field lines of spiral null is away from the null point and towards the null point in the fan plane resulting the topological degree $+1$. Therefore, the net topological degree of this pair is zero, and the net topological degree of the system remains unaffected. Similarly, panel (b) illustrates details of the third quadrant null pair, which also consists of a radial null and a spiral null. The field lines of radial and spiral null are drawn in yellow and blue, respectively. The direction of spine field lines of radial null is towards the null point and receding away from the null point in the fan plane making the topological degree -1 whereas the direction of spine field lines of spiral null is away from the null point and towards the null point in the fan plane resulting the topological degree $+1$. The conservation of the topological degree is self-explanatory.

To determine the topological degree of the generated nulls, Figure 4.8 magnifies the pairs. Panel (a) depicts the null pair in the first quadrant, whereas the null pair in the third quadrant is illustrated in panel (b). In panel (a), the spine and fan field lines of the radial and spiral null along with their directions are clearly marked. The direction of fan field lines (green) of the radial null is away from the null, making its topological degree -1 . The spiral null has its fan plane field lines (pink) toward the null and, hence, has a topological degree $+1$. Consequently, the net topological degree of the pair becomes zero. A similar topology is observed in the null pair in the third quadrant. From panel (b), it is self-explanatory that the topological degree of the radial null is again -1 , whereas that of the spiral null is $+1$. The net topological degree for the pair is again zero, making the overall degree to be -1 —the same as its initial value. In the rest of the paper, these two null pairs generated by the sinusoidal flow are called primary pairs in order to differentiate them from the spontaneously generated nulls observed throughout the computational domain and time. It is imperative to correlate the evolution of kinetic and magnetic energies with the aforementioned field line dynamics. For this purpose, we focus on the dynamics of field lines near the central null (Figure 4.9). An important observation is the slippage of fan field lines (visible in the accompanying animation <https://doi.org/10.1063/5.0107601.4>) from $t \approx 7$ s, changing magnetic connectivity and resulting in magnetic reconnection. The plasma flow is found to be in a direction other than the slippage (not shown), and reconnection is confirmed to be the cause of the connectivity change. An important epoch is the $t \in \{10, 15\}$ s, where the magnetic energy remains somewhat flattened, but kinetic energy shows a sharp rise (see Figure 4.2). The flattening of the magnetic energy is suggestive of possible reconnections, which arrest its initial rise owing to the deformation of field lines by the flow as reconnections are known to decrease magnetic energy; see Olshevsky et al. (2013) for details. Indeed, a current sheet develops (panel (b)) and later facilitates magnetic reconnections near the central null cf. panels (d) to (h).

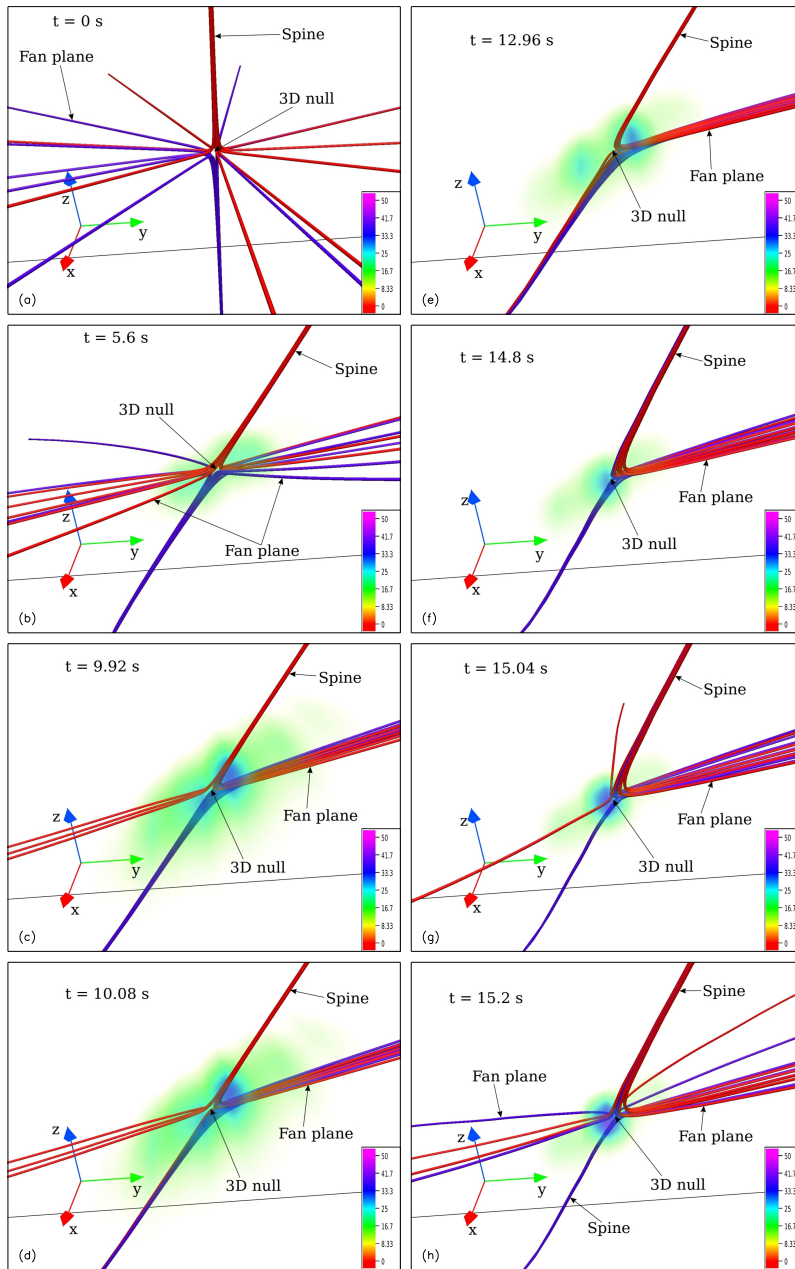


Figure 4.9: The snapshots of field lines spanning the $t \in \{0, 15.2\}$ s illustrate the evolution of central null marked by 3D null in the figure (the initial current free radial null located at the center of the box). The spine and fan field lines of the initial null are plotted in red and blue (panel(a)), with red field lines constituting the upper spine while field lines in blue belong to the lower spine. With the evolution, the current sheet (CS) near the central null develops which facilitates the magnetic reconnection in the current sheet. Panel (b) shows an intermediate field line structure in which the current sheet has been started to develop (identified with DVR of large $|\mathbf{J}|/|\mathbf{B}|$). The color scale of the DVR (right bottom corner) represents the magnitude of the current intensity. The blue and red field lines slip over the fan plane, and an intermediate structure is shown in panel(c) before the reconnection in the CS near the central null. The red and blue field lines are changing their connectivity (evident by panels (d)-(h)) and become part of the lower and upper spine, earlier at $t = 0$ s (panel (a)), red and blue field lines were only part of the upper and lower spine respectively. The corresponding magnetic energy decrease is shown in Fig. 4.10.

The magnetic energy in a subvolume of physical extent $\{(-0.111\pi, 0.079\pi); (-0.111\pi, 0.079\pi); (-0.111\pi, 0.079\pi)\}$ in x , y and z directions constituting the central null is also calculated. Its plot in the corresponding time interval shows a monotonic decrease (Figure 4.10) and corroborates the reconnection.

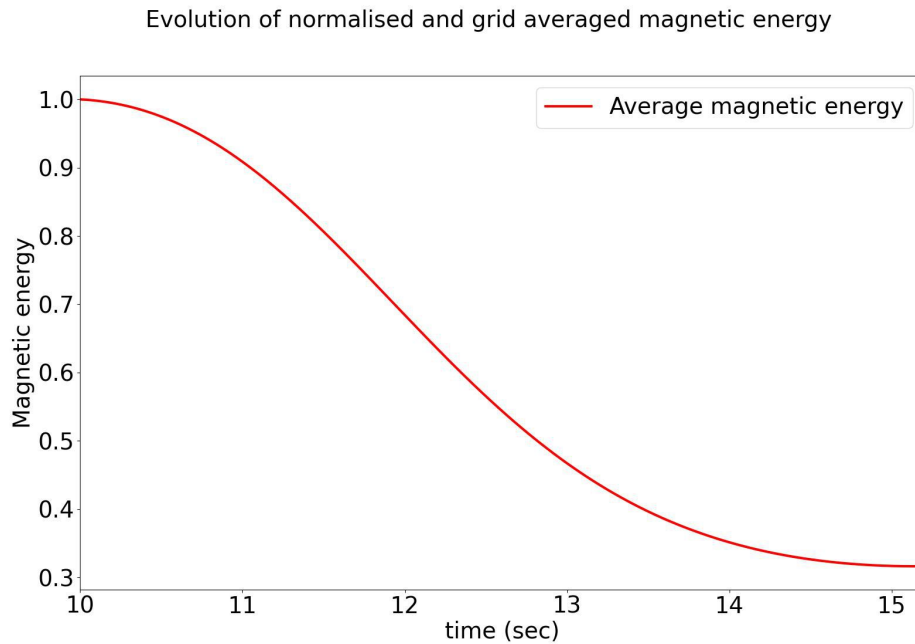


Figure 4.10: The plot shows the variation in average magnetic energy spanning time $t \in \{10.0, 15.2\}$ s. The vertical axis represents the normalized average magnetic energy, and the horizontal axis represents the time (in seconds). The plot shows the decrease in magnetic energy with time, which is averaged over the subvolume of physical extent $\{(-0.111\pi, 0.079\pi); (-0.111\pi, 0.079\pi); (-0.111\pi, 0.079\pi)\}$ in x , y and z directions constituting the central null and normalized to its initial value at $t = 10$ s (the approximate time when reconnection started in the current sheet near the central null). The decrease in magnetic energy corroborates the magnetic reconnection near the central null. In the same time span, the increase in the kinetic energy is seen (see Fig.. 4.2), the whereas magnetic energy of full volume remains somewhat flattened.

Further, Figure 4.11 depicts flow lines at an approximate time instance from which the inflow and outflow regions can be readily identified.

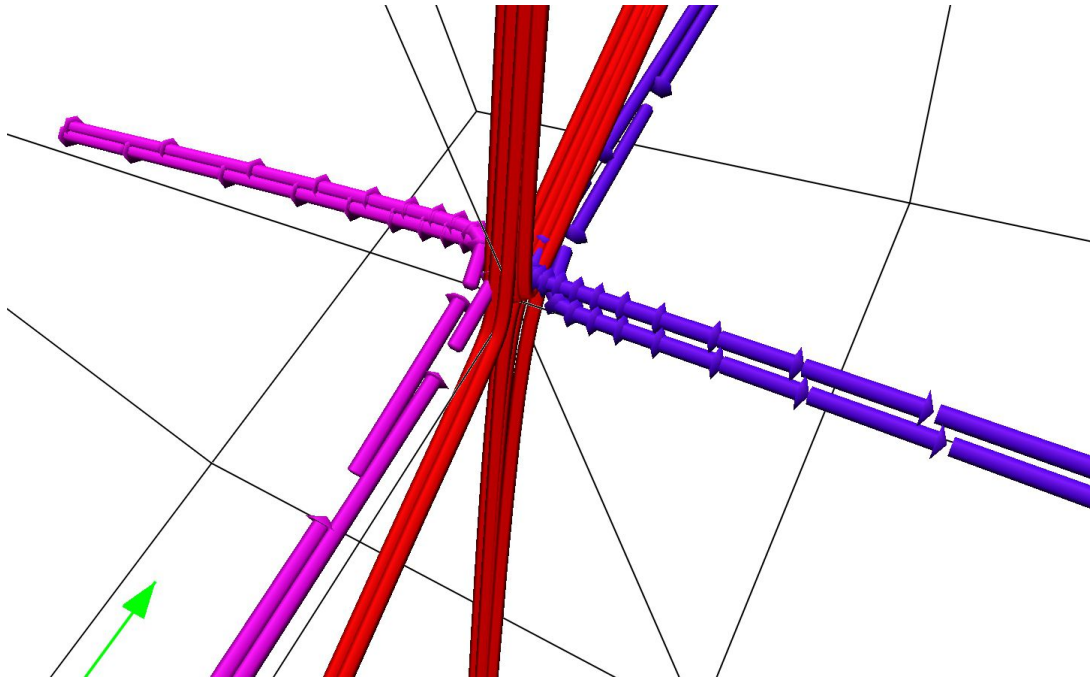


Figure 4.11: Figure illustrates the inflow and reconnection outflow at the central null using pink and blue arrows at a time $t = 10.56$ s. The red field lines are drawn to demonstrate the central null. The pink and blue arrows heading toward null represent the inflow, whereas those pointing away from central null represent the reconnection outflow. This outflow further confirms the reconnection at central null. The plotting of reconnection outflow is possible here because the central null is also a stagnation point. In contrast, in other reconnection locations, the flow is a superposition of evolved plasma flow and reconnection outflow (not separable).

In the overlapping time span $t \in \{14, 16\}$ s, (Panels (a) and (j) of Figure 4.7), the spiral nulls are created and their twist get enhanced. The corresponding increase in the magnetic energy may supersede the arrest, allowing magnetic energy to rise again from $t \approx 15$ s onward. The primary null pairs get annihilated as the magnetofluid evolves in time. For the demonstration and analyses, the null pair in the first quadrant is selected. The snapshots of Figure 4.12 spanning $t \in \{16.608, 19.808\}$ s show the evolution of null pair by tracing their locations and plotting field lines near them. At $t = 16.608$ s, the radial (in green) and spiral (in pink) null are at some distance from each other (panel (a)). With time, their separation decreased (panel (b)) and ultimately got annihilated at $t = 19.808$ s (panel (c)).

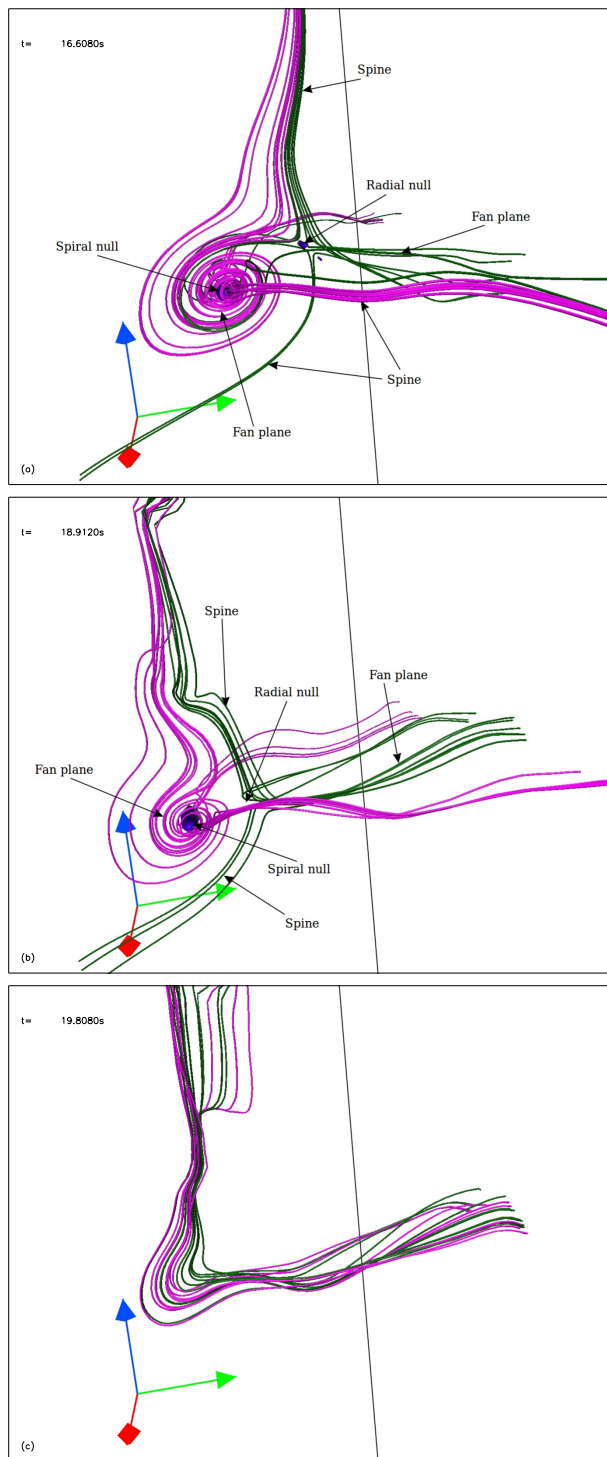


Figure 4.12: The snapshots of the figure illustrate the evolution of the null first quadrant pair, which consists of a radial null and a spiral null. Here, nulls are traced in time, and field lines are plotted near them to show evolution. Radial (pink) and Spiral (green) null, along with its fan and spine, are marked by arrows. Panel (a) depicts radial and spiral null field line configurations at $t = 16.608$ s. The twist of the spiral null decreases, and consequently, nulls come closer to each other (the decrease in separation can be seen by comparing panels (a) and (b)) as they evolve in time. The decrease continues until the nulls in the pair is annihilated (panel (c)). The physical process behind annihilation is identified and is shown in Fig.4.13. A similar process is also seen in the case of the third quadrant null pair.

The field lines are selected and traced in time span $t \in \{16.64, 16.992\}$ to neatly identify the physical process and shown in Figure 4.13. The pink field lines mainly constitute the spiral null along with the lower spine and fan plane of the radial null, and the green field lines only belong to the radial null (panel (a)). With the advancement in time, the pink field lines changed their connectivity and became part of the upper spine of the radial null (panels (b) and (c)); earlier, they were part of the lower spine. Consequently, the pink field lines open up and reduce the twist of the spiral null. They become part of the radial null in further evolution (panel (d)). The corresponding decrease in magnetic tension allows the nulls to come close to each other and also enables lower-lying twisted field lines to expand and ultimately reconnect further. This process continues along with the decrease in a twist of the spiral null and the separation between the nulls until the pairs are annihilated. The conservation of the topological degree is self-explanatory. To further establish the reconnection, Fig.4.14 highlights the dynamics of selected magnetic field lines belonging to the first quadrant nulls and advected with the plasma flow velocity. The change in connectivity of field lines from panel (a) to (d) is a clear indication of reconnection. Figure 4.15 plots the separation

$$\Delta s = \sqrt{\sum_{i=1}^3 (x_2^i - x_1^i)^2} \quad (4.9)$$

where the subscripts refer to the two nulls of the pair while the superscript denotes the Cartesian coordinates. The plot in Figure 4.15 shows the nulls initially recede from each other for $t \in \{14.544, 18.2\}$ s, after their generation at $t = 14.544$ s and the separation being maximum approximately at $t \approx 18.2$ s. Subsequently, they start to move toward each other—ultimately leading to their annihilation at $t = 19.312$ s. Similar dynamics are seen to be responsible for the annihilation of the primary null pair in the third quadrant also. Toward establishing the role of magnetic tension in increasing and decreasing the separation between the spiral and the radial null, Figure 4.16 plots evolution of volume averaged $|\mathbf{B} \cdot \nabla \mathbf{B}|$ normalized to its initial value in the range $t \in \{14.54, 19.31\}$ s—covering the total duration in which the nulls (in the first quadrant) get generated

and, later, annihilated.

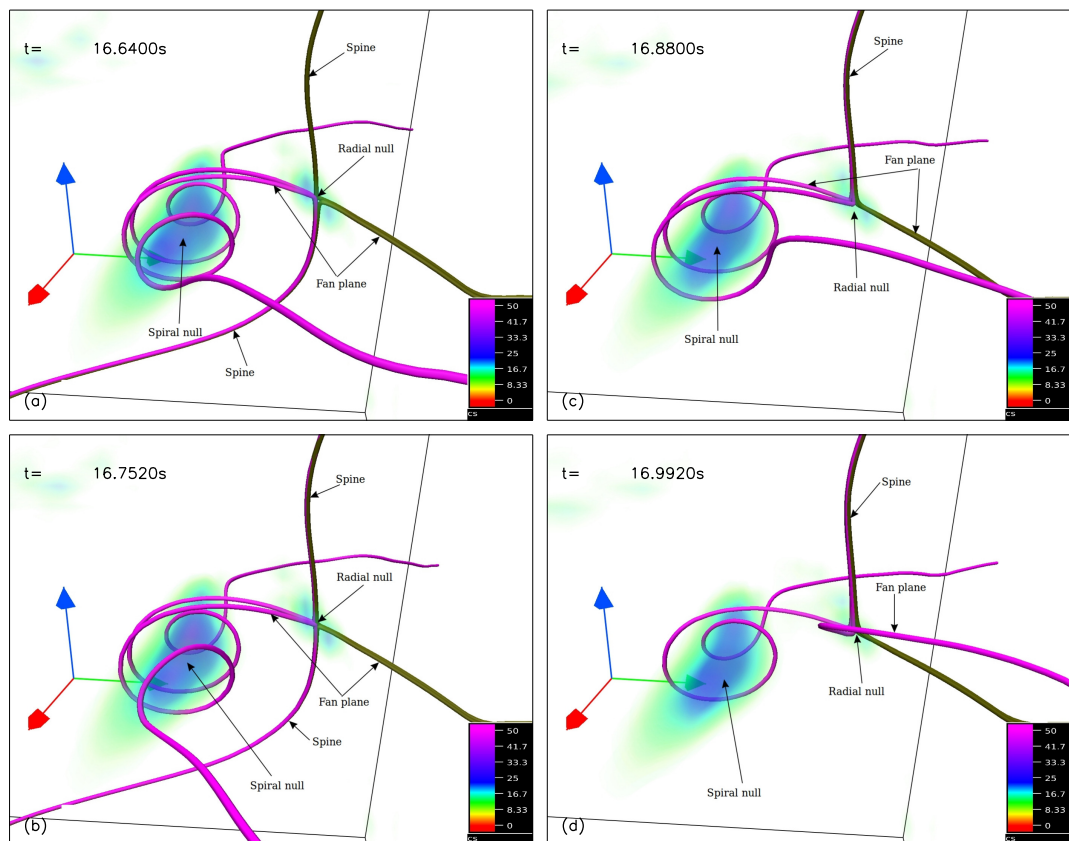


Figure 4.13: The snapshots of the figure spanning $t \in \{16.640, 16.992\}$ illustrate the physical process responsible for the annihilation of nulls of the first quadrant pair (shown in figure 4.12). The field lines are traced in time, and the time span of this figure is chosen for demonstration purposes of the physical process. Panel (a) illustrates the configuration at $t = 16.640$ s with the pink field lines mainly constituting the spiral null, fan plane, and the lower spine of the radial null, and the green field lines belonging to the radial null constituting the upper spine and fan plane (marked by arrows). The current intensity is shown with the help of DVR of $|\mathbf{J}| / |\mathbf{B}|$. In subsequent panels, the pink field lines change the connectivity through reconnection at the radial null, and simultaneously, the twist is reduced. The pink field lines become part of the upper spine and fan plane of radial null (panel (a)-(d)). Consequently, nulls will come close to each other as the twist decreases. This process continues till the nulls get annihilated.

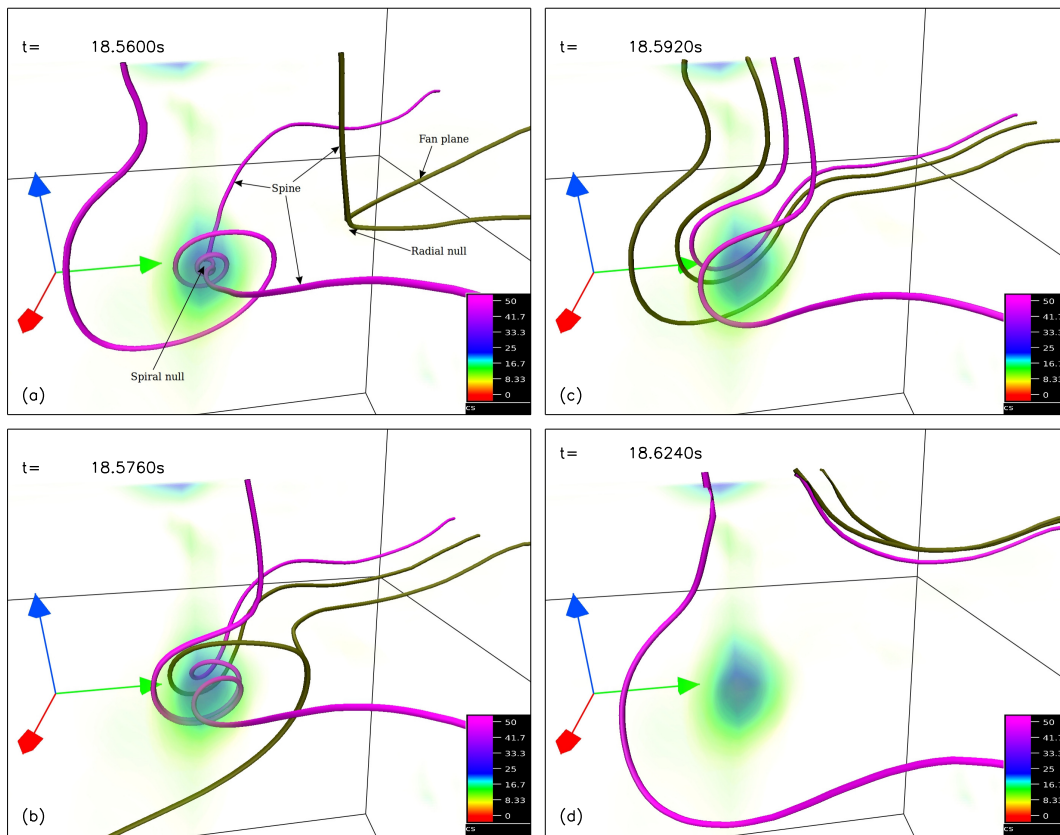


Figure 4.14: The snapshots of the figure spanning $t \in \{18.5600, 18.624\}$ highlight the dynamics of selected magnetic field lines belonging to the first quadrant nulls and advected with the plasma flow velocity. The change in connectivity of field lines from panel (a) to (d) is a clear indication of reconnection.

The average is taken over a physical volume of extent $\{(-0.174\pi, 0.143\pi); (0.333\pi, 0.650\pi); (0.111\pi, 0.429\pi)\}$ in x , y and z coordinates, enclosing the null pair throughout their evolution. The plot shows an initial increase in magnetic tension along with the increase in separation between the nulls. Subsequently, as the nulls approach each other, the tension decreases. A similar variation of magnetic tension is also found in the third quadrant. Astoundingly, null pairs also get spontaneously generated from $t = 18.4$ s onward (panel (c) onward of Figure 4.17). In the figure, the locations of these nulls are indicated with green colored dots whereas the red and blue dots locate central and primary nulls respectively. The locations are determined by the trilinear method and plotted using a 3D point plot in Python. The panels of Figure 4.17 cover $t \in \{0, 20.32\}$ s, where initially only a central null (red dot) at $t = 0$ s is

present (panel (a)) and at $t = 14.72$ s primary nulls (blue dot) are there together with central null (panel (b)). The locations of spontaneously generated nulls are represented by green dots (panel (c)-(f)).

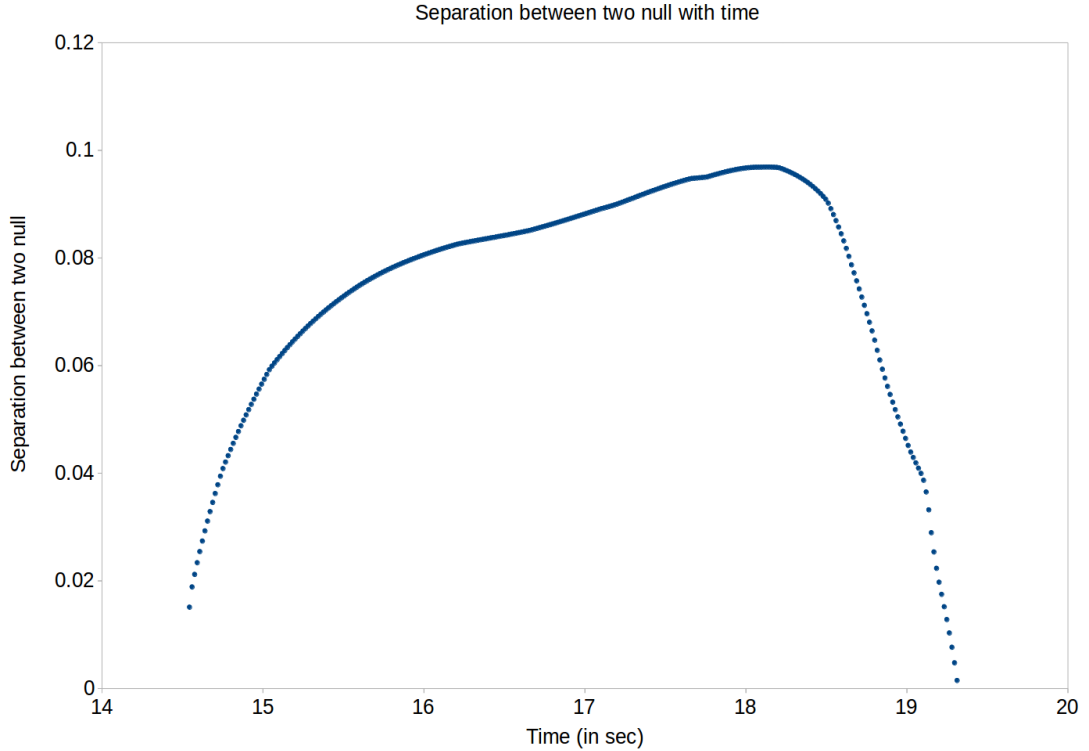


Figure 4.15: The plot shows the variation in separation with time between nulls of the first quadrant null pair. The vertical axis represents the separation between the two nulls of a first quadrant pair, and the horizontal axis represents the time (in seconds). The separations of nulls start increasing with time and show a peak around $t = 18.2$ s, then decrease with time, and finally, nulls get annihilated around $t = 19.3$ s. A similar variation is also seen for the third quadrant null pair.

Importantly, these spontaneously generated nulls also get annihilated. To explore the spontaneous generation and annihilation of null pairs, one pair of spontaneously generated null has been selected (green dot plotted in panel (d) of Figure 4.17). The selection of the pair is based on the clarity of the field line dynamics and tractability of the involved null pair over sufficient time (the time can be validated by calculating the total time of presence of the null pair in the system with the help of panel (d) to (f), where panel (d) and (f) represents the approximate time when nulls are generated and annihilated in the system respectively. Panels (a)-(c) of Figure 4.18 show the snapshots of field line evolution by

tracing the field lines in time, leading to the spontaneous creation of the null pair (panel (c)). The null pairs are detected once again using the trilinear method. Panels (a)-(c) plot two field lines (in red and blue) and green field lines, which, during their evolution, develop complementary elbow-type structures similar to the one developed by the auxiliary field lines participating in the formation of the primary nulls. The current intensity also increases accordingly. Further evolution introduces a sharp change in topology and makes the field lines helical (panel (c) of Figure 4.18). Such change in topology indicates magnetic reconnection, albeit the participating field lines cannot be identified because of their complex geometry. Astoundingly, the spiral null appears at the same instant ($t = 18.688$ s) with distinct lower, upper spine and the fan plane (the upper spine is shown in the subsequent panels only).

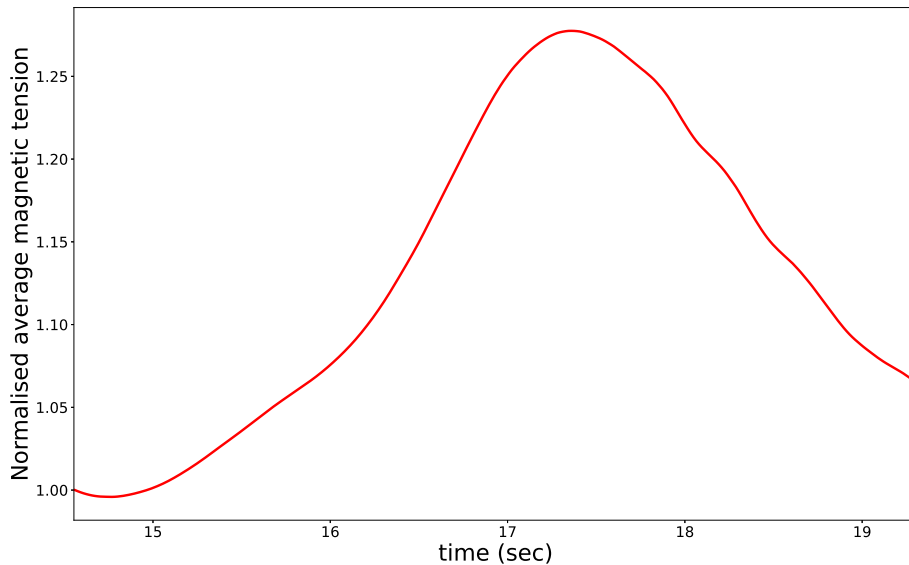


Figure 4.16: The plot illustrates the evolution of volume averaged $|\mathbf{B} \cdot \nabla \mathbf{B}|$ normalized to its initial value in the range $t \in \{14.54, 19.31\}$ s—covering the total duration in which the nulls (in the first quadrant) get generated and later, annihilated. The average is taken over a physical volume of extent $\{(-0.174\pi, 0.143\pi); (0.333\pi, 0.650\pi); (0.111\pi, 0.429\pi)\}$ in x , y and z coordinates, enclosing the null pair throughout their evolution. The plot shows an initial increase in magnetic tension along with the increase in separation between the nulls. Subsequently, as the nulls approach each other, the tension decreases. The vertical axis represents the modulus of normalized averaged magnetic tension, and the horizontal axis represents time (in seconds).

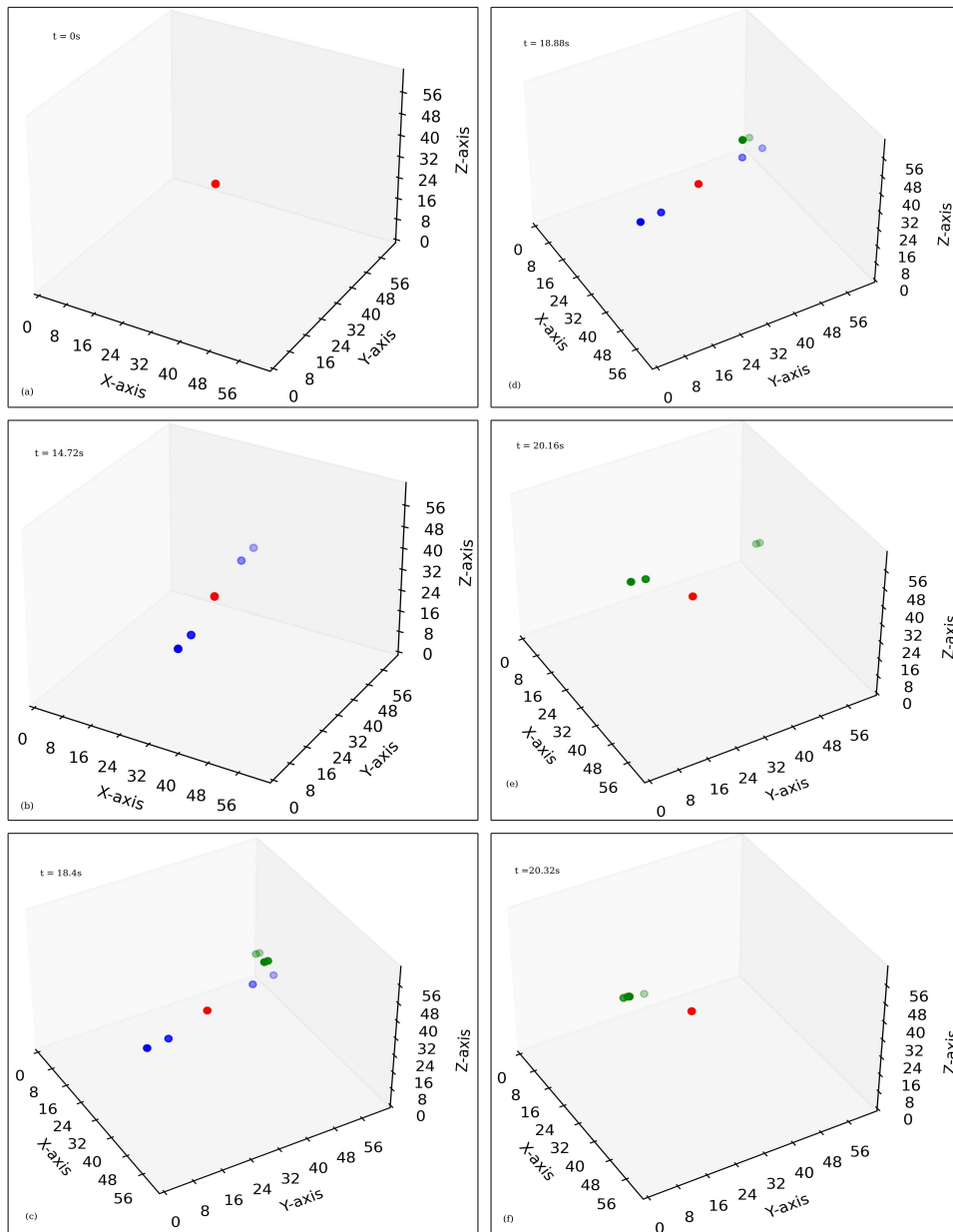


Figure 4.17: Panels ((a)-(f)) illustrate the locations of nulls with time. The location of nulls is traced through the trilinear null detection technique and located then in the 64^3 grid by using a Python 3D point plot. The red, blue, and green dots represent the locations of central, primary, and spontaneously generated nulls, respectively. At $t = 0$ s, only a central null is present (panel (a)). With evolution, the primary nulls are generated, and locations are shown in panel (b) along with central null at time $t = 14.72$ s. The nulls also get generated spontaneously with further evolution in time. The locations of spontaneously generated along with the central and primary nulls at time $t = 18.4$, 18.88 , 20.16 and 20.32 s are shown in subsequent panels (c)-(f). The spontaneously generated null pair (shown in panel (d)) is considered for the detailed study based on the time tractability of the pair and can be confirmed by the estimating time from panels (d) and (f), which mark the approximate time of generation and annihilation, respectively.

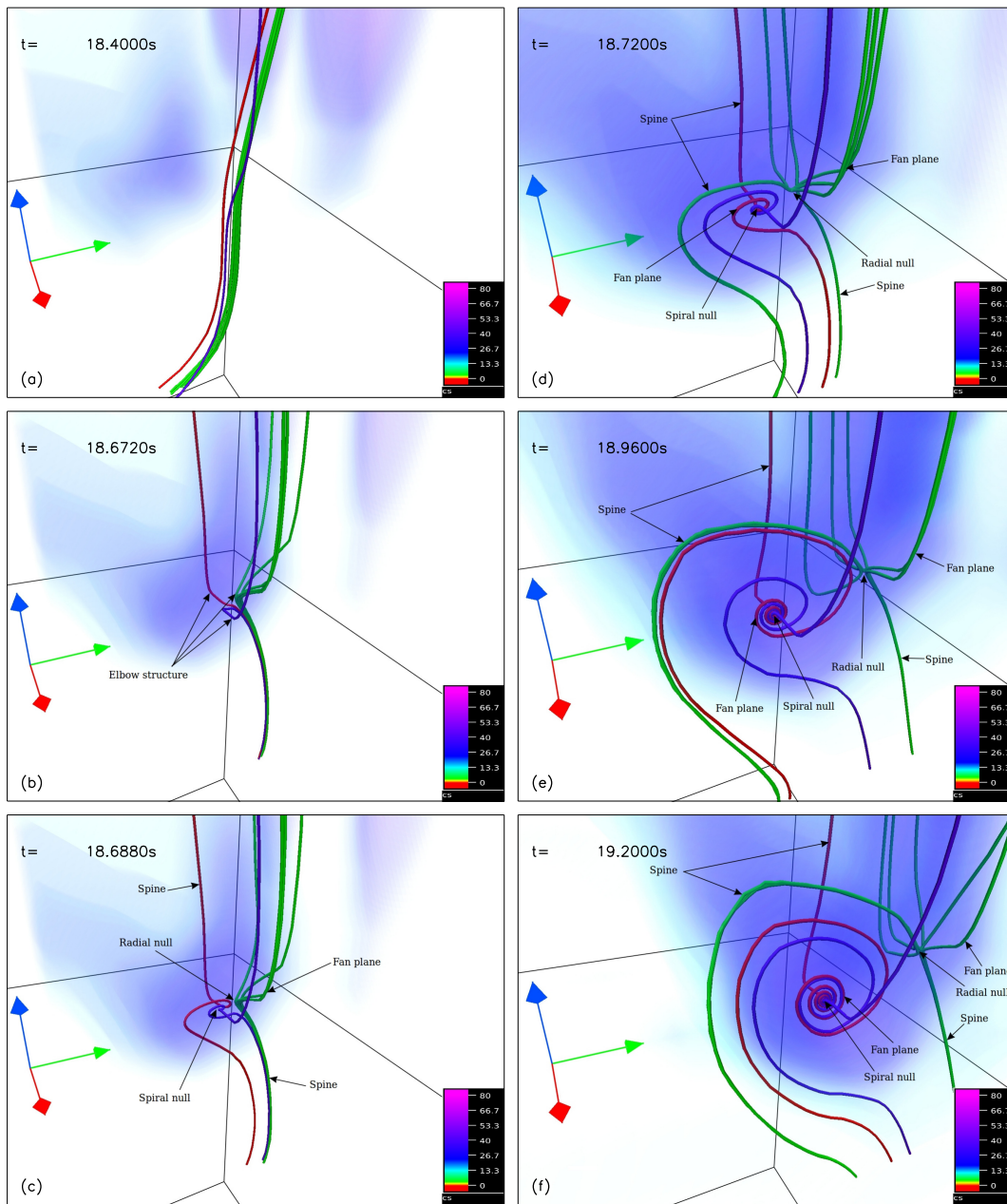


Figure 4.18: The panels (a)-(c) illustrate the evolution of field lines by tracing in time, which leads to the spontaneous generation of null pairs. The field line configuration at $t = 18.400\text{s}$ (panel (a)) changes to another configuration at $t = 18.762\text{s}$ and develops the elbow-type structure (marked by an arrow in panel (b)). The enhancement in current intensity (identified by DVR of $|\mathbf{J}|/|\mathbf{B}|$) is seen accordingly. Further evolution makes the red and blue field lines helical through magnetic reconnection and, as a consequence, spontaneously generates a radial and a spiral null (marked by arrows in panel (c)). In subsequent panels (d)-(f), nulls are traced, and field lines are drawn at them. With evolution, the twist of the spiral null increases, and consequently, the nulls recede from each other. The increase in separation can be clearly seen by comparing panels (c)-(f).

The snapshots shown in panels (d)-(f) show the further evolution, where nulls are traced in time, and the field lines are plotted at the nulls. With the evolution, the twist of spiral null increases, so enhancement in magnetic tension, which pushes the nulls away from each other and increases the separation between the radial 3D and spiral null cf. panels (d)-(f).

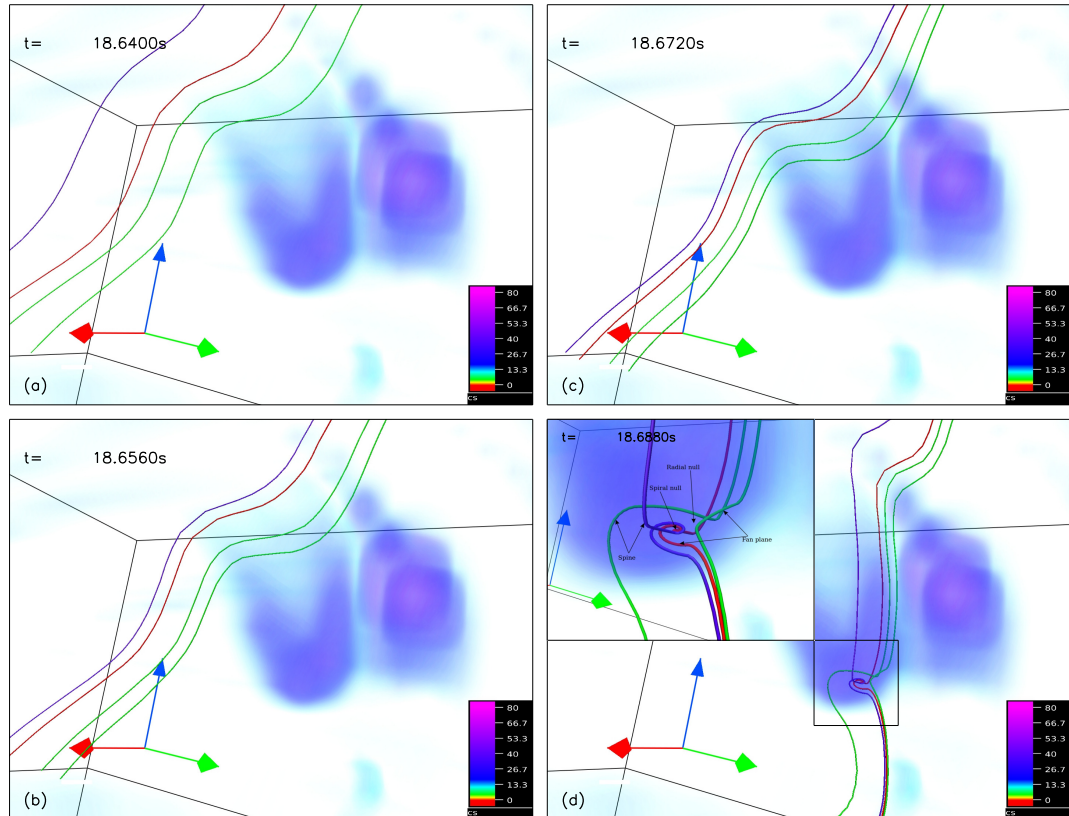


Figure 4.19: The selected field lines (one blue, one red, and two green colors) are plotted and advected with plasma flow to illustrate the magnetic reconnection in spontaneous null generation. The field lines are moving with the plasma velocity (panels (a)-(c)). Later, across panels (c) and (d), one of the two green field lines is changes its connectivity and traverses through the left of the red and blue field lines. Such change in connectivity is through magnetic reconnection. To illustrate the developed structure clearly, the region marked by a rectangular box has been zoomed in and shown in the inset of panel (d), in which the spine and fan plane of radial and spiral null are marked by arrows.

To establish the reconnection, in Figure 4.19, selected field lines (one blue, one red, and two in green color) are plotted and advected with plasma flow. Across panels (c) and (d), one of two green field lines changes its connectivity and traverses through the left of the red and blue field lines. Earlier, they were

traversing through the right of blue and red field lines. Such change in connectivity is through magnetic reconnection. The region marked by a rectangular box has been zoomed in and shown in the inset of the panel (d) to identify the topological features, such as the spine and fan plane of radial and spiral null, which are marked by arrows.

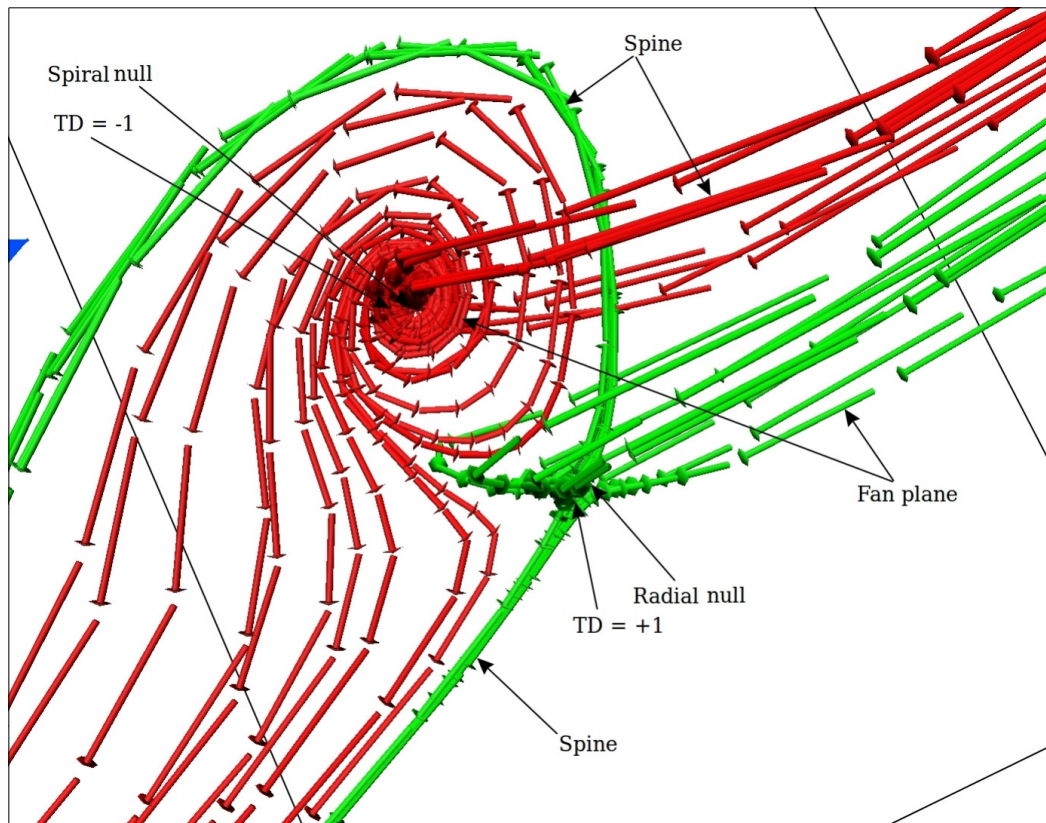


Figure 4.20: Figure illustrates the details of a spontaneously generated null pair, which also consists of a radial and spiral null. The field lines are drawn near the radial (in green) and that of the spiral null (in red). The spine and fan plane of both nulls are marked in the figure. The direction of fan field lines of radial null is towards the null point and that of the spine field lines is directed away from the null point making topological degree +1 whereas the spine field lines of spiral null are directed towards the null point and directed away from the null point in the fan plane resulting the topological degree -1 . The net topological degree of this pair is zero and the conservation of net topological is self-explanatory.

The selected pair also consists of a spiral null (in green) and a spiral null (in red), the fan plane field lines of the spiral null are directed towards the null, making topological degree: +1 and the field lines in the fan plane of the spiral null are

directed away from the null constituting topological degree -1 , shown in Figure 4.20. The net topological degree of the system is yet again constant and has the value -1 . The increase in separation in the span $t \in \{18.688, 19.2\}$ s, can be confirmed by Figure 4.21. Later, the separation between the nulls decreases until the nulls annihilated at $t = 20.32$ s. The decrease in separation can also be confirmed by Figure 4.21.

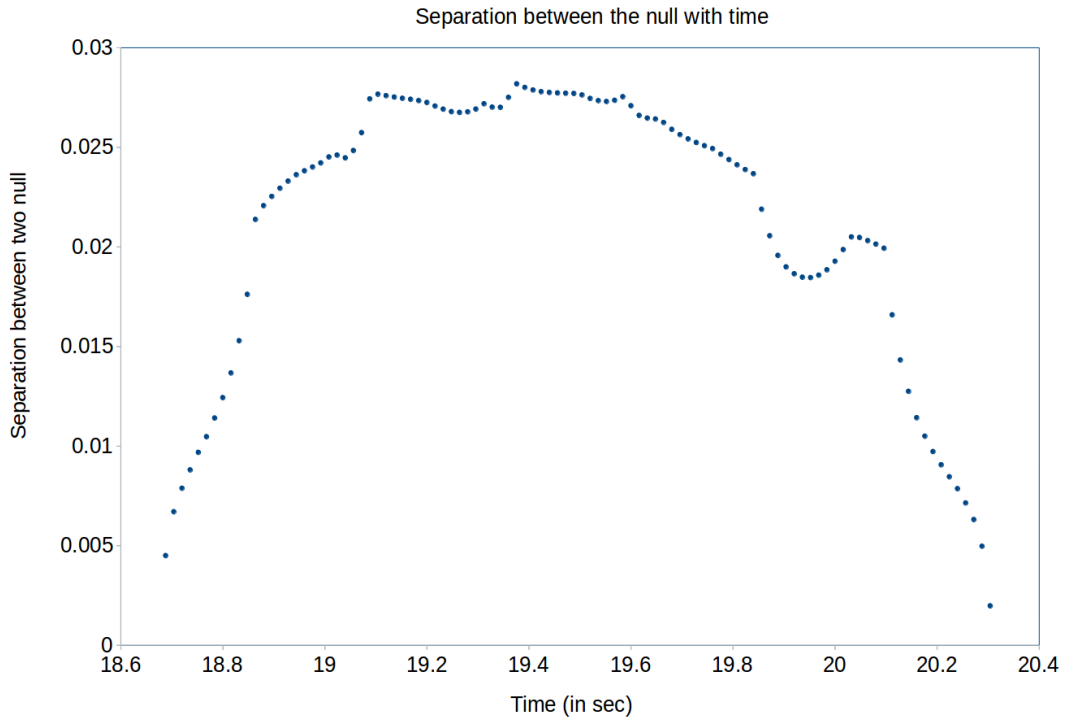


Figure 4.21: This plot shows the variation in separation with time between nulls of a spontaneously generated pair. The vertical axis represents the separation between the two nulls, and the horizontal axis represents the time (in seconds). The nulls are being generated around $t \approx 18.688$ s with a separation. The separation initially increases, followed by a decrease, ultimately leading to the annihilation around $t \approx 20.35$ s. The spontaneous null pair shows a similar behavior as seen in the case of primary null (see Fig.. 4.15).

The sequence of field line evolution leading to the annihilation is shown in Figure 4.22 (panels (a)-(f)). The decrease in separation between the spiral null and radial null is due to a reduction in the twist of the spiral null. To identify the physical process behind this phenomenon, field lines are traced (panels (a) to (b) of Figure 4.22) in time. The current density is plotted along with field lines. The red field lines constitute the spine and fan plane of the spiral null.

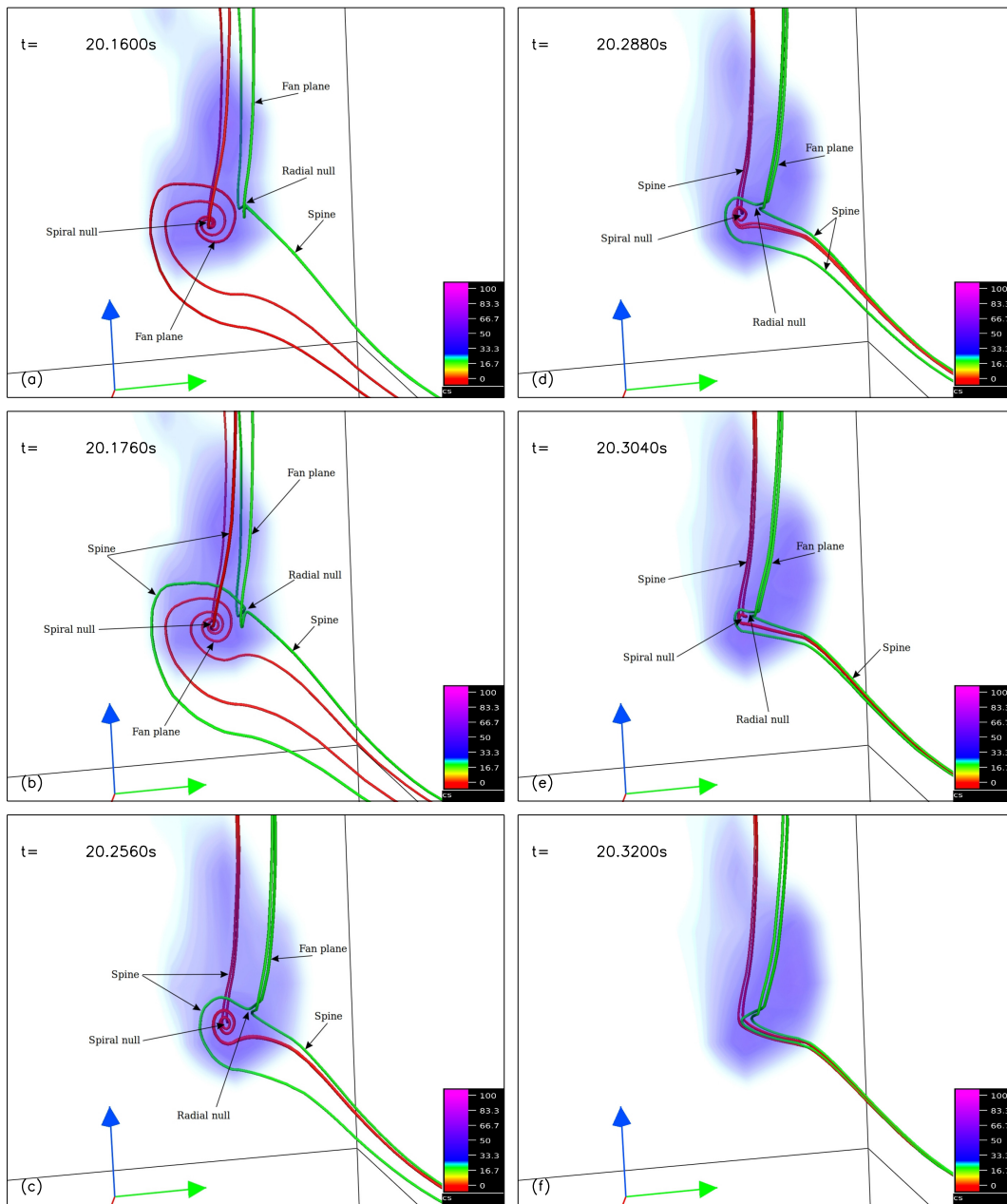


Figure 4.22: The snapshots of magnetic field lines illustrate the annihilation of spontaneously generated null pairs. To identify the physical process behind this phenomenon, field lines are traced (panels (a) to (b)) in time. The current density near the nulls is shown using DVR of $|\mathbf{J}|/|\mathbf{B}|$. In panel (a), the red field lines constitute the spine and fan plane of the spiral null, and the two green field lines constitute the lower spine of the radial null traverses through the right side of the spiral null. One of the two green field lines changes its connectivity, belongs to the upper spine of the radial null, and traverse the left of the spiral nulls (panel (b)). Such changes in connectivity are a telltale sign of magnetic reconnection. The twist of the spiral null decreases with time, and consequently, nulls come towards each other. This process continues until the nulls annihilate. Panels (c)-(f) illustrate the null annihilation in which nulls are traced in time, and the neighboring field lines are drawn near them. The nulls get annihilated at $t \approx 20.320$ s in pair as expected from the conservation of the topological degree (panel (f)).

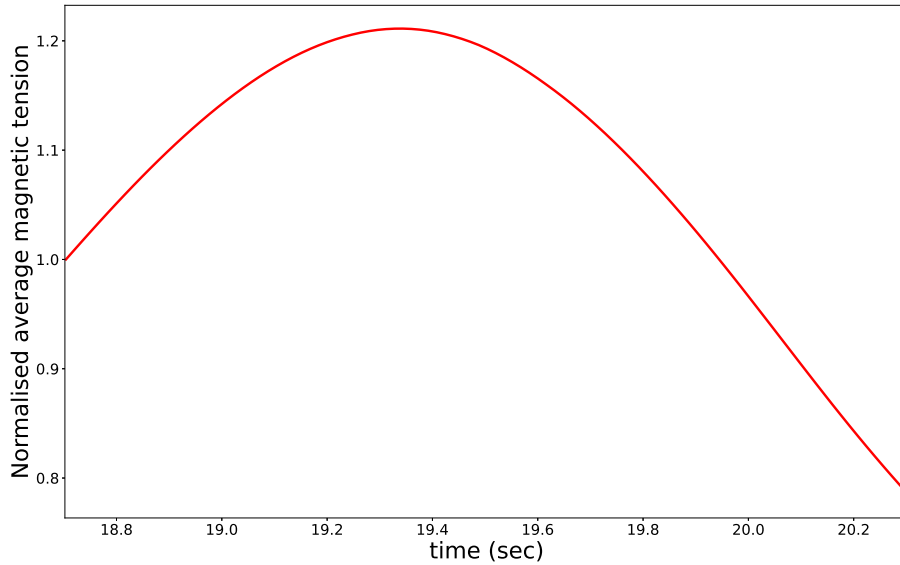


Figure 4.23: The plot shows the variation in average magnetic tension spanning the time $t \in \{18.688, 20.304\}$ s and normalized to its corresponding initial value at $t = 18.688$ s. The average is over a subvolume of physical extent $\{(-0.047\pi, 0.016\pi); (0.396\pi, 0.555\pi); (0.396\pi, 0.429\pi)\}$ in x , y and z directions constituting the spontaneously generated null pair. The vertical axis represents the normalized average magnetic tension, and the horizontal axis represents the time (in seconds). The increase and decrease of magnetic tension is visibly compatible with the corresponding change in inter-null separation of spontaneously generated pair.

The two green field lines constituting the lower spine of the radial null traverse through the right side of the spiral null, viz. panel (a). In panel (b), one of the two green field lines changes its connectivity. It belongs to the upper spine of the radial null and is located at the left of the spiral nulls. Such changes in connectivity are a telltale sign of magnetic reconnection. The panels (c)-(f) trace the null pair along with neighboring field lines. The untwisting of field lines ultimately destroys the spiral null—simultaneously annihilating the null pair as expected from the conservation of the topological degree (panel (f) of Figure 4.22). Similarly, the spontaneously generated nulls are also annihilated through magnetic reconnection (not shown). Figure 4.23 plots the modulus of magnetic tension with time in the range $t \in \{18.688, 20.304\}$ s, averaged over a subvolume of physical extent $\{(-0.047\pi, 0.016\pi); (0.396\pi, 0.555\pi); (0.396\pi, 0.429\pi)\}$ in x ,

y and z directions. The increase and decrease of magnetic tension are visibly compatible with the corresponding change in inter-null separation and in support of the scenario proposed above.

Comparing our results to previous studies of 3D null creation and annihilation, we emphasize (as discussed above) that the formation process of the primary null pairs is away from the central null and different from that presented by [Wyper & Pontin \(2014\)](#): in that study the first additional nulls to be created formed by a pitchfork bifurcation of the original null (within the current sheet) and hypothesize that it is because of the outflow generated from reconnection in the central current sheet and imposed flow. All such nulls are created in a “symmetry plane” in both cases. Following this, we found the spontaneous formation of nulls outside of this symmetry plane. This is consistent with the results of [Wyper & Pontin \(2014\)](#), who described the formation of additional nulls away from the symmetry plane in what they called “secondary bifurcations”. Such formation of additional nulls in the complex, evolving magnetic field close to other nulls is expected based on theoretical expectations [Albright \(1999\)](#) and here is explicitly demonstrated.

For completeness, the simulations are repeated in different resolutions: $32 \times 32 \times 32$, $96 \times 96 \times 96$ and $128 \times 128 \times 128$ over the same physical time span of $t \in \{0, 20.4\}$ s. Overall, the results are found to be similar, i.e., the spines bend toward the fan planes and develop elbow shape with the evolution. Further evolutions show the generation of the 3D nulls in pairs and subsequently moving away from each other, resulting in an increase in the separation. The separation between the two nulls decreased after the initial increase and continued until the nulls were annihilated in pairs. [Figure 4.24](#) depicts the null points evolution in 128^3 resolution as an example. Panel (a) depicts the initial magnetic field configuration (field lines are drawn in red) near a potential 3D null. Four sets of auxiliary field lines (in Blue, Pink, Cyan, and Green) are drawn to demonstrate the generation and annihilation of nulls with the evolution.

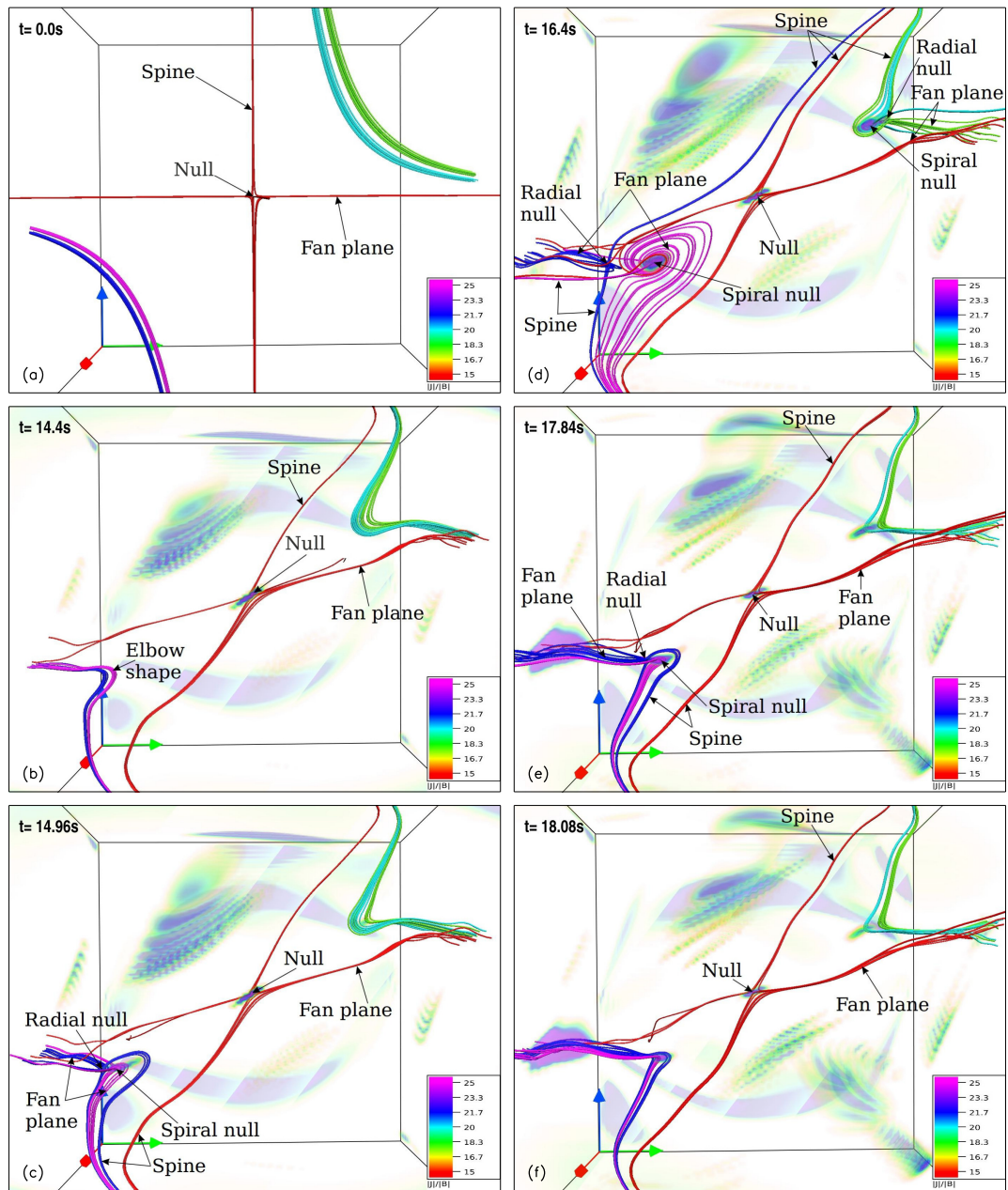


Figure 4.24: The figure illustrates the evolution of magnetic configuration enclosing a potential 3D null (panel (a)) in 128^3 resolution. Four sets of auxiliary field lines (in Blue, Pink, Cyan, and Green) are drawn to demonstrate the generation and annihilation of nulls. With the evolution, the auxiliary field lines develop an elbow shape (panel (b)), and subsequently, a pair of 3D nulls, which consists of radial and spiral 3D nulls, get generated (panel (c)) at $t = 14.96$ s. As they evolve, the separation between the nulls increases after their generation till around $t = 16.40$ s (panel (d)), and subsequently, starts decreasing (panel (e)) until their pairwise annihilation (panel (f)). The increase and decrease of magnetic tension is visibly compatible with the corresponding change in inter-null separation of spontaneously generated pair

The auxiliary field lines develop an elbow shape (panel (b)) with the evolution. Subsequently, a 3D null pair consisting of radial and spiral 3D nulls gets generated (panel (c)) at $t = 14.96$ s. Further, the separation between the nulls increases with time after their generation, till around $t = 16.40$ s (panel (d)), and starts decreasing (panel (e)) until they get annihilated in pair (panel (f)). Interestingly, a higher resolution run in an ILES delays magnetic reconnection. Correspondingly, the generation and annihilation of both primary and spontaneous nulls got slightly delayed (nulls were created at $t = 14.54$ s in 64^3 whereas they get created at around $t = 14.96$ s in 128^3 resolution), confirming further the role of magnetic reconnection in their genesis and destruction. Additionally, the topological degree is found to be conserved at every instance for all the simulations.

4.3 Summary

Implicit Large Eddy Simulations are carried out to explore the dynamics of 3D null generation and annihilation, along with the evolution of null pairs after their generation. The novelty of the work lies in documenting the creation of nulls away from the central null, which has been studied earlier. Further, spontaneously generated nulls have been identified in the simulation. The results are important since contemporary research indicates abundant 3D nulls in nature, particularly in the solar atmosphere. The extent of physical domain is $-\pi \leq x \leq \pi$, $-\pi \leq y \leq \pi$, $-\pi \leq z \leq \pi$ in Cartesian coordinates which morphed on a computational grid of $64 \times 64 \times 64$ resolution. In the simulation, a current-free 3D null has been deformed through a prescribed initial sinusoidal flow. The deformation of the spine pushes a set of auxiliary field lines to bend and form elbow shapes. In the process, the magnetic energy is increased. The kinetic energy increases initially but forms a peak as the flow gets arrested by viscosity. The magnetic field lines are seen to slip over the fan plane, and further deformation generates current sheets near the central null. Consequently, magnetic reconnections onset—flattening out the magnetic energy curve. The kinetic energy gets increased, typical to magnetic reconnection. Further evolution from

elbow shape structure generates two null pairs through reconnection of auxiliary field lines while preserving the net topological degree. Notably, the preservation of net topological degree is a stringent constraint that must be satisfied by the generation and annihilation of 3D nulls. The model preserves this constraint throughout the simulation, adding credibility to the computation. Each pair of generated nulls consists of a radial null and a spiral null. During the evolution, the separation between the nulls increases, the increase being caused by an enhancement in the twist of the spiral null—generating more magnetic tension force. After reaching a maximal value, the separation decreases along with a decrease in twist. The decrease continues until the involved primary null pair annihilates, once again preserving the net topological degree. Astoundingly, the simulation documents the spontaneous creation and annihilation of null pairs. The pairs are found to consist of a radial null and a spiral null—as in the case of the primary nulls, conserving the total topological degree. Field line dynamics leading to the generation/annihilation of null pairs are analyzed extensively, and the creation/annihilation is found to be due to magnetic reconnections. The field line dynamics is similar to that of the primary null pairs, showing a decrease in separation of the constituent nulls after an initial increase. The decrease ultimately ends as the nulls annihilate. In the work presented in this chapter, a tailored flow has been considered to initiate magnetic reconnection, which can not be expected to present naturally in the solar active regions. It is then natural to study the possibility of spontaneous null generation/annihilation in a realistic system like the solar corona, which will be presented in the next chapter.

Chapter 5

Spontaneous generation and annihilation of 3D magnetic nulls in the solar atmosphere

5.1 Introduction

To achieve the objective, in this work, a novel approach is adopted by carrying out a data-based ILES for a flaring active region where the initial coronal magnetic field is computed by extrapolating photospheric vector magnetogram data. Additionally, solar active regions have complex magnetic topologies, suggesting that the 3D nulls have similar complexity. Understanding this process is crucial for insights into chromospheric and coronal heating. To explore the aim, a new approach is adopted by employing a data-based ILES MHD simulation for a flaring active region which hosted a C6.6 class flare on February 17, 2014. The active region is chosen based on its proximity to the solar disk center, ensuring minimal errors in the observed photospheric magnetic field, the constancy of the photospheric magnetic flux across the active region during the flare, allowing for a line-tied boundary condition to simplify simulations and the availability of contemporary multiwavelength observations. Using the Non-Force Field extrapolation technique, the initial coronal magnetic field is obtained by extrapolating photospheric vector magnetogram data. The resulting non-zero Lorentz force

drives the plasma, generating initial dynamics, and the simulation focuses on the part of the flare’s reconnection-dominated impulsive phase aligned with the objectives.

The theory of 3D nulls is well-established, Sect. 2.4 discusses this in detail, and the following properties are worth mentioning. Straightforward manipulation of the ideal induction equation for an incompressible fluid shows

$$\frac{d\mathbf{B}}{dt} = 0, \tag{5.1}$$

at the null point (Hornig & Schindler, 1996); the d/dt being the Lagrangian derivative. Consequently, a 3D null maintains identity during evolution, enabling its tracing in numerical simulations. Moreover, the net topological degree of a system consisting of a number, N_0 , of nulls is defined by Greene (1992) and Longcope (2005) as

$$D = \sum_{N_0} \text{Sign} (\det(\nabla\mathbf{B}|_{x_{N_0}})), \tag{5.2}$$

and remains conserved (Hornig & Schindler, 1996; Pontin & Priest, 2022) in any evolution. Any credible simulation targeted to explore generation or annihilation of nulls must satisfy this stringent conservation. Additionally, nulls that enter or exit the computational domain need to be accounted for as they may seemingly violate the conservation of topological degree.

The magnetic topology of 3D nulls can be put in perspective through a 3D generalization of a two-dimensional (2D) separatrix: the line in 2D that segregates magnetic field lines having separate connectivities. As could be expected, in 3D, the separatrix lines get replaced by surfaces – called separatrix surfaces, or just separatrices – separating sub-volumes having disjoint field line connectivities. To maintain different subvolumes connection-wise disjoint, the separatrices need to be magnetic flux surfaces with only tangential field lines. Consequently, if two such separatrices intersect, they intersect along a line having two magnetic nulls at the endpoints. This line is called a separator. The concept can be straightforwardly applied to magnetic structures in the solar corona. Traditionally, such field line topologies are often realized in the solar corona when a

parasitic polarity region emerges inside a larger opposite polarity region on the photosphere. In such a case, the topological structure of a 3D null point defines a dome-like separatrix, the fan, and two singular field lines, the spines, originating from the null point. With the onset of reconnection at the null, magnetic field lines are transferred across the separatrices from one magnetic domain to another (Pontin et al., 2013).

The organization of the chapter is as follows: Sect. 5.1.1 describes the extrapolation technique along with the rationale behind selecting the particular active region and Sect. 5.1.2 summarizes the governing magnetohydrodynamic (MHD) equations while briefly describing salient features of the numerical model. Sects. 5.1.3 and 5.2 are dedicated to numerical setup and simulation results respectively. Sect. 5.3 summarizes the findings.

5.1.1 Non-Force Free Field Extrapolation of NOAA AR 11977

The C6.6 class eruptive flare that occurred on February 17, 2014, emanating from active region NOAA AR11977 at heliographic coordinates $S13W05$, has been chosen for analyses for three key reasons: (a) its proximity to the solar disk center, which ensures minimal errors in the observed photospheric magnetic field, (b) the photospheric magnetic flux integrated across the active region remains approximately constant throughout the flare, allowing for the application of a line-tied boundary condition to simplify simulations, (c) contemporary observations in multiwavelengths (Mitra & Joshi, 2021; Ibrahim et al., 2022). In Fig. 5.1(a), the Geostationary Operational Environmental Satellite (GOES) soft X-ray flux in the $1 - 8 \text{ \AA}$ channel is depicted over the duration of the flare. The plot illustrates a gradual increase in intensity starting around 02 : 45 UT (marked by a dashed vertical line), with the peak occurring at 03 : 04 UT (dash-dot vertical line). Magnetic field line dynamics in the time interval from 02:48 to 02:56 UT, as indicated by the two solid blue vertical lines during the flare's ascending phase, is numerically explored here. Notably, panel (b) depicts the

evolution of the horizontally averaged positive (solid line) and negative (dashed line) photospheric magnetic flux obtained from the *hmi.M45* series of the Helioseismic Magnetic Imager (SDO/HMI), as described by Schou et al. (2012) and Scherrer et al. (2012). The flux plot covers approximately 13 minutes, commencing around 02 : 44 : 41 UT. The magnetic flux remains relatively stable during the flare, with both positive and negative fluxes exhibiting relative changes well within 1 %.

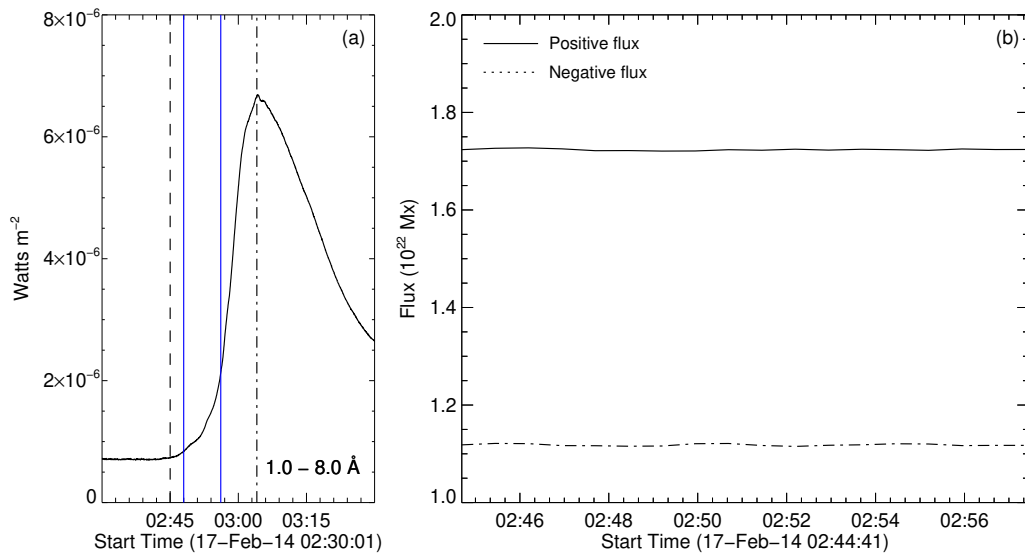


Figure 5.1: Panel (a) depicts the Geostationary Operational Environmental Satellite (GOES) soft X-ray flux over the duration of the flare in the 1 – 8 Å channel. This graph illustrates a gradual increase in intensity starting around 02 : 45 UT (marked by the dashed vertical line), with the peak occurring at 03 : 04 UT (dash-dot vertical line). Our simulations cover the time range from 02:48 to 02:56 UT, as marked by two blue vertical solid lines during the rising phase of the flare. The photospheric flux variation for approximately 13 minutes, starting from 02 : 44 : 41 UT, is shown in panel (b), where the solid line represents positive flux and the dashed line represents negative flux.

The MHD simulation carried out here uses an extrapolated magnetic field from a vector magnetogram as an initial magnetic field. For extrapolation, the Active Region AR11977 at 02 : 48 : 00 UT on February 17, 2014 is selected based on its prior analysis in terms of identifying the primary reconnection site (Agarwal et al., 2022). The corresponding magnetogram is obtained from the Helioseismic Magnetic Imager (HMI; Schou et al. (2012)) on board the Solar Dynamic Observatory (SDO) and is taken from the ‘hmi.sharpcea720s’ data se-

ries. This data series provides the magnetic field on a Cartesian grid, which is initially remapped onto a Lambert cylindrical equal-area (CEA) projection and then transformed into heliographic coordinates (Bobra et al., 2014). The extrapolation utilizes a non-force-free field (NFFF) extrapolation model for the magnetic field, \mathbf{B} , obtained by minimization of total energy dissipation rate, described in Bhattacharyya et al. (2007). The NFFF \mathbf{B} obeys a double-curl Beltrami equation for which a solution can be attempted by expressing it as

$$\mathbf{B} = \mathbf{B}_1 + \mathbf{B}_2 + \mathbf{B}_3; \quad \nabla \times \mathbf{B}_i = \alpha_i \mathbf{B}_i, \quad (5.3)$$

where $i = 1, 2, 3$ (Hu & Dasgupta, 2008; Hu et al., 2008). Here, each sub-field \mathbf{B}_i represents a linear force-free field (LFFF) characterized by specific constants α_i . Without a loss of generality, a selection $\alpha_1 \neq \alpha_3$ and $\alpha_2 = 0$ can be made, rendering \mathbf{B}_2 a potential field. Subsequently, an iterative approach is employed to determine the optimal pair $\alpha = \alpha_1, \alpha_3$, which finds the pair by minimizing the average deviation between the observed (\mathbf{B}_t) and the calculated (\mathbf{b}_t) transverse field on the photospheric boundary. Effectively, the metric

$$E_n = \left(\sum_{i=1}^M |\mathbf{B}_{t,i} - \mathbf{b}_{t,i}| \times |\mathbf{B}_{t,i}| \right) / \left(\sum_{i=1}^M |\mathbf{B}_{t,i}|^2 \right), \quad (5.4)$$

where $M = N^2$ represents the total number of grid points on the transverse plane is iteratively minimized (Prasad et al., 2018). To achieve an optimal value of E_n , a corrector potential field to \mathbf{B}_2 is further derived from the difference transverse field, i.e., $\mathbf{B}_t - \mathbf{b}_t$, and added to the previous \mathbf{B}_2 in anticipation of an improved match between the transverse fields, as measured by the E_n . The grid points are weighted with respect to the strength of the observed transverse field to minimize the contribution from the weaker fields (see Hu & Dasgupta (2008); Hu et al. (2010), for further details).

To optimize computational cost while preserving the original magnetic morphology, the magnetogram having dimension 896×512 pixels is re-scaled to the dimension 448×256 pixels in x and y -directions, respectively. The NFFF ex-

trapolation is carried out on the re-scaled computational grid, which corresponds to physical dimensions of $\sim 324.8\text{Mm} \times 185.6\text{Mm} \times 139.2\text{Mm}$ in the x , y , and z directions, respectively, and variation of E_n with iteration number is shown in the Figure 5.2. As expected, the overall field line morphology is found to be identical to the one depicted in Agarwal et al. (2022). Notably, the re-scaling reduces the initial number of nulls. Nevertheless, such reductions are not expected to affect the dynamics of null pair generation/annihilation through magnetic reconnection—which is a dissipative process and is likely to be independent of the initial condition, as suggested in Agarwal et al. (2022).

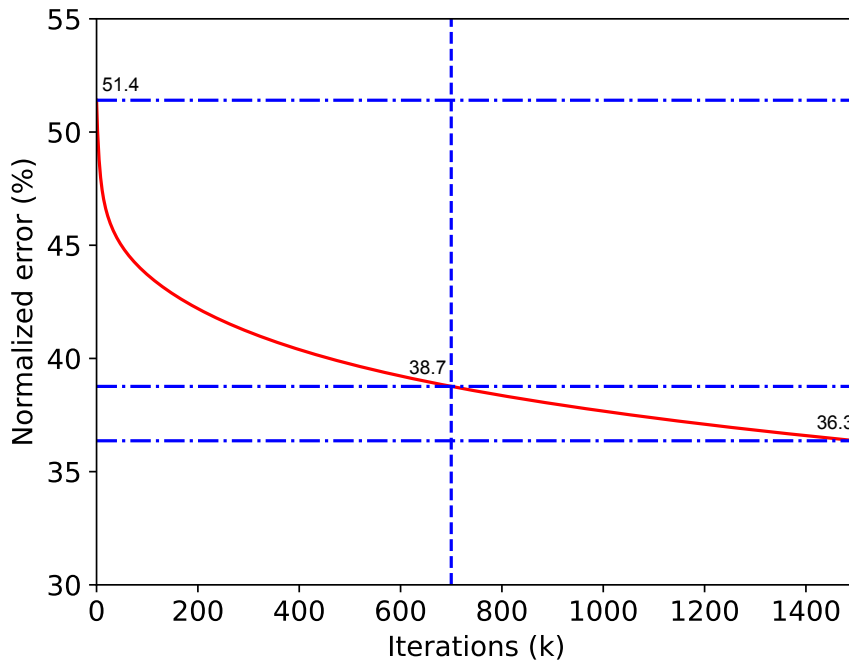


Figure 5.2: The plot illustrates the variation in minimized deviation (E_n) with the number of iterations (k) for Non-Force Free Field extrapolation. This deviation decreases monotonically and saturates approximately at $\approx 36.3\%$ for 1500 iterations.

Panel (a) of Figure 5.3 illustrates direct volume rendering (DVR) of the Lorentz force amplitude, showing it to be dominant at lower heights. To further corroborate, the logarithmic variation of horizontally averaged Lorentz force with pixel height z is shown in panel (b) of Figure 5.3, showing a decreasing trend. Effectively, the NFFF model treats the corona as reasonably force-free, with

non-zero magnetic forces being localized at the photosphere/lower heights, in agreement with the general expectation of a force-free corona (Liu et al., 2020; Yalim et al., 2020).

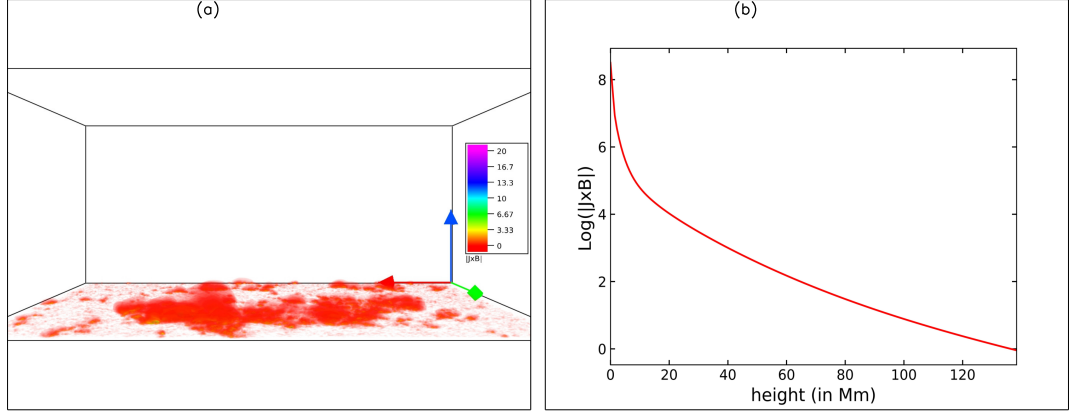


Figure 5.3: Panel (a) of the Figure depicts the direct volume rendering (DVR) of the magnitude of Lorentz force, showing the presence of the Lorentz force at lower heights. To further corroborate this observation, the logarithmic variation in the horizontally averaged strength of Lorentz force with height (z) is shown in panel (b). As expected, the logarithmic value of horizontally averaged Lorentz force decreases with height. Notably, the Lorentz force density is non-zero near the photosphere and nearly vanishes at coronal heights, similar to the typical description of the solar corona.

5.1.2 Governing Equations and Numerical Model

The simulations are carried out using the magnetohydrodynamic numerical model EULAG-MHD (Smolarkiewicz & Charbonneau, 2013), assuming the plasma to be thermodynamically inactive, incompressible, and perfectly electrically conducting. The dimensionless governing equations are

$$\frac{\partial \mathbf{v}}{\partial t} + (\mathbf{v} \cdot \nabla) \mathbf{v} = -\nabla p + (\nabla \times \mathbf{B}) \times \mathbf{B} + \frac{1}{R_F^A} \nabla^2 \mathbf{v}, \quad (5.5)$$

$$\nabla \cdot \mathbf{v} = 0, \quad (5.6)$$

$$\frac{\partial \mathbf{B}}{\partial t} = \nabla \times (\mathbf{v} \times \mathbf{B}), \quad (5.7)$$

$$\nabla \cdot \mathbf{B} = 0, \quad (5.8)$$

achieved with

$$\mathbf{B} \rightarrow \frac{\mathbf{B}}{B_0}, \mathbf{v} \rightarrow \frac{\mathbf{v}}{V_A}, L \rightarrow \frac{L}{L_0}, t \rightarrow \frac{t}{\tau_a}, p \rightarrow \frac{p}{\rho_0 V_A^2}, \quad (5.9)$$

where $R_F^A = \frac{V_A L}{\nu}$ is an effective fluid Reynolds number with V_A as the Alfvén speed and ν as the kinematic viscosity. The B_0 and L_0 are characteristic values of the system under consideration whereas, ρ_0 represents the constant mass density. Although not strictly applicable in the solar corona, the incompressibility is invoked in other works also (Dahlburg et al., 1991; Aulanier et al., 2005). The details about the employed numerical model can be found in Sect. 3.4.2.

5.1.3 Numerical Setup

The active-region cutout is mapped on a grid having $448 \times 256 \times 192$ pixels resolved on a computational grid of $x \in \{-0.875, 0.875\}$, $y \in \{-0.5, 0.5\}$, and $z \in \{-0.375, 0.375\}$ in a Cartesian coordinate system, spanning a physical domain of $324.8\text{Mm} \times 185.6\text{Mm} \times 139.2\text{Mm}$ in x , y and z directions. The dimensionless spatial step sizes are $\Delta x = \Delta y = \Delta z \approx 0.0039$ (≈ 725 km) and the dimensionless time step is $\Delta t = 2 \times 10^{-3}$ (≈ 1.936 s). The initial state is motionless ($\mathbf{v} = 0$), and the initial magnetic field is provided from the NFFF extrapolation. The non-zero Lorentz force associated with the extrapolated field pushes the plasma to generate dynamics. The mass density is set to $\rho_0 = 1$. The effective fluid Reynolds number is set to 5000, which is 5 times smaller than the coronal value of ≈ 25000 (calculated using kinematic viscosity $\nu = 4 \times 10^9$ m² s⁻¹ in solar corona, p. 791 of Aschwanden (2005)). Without any loss in generality, the reduced R_F^A can be realized as a reduction in computed Alfvén speed, $V_A|_{\text{computed}} \approx 0.14 \times V_A|_{\text{corona}}$. The Alfvén speeds are estimated with characteristic scales $L_{\text{computational}} = 139.2\text{Mm}$ for the computational domain and $L_{\text{corona}} = 100\text{Mm}$ for typical corona. The results presented herein pertain to a run for $250\Delta t$, which, with $\tau_A \approx 9.68 \times 10^2$ s, correlates to an observation time of ≈ 8 minutes. The interval is marked by the two vertical blue lines of goes X-ray flux curve during ascending phase of the flare (Fig. 5.1). The reduced R_F^A slows down the dynamics

and does not affect the reconnection mechanism or its consequence, reducing the computational costs and making data-based simulations computationally less costly—realized by [Jiang et al. \(2016\)](#). Nevertheless, such reduction in Alfvén speed will directly affect the wave dynamics, which is overlooked in this work in favor of the reconnection dynamics.

5.2 Results

A modified trilinear null detection technique is used to detect magnetic nulls which, now additionally provides the topological degree (TD) of the nulls as either +1 or -1 based on the sign of the determinant of $\nabla B|_{\text{null}}$. In the simulation, the overall number of nulls is found to decrease with time (see panel (a) of [Figure 5.4](#)). At the beginning ($t = 0$ s), around 4000 nulls are found to be primarily located in the lower solar atmosphere, as depicted in panels (b) and (c) of [Figure 5.4](#), with some also found in the higher solar atmosphere. Focus is set on the generation/annihilation of three types of null pairs, selected a posteriori; based on their traceability, diversity, and tractability of corresponding field lines that reconnect. Throughout the simulation, many such generation and annihilation processes of each type occur, as the total number of nulls varies, as shown in [Figure 5.4\(a\)](#). In the remainder of this section, we describe one characteristic example of each of the three types. The three pairs of nulls are positioned away from the computational boundary and, as per their topology and dynamics, are labeled as (i) radial-radial-pair, (ii) radial-spiral-pair-1, and (iii) radial-spiral-pair-2; listed sequentially as per their generations. The dynamics of field lines leading to the generation/annihilation of each pair are discussed below.

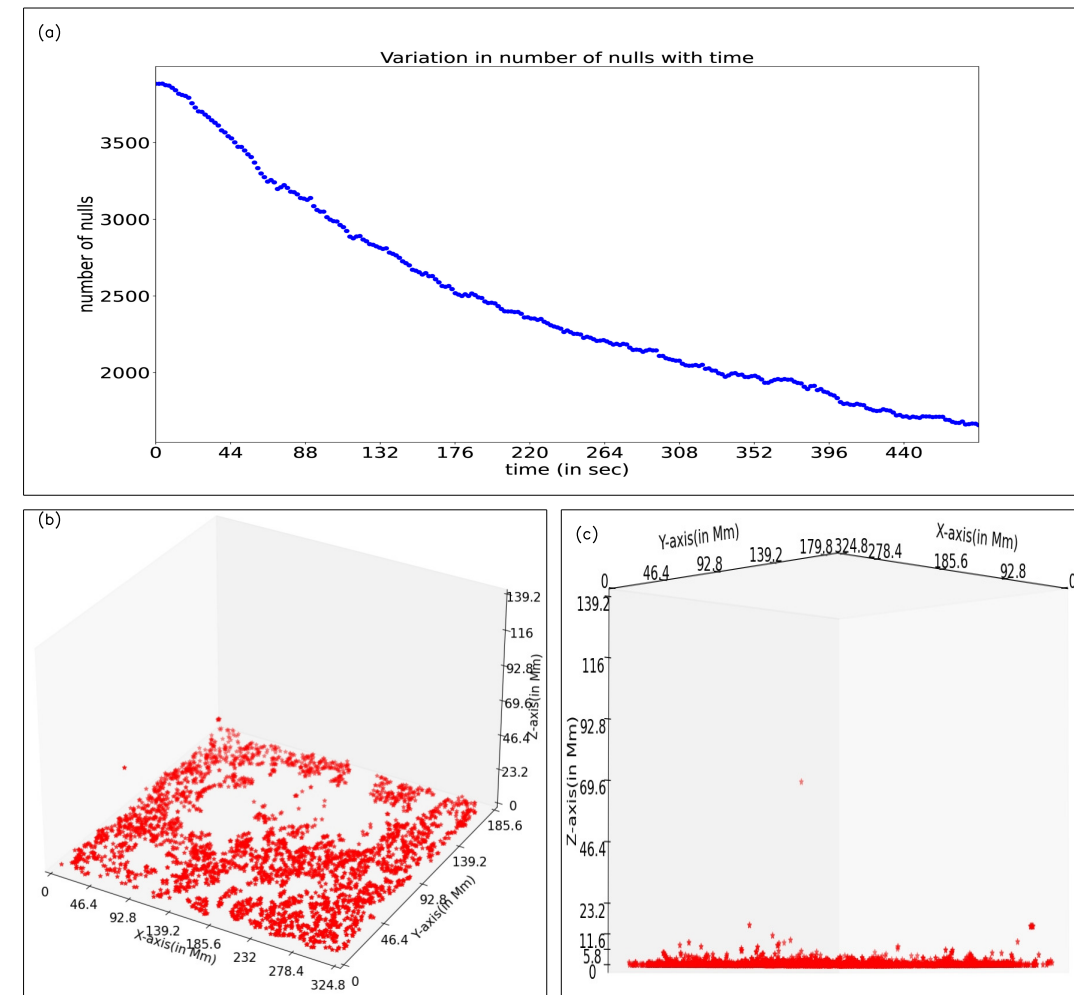


Figure 5.4: The panel (a) illustrates the overall evolution of the number of nulls over time. The vertical axis represents the number of nulls, while the horizontal axis represents time (in seconds). As time progresses, the overall number of nulls decreases. At $t = 0$ s, there are approximately 4000 nulls are present, which are distributed as depicted in panels (b) and (c) (panel (c) is from a different angle to show the distribution). The size of the box is 324.8Mm, 185.6Mm and 139.2Mm in x-, y- and z-direction respectively. The nulls are primarily located in the lower solar atmosphere, with some also found in the higher solar atmosphere (refer to panel (c)).

5.2.1 Radial-radial-pair

The use of the trilinear null detection technique provides coordinates of each null along with their TD at each time step. The nulls' coordinates at two consecutive time steps are compared to segregate the new nulls from existing nulls at the previous time step.

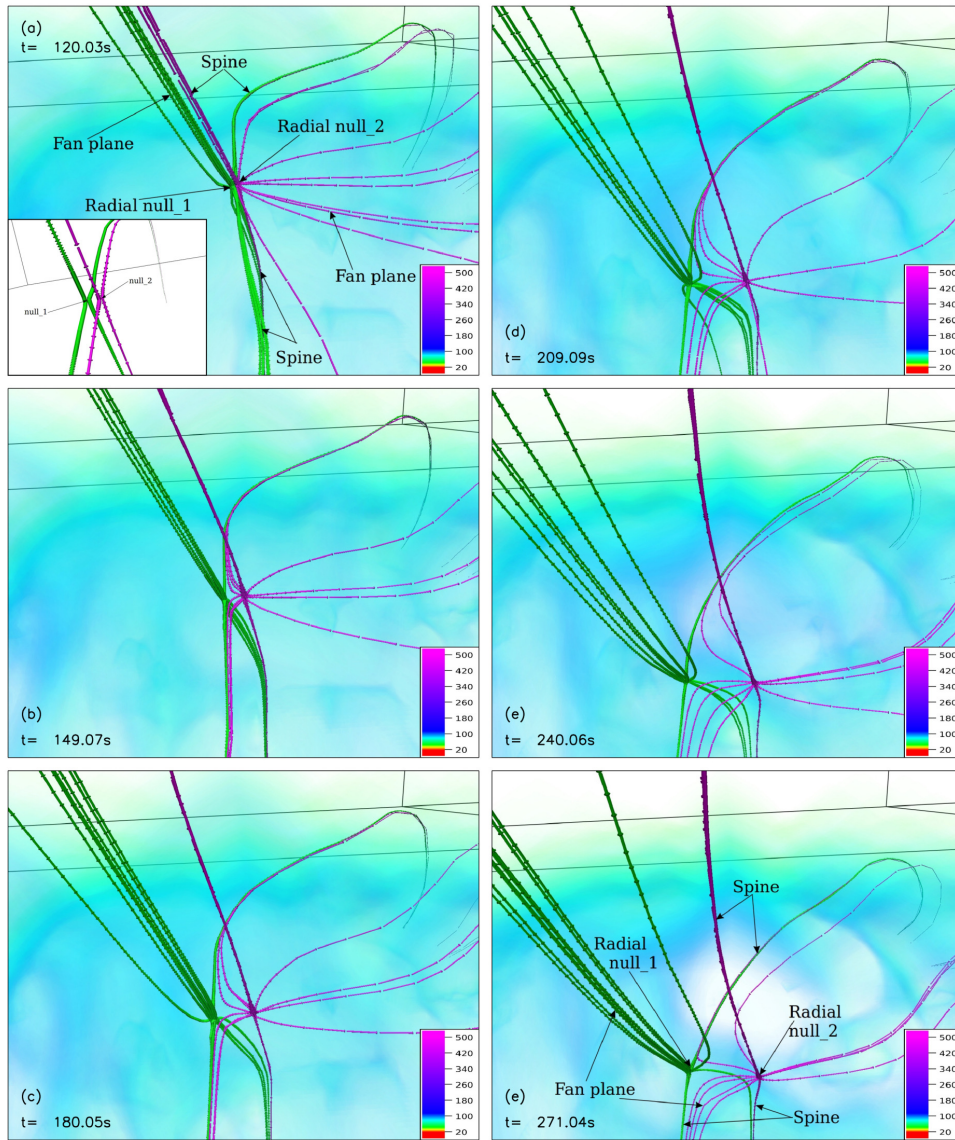


Figure 5.5: The figure illustrates the evolution of radial nulls over time. Nulls are traced in time, and field lines are drawn at their locations. The variation in magnitude of current intensity (identified by the Direct Volume Render (DVR) of $|\mathbf{J}|/|\mathbf{B}|$) is shown by the color bar. At $t = 120.032\text{s}$ (panel (a)), nulls are spontaneously created in pairs, and the trilinear null detection technique detects them simultaneously. The generated null pair consists of two radial nulls and are shown as radial null_1 and radial null_2 in the figure. It can be verified by collapsing them into 2D, where they appear to be akin to X-type nulls (shown in the inset of panel (a)). As the evolution continues, both radial nulls move away from each other after their generation (see panels (a)-(f)).

Applying the procedure, a pair of nulls (marked as radial null_1 and null_2) having coordinates $\{(116.045, 46.893, 5.632), (116.047, 46.893, 5.633)\}$ Mm at $t = 120.03\text{ s}$ are selected for analyses; depicted in Figure 5.5, Panel (a). The eigenvalues of

the Jacobian matrix $\nabla\mathbf{B}$ at each null are calculated at $t = 120.03\text{s}$. The eigenvalues of each null are found to be purely real, implying that the nulls are radial nulls. The field lines are plotted near locations of the nulls for further visualization. The pair consists of radial nulls as can be verified by collapsing them into 2D where they appear to be akin to X-type nulls (shown in the inset of panel (a))—a property mentioned in [Parnell et al. \(1996\)](#); [Liu et al. \(2018\)](#); [Liu et al. \(2019\)](#). The nulls are further traced in time, indicating they are getting spatially separated with time. The cause of their separation is checked and found that it is because of Lorentz force (not shown). To understand the field line dynamics responsible for the generation of the nulls, two selected green and pink field lines at $t = 118.09\text{s}$ are shown in panel (a) of [Fig. 5.6](#). The initial points of these green and pink field lines are located away from the reconnection region and in the ideal plasma region, allowing identification of reconnection ([Schindler et al., 1988](#); [Priest et al., 2003](#); [Knizhnik & Cabral-Pelletier, 2022](#)), specifically at coordinates $(116.07, 47.05, 5.58)\text{Mm}$ for the green lines and $(116.45, 46.80, 5.40)\text{Mm}$ for the pink lines. The green field lines are connected from regions b to a and regions d to e, whereas pink field lines are connected from region c to region d (panel (a)). These field lines are traced over time and advected with plasma flow. During their evolution, one of the two green field lines changes its connectivity from regions b to a and connects regions b to d. Similarly, one out of the two pink field lines also changed its connectivity from regions c to d and gets connected from regions c to a. Such changes in the connectivity of field lines equate with the basal definition of magnetic reconnection ([Axford, 1984](#)). Simultaneous to the reconnection, the field line topology displays the formation of the radial-radial null pair (marked by arrows in panel (b)), which is further corroborated by the trilinear method. Notably, such radial-radial null pair generation was absent in the earlier work by [Maurya et al. \(2023\)](#), hereafter referred to as the paper-I. For details of topology, in [Fig. 5.7](#), we present magnetic field lines at the near neighborhood of the nulls. In the figure, the fan field lines (in green) of radial null_1 are directed toward the null and are directed away from the null along the spine of the null, making its topological degree +1.

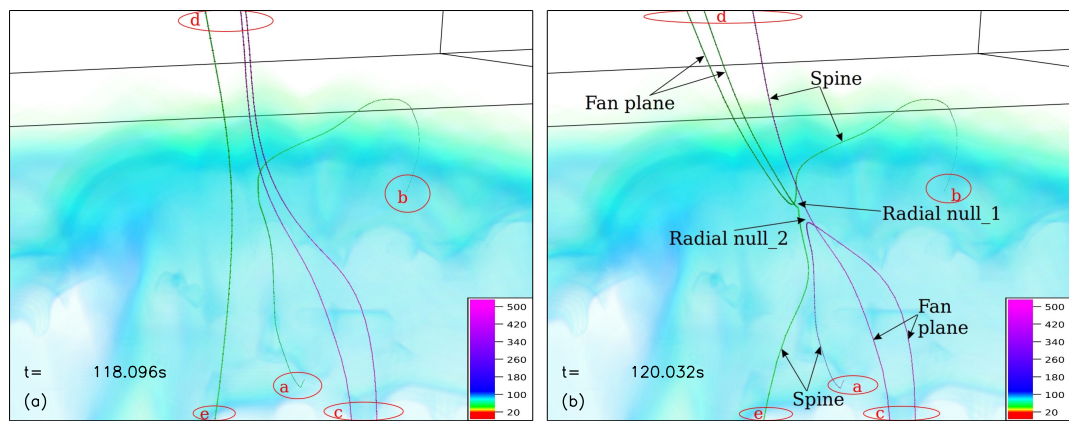


Figure 5.6: Magnetic field lines are traced in time and advected with plasma flow. The evolution shows the creation of nulls in pairs, consisting of two radial nulls marked as radial null_1 and radial null_2. The enhanced current intensity is overlaid using the DVR tool in VAPOR. At $t = 118.096\text{s}$, two green field lines connect from regions a to b and from e to d, while two pink field lines connect from regions c to d (panel (a)). During the evolution, one pink field line changes its connectivity from regions c to d and reconnects to regions c to a, and one green field line also changes its connectivity from regions b to a to regions b to d (panel (b)). Simultaneously, two radial nulls are created and marked by arrows in panel (b). Such changes in the connectivity of field lines represent magnetic reconnection.

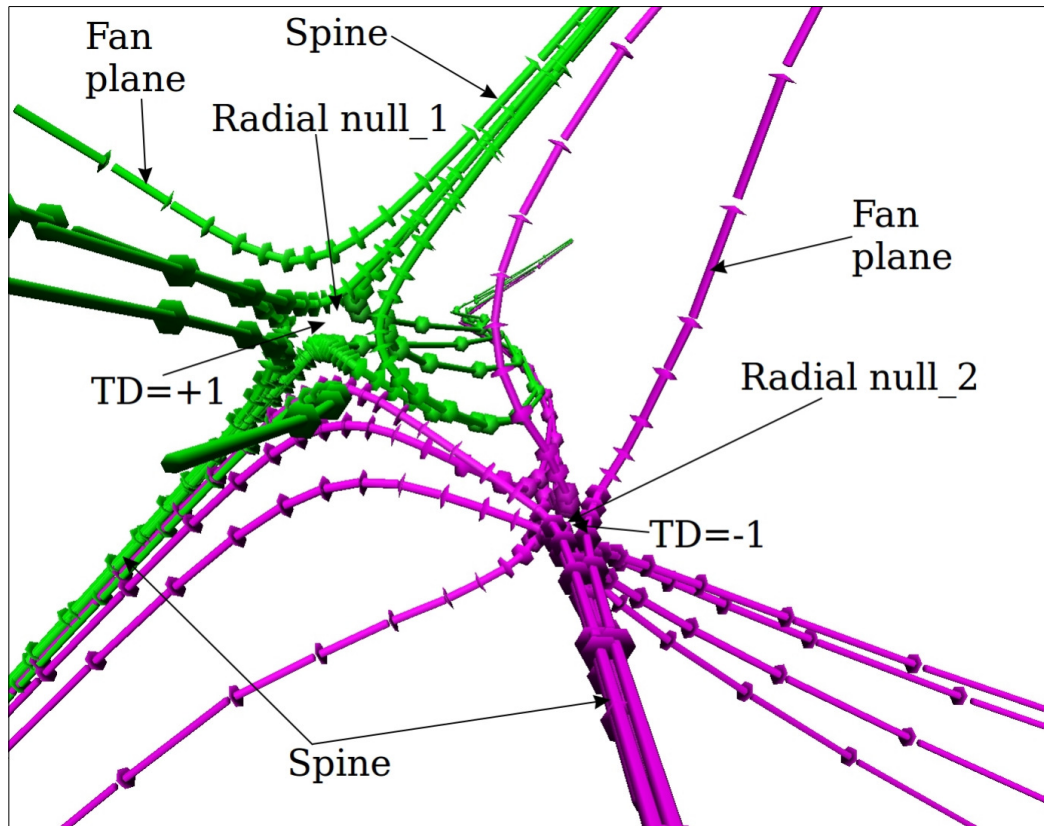


Figure 5.7: The figure details the topological features of spontaneously generated radial nulls at time $t = 193.6\text{s}$. Two radial nulls are generated simultaneously and are marked by arrow as radial null_1 and radial null_2. Green and pink field lines are drawn near the radial null_1 and radial null_2, respectively. The fan field lines (in green) of radial null_1 are directed toward the null, making topological degree +1, while the fan field lines (in pink) of radial null_2 are directed away from the null, making topological degree -1 .

The fan field lines (in pink) of radial null_2 are directed away from the null resulting in its topological degree being -1 .

The data-based simulation presents a unique opportunity to check if these spontaneously generated nulls also contribute to footpoint brightening or not, another novelty of this paper. A positive outcome will strengthen the idea that such null point generation and subsequent reconnection can contribute to chromospheric/coronal heating, a concept floated by Cheng et al. (2023). The reconnections at the spontaneously developed null points are expected to generate heat and accelerate particles that travel along the field lines constituting the fan and spine, resulting in footpoint brightening as they enter denser plasma region

(Wang & Liu, 2012). Relevantly, Figure 5.8 depicts such footpoint brightening in the AIA 1600 Å channel because of slip reconnection. For demonstration, we select a group of field lines constituting the spine and fan of null.2 (indicated as ‘null’). Notably, the fan has the typical dome-shaped structure identified with 3D null in various observations (Mason et al., 2019, 2021). Blue arrows point in the direction of the local plasma flow. In the figure, the red field line, marked by a white arrow at $t = 197.47$ s, and initially anchored at point ‘a’ (panel (a)), changes its connectivity to point ‘b’ (panel (b)) with evolution. With further evolution, the red line changes its connectivity from point ‘b’ and reconnects to point ‘c’ and subsequently to point ‘d’ (refer to panels (c) and (d)). Importantly, the local plasma flow direction differs from the field line motion—a trademark of all magnetic reconnection in 3D (Priest et al., 2003; Aulanier et al., 2006, 2007). The nulls are further traced in time spanning $t \in \{272.97, 342.67\}$ s, and field lines are drawn at nulls (Fig. 5.9). With the evolution, these spontaneously generated radial nulls approach each other and ultimately annihilate at $t = 342.67$ s, as nulls are absent in panel (f). These nulls are also not found in the trilinear method and verified their annihilation. To understand the field line dynamics leading to the pair annihilation, five selected green and pink field lines are drawn in the ideal region, with initial points at the locations (116.14, 47.56, 4.37)Mm and (116.49, 47.55, 4.34)Mm. The selected field lines are traced over time spanning $t \in \{309.76, 315.57\}$ s as they are advected with plasma flow (Figure 5.10). At $t = 309.76$ s, green field lines are part of the fan plane and spine of radial null.1, anchored to the region a and connected from regions d to a and regions b to a, whereas pink field lines are part of the fan plane and spine of radial null.2, anchored in region b and connected from regions c to b and regions b to a (panel (a)). With the evolution, one green field line has changed its connectivity from regions d to a to the regions d to c, and two pink field lines have changed their connectivity from regions c to b to regions c to d and e (panel (b)). With further evolution, green field lines become part of both the spines of radial null.1, and a pink field line changes its connectivity from regions b to a to regions b to c (panel (c)). In panel (d), a pink field line becomes part of the

upper spine of radial null₂, and as a result, the radial nulls approach each other. These changes in connectivity of field lines—magnetic reconnections—continue until the radial nulls annihilate each other. Figure 5.11 depicts brightening in AIA 1600 Å channel, co-spatial with footpoints of the reconnecting field lines (marked by circles).

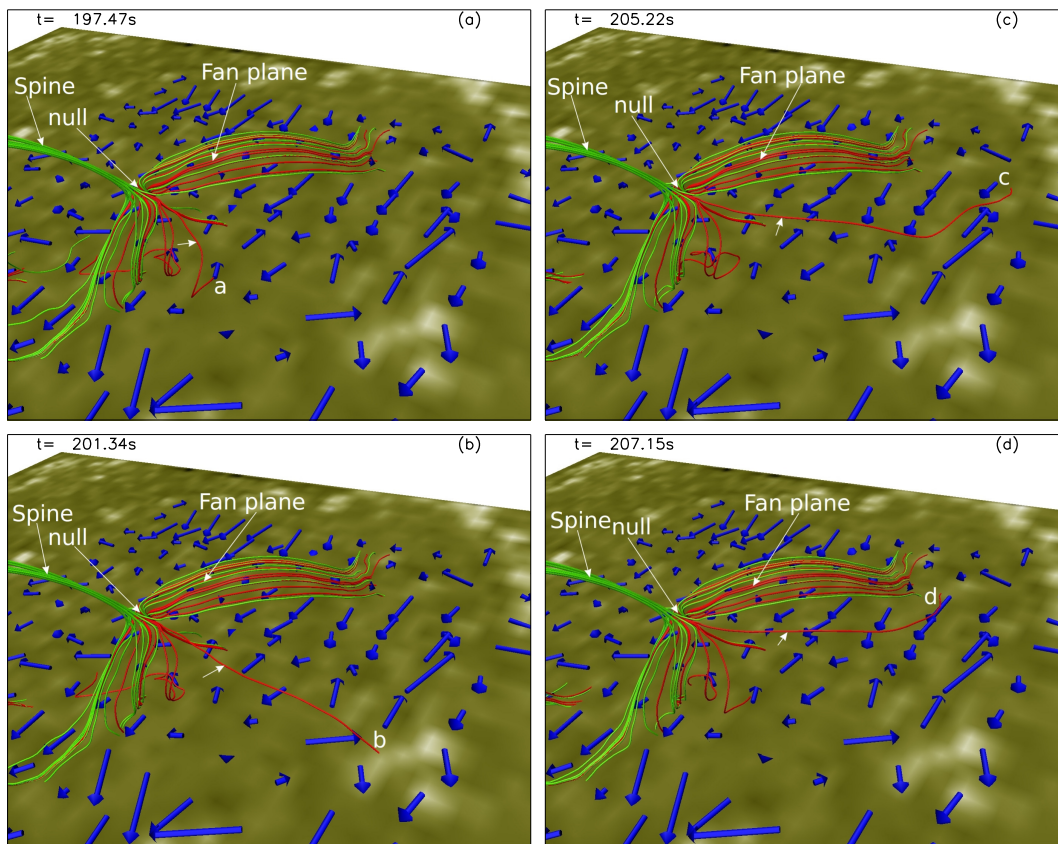


Figure 5.8: The figure depicts the footpoint brightening in the AIA 1600Å channel associated with slip reconnection. The spine and the fan plane of the radial null (marked as ‘null’) are indicated by white arrows. Two sets of field lines drawn near the radial null₂ demonstrate the foot point brightening associated with slip reconnection. The plasma flow is plotted near the $z = 0$ plane and shown by blue arrows. Notably, the red field line, marked by the white arrow at $t = 197.47\text{s}$, is initially anchored to point ‘a’ (panel (a)) changes its connectivity from point ‘a’ to point ‘b’ through slip reconnection (plasma flow direction is different from the field line motion), resulting in the associated brightening seen in panel (b). Subsequently, the red field line changes its connectivity from point ‘b’ to point ‘c’ and then to point ‘d’ (refer to panels (c) and (d)). The overlaid AIA channel has dimension approximately $32.63\text{Mm} \times 63.80\text{Mm}$ in x and y , respectively.

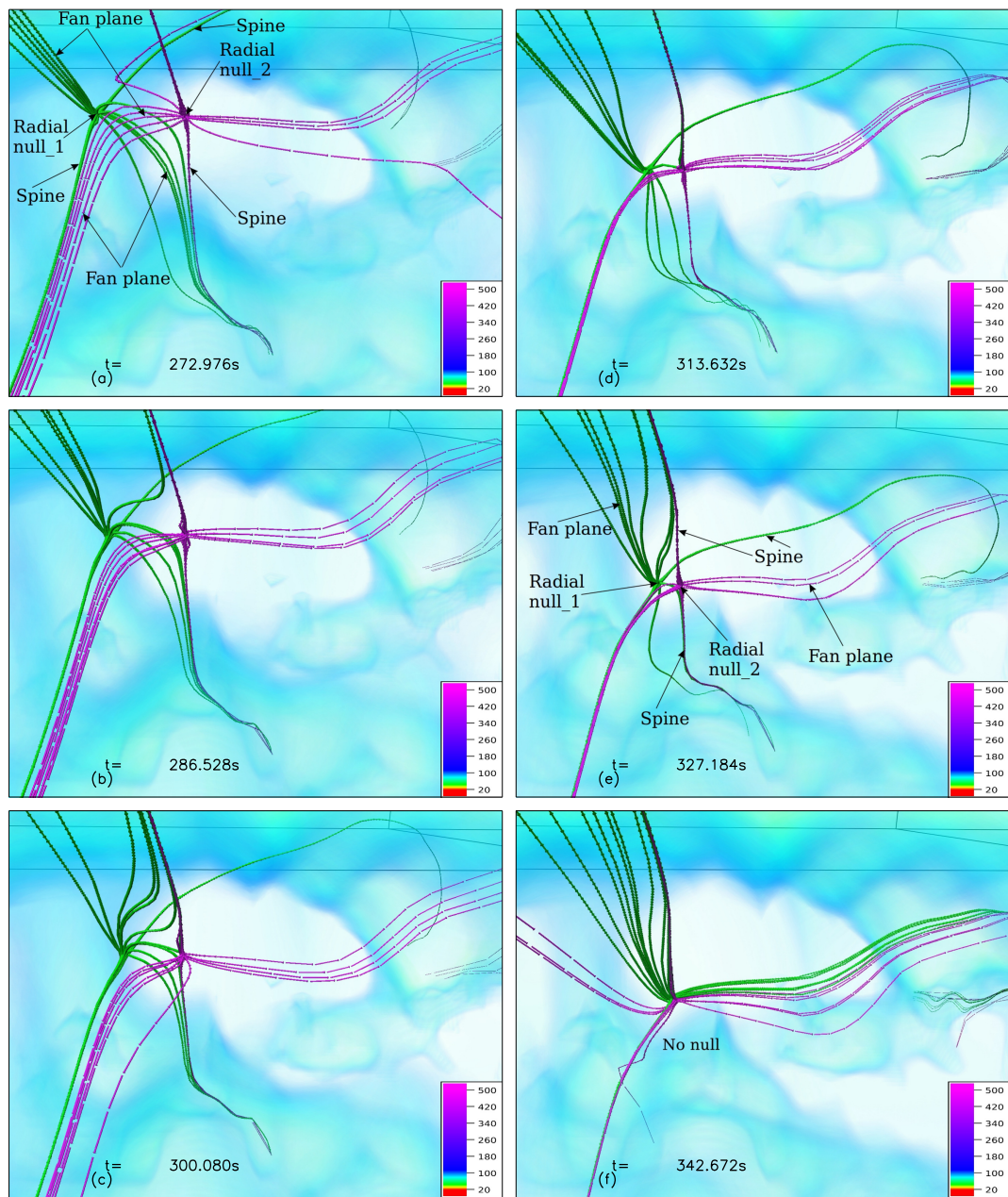


Figure 5.9: In this figure, the evolution of radial nulls is shown by tracing and drawing field lines over time. The field lines (in green) are drawn near the radial null_1, and field lines (in pink) are drawn at radial null_2. The spine and fan plane of radial nulls are marked by arrows. With the evolution, radial nulls are approaching each other (panels (a)-(e)) and ultimately get annihilated at $t = 342.672$ s (panel (f)).

5.2.2 Radial-spiral-pair-1

In addition to the radial-radial pair generation, the simulation also shows

the generation of other pairs. This subsection focuses on the generation and annihilation of a radial-spiral null pair. The generation and annihilation mechanism is similar to the ones presented in paper-I; here, only a brief description is provided. The generation can be visualized by tracking magnetic structure in the immediate vicinity of the null pair, shown in Fig. 5.12. The uniqueness in this case is the role of a pre-existing null in annihilating the pair. For visualization, magnetic field lines (in red) are drawn near the pre-existing null while sky-blue and green field lines are drawn to facilitate demonstration of the null generations (panel (a) of Fig. 5.12) and their evolution (subsequent panels). With evolution, sky-blue and green field lines get elbow-shaped at around $t = 160.69\text{s}$, and an enhancement in current intensity (identified in DVR of $|\mathbf{J}| / |\mathbf{B}|$) is seen accordingly (panel (b)). At $t = 164.56\text{s}$, nulls in a pair comprising of a radial and spiral null get spontaneously created (panel (c)). Across panels (c) and (d), nulls are traced in time, and field lines are drawn at their near neighborhood, depicting an increasing separation between the radial and spiral nulls with time. The pair generation is due to reconnection, confirmed by advecting participating field lines as in the previous case (not shown here).

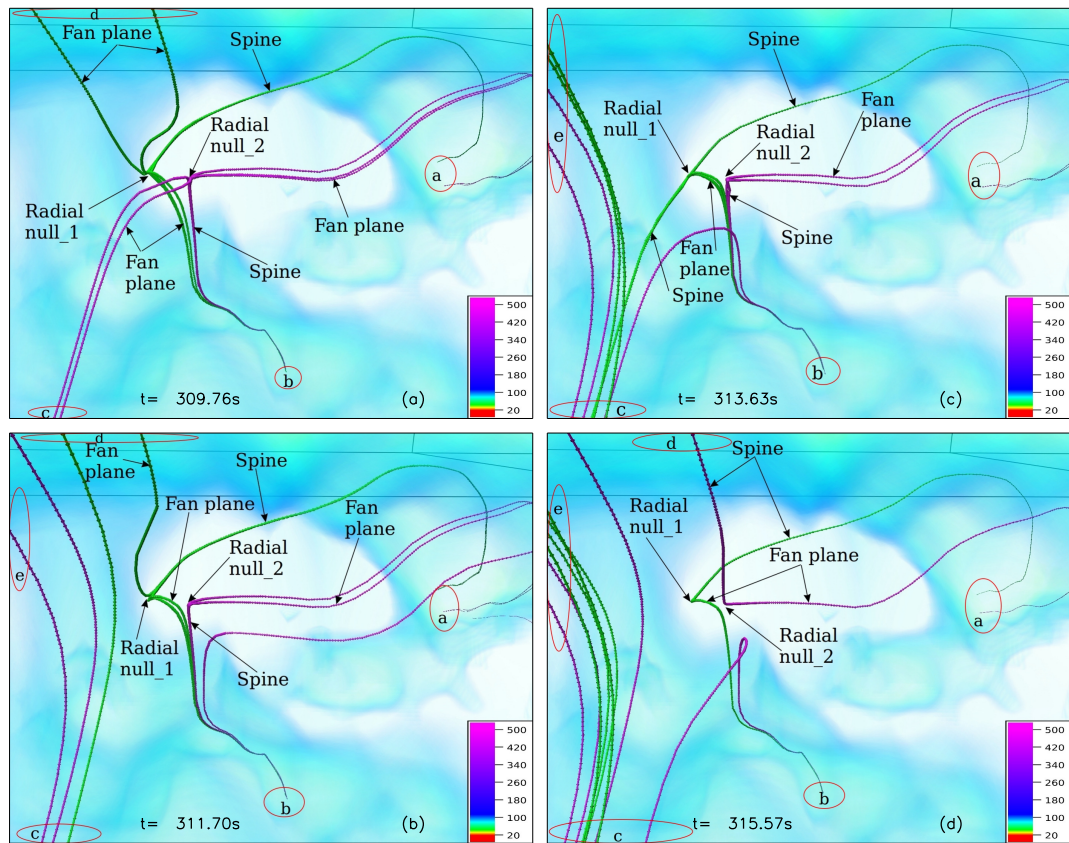


Figure 5.10: Field lines are traced in time and advected with plasma flow. Five green and pink field lines are initially part of the spine and fan plane of radial null_1 and radial null_2, respectively (panel (a)). With the evolution, the green and pink field lines change their connectivity and get disconnected from the nulls. Consequently, the nulls are approaching each other and ultimately annihilate each other, as shown in Figure 5.9.

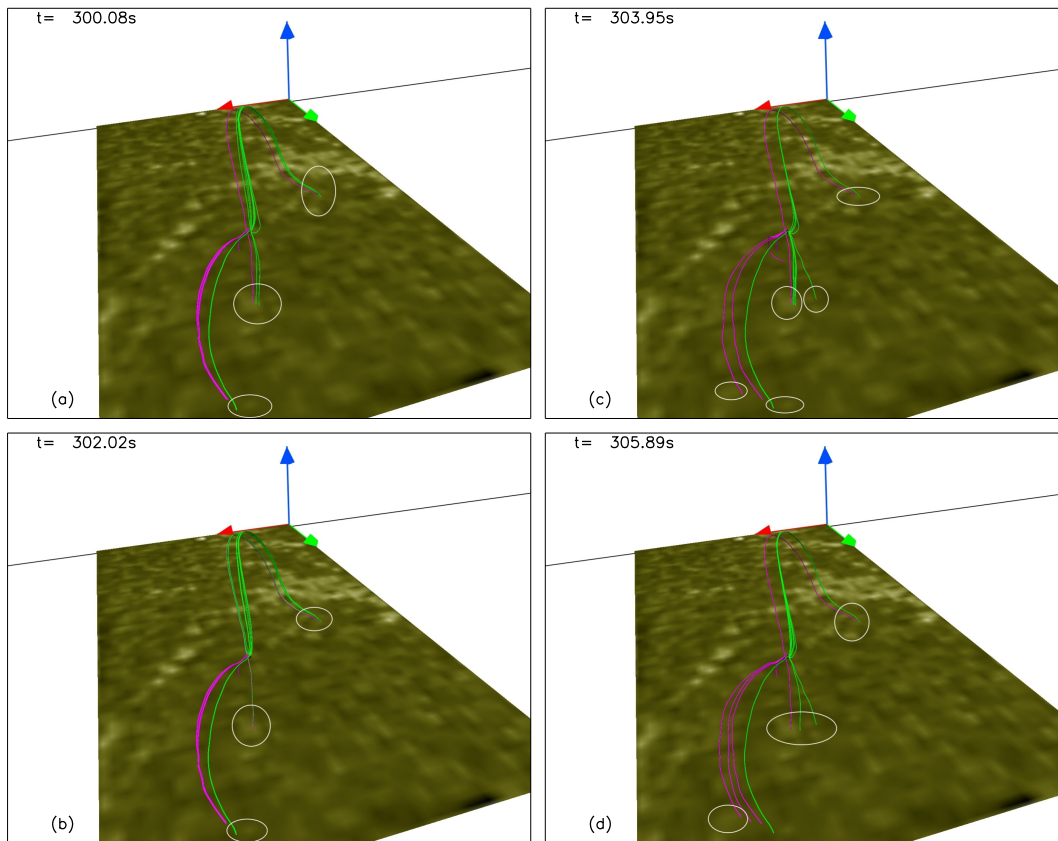


Figure 5.11: The figure depicts foot point brightening (marked by circles) in the AIA 1600 Å channel associated with magnetic reconnection, which annihilates the radial nulls. With the evolution (panels (a)-(d)), nulls are approaching each other with a change in connectivity of field lines, and the corresponding foot-point locations of field lines are co-spatial with the increased intensity in AIA 1600 Å filter, emulating the telltale signs of magnetic reconnection. The overlaid AIA channel has dimension approximately $32.63\text{Mm} \times 63.80\text{Mm}$ in x and y , respectively.

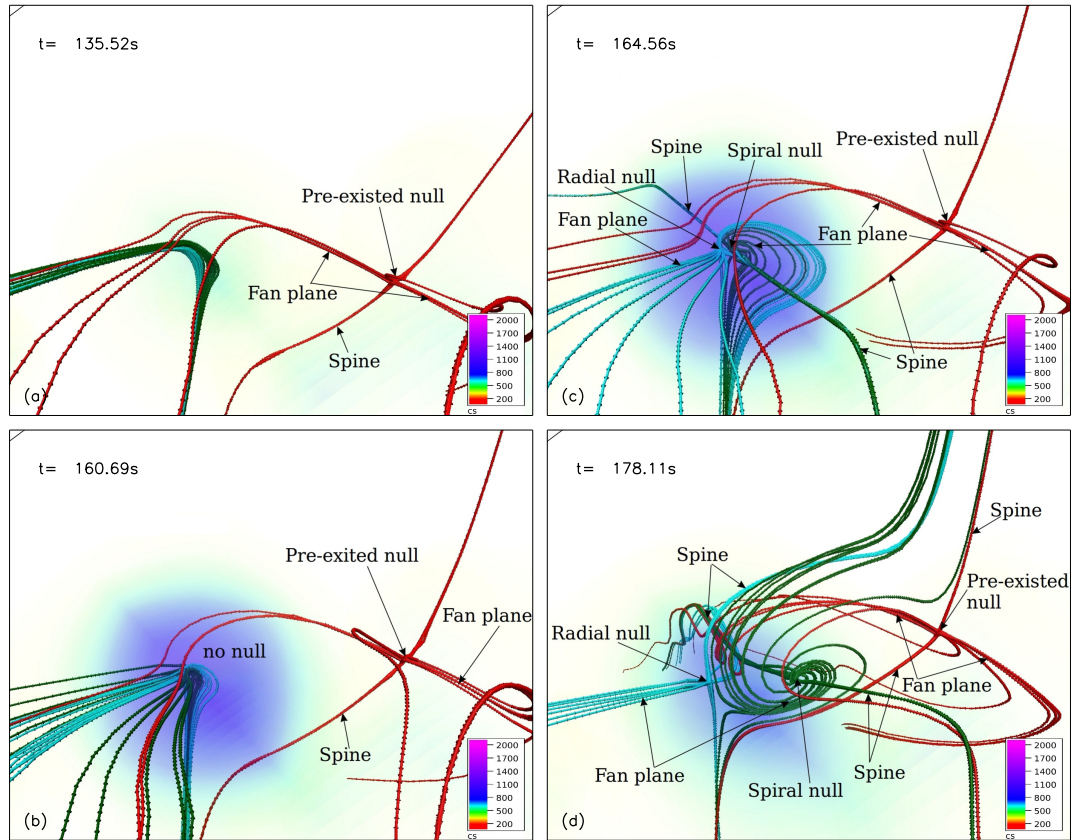


Figure 5.12: The panels of the figure illustrate the generation of nulls in a pair near a pre-existing 3D null. Magnetic field lines (in red) are drawn near the pre-existing null (a null already present at $t = 135.52$ s), while sky-blue and green field lines are included to facilitate the generation of nulls at a later time (panel (a)). With the evolution, the sky-blue and green field lines develop an elbow shape at around $t = 160.69$ s, and an enhancement in current intensity (identified by the Direct Volume Render of $|\mathbf{J}|/|\mathbf{B}|$), marked as ‘cs’, is seen accordingly (panel (b)). In panel (c), a pair of nulls consisting of a radial and a spiral null is generated at $t = 164.56$ s. Panels (c)-(d), spanning $t \in 164.56, 178.11$ s, depict the tracing of nulls and the plotting of field lines. As the evolution progresses, the radial and spiral nulls move away from each other after their generation, whereas the spiral null of the generated pair approaches the pre-existing null

The topological degree of spontaneously generated nulls together with pre-existing null are depicted in Figure 5.13. The fan field lines (in red) are drawn near the location of the pre-existing null and are directed toward the null rendering, its topological degree to be +1. The direction of the fan field lines (in sky-blue) of radial null is toward the null point, resulting in a topological degree of +1, whereas the fan field lines (in green) of spiral null are directed away from the null point, resulting in a topological degree of -1 . The net topological degree

of the generated pair is zero, indicating its preservation during the formation of the pair.

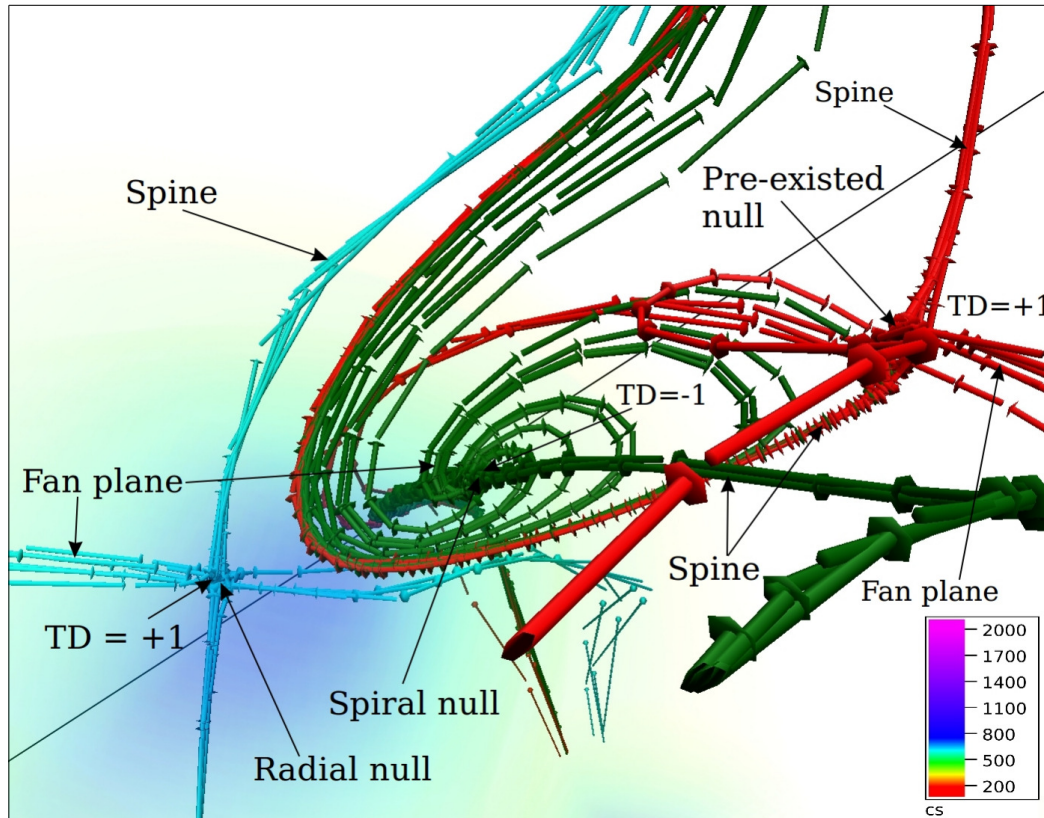


Figure 5.13: The figure illustrates the details of a pre-existing null along with a spontaneously generated null pair, which consists of a radial null and a spiral null at $t = 178.11s$. The field lines (in red) are drawn near the location of the pre-existing null. The fan field lines are directed toward the null, resulting in a topological degree of $+1$. Field lines drawn near the radial null (in sky blue) and those of the spiral null (in green) are also shown. The spine and fan planes, along with the topological degrees of both nulls, are marked in the figure. The direction of the fan field lines of the radial null is toward the null point, and the spine field lines are directed away from the null point, resulting in a topological degree of $+1$. On the other hand, the spine field lines of the spiral null are directed toward the null point in the fan plane and away from the null point, resulting in a topological degree of -1 . The net topological degree of this generated pair is zero, and the spiral null gets annihilated with the pre-existing null (in a pair). Therefore, the conservation of the net topological degree is self-explanatory.

The expected slip reconnection by the fan field lines (Pontin et al., 2013) and the corresponding brightening in AIA 1600 Å channel can be inferred from Fig. 5.14. Panels depict the footpoint brightening corresponding to the slip

reconnection of fan field lines of the radial null of the spiral-radial null pair-1. The radial null is marked as “null” and the local plasma flow is shown by blue arrows. Initially, at $t = 164.35$ s, the green field line indicated by the white arrow is anchored to point a (panel (a)). With the evolution, the footpoints of the green field lines are changing their connectivity to points b and c (panel (b)) and subsequently to points d, e, f, and g due to slip reconnection. Importantly, the local plasma flow direction differs from the field line motion—a trademark of slip reconnection.

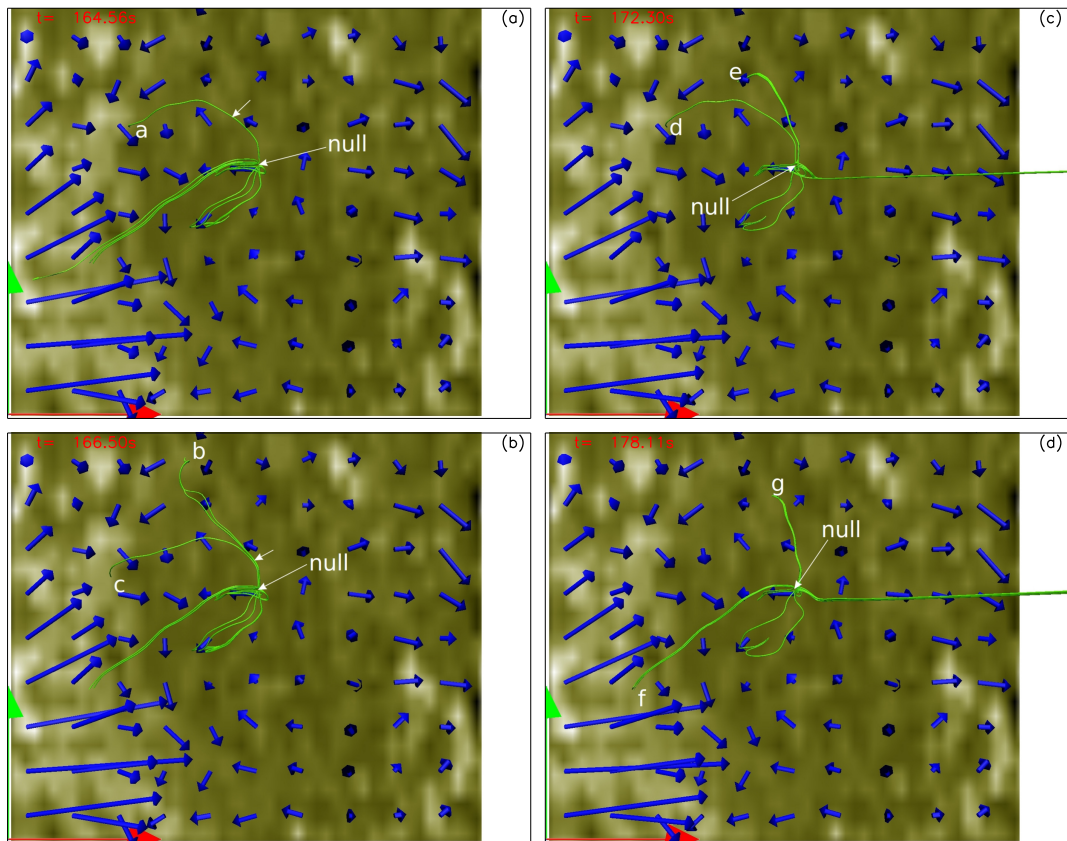


Figure 5.14: Panels depict the footpoint brightening corresponding to the slip reconnection of fan field lines of the radial null of the spiral-radial null pair-1. The radial null is marked as “null” and the local plasma flow shown by blue arrows is plotted near the $z = 0$ plane. Initially, at $t = 164.35$ s, the green field line indicated by the white arrow is anchored to point a (panel (a)). With the evolution, the footpoints of the green field lines are changing their connectivity to points b and c (panel (b)) and subsequently to points d, e, f, and g due to slip reconnection. The overlaid AIA channel has dimension approximately $21.75\text{Mm} \times 21.75\text{Mm}$ in x and y , respectively.

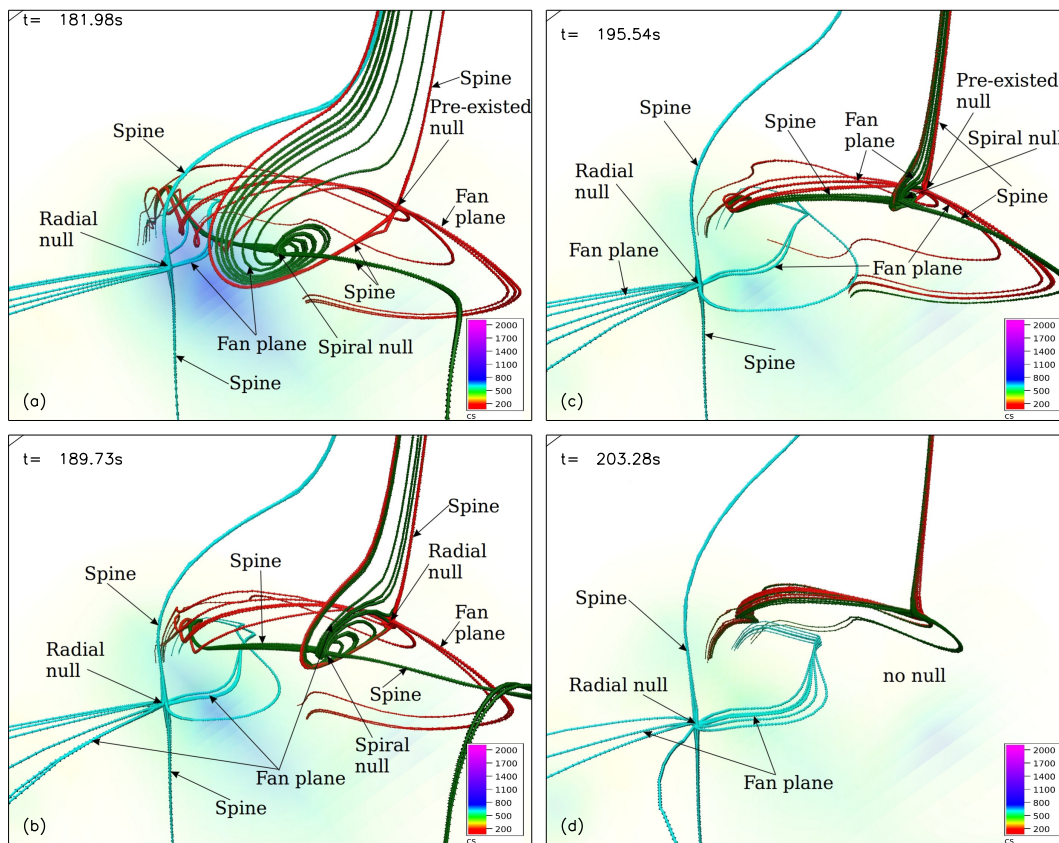


Figure 5.15: Nulls are traced over time, and field lines are drawn near the locations of the nulls. Panels (a)-(d) of this figure illustrate the annihilation of a spiral null and a pre-existing null. The spine and fan planes of the radial, spiral, and pre-existing nulls are indicated by the arrows.

Figure 5.15 illustrates the evolution of spontaneously generated nulls together with the pre-existing null. The nulls are traced in time, and field lines are drawn near their locations. Across panels (a)-(d), the spiral null is receding away from the radial null and approaches the pre-existing null. At $t = 203.28\text{s}$, the spiral and pre-existing nulls are annihilated, and correspondingly, only the spontaneously generated radial null is present in panel (d)—independently verified using the trilinear method. The cause of the null annihilation has been investigated by advecting the relevant field lines (not shown here) and found to be due to magnetic reconnection. The field line topology of the remaining radial null is shown in Figure 5.16. Its topological degree is +1 as the fan field lines are directed toward the null, in conformity with the conservation of the topological degree.

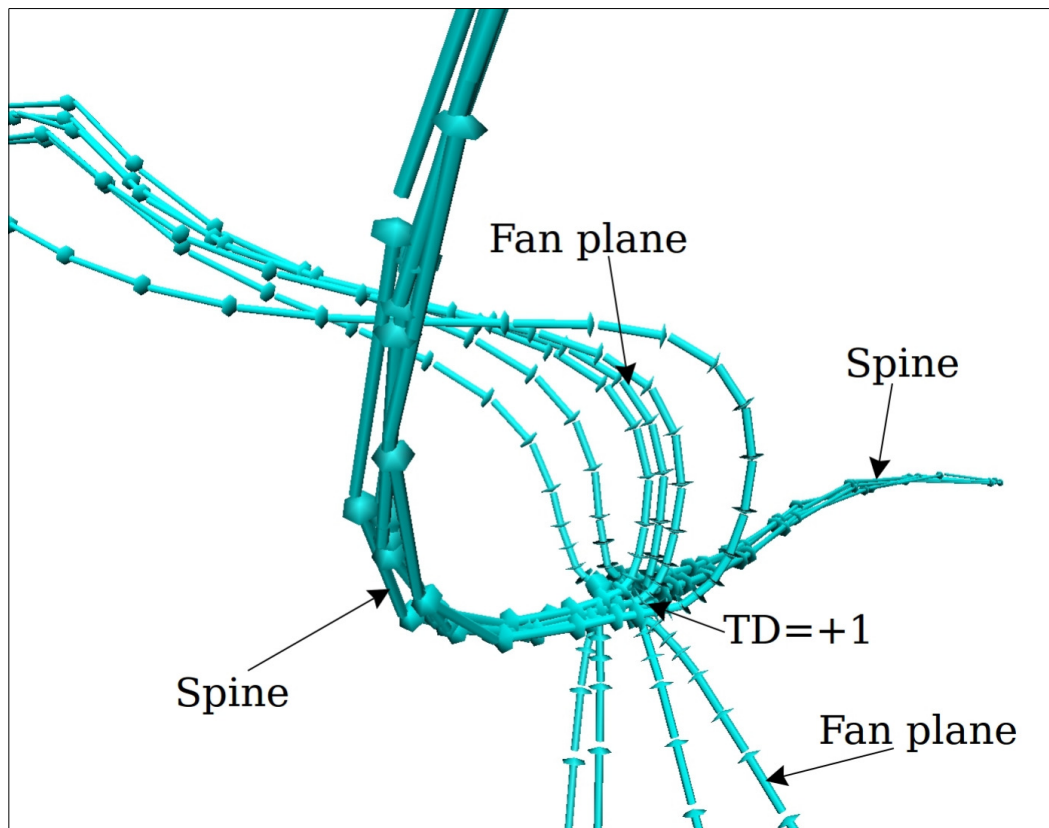


Figure 5.16: The figure illustrates the details of the radial null $t = 203.28\text{s}$, left in the domain after the annihilation of the generated spiral null with the pre-existing null. The fan field lines of the radial null point toward the null point, while the spine field lines are directed away from the null point, resulting in a topological degree of +1.

5.2.3 Radial-spiral-pair-2

This subsection emphasizes the generation and annihilation of the radial-spiral-pair-2, where a radial-spiral null pair spontaneously generates and moves away from each other after the generation (panels (a)-(d) of Figure 5.17) and subsequently annihilates. Magnetic reconnection is once again the cause of the pair generation and annihilation—nevertheless, the uniqueness here is the conversion of the spiral null into a radial null, which later annihilates with another spiral null of a newly generated radial-spiral null pair. To highlight this uniqueness, eigenvalues of the Jacobian matrix $\nabla\mathbf{B}$ at the spiral null are calculated during its evolution. The imaginary part of the eigenvalue is zero at $t = 267.17\text{s}$ while being non-zero earlier than that, implying the transition from spiral to radial.

For further visualization, field lines are plotted near locations of the nulls. In 2D, a spiral null will appear as an “O” type, and a radial null will appear as an “X” type null (Parnell et al., 1996; Liu et al., 2018; Liu et al., 2019). Panels (e) and (f) depict such projections of the spiral null at $t = 199.41$ s and $t = 267.17$ s, illustrating similar conversion from “O” to “X” type. The spine, fan plane, and the topological degree of nulls at $t = 199.41$ s are shown in Figure 5.18. The fan field lines (in yellow) of the spiral null are directed toward the null point, making its topological degree +1, whereas the spine field lines (in pink) of radial null are directed toward the null, resulting in a topological degree of -1 . Consequently, the net topological degree of this pair is zero, and the generation is in congruence with the conservation of the net topological degree. Fig. 5.19 demonstrates the annihilation of the converted radial null along with the spiral null of the newly generated radial-spiral null pair where the green field lines correspond to the spiral null whereas the red field lines belong to the radial null. Across panels (a)-(c), spanning the time $t \in \{267.17, 286.53\}$ s, the radial null of the radial-spiral-pair-2 and the spiral null of generated pair approach each other and ultimately annihilate at $t = 294.27$ s. Post annihilation, a radial null remains in the system (panel (d)), and the conservation of net topological degree is self-explanatory. The topological degree, spine, and fan plane of the radial null and the spontaneously generated nulls are depicted in Fig. 5.20.

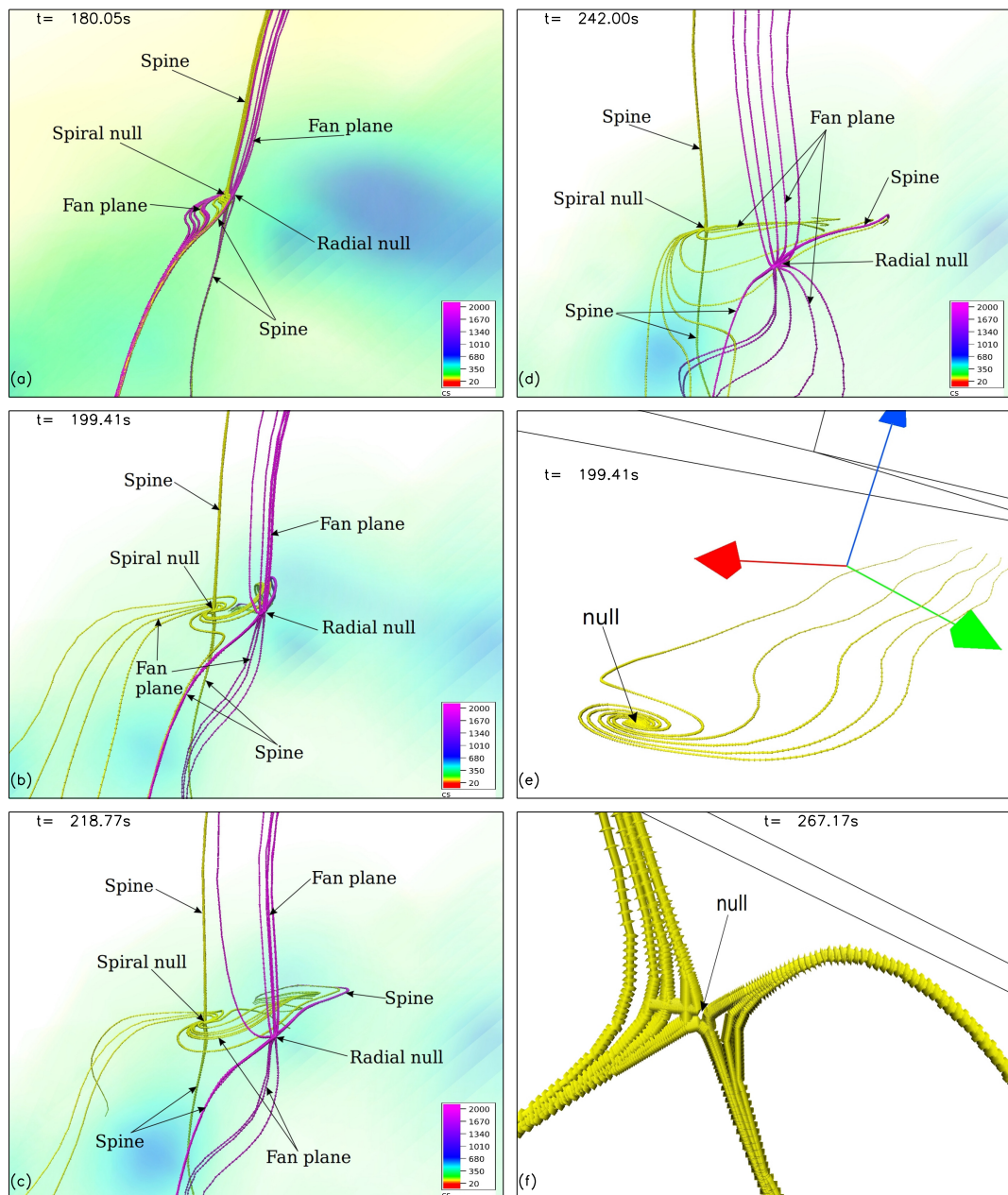


Figure 5.17: The snapshots of the field lines represent the evolution of nulls as they are traced over time. At $t = 180.05$ seconds, it is the first instance when nulls in a pair first appear using the trilinear detection technique, and field lines are drawn near their locations (panel (a)). These spontaneously generated nulls are named radial-spiral-pair-2 and consist of a spiral null (in yellow) and a radial null (in pink). As the evolution progresses, the spiral and radial nulls are moving away from each other (panels (a)-(d)). The spiral null loses its spirality and gets converted into a radial null; the conversion from spiral to radial null can be verified by collapsing the null's structure in 2D, where a spiral null will appear as an “O” type and a radial null will appear as an “X” type null. Panels (e) and (f) depict the 2D projections of the spiral null and converted radial null at $t = 199.41\text{s}$ and $t = 267.17\text{s}$, respectively. This illustration shows a similar conversion from “O” to “X” type.

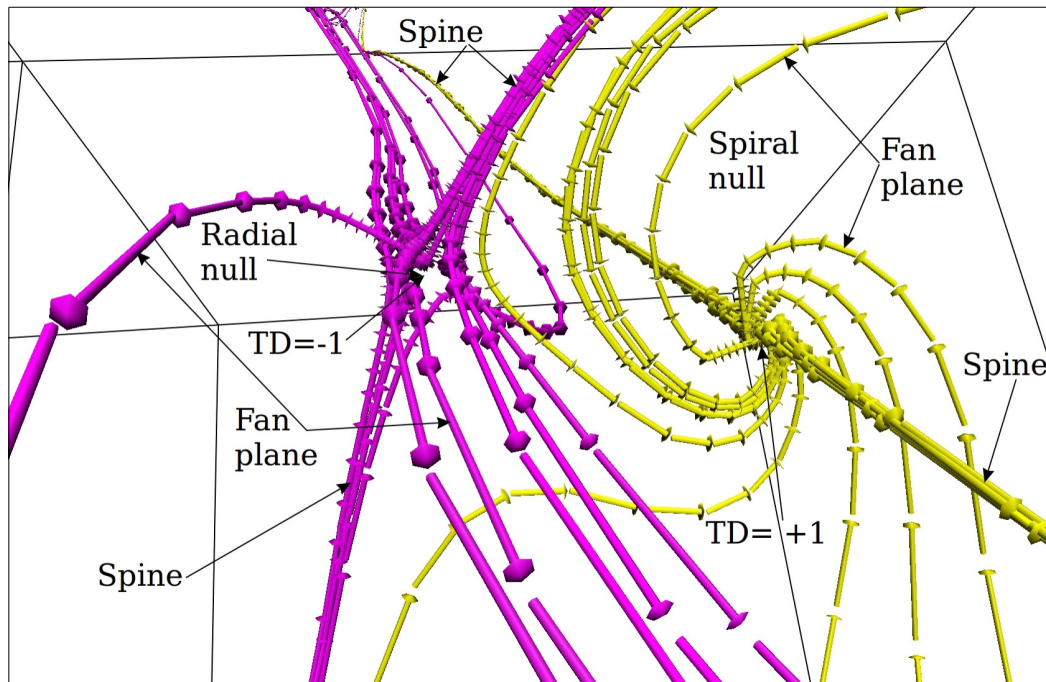


Figure 5.18: The figure illustrates the topological details of spontaneously generated radial-spiral-pair-2 nulls at $t = 199.41s$. These nulls are generated in a pair and consist of a spiral null (in yellow) and a radial null (in pink). The spine field lines (in pink) of the radial null are directed toward the null point, resulting in a topological degree of -1 , while the fan field lines (in yellow) of the spiral null are directed toward the null point, making a topological degree $+1$. The net topological degree of this local system is zero, and hence, the overall topological degree of the system remains unaffected by the generation of these new nulls.

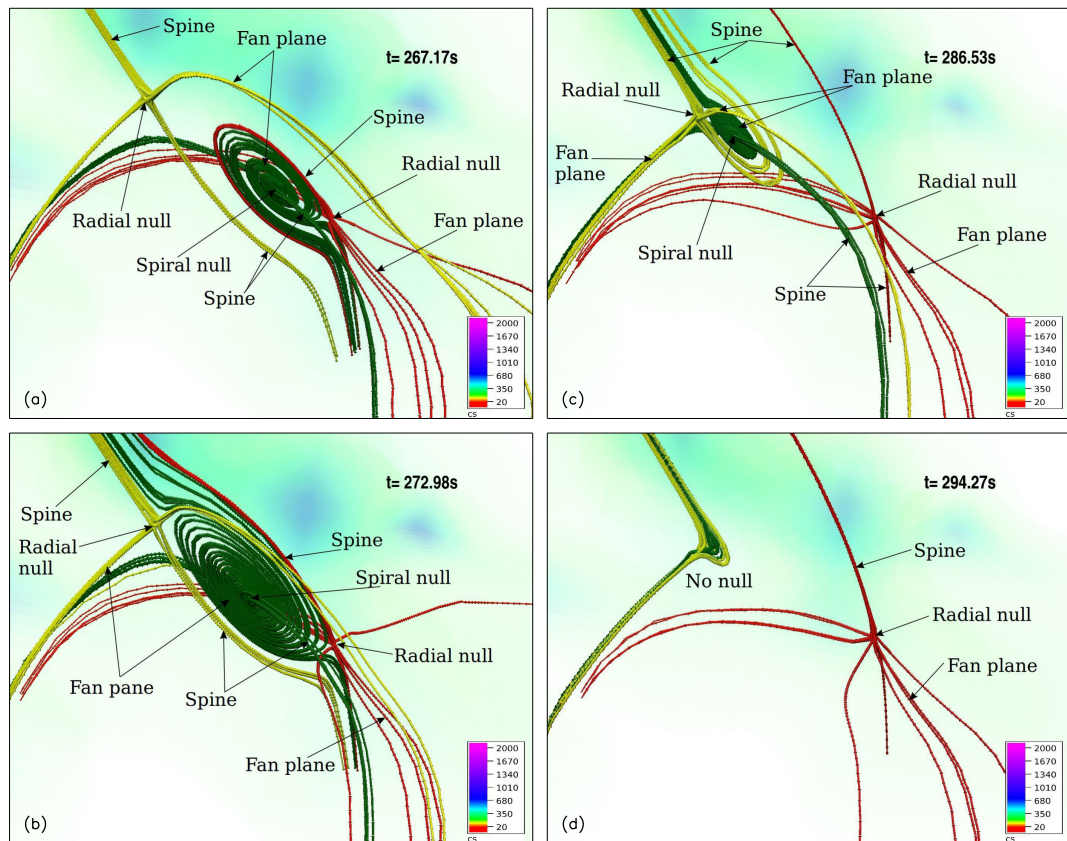


Figure 5.19: The figure illustrates the evolution of nulls over time. These nulls are tracked as they evolve, and field lines are drawn at their locations. Yellow, green, and red field lines are drawn near the radial null of the radial-spiral-pair-2 null pair, the spiral null, and the radial null of a spontaneously generated new null pair, respectively. The spontaneously generated new nulls are first detected by the trilinear null detection technique at $t = 267.17$ seconds, and the corresponding structure is shown in panel (a). As the evolution continues, the spiral and radial nulls of the newly generated pair move away from each other, while the radial null of the radial-spiral-pair-1 pair and the spiral null of the newly generated null approach each other simultaneously (panels (a)-(c)), ultimately resulting in annihilation around $t = 294.27$ s (marked by no null in panel (d)). The pairwise annihilation does not affect the net topological degree of the system. Consequently, one radial null, with a topological degree of +1, is left in the system.

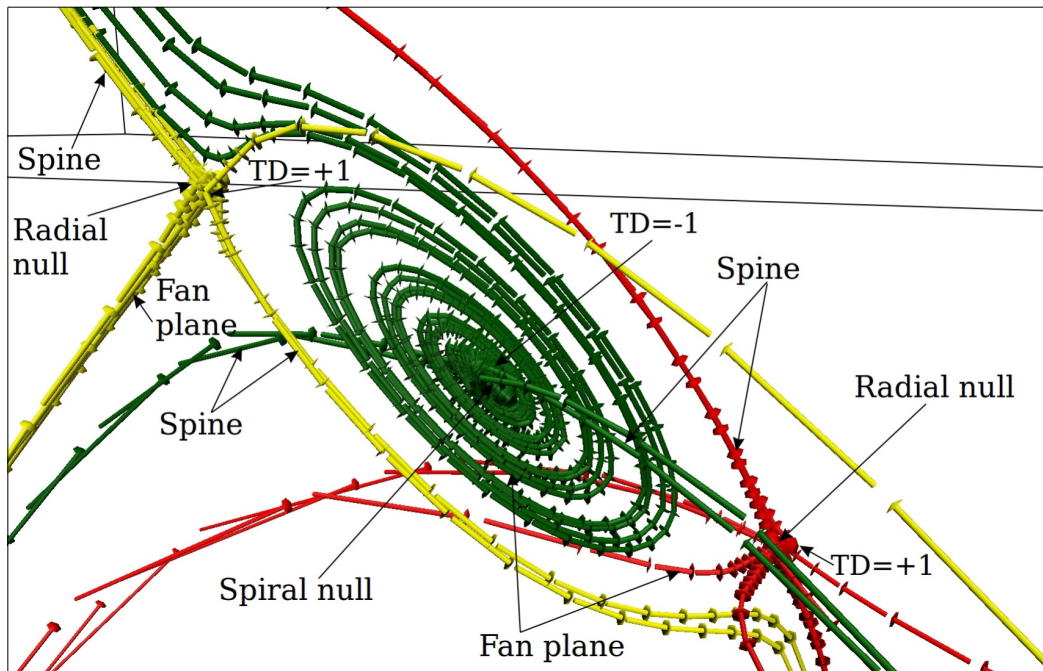


Figure 5.20: The figure illustrates the topological details of spontaneously generated new nulls near the radial null of the radial-spiral-pair-2 pair at $t = 274.91s$. These new nulls are generated in pairs and are marked by the arrows. The fan field lines (in yellow) of the radial null of the radial-spiral-pair-1 pair are directed toward the null point, resulting in a topological degree of $+1$. Meanwhile, the fan field lines (in green) of the spiral null of the spontaneously generated new pair are directed away from the null point, resulting in a topological degree of -1 . Lastly, the fan field lines (in red) of the radial null of the spontaneously generated pair are directed toward the null point, making the topological degree $+1$. Hence, spontaneous generation occurs in a pair, and the annihilation of the radial null of the radial-spiral-pair-1 pair is with the spiral null of the generated pair. Therefore, the net topological degree of the system remains unaffected by the generation and annihilation of 3D nulls.

For completeness, Figure 5.21 illustrates changes in field line connectivity during the annihilation. Two selected yellow and green field lines are traced in time and advected with the plasma flow, preserving their uniqueness. At $t = 274.91s$, initially, yellow field lines belong to the spine and fan plane of the converted radial null, while green field lines are part of the spiral null (panel (a)). With the evolution, one yellow field line changes its connectivity from regions c to d to regions c to b and becomes part of the fan plane of the spiral null. The two green field lines are changing their connectivity from regions b to a to regions b to e (panel (b)). Subsequently, during the evolution, the yellow field

line further changes its connectivity from regions b to c and gets connected from regions b to e' (panel (c)) and then from regions b to e' to regions b to a' . Slip reconnection and brightening in the AIA 1600Å channel similar to the other pairs have also been found but are not shown here to avoid repetitions.

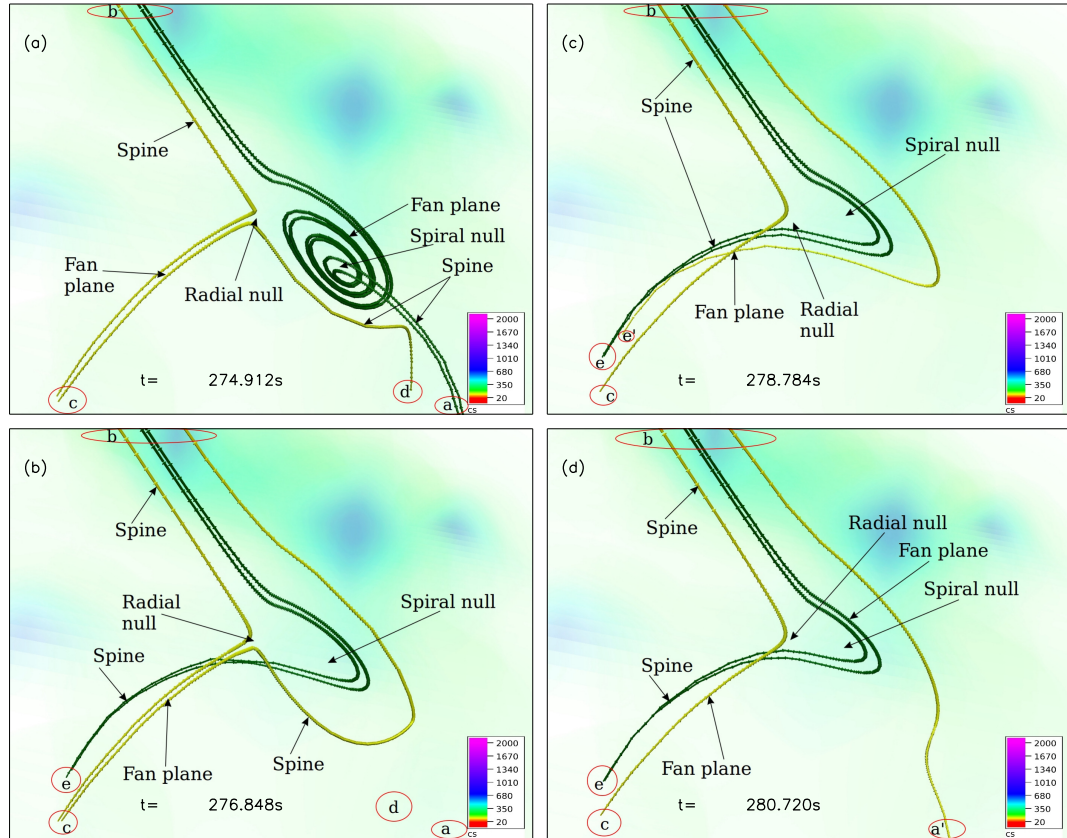


Figure 5.21: Magnetic field lines are traced over a time span of $t \in 274.912, 280.720$ s and advected with plasma flow. This time span is selected to investigate the dynamics of field lines responsible for annihilation. Four selected field lines, two green and two yellow, are drawn to illustrate magnetic reconnection. At $t = 274.912$ seconds, the two green field lines are part of the spine and fan plane of the spiral null, connecting from region b to region a (panel (a)), while the two yellow field lines are part of the upper and lower spine along with the fan plane of the radial null, connecting regions c to d and b. As the evolution progresses, the green field lines change their connectivity from region b to region a to region b to e. Similarly, one yellow field line also changes its connectivity from region c to d to region c to b (panel (b)). With further evolution, one yellow field line changes its connectivity from region c to b to region e' (panel (c)), and then from region e' to region b to region a' to region b. These changes in connectivity occur through magnetic reconnection, ultimately resulting in the annihilation of nulls in a pair.

5.3 Summary

This chapter establishes, for the first time, reconnection-assisted spontaneous generation and annihilation of magnetic nulls in the solar atmosphere through a combination of data-based Implicit Large Eddy simulation, a modified trilinear null detection technique, and observation of collocated footpoint brightening caused by these generated nulls through slip reconnection—a novel work. For this purpose, magnetic field lines corresponding to Active Region AR11977 hosting a C-class flare on February 17, 2014, are selected. The magnetic field line configuration just before the flare has been constructed with a non-force free extrapolation of the photospheric magnetic field obtained from the HMI onboard the SDO. The corresponding finite Lorentz force initiates the dynamics without the requirement of any prescribed flow. Since this Lorentz force depends on the photospheric magnetic field, it is inherent to the field line complexity of the active region, and hence, the subsequent null generation can be envisaged to be spontaneous in its true sense. The modified trilinear method sheds light on the topological degree of a null, in addition to finding the location of a null—as its predecessor. This new information makes it convenient to identify members of a null pair and trace them in time. The physics of reconnection being scale independent, these spontaneously generated nulls are further expected to exhibit signatures analogous to observed 3D null-assisted solar flares, particularly the footpoint brightening because of slip reconnection (Masson et al., 2009; Pontin et al., 2013). Accordingly, it is attempted to look for the brightening and slip reconnections associated with these spontaneously generated null points. Overall, the article establishes the spontaneous generation of 3D nulls in the solar atmosphere in a realistic scenario by carrying out a data-based numerical simulation of the solar atmosphere and explores their observational implications.

The initial magnetic field is provided from by non-FFF extrapolation, and the initial plasma flow is set to zero. The non-zero Lorentz force pushes the plasma to generate initial dynamics. The simulation covers a fraction of the rising phase of the flare, which is expected to be reconnection dominated. The magnetic

field initially contains over a thousand null points, with this number varying throughout the simulation as pair creation and annihilation processes occur. As is expected from previous works, as the system relaxes towards an equilibrium (due to the non-zero viscous damping), the overall number of nulls decreases. Three particular null creation/annihilation events are selected for detailed study and are representative of the many further events that occur within the domain. One of these identifies that two radial nulls are spontaneously created and move away from each other after their generation. The result is novel, as the creation of radial nulls in pairs has not been studied in earlier works. The underlying cause of their generation is magnetic reconnection, identified by advecting the magnetic field lines while selecting seed points away from reconnection sites. The spontaneously generated radial null exhibits the typical dome-shaped structure of fan field lines, along with footpoint brightening in 1600 Å channel of AIA associated with slip reconnection. With further evolution, both radial nulls approach each other and spontaneously annihilate, the underlying cause being identified as magnetic reconnection. The simulation also shows the spontaneous generation of a pair of nulls, consisting of a spiral and a radial null with topological degrees -1 and $+1$, respectively. This pair is spontaneously created near a pre-existing 3D null with a topological degree of $+1$. The spontaneously generated radial null also exhibits the typical footpoint brightening corresponding to slip reconnection. With evolution, the spiral null moves away from the radial null while simultaneously approaching the pre-existing null, ultimately resulting in their annihilation. Here, the unique aspect of the finding is the spontaneous annihilation of the generated spiral null with a pre-existing radial null, which has not been explored in previous studies. During the evolution, another pair of nulls, consisting of a spiral null and a radial null with topological degrees of $+1$ and -1 , respectively, get spontaneously created. The spiral and radial nulls move away from each other after their generation, and the spiral null loses its spirality as it evolves and transforms into a radial null, making this pair unique for study. Another uniqueness here is that the annihilation of the converted radial null involves another spiral null from a newly generated radial-spiral null pair. The

newly generated spiral and radial null have topological degrees of -1 and $+1$, respectively. By tracing the field lines in time, it was found that the magnetic reconnection generates and annihilates the 3D null pairs. The generation and annihilation of 3D nulls in all the above pairs maintain the conservation of net topological degree, contributing to the credibility of the simulation. Magnetic reconnection, identified as the underlying cause of the spontaneous generation and annihilation of nulls, is noteworthy. The spontaneously generated nulls also exhibit slip-reconnection, a phenomenon typically observed in a 3D null of the solar atmosphere. The findings shed light on the underlying magnetic field line dynamics governing 3D null generation, annihilation, and their evolution. In each selected case, the field lines in the vicinity of the null are rooted in the photosphere near brightenings. Such brightenings may be produced by the impact of non-thermal particles with the plasma of the lower solar atmosphere. Although both previous studies have established spontaneous null generation through reconnection, the initial magnetic field supported pre-existing nulls. A natural question is then whether magnetic reconnection can generate 3D nulls from an initial magnetic field with no such nulls. The plausibility of such a scenario will be explored in the next work and presented in the next chapter, where the initial magnetic field will be chaotic and devoid of any 3D null.

Chapter 6

Generation of 3D magnetic nulls in an initially chaotic magnetic field devoid of any nulls

6.1 Introduction

Toward the objective, the plausibility of such a scenario has been briefly explored in the simulation by [Nayak et al. \(2020\)](#), where the initial magnetic field was chaotic and devoid of any 3D null. However, that study demonstrated the generation of magnetic nulls; it failed to precisely identify their location, topological degree, and nature (spiral or radial) using presently available standard tools like the upgraded null detection technique. Moreover, a claim of magnetic reconnection demonstrated by the change in field line connectivity requires strict maintenance of the involved magnetic field lines, which was approximated in [Nayak et al. \(2020\)](#) by keeping the initial point of field line integration constant at every instant whereas a more precise requirement is to follow the reconnecting field lines as they advect with plasma flow (in the ideal MHD region). For completeness, it is then indispensable to revisit those findings in the light of recent understanding and tools developed and used in the previous two works and put the idea of spontaneous generation of 3D nulls from an initially chaotic field devoid of nulls on a firmer footing. Towards this aim, the following presents a brief

discussion of the initial magnetic field. The field is constructed by superposing two Arnold-Beltrami-Childress (ABC) fields [Ram et al. \(2014\)](#), each satisfying the linear force-free equation

$$\nabla \times \mathbf{B}' = \lambda \mathbf{B}', \quad (6.1)$$

having solution

$$B'_x = A \sin \lambda z + C \cos \lambda y, \quad (6.2)$$

$$B'_y = B \sin \lambda x + A \cos \lambda z, \quad (6.3)$$

$$B'_z = C \sin \lambda y + B \cos \lambda x. \quad (6.4)$$

and being represented as

$$\mathbf{B} = \mathbf{B}'_1 + d_0 \mathbf{B}'_2. \quad (6.5)$$

The constant d_0 relates the amplitudes of the two superposed fields. In Cartesian coordinates the components of \mathbf{B} are

$$B_x = A (\sin \lambda_1 z + d_0 \sin \lambda_2 z) + C (\cos \lambda_1 y + d_0 \cos \lambda_2 y), \quad (6.6)$$

$$B_y = B (\sin \lambda_1 x + d_0 \sin \lambda_2 x) + A (\cos \lambda_1 z + d_0 \cos \lambda_2 z), \quad (6.7)$$

$$B_z = C (\sin \lambda_1 y + d_0 \sin \lambda_2 y) + B (\cos \lambda_1 x + d_0 \cos \lambda_2 x). \quad (6.8)$$

Equation (6.1) is an eigenvalue equation of the Curl operator ($\nabla \times$), eigenfunctions of which form a complete orthonormal basis when eigenvalues λ are real ([Yoshida & Giga, 1990](#)). Further simplification of (6.6) can be made by selecting $\lambda_1 = -\lambda_2 = \lambda$, rendering

$$B_x = 0.5A \sin z + 1.5C \cos y, \quad (6.9)$$

$$B_y = 0.5B \sin x + 1.5A \cos z, \quad (6.10)$$

$$B_z = 0.5C \sin y + 1.5B \cos x, \quad (6.11)$$

for the selection $d_0 = 0.5$ and $\lambda = 1$. The resulting Lorentz force

$$(\mathbf{J} \times \mathbf{B})_x = B^2 \sin 2x - 2AC \sin y \cos z, \quad (6.12)$$

$$(\mathbf{J} \times \mathbf{B})_y = C^2 \sin 2y - 2AB \cos x \sin z, \quad (6.13)$$

$$(\mathbf{J} \times \mathbf{B})_z = A^2 \sin 2z - 2BC \sin x \cos y, \quad (6.14)$$

can be utilized to drive the plasma from an initial static state to develop dynamics. Importantly, the \mathbf{B} is chaotic and a detailed discussion can be found in [Kumar et al. \(2017\)](#) and [Nayak et al. \(2020\)](#). Also important is the relative magnitudes of the constants A , B , and C . For instance, if $A=B=1$, an increasing C makes the volume occupied by chaotic field larger—a conclusion derived in [Kumar et al. \(2017\)](#), which can be used as a measure of chaoticity. For the simulations executed here, notable is the range $0 \leq C \leq 0.3142$, for $A = B = 1$, for which \mathbf{B} is entirely devoid of any magnetic nulls. Consequently, using the \mathbf{B} as an initial condition provides the unique opportunity to explore null generation from a state having no preexisting nulls—the objective of this communication, along with understanding null dynamics in an environment of chaotic magnetic field, left as a future exercise.

6.2 Results

The simulations are carried out using the magnetohydrodynamic numerical model EULAG-MHD described in Sect. 3.4. The simulations have been performed for the aforementioned field with $C \in \{0.15, 0.3\}$ to explore null generations with an increase in chaoticity. The kinematic viscosity is set as $\nu = 0.010 \text{ cm}^2\text{s}^{-1}$, while the spatial and temporal grid increments are $\Delta x = \Delta y = \Delta z = 0.09973 \text{ cm}$ along the x, y, z -axes, respectively and $\Delta t = 0.016 \text{ s}$, in CGS units. Triply periodic boundary conditions are applied, and the grid having $64 \times 64 \times 64$ pixels resolved on a computational grid of $x, y, z \in \{-\pi, \pi\} \text{ cm}$ in a Cartesian coordinate system, mapping a physical dimension of $(2\pi)^3 \text{ cm}^3$ to facilitate magnetic reconnection while optimizing the computation costs. Each simula-

tion spans a physical time of 32 s. Figure 6.1 plots the number of nulls with time for different values of C , depicting an increase in the number of nulls at a given instant and its maximal value over the temporal range with an increase in chaoticity. Additionally, nulls appear earlier for larger values of C , precisely at $t = (31, 23, 9, 8)s$ for $C = (0.15, 0.2, 0.25, 0.3)$. Interestingly, the null generation for all C values is in bursts, most pronounced for $C = 0.3$, which shows three identifiable peaks at $t = \{9.26, 16.18, 23.28\}$ seconds. A possible reason can be a sudden increase in chaoticity near the peaks, followed by its decrease.

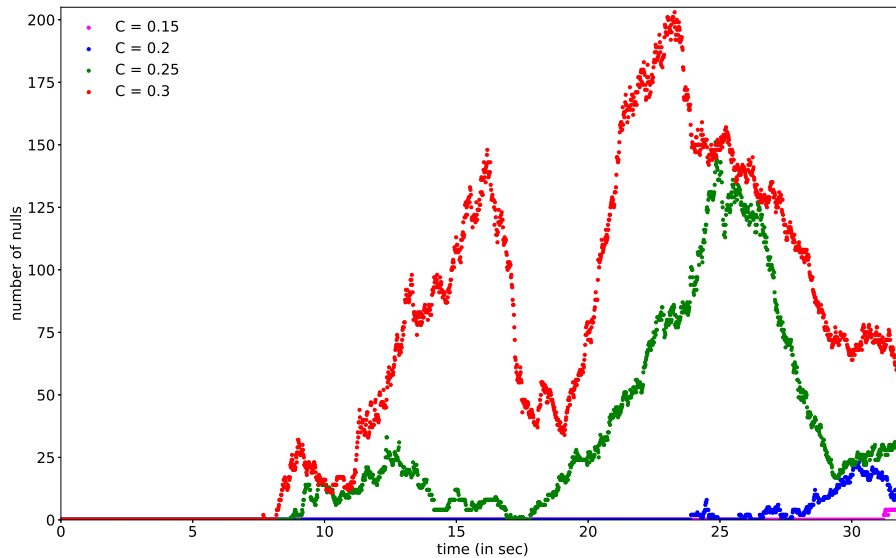


Figure 6.1: The plot shows an increase in the number of nulls at a given instant and its maximal value over the temporal range with an increase in chaoticity. The vertical axis represents the number of nulls, and the horizontal axis represents time. The plots in different colors (pink, blue, green, and red) represent the variation in number of nulls for a particular value of the chaoticity (0.15, 0.20, 0.25, 0.30, respectively). Generation of nulls occur earlier in time as the chaoticity C increases, i.e., $t = (31, 23, 9, 8)s$ for $C = (0.15, 0.20, 0.25, 0.30)$.

Figure 6.2 verifies this ansatz by following a local flux surface traversed by a single field line for $C = 0.3$ in $t \in \{16.08, 16.29\}s$, spanning the second prominent peak at $t = 16.18s$. Clearly, the surface loses its coherent structure as the line becomes more volume-filling and hence chaotic. At $t = 16.18s$ (Panel (c)), which marks the second peak, the local flux surface is almost destroyed but

reorganized itself at later times (panels (d) to (f)). It has been proposed that the presence of chaotic field lines may promote the occurrence of magnetic reconnection in fields without nulls [Eyink et al. \(2011\)](#); [Boozer \(2019\)](#), and in this case, the increase in chaoticity is cotemporal with the generation of nulls and with reconnection (see below). The causal link remains to be fully explored in future investigations, along with the plausibility of the local flux surfaces being attractors because of their repetitive destruction and reformation throughout the simulation. The subsequent retrieval of the flux surface arrests this increase in reconnection—leading to a peak in the number of nulls. With no nulls entering or leaving the computational domain while chaoticity being directly related to the onset of current sheets ([Kumar et al., 2017](#)) and consequent reconnections, the underlying mechanism for null pair generation can be attributed to these reconnections. A comprehensive study of field line dynamics is carried out in detail to explore the relation between reconnection and the formation/annihilation of null pairs. For this purpose, the dynamics corresponding to $C = 0.3$ are selected as the nulls are generated earlier in time and mostly away from the boundaries of the computational domain, leading to their better tractability over time. The focus is set on the nulls generated in a pair with coordinates $(x, y, z) \in \{(0.166, 0.034, 0.101)\pi, (0.169, 0.034, 0.101)\pi\}$, at $t = 8.27\text{s}$ —panel (a) of [Fig. 6.3](#) as it involves spiral-spiral pair generation and annihilation, hitherto unexplored in YRD1 and YRD2. Additionally, the pair is created almost at the beginning of the null pair generation, being third in the chronology. With the experience gained from YRD1 and YRD2, the field lines are advected with the plasma flow and traced in time to reveal the magnetic field line dynamics. For this purpose, two sets of field lines (one in green and two in pink) having initial points at coordinates $x, y, z \in \{(0.359, 0.061, 0.235)\pi, (0.359, 0.061, 0.234)\pi\}$, away from the reconnection region are selected. The corresponding field lines are advected with the plasma flow and are traced in time ([Fig. 6.4](#)) within a subvolume $\in \{(0.266, 0.018, 0.159)\pi - (0.580, 0.207, 0.434)\pi\}$. This subvolume is far away from the periodic boundaries of the computational domain necessary for showing up in the chaotic field, so presumably, the selected field lines maintain

their discreteness.

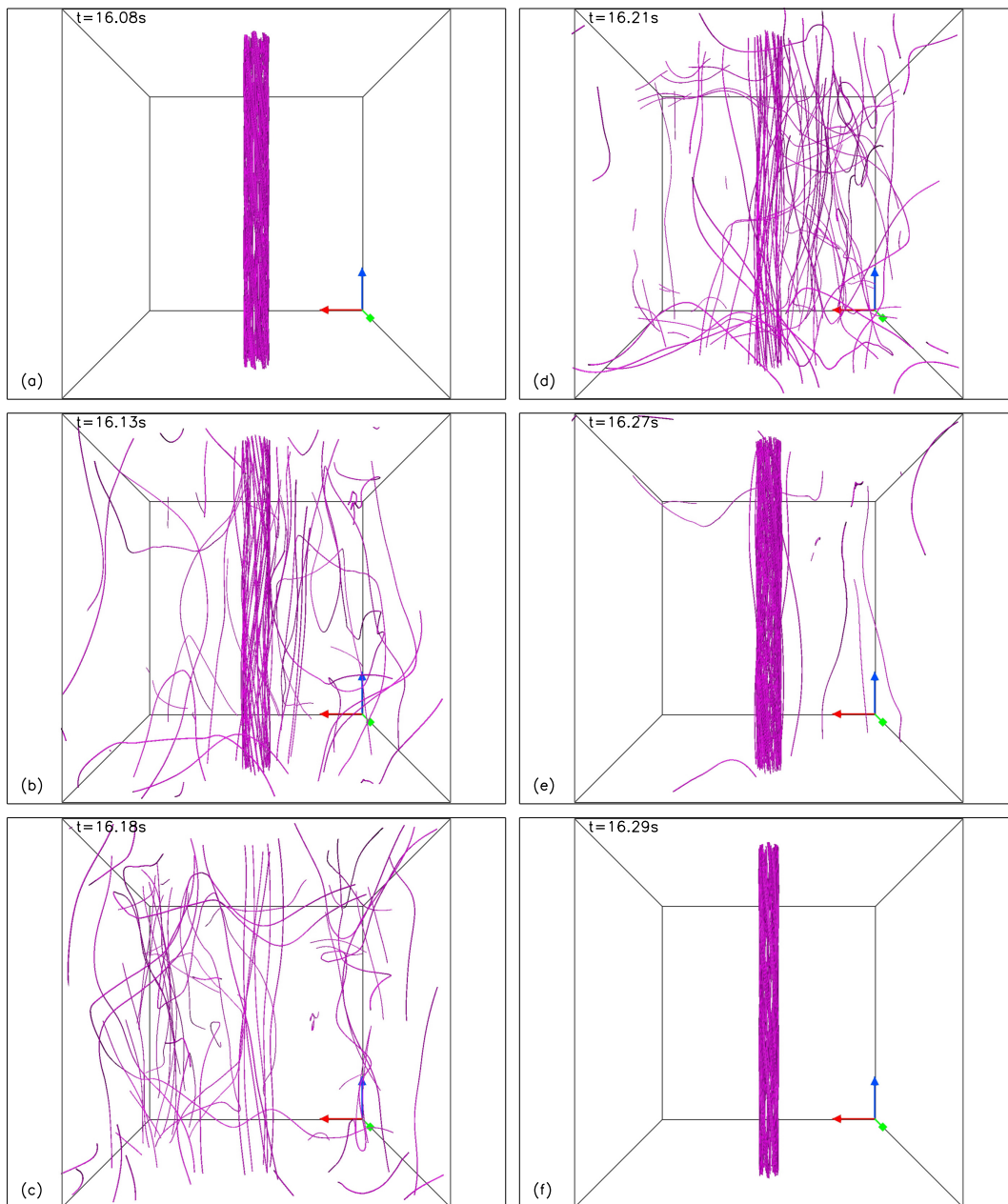


Figure 6.2: Panels depict a sudden increase in chaoticity near the second peaks in number of nulls, followed by its decrease. The figure shows a local flux surface traversed by a single field line for $C = 0.3$ in $t \in \{16.08, 16.29\}s$, spanning the second prominent peak at $t = 16.18$. Panel (a) depicts a flux surface structure drawn at $t = 16.08s$, and the traversing field line is almost perfectly tangential to the surface and becomes part of the chaotic region with the evolution (panel (b)). Subsequently, the surface loses its coherent structure as the field line becomes more volume filling and hence chaotic. At $t = 16.18s$ (Panel (c)), which marks the second peak, the local flux surface is almost destroyed but reorganized itself at later times (panels (d) to (f)).

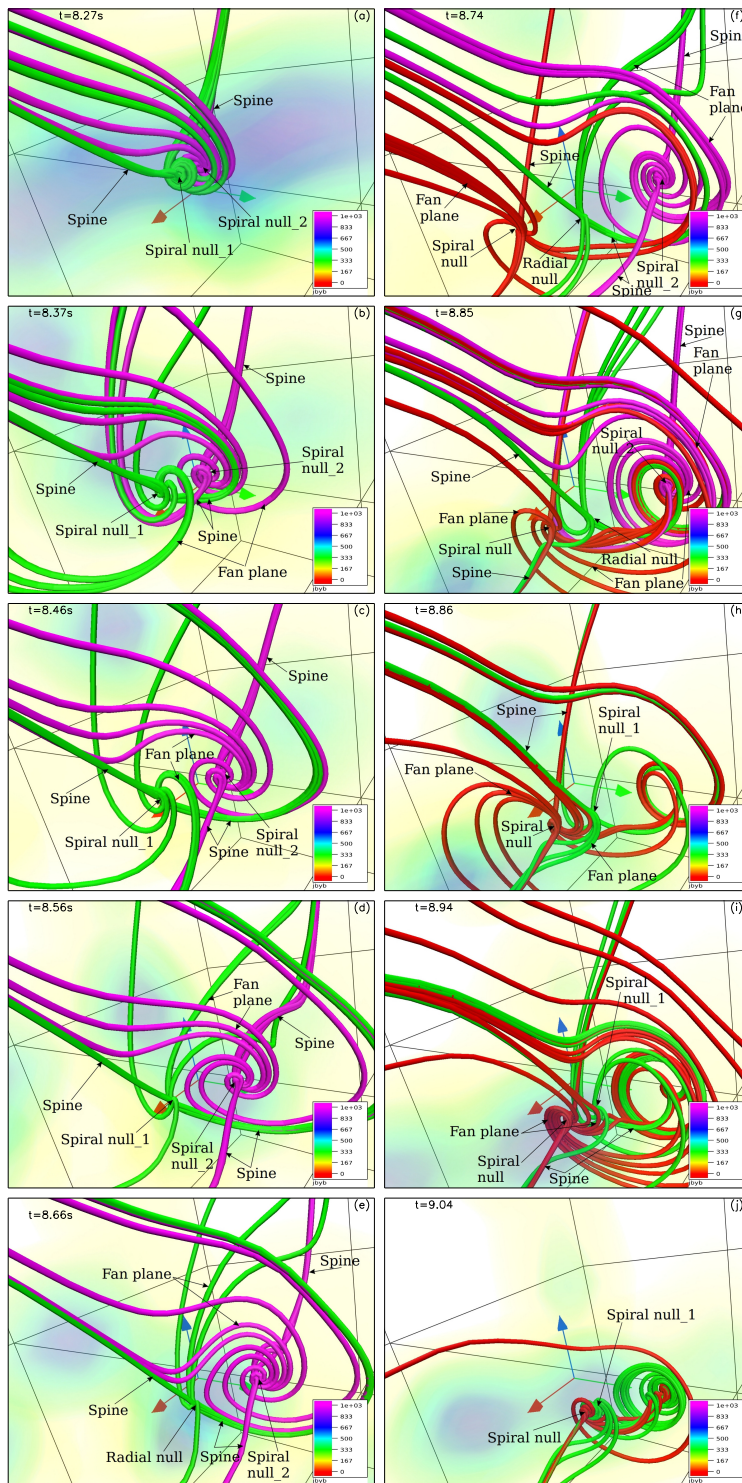


Figure 6.3: Figure depicts the evolution of nulls with time after their generation. Nulls are traced in time, and field lines in green, pink, and red are drawn near the spiral null₁ ($SN1$), spiral null₂ ($SN2$), and spiral null₃ ($SN3$), respectively. The color bar in panels depicts the magnitude of the $|\mathbf{J}|/|\mathbf{B}|$, where \mathbf{J} and \mathbf{B} represent current density and magnetic field. Panel (a) depicts the field lines structure near the nulls at $t = 8.27\text{s}$ when two spiral nulls ($SN1, SN2$) first appear. With the evolution, $SN1$ and $SN2$ move away from each other (Panels (b)-(e)), and $SN1$ changes its nature from a spiral to a radial null (panel (e)). Subsequently, this radial null reverts back to a spiral null (panels (f)-(h)) and eventually annihilates with a different spiral null₃ ($SN3$) formed in a distinct null pair generation process (panel (j)).

The figure is further overlaid with a probe depicting values of $|\mathbf{J}|/|\mathbf{B}|$, located approximately at the reconnection plane identified from figure 6.3. All three field lines (two pink and one green) are connected from region a to region b at $t = 8.21\text{s}$ (panel (a)). As depicted from panels (a)-(c), the green field line gets more prominently elbow-shaped compared to the other two, along with becoming co-spatial with the high-value region of $|\mathbf{J}|/|\mathbf{B}|$. Subsequently, across panels (c) to (d), the green and one of the two pink field lines change their connectivity from regions a to b to regions a to d and c, respectively, at $t = 8.26\text{s}$ — a telltale sign of magnetic reconnection. Importantly, this reconnection precedes the null pair generation and indicates a causal connection between the two. Moreover, an auxiliary simulation having 128^3 grid resolution, mapping the same physical domain, has been carried out. The result (not shown) confirms null pair generations getting delayed in time and with the onset of magnetic reconnection being deferred because of the employed ILES spirit of the simulations, further corroborates this causal connection.

The null pair is generated at $t = 8.27\text{s}$ (panel (e)), their structure elaborated in panel (f), along with changes in field line connectivity. In detail, the second pink field line connects regions a to d instead of a to b, while the first pink field line now connects a to d (c.f. panels (d)-(e)). An important further endeavor would be to identify separators and investigate their role in reconnections occurring in the post-null pair generation phase but left as a future exercise as achieving the involved numerical technicality is challenging, and the exercise is not within the central scope of this paper. Nevertheless, recent work by [Parnell \(2024\)](#) in this direction is worth mentioning here as an example for setting up the tone for future numerical simulations in this direction. The work demonstrates the importance of intra- and inter-cluster separators in the context of clusters of magnetic nulls and suggests that reconnection is not taking place in cluster—which can further be explored in the context of pair production of magnetic nulls.

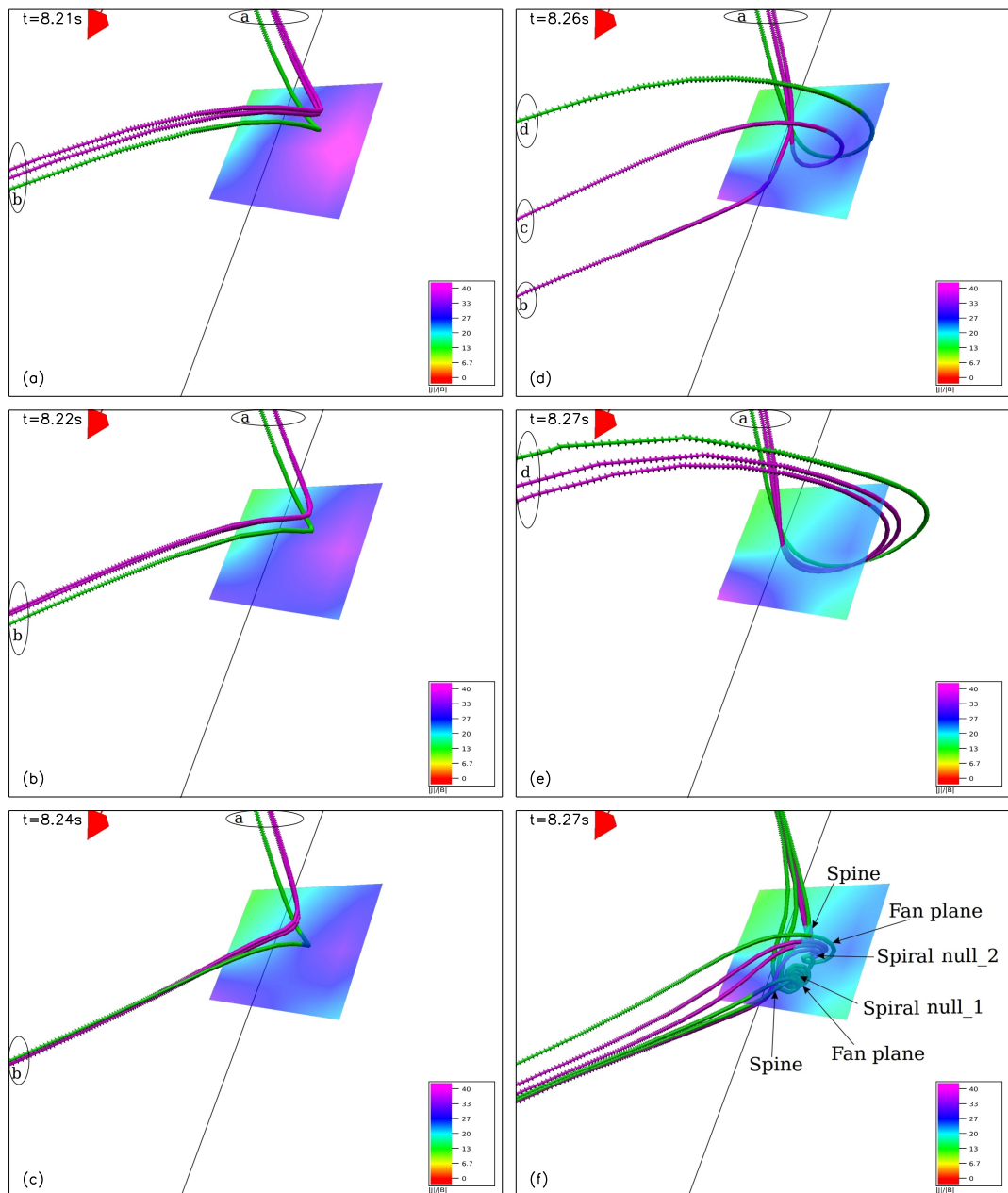


Figure 6.4: The figure illustrates the magnetic reconnections leading to the generation of two spiral nulls. Two pink and one green magnetic field lines are traced in time from ideal plasma elements in the vicinity of the footpoint marked ‘a’. The colorbar represents the same quantity $|\mathbf{J}|/|\mathbf{B}|$ as mentioned in Fig. 6.3. At $t = 8.21s$, all field lines connect from region a to region b (panel (a)). Subsequently (panels (a)-(c)), the green field line develops a more prominent elbow shape, but connectivity remains unchanged. Across panels (c) and (d), a green and one pink field line change connectivity—a telltale sign of reconnection. Subsequently, the second pink field line also changes connectivity (panels (d)-(e)) and generates two spiral nulls at $t = 8.27s$ (panel (e)). The spontaneously generated two spiral nulls are elaborated in panel (f).

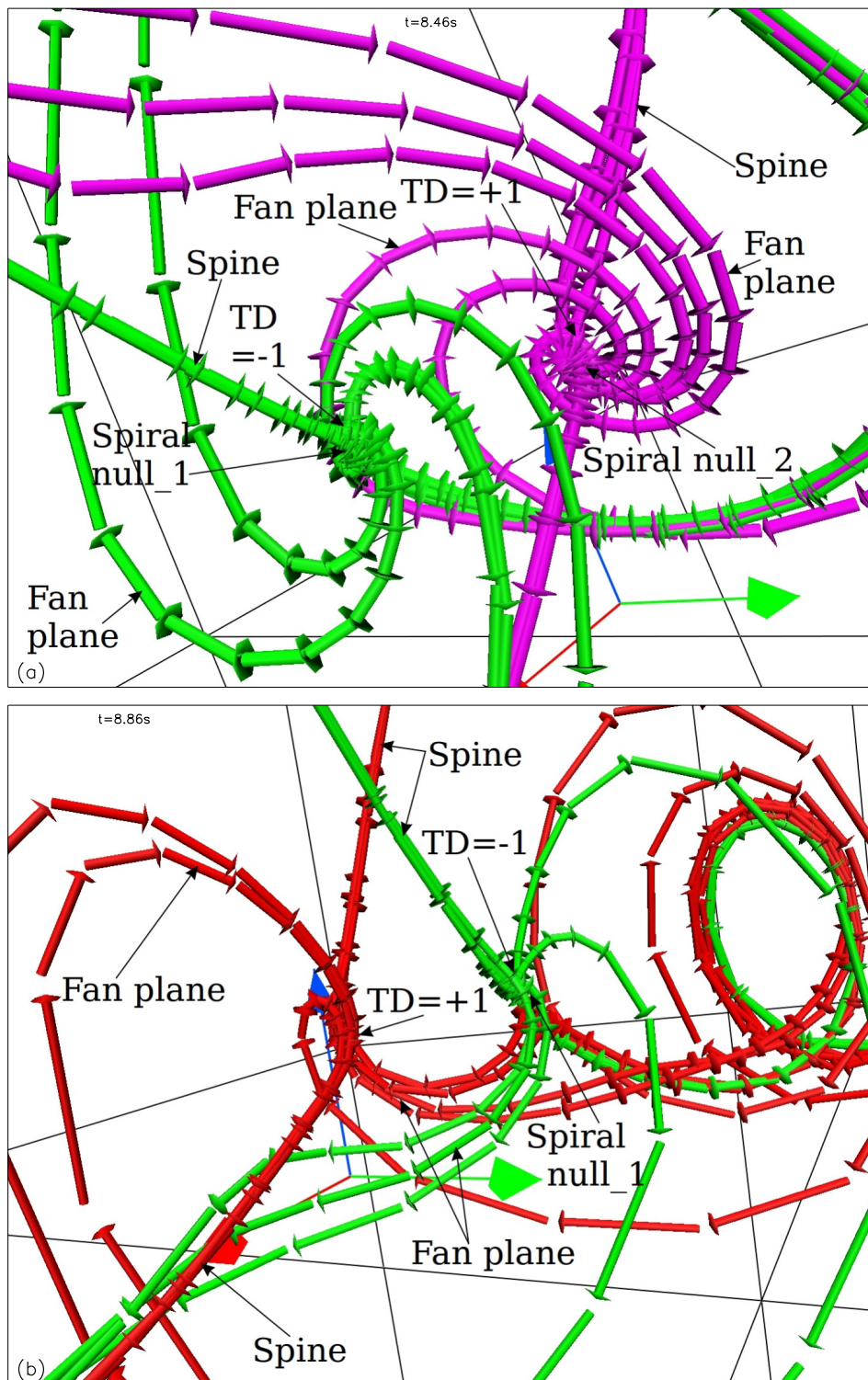


Figure 6.5: Figure depicts the topological details of the two spontaneously generated spiral nulls at $t = 8.46s$ (panel (a)) and the null pair at $t = 8.86s$ (panel (b)). The fan field lines (in green) of spiral null_1 (*SN1*) are directed away from the null, resulting in a topological degree of -1 (panels (a) and (b)), whereas the fan field lines (in pink) of spiral null_2 (*SN2*) are directed towards the null, making a topological degree $+1$. The fan plane field lines of spiral null_3 (*SN3*) (in red) are directed towards the null point making topological degree $+1$ (panel (b)). With time, these two nulls get annihilated.

The eigenvalues of the Jacobian matrix $\nabla\mathbf{B}$ at each null are calculated, and it is found that the imaginary part of the eigenvalues is non-zero for each of the two nulls, which are associated with the current along the spine of nulls. Consequently, the fan field lines of each null become spiral due to non-zero current along the spine; hence, both nulls are spiral nulls (hereafter referred to as $SN1$ and $SN2$, respectively). These nulls are traced in time, and field lines are drawn from the close vicinity of the nulls, as shown in Figure 6.3. The nulls move away from each other after their generation (c.f. panels (a)-(e)). The topological details of the nulls are illustrated in Figure 6.5 (a). The fan field lines (in green) of $SN1$ are directed away from the null, resulting in a topological degree of -1 , whereas the fan field lines (in pink) of $SN2$ are directed towards the null, making a topological degree $+1$. The generation of nulls in pairs satisfies the conservation of net topological degree. With further evolution, the imaginary part of the eigenvalues of $SN1$ becomes zero, resulting in no current along the spine, implying that the $SN1$ has lost its spirality and become a radial null and remains radial until $t = 8.85\text{s}$. The average value of the current density ($|\mathbf{J}|$) in a subvolume enclosing that spiral null is calculated and found that it drops by 0.6% of its value at $t = 8.4\text{s}$ (the time at which null was spiral in nature). Subsequently, at $t = 8.86\text{s}$, the imaginary part of the eigenvalues again becomes non-zero, implying non-zero current along the spine, causing it to revert back to a spiral null $SN1$ (Fig. 6.3). Accordingly, the average value of $|\mathbf{J}|$ in that subvolume enclosing the null increased by 10%. Simultaneously, $SN1$ approaches another spiral null (panels (f), (g)), which is one of the spiral-spiral null pair generated earlier at $t = 8.68\text{s}$ and marked as spiral null_3 ($SN3$) in Fig.6.3. $SN1$, $SN2$, and $SN3$ are traced in time, and the green, pink, and red field lines are drawn near $SN1$, $SN2$, and $SN3$, respectively (panels (f)-(g)). $SN1$ and $SN3$ approach each other and ultimately annihilate pairwise (panels (h)-(j) of Fig. 6.3). Similar to Figure 6.4, the annihilation coincides with a change in global field line connectivity (not shown). The spine, fan plane, and topological degree are depicted in Fig. 6.5 (b). The fan field lines (depicted in red) of $SN3$ are directed towards the null, making topological degree $+1$, and the fan field

lines (in green) of $SN1$ are directed away from the null, resulting in a topological degree -1 . The conservation of net topological degree is self-explanatory.

6.3 Summary

This chapter presents the study of reconnection-assisted spontaneous generation/annihilation of 3D nulls with the analytically constructed initially chaotic fields that do not contain any null—novelty of the work. The initial magnetic fields have been derived by superposing two ABC fields, each satisfying the linear force-force condition. The updated trilinear 3D null detection technique has been employed to locate the nulls and calculate their topological degrees and nature (spiral or radial) based on eigenvalues. Further, to explore null generation/annihilation in more detail, the chaoticity is set at $C = 0.3$ as the generation of nulls started earlier in time is selected. As an example of the null generation process, a spontaneously generated pair of spiral nulls is selected. Interestingly, one of the nulls changes its nature from spiral to radial with evolution. Subsequently, this radial null reverts back to a spiral null, which later annihilates with a different spiral null formed in a distinct null pair generation process. It is already known that null generation and annihilation require local, non-ideal MHD effects [Hornig & Schindler \(1996\)](#). To elucidate the global impact of the creation and annihilation of nulls, the relevant magnetic field lines are traced in time and advected with the plasma flow in the ideal region. It is found that the field lines change their connectivity from one domain to a different domain—demonstrating that the spontaneous generation (and annihilation) of 3D null point pairs leads to a change in the global field topology. The study also demonstrates a direct correlation between chaoticity levels and the number of null generations, with higher chaoticity leading to earlier null creations and increased null count.

Chapter 7

Summary and Future Scopes

7.1 Summary

Magnetic topology is crucial for understanding how magnetic fields behave, especially in the solar corona, where magnetic reconnections are ubiquitous in nature and cause transients like solar flares, coronal jets, bright points, and mass ejections. In 2D, reconnection can occur at O-type (elliptic) or X-type (hyperbolic) nulls where the magnetic field vanishes. In three dimensions, reconnection takes place at 3D nulls (where the magnetic field is zero) and separators; the curve formed through the intersection of two fan planes. The magnetic field is non-zero along separators, except at the endpoints. The spine and fan plane are the structures associated with 3D magnetic null point. The spine is made of two sets of field lines (directed toward/away from the null) bunched together and oriented along an axis. These field lines further fan out on a plane—the fan plane—containing the null.

Recent observations, theory, extrapolations, and simulations have shown that 3D magnetic nulls are present in the solar atmosphere and serve as preferential sites for reconnections, resulting in coronal transients like solar flares, coronal jets, bright points, and coronal mass ejections. Nevertheless, the generation of 3D nulls in the solar atmosphere is yet to be fully understood, a problem which the thesis attempts to explore utilizing numerical means.

Toward this objective, spontaneous generation and annihilation of 3D mag-

netic nulls in the solar atmosphere through a combination of MHD simulations, a modified trilinear null detection technique, and observational data are explored in the thesis. The study focuses on three primary scenarios: the dynamics of the initial analytical magnetic field having a proper radial null, a realistic solar atmosphere scenario using data from Active Region AR 11977 during a C-class flare on February 17, 2014, and an initially chaotic magnetic field devoid of any null. Notably, pre-existing 3D nulls are present in the first two cases.

The first study considered the initial analytical magnetic field having proper radial 3D magnetic null. The magnetofluid is idealized as thermodynamically inactive, implicitly dissipative, and viscid, with the physical domain and computational grid set in Cartesian coordinates. The pre-existing current-free 3D null is deformed through a prescribed initial sinusoidal flow. This leads to the formation of current sheets and the onset of magnetic reconnections, generating a null pair consisting of a radial and a spiral null. Importantly, the creation of nulls is away from the central null—a new result. The subsequent evolution shows the reconnection-assisted spontaneous generation of nulls—a novel finding, given contemporary research indicating the presence of 3D nulls in nature, including the solar atmosphere.

In the second scenario, the initial magnetic field is constructed by extrapolating the photospheric magnetic field obtained from the HMI on board the SDO using a non-force-free extrapolation model. The simulation started with an extrapolated magnetic field and covered a fraction of the rising phase of the flare, dominated by magnetic reconnection. Initially, around four thousand nulls are present, and the number of nulls decreases with time, probably due to annihilation and nulls leaving the computational domain. The detailed analysis of specific pairs showcases the creation of radial nulls, pairs of spiral and radial nulls through reconnection, and transformations between various null types along with their subsequent annihilations. The spontaneously generated nulls exhibit the footpoint brightening of fan field lines due to slip reconnection, a phenomenon typical to observed large-scale 3D nulls.

In the third scenario, magnetic fields are derived by superposing two linear

force-free ABC fields. The simulations demonstrate a direct correlation between the level of chaoticity and the number of nulls generated, with higher chaoticity resulting in earlier and more frequent null creations. The updated trilinear null detection technique enables the identification of null types, calculation of their topological degrees, and distinction between spiral and radial nulls. The findings highlight the generation of a spiral 3D null pair, which was not explored earlier. It also highlights the null generation and annihilation, driven by magnetic reconnection. Consequently, the global magnetic field topology changes as the involved field lines alter their connectivity.

Overall, the work presented in the thesis establishes that magnetic reconnection is a key mechanism in the spontaneous generation and annihilation of 3D nulls, influencing the global magnetic field topology. The findings are not only interesting but also intriguing. In all three cases, magnetic reconnection creates magnetic nulls, which, in turn, are also sites for magnetic reconnection. It is then tempting to envisage a scenario where reconnections spontaneously generate 3D nulls, which sustain further reconnections—a continuous process that can explain the abundance of nulls in the solar atmosphere and contribute to chromospheric and coronal heating.

7.2 Future Scopes

Based on the findings of this thesis, several avenues for future research emerge. A critical next step is to investigate the energetics of spontaneous 3D null generation and annihilation processes. This involves quantifying the energy conversion during magnetic reconnection and its implications for heating the solar corona and chromosphere. Moreover, the fact that nulls being ordered entities, having a well-defined spine and fan field lines, and their spontaneous creation suggests them as possible self-organized structures. Further research in this direction will have far-reaching consequences on the understanding of 3D nulls.

The plasma flow responsible for bringing field lines together to initiate the magnetic reconnection and generate null will be explored. Understanding this

inflow can provide insights into the conditions necessary for reconnection events generating the nulls and their frequency in the solar atmosphere.

Another promising direction is to correlate particle acceleration with the null generation/annihilation, as their interactions can lead to significant particle energization. Investigating the impact of null dynamics on space weather phenomena, such as solar energetic particle events and geomagnetic storms, could also enhance our understanding of their broader implications.

Contemporary research suggests that the reconnection is not occurring within the null cluster and highlights the importance of intra- and inter-cluster separators in magnetic reconnection. An important future study would be the identification of separators and exploring their role in null pair generation and subsequent evolution.

Last but not the least, extending the study of 3D nulls to other astrophysical contexts, such as the magnetospheres of planets and the interstellar medium, can reveal the universality of these processes and their relevance beyond the solar atmosphere. This cross-disciplinary approach can foster a more comprehensive understanding of magnetic reconnection and its fundamental role in astrophysical plasmas.

Bibliography

- Agarwal, S., & Bhattacharyya, R. 2024, *Physics of Plasmas*, 31, 054501 [2](#)
- Agarwal, S., Bhattacharyya, R., & Wiegelmann, T. 2022, *Solar Phys.*, 297, 91 [124](#), [126](#)
- Agarwal, S., Bhattacharyya, R., & Yang, S. 2024, *Solar Phys.*, 299, 15 [2](#)
- Albright, B. J. 1999, *Phys. Plasmas*, 6, 4222 [116](#)
- Alexander, C. E., Del Zanna, G., & Maclean, R. C. 2011, *Astron. Astrophys.*, 526, A134 [40](#)
- Alfvén, H. 1942, *Nature*, 150, 405 [4](#), [7](#)
- Amari, T., & Luciani, J. F. 1999, *Astrophys. J. Lett.*, 515, L81 [34](#)
- Antalova, A. 1996, *Contributions of the Astronomical Observatory Skalnaté Pleso*, 26, 98 [59](#)
- Antiochos, S. K., Dahlburg, R. B., & Klimchuk, J. A. 1994, *Astrophys. J. Lett.*, 420, L41 [34](#)
- Aschwanden, M. J. 2005, *Physics of the Solar Corona. An Introduction with Problems and Solutions (2nd edition)* (Springer Berlin, Heidelberg) [18](#), [128](#)
- Aulanier, G., DeLuca, E. E., Antiochos, S. K., McMullen, R. A., & Golub, L. 2000, *Astrophys. J.*, 540, 1126 [3](#), [27](#)
- Aulanier, G., & Demoulin, P. 1998, *Astron. Astrophys.*, 329, 1125 [34](#)

- Aulanier, G., Pariat, E., & Démoulin, P. 2005, *Astron. Astrophys.*, 444, 961 [77](#), [128](#)
- Aulanier, G., Pariat, E., Démoulin, P., & Devore, C. R. 2006, *Solar Phys.*, 238, 347 [26](#), [135](#)
- Aulanier, G., Golub, L., DeLuca, E. E., et al. 2007, *Science*, 318, 1588 [22](#), [26](#), [135](#)
- Axford, W. I. 1984, Geophysical Monograph Series, 30, 1 [21](#)
- Axford, W. I. 1984, Magnetic Field Reconnection (American Geophysical Union (AGU)), 1–8 [132](#)
- Beaudoin, P., Charbonneau, P., Racine, E., & Smolarkiewicz, P. K. 2013, *Solar Phys.*, 282, 335 [83](#)
- Benz, A. O. 2017, Living Reviews in Solar Physics, 14, 2 [xii](#), [32](#), [33](#), [35](#)
- Bhattacharyya, R., & Janaki, M. S. 2004, *Physics of Plasmas*, 11, 5615 [60](#)
- Bhattacharyya, R., Janaki, M. S., Dasgupta, B., & Zank, G. P. 2007, *Solar Phys.*, 240, 63 [60](#), [125](#)
- Bhattacharyya, R., Low, B. C., & Smolarkiewicz, P. K. 2010, *Physics of Plasmas*, 17, 112901 [90](#)
- Birn, J., Hesse, M., & Schindler, K. 1997, *Advances in Space Research*, 19, 1763, proceedings of the D0.4 Symposium of COSPAR Scientific Commission D [21](#)
- Bobra, M. G., Sun, X., Hoeksema, J. T., et al. 2014, *Solar Phys.*, 289, 3549 [57](#), [125](#)
- Book, D. L., Boris, J. P., & Hain, K. 1975, *Journal of Computational Physics*, 18, 248 [76](#)
- Boozer, A. H. 2019, *Phys. Plasmas*, 26, 042104 [159](#)

- Bora, K., Bhattacharyya, R., & Smolarkiewicz, P. K. 2021, *Astrophys. J.*, 906, 102 [90](#)
- Boris, J. P., & Book, D. L. 1973, *Journal of Computational Physics*, 11, 38 [76](#)
- . 1976, *Journal of Computational Physics*, 20, 397 [76](#)
- Borrero, J. M., Tomczyk, S., Kubo, M., et al. 2011, *Solar Phys.*, 273, 267 [56](#), [57](#)
- Bowen, T. A., Testa, P., & Reeves, K. K. 2013, *Astrophys. J.*, 770, 126 [59](#)
- Brown, D. S., Parnell, C. E., Deluca, E. E., Golub, L., & McMullen, R. A. 2001, *Solar Phys.*, 201, 305 [40](#)
- Bruevich, E. A. 2020, *Journal of Astrophysics and Astronomy*, 41, 3 [59](#)
- Bulanov, S. V., & Olshanetsky, M. A. 1984, *Phys. Lett.*, 100, 35 [91](#)
- Bulanov, S. V., & Sakai, J. 1997, *J. Phys. Soc. Jpn.*, 66, 3477 [92](#)
- Canfield, R. C., Reardon, K. P., Leka, K. D., et al. 1996, *Astrophys. J.*, 464, 1016 [38](#)
- Carmichael, H. 1964, in *NASA Special Publication*, ed. W. N. Hess, Vol. 50, 451 [20](#), [32](#)
- Charbonneau, P., & Smolarkiewicz, P. K. 2013, *Science*, 340, 42 [76](#)
- Cheng, X., Priest, E. R., Li, H. T., et al. 2023, *Nature Communications*, 14, 2107 [21](#), [23](#), [27](#), [134](#)
- Chiti, F. 2020, *FedericaChiti/Null_Finder: Null Finder - Release 1*, doi:10.5281/zenodo.4308622 [68](#)
- Choudhuri, A. R. 1998, *The Physics of Fluids and Plasmas: An Introduction for Astrophysicists*, doi:10.1017/CBO9781139171069 [15](#)
- Close, R. M., Parnell, C. E., & Priest, E. R. 2004, *Solar Phys.*, 225, 21 [25](#)
- Clyne, J., Gruchalla, K., & Rast, M. 2010 [82](#)

- Cowley, S. W. H. 1973, *Radio Science*, 8, 903
- Dahlburg, R. B., Antiochos, S. K., & Zang, T. A. 1991, *Astrophys. J.*, 383, 420
[77](#), [128](#)
- De Pontieu, B., Title, A. M., Lemen, J. R., et al. 2014, *Solar Phys.*, 289, 2733
[37](#)
- Demoulin, P., Bagala, L. G., Mandrini, C. H., Henoux, J. C., & Rovira, M. G. 1997, *Astron. Astrophys.*, 325, 305 [26](#)
- Demoulin, P., Henoux, J. C., Priest, E. R., & Mandrini, C. H. 1996, *Astron. Astrophys.*, 308, 643 [26](#)
- Domaradzki, J. A., & Radhakrishnan, S. 2005, *Fluid Dynamics Research*, 36, 385 [82](#)
- Domaradzki, J. A., Xiao, Z., & Smolarkiewicz, P. K. 2003, *Physics of Fluids*, 15, 3890 [82](#), [83](#)
- Domingo, V., Fleck, B., & Poland, A. I. 1995, *Solar Phys.*, 162, 1 [36](#)
- Dorelli, J. C., & Bhattacharjee, A. 2008, *Physics of Plasmas*, 15, 056504 [25](#)
- Dorelli, J. C., Bhattacharjee, A., & Raeder, J. 2007, *Journal of Geophysical Research (Space Physics)*, 112, A02202 [25](#), [26](#)
- Drenkhahn, G., & Spruit, H. C. 2002, *Astron. Astrophys.*, 391, 1141 [32](#)
- Dungey, J. 1953, *The London, Edinburgh, and Dublin Philosophical Magazine and Journal of Science*, 44, 725 [32](#)
- Dungey, J. W. 1959, *Quarterly Journal of the Royal Meteorological Society*, 85, 450 [23](#)
- Edgar, R. L., & Régnier, S. 2024, *Mon. Not. Roy. Astron. Soc.*, 532, 755 [3](#)
- Eisenstat, S. C. 1983, *SIAM Journal on Numerical Analysis*, 20, 358 [80](#)

- Eisenstat, S. C., Elman, H. C., & Schultz, M. H. 1983, *SIAM Journal on Numerical Analysis*, 20, 345 [80](#)
- Eyink, G. L., Lazarian, A., & Vishniac, E. T. 2011, *Astrophys. J.*, 743, 51 [159](#)
- Fletcher, L., Metcalf, T. R., Alexander, D., Brown, D. S., & Ryder, L. A. 2001, *The Astrophysical Journal*, 554, 451 [27](#)
- Fletcher, L., Metcalf, T. R., Alexander, D., Brown, D. S., & Ryder, L. A. 2001, *Astrophys. J.*, 554, 451 [27](#)
- Galsgaard, K., Madjarska, M. S., Moreno-Insertis, F., Huang, Z., & Wiegmann, T. 2017, *Astron. Astrophys.*, 606, A46 [xiii](#), [42](#), [44](#)
- Galsgaard, K., Parnell, C. E., & Blaizot, J. 2000, *Astron. Astrophys.*, 362, 395
- Gary, G. A. 2001, *Solar Phys.*, 203, 71 [xiv](#), [59](#), [61](#)
- Ghizaru, M., Charbonneau, P., & Smolarkiewicz, P. K. 2010, *Astrophys. J. Lett.*, 715, L133 [83](#)
- Giannios, D. 2010, *Mon. Not. Roy. Astron. Soc.*, 408, L46 [32](#)
- Giovanelli, R. G. 1947, *Mon. Not. Roy. Astron. Soc.*, 107, 338 [32](#)
- . 1948, *Mon. Not. Roy. Astron. Soc.*, 108, 163 [32](#)
- Golub, L., Krieger, A. S., Harvey, J. W., & Vaiana, G. S. 1977, *Solar Phys.*, 53, 111 [40](#)
- Golub, L., Krieger, A. S., & Vaiana, G. S. 1976a, *Solar Phys.*, 49, 79 [40](#)
- . 1976b, *Solar Phys.*, 50, 311 [40](#)
- Gray, T., Lukin, V. S., Brown, M. R., & Cothran, C. D. 2010, *Physics of Plasmas*, 17, 102106 [26](#)
- Greene, J. M. 1992, *Journal of Computational Physics*, 98, 194 [51](#), [54](#), [86](#), [122](#)
- Griebel, M., Dornseifer, T., & Neunhoeffler, T. 1997 [71](#)

- Grinstein, F. F., & Drikakis, D. 2007, *Journal of Fluids Engineering*, 129, 1481
[82](#)
- Guo, R., Pu, Z., Wang, X., Xiao, C., & He, J. 2022, *Journal of Geophysical Research (Space Physics)*, 127, e2021JA030248 [25](#)
- Guo, R., Pu, Z., Xiao, C., et al. 2013, *Journal of Geophysical Research (Space Physics)*, 118, 6116 [25](#)
- Habbal, S. R. 1992, *Annales Geophysicae*, 10, 34 [40](#)
- Handy, B. N., Acton, L. W., Kankelborg, C. C., et al. 1999, *Solar Phys.*, 187, 229 [36](#)
- Haynes, A. L., & Parnell, C. E. 2007, *Physics of Plasmas*, 14, 082107 [64](#), [65](#), [68](#)
- Haynes, A. L., Parnell, C. E., Galsgaard, K., & Priest, E. R. 2007, *Proceedings of the Royal Society of London Series A*, 463, 1097 [24](#)
- Hesse, M., & Schindler, K. 1988, *J. Geophys. Res.*, 93, 5559 [21](#)
- Hirayama, T. 1974, *Solar Phys.*, 34, 323 [20](#), [32](#)
- Hornig, G., & Schindler, K. 1996, *Physics of Plasmas*, 3, 781 [xi](#), [3](#), [6](#), [11](#), [54](#), [86](#), [122](#), [166](#)
- Hoyle, F. 1950, *Quarterly Journal of the Royal Meteorological Society*, 76, 112
[32](#)
- Hu, Q., & Dasgupta, B. 2008, *Solar Phys.*, 247, 87 [60](#), [62](#), [64](#), [125](#)
- Hu, Q., Dasgupta, B., Choudhary, D. P., & Büchner, J. 2008, *Astrophys. J.*, 679, 848 [60](#), [62](#), [125](#)
- Hu, Q., Dasgupta, B., Derosa, M. L., Büchner, J., & Gary, G. A. 2010, *Journal of Atmospheric and Solar-Terrestrial Physics*, 72, 219 [xiv](#), [63](#), [64](#), [125](#)
- Ibrahim, M. S., Uddin, W., Joshi, B., Chandra, R., & Awasthi, A. K. 2022, *Research in Astronomy and Astrophysics*, 21, 318 [123](#)

- Jiang, C., Wu, S. T., Feng, X., & Hu, Q. 2016, *Nature Communications*, 7, 11522 [129](#)
- Kaiser, M. L., Kucera, T. A., Davila, J. M., et al. 2008, *Space Sci. Rev.*, 136, 5 [37](#)
- Khlystova, A., & Toriumi, S. 2017, *Astrophys. J.*, 839, 63 [60](#)
- Knizhnik, K. J., & Cabral-Pelletier, L. C. 2022, *The Astrophysical Journal*, 937, 93 [93](#), [132](#)
- Komar, C. M., Cassak, P. A., Dorelli, J. C., Glocer, A., & Kuznetsova, M. M. 2013, *Journal of Geophysical Research (Space Physics)*, 118, 4998 [25](#)
- Kopp, R. A., & Pneuman, G. W. 1976, *Solar Phys.*, 50, 85 [20](#), [32](#)
- Kosugi, T., Matsuzaki, K., Sakao, T., et al. 2007, *Solar Phys.*, 243, 3 [36](#)
- Kumar, D., Bhattacharyya, R., & Smolarkiewicz, P. K. 2013, *Physics of Plasmas*, 20, 112903 [83](#)
- . 2015, *Physics of Plasmas*, 22, 012902 [83](#)
- Kumar, P., Nakariakov, V. M., Karpen, J. T., & Cho, K.-S. 2024, *Nature Communications*, 15, 2667 [23](#)
- Kumar, S., & Bhattacharyya, R. 2016, *Physics of Plasmas*, 23, 044501 [83](#)
- Kumar, S., Bhattacharyya, R., Dasgupta, B., & Janaki, M. S. 2017, *Physics of Plasmas*, 24, 082902 [28](#), [157](#), [159](#)
- Lau, Y.-T., & Finn, J. M. 1990, *Astrophys. J.*, 350, 672 [24](#), [45](#), [50](#), [51](#), [86](#)
- Lemen, J. R., Title, A. M., Akin, D. J., et al. 2012, *Solar Phys.*, 275, 17 [xiv](#), [58](#)
- Lin, R. P., Dennis, B. R., Hurford, G. J., et al. 2002, *Solar Phys.*, 210, 3 [36](#)
- Liu, C., Prasad, A., Lee, J., & Wang, H. 2020, *Astrophys. J.*, 899, 34 [127](#)

- Liu, C. M., Chen, Z. Z., Wang, Z., & Liu, Y. Y. 2019, *The Astrophysical Journal*, 871, 209 [132](#), [146](#)
- Liu, C. M., Fu, H. S., Cao, D., Xu, Y., & Divin, A. 2018, *Astrophys. J.*, 860, 128 [132](#), [146](#)
- Liu, R., Kliem, B., Titov, V. S., et al. 2016, *Astrophys. J.*, 818, 148 [26](#)
- Liu, W., Berger, T. E., Title, A. M., Tarbell, T. D., & Low, B. C. 2011, *Astrophys. J.*, 728, 103 [27](#)
- Longcope, D. W. 1996, *Solar Phys.*, 169, 91 [24](#), [27](#)
- . 2005, *Living Reviews in Solar Physics*, 2, 7 [86](#), [122](#)
- Longcope, D. W., McKenzie, D. E., Cirtain, J., & Scott, J. 2005, *Astrophys. J.*, 630, 596 [25](#)
- Longcope, D. W., & Parnell, C. E. 2009, *Solar Phys.*, 254, 51 [27](#)
- Lynch, B. J., Antiochos, S. K., DeVore, C. R., Luhmann, J. G., & Zurbuchen, T. H. 2008, *The Astrophysical Journal*, 683, 1192 [27](#)
- Margolin, L. G., Rider, W. J., & Grinstein, F. F. 2006, *Journal of Turbulence*, 7, 15 [69](#), [82](#)
- Mason, E. I., Antiochos, S. K., & Viall, N. M. 2019, *Astrophys. J. Lett.*, 874, L33 [27](#)
- Mason, E. I., Antiochos, S. K., & Viall, N. M. 2019, *The Astrophysical Journal Letters*, 874, L33 [135](#)
- Mason, E. I., Antiochos, S. K., & Vourlidas, A. 2021, *The Astrophysical Journal Letters*, 914, L8 [135](#)
- Masson, S., Parlat, E., Aulanier, G., & Schrijver, C. J. 2009, *Astrophys. J.*, 700, 559 [3](#), [152](#)

- Masson, S., Pariat, E., Aulanier, G., & Schrijver, C. J. 2009, *The Astrophysical Journal*, 700, 559 [27](#)
- Maurya, Y. K., Bhattacharyya, R., & Pontin, D. I. 2023, *Physics of Plasmas*, 30, 022901 [132](#)
- . 2024, *Physica Scripta*, 99, 075017 [68](#)
- Maurya, Y. K., Bhattacharyya, R., Pontin, D. I., & Kumar, S. 2024, Exploring the generation and annihilation of three dimensional nulls through MHD simulations in initially chaotic magnetic field devoid of nulls, arXiv:2406.06328 [68](#)
- McIntosh, S. W. 2007, *Astrophys. J.*, 670, 1401 [40](#)
- Metcalf, T. R., Alexander, D., Hudson, H. S., & Longcope, D. W. 2003, *Astrophys. J.*, 595, 483 [25](#)
- Metcalf, T. R., Canfield, R. C., Mickey, D. L., & Lites, B. W. 1991, in *Solar Polarimetry*, ed. L. J. November, 376–386 [57](#)
- Mitra, P. K., & Joshi, B. 2021, *Monthly Notices of the Royal Astronomical Society*, 503, 1017 [123](#)
- Mitra, P. K., Joshi, B., Prasad, A., Veronig, A. M., & Bhattacharyya, R. 2018, *Astrophys. J.*, 869, 69 [59](#)
- Moore, R. L., Cirtain, J. W., Sterling, A. C., & Falconer, D. A. 2010, *Astrophys. J.*, 720, 757 [37](#)
- Mou, C., Huang, Z., Xia, L., et al. 2016, *Astrophys. J.*, 818, 9 [40](#)
- Mulay, S. M., Tripathi, D., Del Zanna, G., & Mason, H. 2016, *Astron. Astrophys.*, 589, A79 [38](#)
- Mullan, D. J. 1986, in *NASA Special Publication*, Vol. 492, 455–479 [32](#)
- Murphy, N. A., Parnell, C. E., & Haynes, A. L. 2015, *Physics of Plasmas*, 22, 102117 [51](#), [54](#)

- Nayak, S. S., Bhattacharyya, R., & Kumar, S. 2021, *Physics of Plasmas*, 28, 024502 [xii](#), [27](#), [35](#), [36](#)
- Nayak, S. S., Bhattacharyya, R., Prasad, A., et al. 2019, *Astrophys. J.*, 875, 10 [xii](#), [38](#), [39](#)
- Nayak, S. S., Bhattacharyya, R., Smolarkiewicz, P. K., Kumar, S., & Prasad, A. 2020, *Astrophys. J.*, 892, 44 [28](#), [155](#), [157](#)
- Nayak, S. S., Bhattacharyya, R., Smolarkiewicz, P. K., Kumar, S., & Prasad, A. 2020, *The Astrophysical Journal*, 892, 44 [85](#), [88](#), [89](#)
- Olshevsky, V., Lapenta, G., & Markidis, S. 2013, *Physical review letters*, 111, 045002 [99](#)
- Panesar, N. K., Sterling, A. C., & Moore, R. L. 2017, *Astrophys. J.*, 844, 131 [38](#)
- . 2018, *Astrophys. J.*, 853, 189 [38](#)
- Panesar, N. K., Sterling, A. C., Moore, R. L., & Chakrapani, P. 2016, *Astrophys. J. Lett.*, 832, L7 [38](#)
- Pariat, E., Antiochos, S. K., & DeVore, C. R. 2009, *Astrophys. J.*, 691, 61 [27](#)
- Parker, E. N. 1957, *J. Geophys. Res.*, 62, 509 [15](#)
- . 1973, *Astrophys. J.*, 180, 247 [3](#)
- . 1994, *International Series in Astronomy and Astrophysics*, 1 [3](#)
- Parker, E. N. 1994, *Spontaneous current sheets in magnetic fields: with applications to stellar x-rays*, Vol. 1 (Oxford University Press) [28](#)
- Parnell, C. E. 2024, *Physics of Plasmas*, 31, 082112 [25](#)
- Parnell, C. E. 2024, *On the importance of separators as sites of 3D magnetic reconnection*, arXiv:2403.04076 [162](#)

- Parnell, C. E., & De Moortel, I. 2012, *Philosophical Transactions of the Royal Society of London Series A*, 370, 3217 [23](#)
- Parnell, C. E., Haynes, A. L., & Galsgaard, K. 2010a, *Journal of Geophysical Research (Space Physics)*, 115, A02102 [24](#)
- Parnell, C. E., Maclean, R. C., & Haynes, A. L. 2010b, *Astrophys. J. Lett.*, 725, L214 [25](#)
- Parnell, C. E., Priest, E. R., & Golub, L. 1994a, *Solar Phys.*, 151, 57 [40](#)
- Parnell, C. E., Priest, E. R., & Titov, V. S. 1994b, *Solar Phys.*, 153, 217 [40](#)
- Parnell, C. E., Smith, J. M., Neukirch, T., & Priest, E. R. 1996, *Physics of Plasmas*, 3, 759 [45](#), [46](#), [87](#), [132](#), [146](#)
- Parnell, C. E., Stevenson, J. E. H., Threlfall, J., & Edwards, S. J. 2015, *Philosophical Transactions of the Royal Society of London Series A*, 373, 20140264 [3](#)
- Pérez-Suárez, D., Maclean, R. C., Doyle, J. G., & Madjarska, M. S. 2008, *Astron. Astrophys.*, 492, 575 [40](#)
- Pesnell, W. D., Thompson, B. J., & Chamberlin, P. C. 2012, *Solar Phys.*, 275, 3 [37](#), [55](#)
- Petschek, H. E. 1964, in *NASA Special Publication*, Vol. 50, 425 [18](#)
- Platten, S. J., Parnell, C. E., Haynes, A. L., Priest, E. R., & Mackay, D. H. 2014, *Astron. Astrophys.*, 565, A44 [25](#)
- Pontin, D. I. 2011, *Advances in Space Research*, 47, 1508 [xii](#), [13](#), [23](#), [25](#)
- Pontin, D. I., & Priest, E. R. 2022, *Living Reviews in Solar Physics*, 19, 1 [23](#), [86](#), [122](#)
- Pontin, D. I., Priest, E. R., & Galsgaard, K. 2013, *Astrophys. J.*, 774, 154 [123](#), [142](#), [152](#)

- Prasad, A., Bhattacharyya, R., Hu, Q., Kumar, S., & Nayak, S. S. 2018, *Astrophys. J.*, 860, 96 [22](#), [27](#), [62](#), [125](#)
- Preś , P., & Phillips, K. H. J. 1999, *Astrophys. J. Lett.*, 510, L73 [40](#)
- Priest, E. 2014, Magnetohydrodynamics of the Sun, doi:10.1017/CBO9781139020732 [7](#), [20](#)
- Priest, E., Bungey, T., & Titov, V. 1997, The 3D topology and interaction of complex magnetic flux systems, *geophys Astrophys Fluid Dynam*
- Priest, E., & Forbes, T. 2000, Magnetic Reconnection: MHD Theory and Applications (Cambridge University Press), doi:10.1017/CBO9780511525087 [18](#)
- Priest, E. R., Heyvaerts, J. F., & Title, A. M. 2002, *Astrophys. J.*, 576, 533 [23](#)
- Priest, E. R., Hornig, G., & Pontin, D. I. 2003, *Journal of Geophysical Research (Space Physics)*, 108, 1285 [132](#), [135](#)
- Priest, E. R., Parnell, C. E., & Martin, S. F. 1994, *Astrophys. J.*, 427, 459 [xiii](#), [40](#), [42](#)
- Prusa, J. M., & Smolarkiewicz, P. K. 2003, *Journal of Computational Physics*, 190, 601 [78](#)
- Prusa, J. M., Smolarkiewicz, P. K., & Wyszogrodzki, A. A. 2008, *Computers and Fluids*, 37, 1193 [69](#), [76](#), [80](#), [82](#)
- Pucci, S., Poletto, G., Sterling, A. C., & Romoli, M. 2013, *Astrophys. J.*, 776, 16 [36](#)
- Racine, É., Charbonneau, P., Ghizaru, M., Bouchat, A., & Smolarkiewicz, P. K. 2011, *Astrophys. J.*, 735, 46 [83](#)
- Ram, A. K., Dasgupta, B., Krishnamurthy, V., & Mitra, D. 2014, *Physics of Plasmas*, 21, 072309 [156](#)
- Raouafi, N. E., Patsourakos, S., Parlat, E., et al. 2016, *Space Sci. Rev.*, 201, 1 [36](#), [38](#)

- Régnier, S., & Amari, T. 2004, *Astron. Astrophys.*, 425, 345 [34](#)
- Régnier, S., Parnell, C. E., & Haynes, A. L. 2008, *Astron. Astrophys.*, 484, L47 [27](#)
- Rider, W. J. 2006, *International Journal for Numerical Methods in Fluids*, 50, 1145 [82](#)
- Romanova, M. M., & Lovelace, R. V. E. 1992, *Astron. Astrophys.*, 262, 26 [32](#)
- Roussev, I. I., Forbes, T. G., Gombosi, T. I., et al. 2003, *Astrophys. J. Lett.*, 588, L45 [33](#)
- Ruderman, M. S., & Roberts, B. 2002, *Astrophys. J.*, 577, 475 [77](#)
- Savcheva, A., & van Ballegoijen, A. 2009, *Astrophys. J.*, 703, 1766 [34](#)
- Scherrer, P. H., Schou, J., Bush, R. I., et al. 2012, *Solar Phys.*, 275, 207 [124](#)
- Schindler, K., Hesse, M., & Birn, J. 1988, *J. Geophys. Res.*, 93, 5547 [21](#), [23](#), [26](#), [132](#)
- Schou, J., Scherrer, P. H., Bush, R. I., et al. 2012, *Solar Phys.*, 275, 229 [56](#), [124](#)
- Shen, Y. 2021, *Proceedings of the Royal Society of London Series A*, 477, 217 [xii](#), [37](#), [38](#)
- Shibata, K., & Magara, T. 2011, *Living Reviews in Solar Physics*, 8, 6 [32](#), [35](#)
- Shibata, K., Masuda, S., Shimojo, M., et al. 1995, *Astrophys. J. Lett.*, 451, L83 [xii](#), [34](#)
- Shibata, K., Nitta, N., Matsumoto, R., et al. 1994, in *X-ray solar physics from Yohkoh*, ed. Y. Uchida, T. Watanabe, K. Shibata, & H. S. Hudson, 29 [37](#)
- Shimojo, M., Hashimoto, S., Shibata, K., et al. 1996, *Pub. Astron. Soc. Japan*, 48, 123 [37](#)
- Shimojo, M., & Shibata, K. 2000, *Astrophys. J.*, 542, 1100 [38](#)

- Shimojo, M., Shibata, K., & Harvey, K. L. 1998, *Solar Phys.*, 178, 379 [38](#)
- Smolarkiewicz, P., & Szmelter, J. 2011, *Acta Geophysica*, 59, 1109 [80](#)
- Smolarkiewicz, P. K. 1983, *Monthly Weather Review*, 111, 479 [69](#), [73](#), [76](#)
- . 1984, *Journal of Computational Physics*, 54, 325 [69](#), [76](#)
- . 1991, *Monthly Weather Review*, 119, 2505 [75](#), [76](#)
- . 2006, *International Journal for Numerical Methods in Fluids*, 50, 1123 [69](#)
- Smolarkiewicz, P. K. 2006, *International Journal for Numerical Methods in Fluids*, 50, 1123 [70](#), [71](#), [73](#), [75](#)
- Smolarkiewicz, P. K., & Charbonneau, P. 2013, *Journal of Computational Physics*, 236, 608 [69](#), [78](#), [127](#)
- Smolarkiewicz, P. K., & Clark, T. L. 1986, *Journal of Computational Physics*, 67, 396 [69](#), [74](#), [75](#), [76](#)
- Smolarkiewicz, P. K., & Grabowski, W. W. 1990, *Journal of Computational Physics*, 86, 355 [76](#)
- Smolarkiewicz, P. K., & Margolin, L. G. 1993, *Monthly Weather Review*, 121, 1847 [75](#), [76](#)
- Smolarkiewicz, P. K., & Margolin, L. G. 1997, *Atmosphere-Ocean*, 35, 127 [75](#), [80](#)
- Smolarkiewicz, P. K., & Margolin, L. G. 1998, *Journal of Computational Physics*, 140, 459 [69](#), [70](#), [71](#), [73](#), [75](#)
- Smolarkiewicz, P. K., & Prusa, J. M. 2002, *International Journal for Numerical Methods in Fluids*, 39, 799 [82](#)
- Smolarkiewicz, P. K., & Pudykiewicz, J. A. 1992, *Journal of the Atmospheric Sciences*, 49, 2082 [76](#)

- Smolarkiewicz, P. K., & Szmelter, J. 2009, *Journal of Computational Physics*, 228, 33 [80](#)
- Smolarkiewicz, P. K., & Szmelter, J. 2009, *Journal of Computational Physics*, 228, 33 [83](#)
- Sonnerup, B. U. Ö. 1979, in *Solar System Plasma Physics*, Vol. 3, 45–108 [21](#)
- Stevenson, J. E. H., Parnell, C. E., Priest, E. R., & Haynes, A. L. 2015, *Astron. Astrophys.*, 573, A44 [24](#)
- Sturrock, P. A. 1966, *Nature*, 211, 695 [20](#), [32](#)
- Su, Y. 2007, PhD thesis, CAS, Purple Mountain Observatory [34](#)
- Svestka, Z., & Cliver, E. W. 1992, in *IAU Colloq. 133: Eruptive Solar Flares*, ed. Z. Svestka, B. V. Jackson, & M. E. Machado, Vol. 399, 1 [32](#)
- Sweet, P. A. 1958, in *Electromagnetic Phenomena in Cosmical Physics*, ed. B. Lehnert, Vol. 6, 123 [15](#)
- Taylor, J. B. 1974, *Phys. Rev. Lett.*, 33, 1139 [2](#)
- Threlfall, J., Stevenson, J. E. H., Parnell, C. E., & Neukirch, T. 2016, *Astron. Astrophys.*, 585, A95 [25](#)
- Titov, V. S. 2007, *Astrophys. J.*, 660, 863 [26](#)
- Török, T., Aulanier, G., Schmieder, B., Reeves, K. K., & Golub, L. 2009, *Astrophys. J.*, 704, 485 [27](#)
- Ugarte-Urra, I., Warren, H. P., & Winebarger, A. R. 2007, *Astrophys. J.*, 662, 1293 [3](#)
- Vaiana, G. S., Krieger, A. S., & Timothy, A. F. 1973, *Solar Phys.*, 32, 81 [40](#)
- van Ballegoijen, A. A. 2004, *Astrophys. J.*, 612, 519 [34](#)
- Vasyliunas, V. M. 1975, *Reviews of Geophysics and Space Physics*, 13, 303 [13](#), [21](#)

- Vekstein, G. 2016, *Journal of Plasma Physics*, 82, 925820401 [60](#)
- Venkatakrishnan, P., & Gosain, S. 2008, in *Physics of the Sun and its Atmosphere*, ed. B. N. Dwivedi & U. Narain, 39–60 [57](#)
- Verbunt, F. 1982, *Space Sci. Rev.*, 32, 379 [32](#)
- von Rekowski, B., & Hood, A. W. 2008, *Mon. Not. Roy. Astron. Soc.*, 384, 972 [40](#)
- von Rekowski, B., Parnell, C. E., & Priest, E. R. 2006a, *Mon. Not. Roy. Astron. Soc.*, 366, 125 [40](#)
- . 2006b, *Mon. Not. Roy. Astron. Soc.*, 369, 43 [40](#)
- Waite, M. L., & Smolarkiewicz, P. K. 2008, *Journal of Fluid Mechanics*, 606, 239–273 [83](#)
- Wang, H., & Liu, C. 2012, *The Astrophysical Journal*, 760, 101 [135](#)
- Wang, X., & Bhattacharjee, A. 1996, *J. Geophys. Res.*, 101, 2641 [25](#)
- Webb, D. F., Martin, S. F., Moses, D., & Harvey, J. W. 1993, *Solar Phys.*, 144, 15 [40](#)
- Wyper, P., & Jain, R. 2010, *Physics of Plasmas*, 17, 092902 [23](#)
- Wyper, P. F., Antiochos, S. K., & DeVore, C. R. 2017, *Nature*, 544, 452 [38](#)
- Wyper, P. F., & Pontin, D. I. 2014, *Physics of Plasmas*, 21, 102102 [85](#), [116](#)
- Wyper, P. F., & Pontin, D. I. 2014, *Physics of Plasmas*, 21, 082114 [28](#)
- Wyper, P. F., & Pontin, D. I. 2014, *Physics of Plasmas*, 21, 082114 [116](#)
- Xiao, C. J., Wang, X. G., Pu, Z. Y., et al. 2006, *Nature Physics*, 2, 478 [26](#)
- . 2007, *Nature Physics*, 3, 609 [25](#), [26](#)
- Yalim, M. S., Prasad, A., Pogorelov, N. V., Zank, G. P., & Hu, Q. 2020, *Astrophys. J. Lett.*, 899, L4 [127](#)

- Yamada, M., Kulsrud, R., & Ji, H. 2010, *Reviews of Modern Physics*, 82, 603 [27](#)
- Yan, Y., Deng, Y., Karlický, M., et al. 2001, *Astrophys. J. Lett.*, 551, L115 [33](#)
- Yang, S.-D. 2017, *Physics of Plasmas*, 24, 012903 [47](#)
- Yokoyama, T., & Shibata, K. 1995, *Nature*, 375, 42 [37](#)
- Yoshida, Z., & Giga, Y. 1990, *Mathematische Zeitschrift*,
doi:10.1007/BF02570870 [156](#)
- Zeeman, P. 1897, *Nature*, 55, 347 [56](#)
- Zhang, J., Kundu, M. R., & White, S. M. 2001, *Solar Phys.*, 198, 347 [xiii](#), [41](#)
- Zhang, Q. M., Chen, P. F., Ding, M. D., & Ji, H. S. 2014, *Astron. Astrophys.*,
568, A30 [40](#)
- Zhang, Q. M., Chen, P. F., Guo, Y., Fang, C., & Ding, M. D. 2012, *Astrophys. J.*, 746, 19 [xiii](#), [40](#), [43](#), [44](#)
- Zweibel, E. G., & Yamada, M. 2009, *Annu. Rev. Astron. Astrophys.*, 47, 291 [27](#)

List of Publications

Publications in Journals

1. **Yogesh Kumar Maurya**, Ramit Bhattacharyya, and David I. pontin, “Magnetic reconnections as the underlying cause of spontaneous generation and annihilation of three-dimensional magnetic nulls”, *Physics of Plasmas*, 2023, 30, 022901, doi: <https://doi.org/10.1063/5.0107601>
2. **Yogesh Kumar Maurya**, Ramit Bhattacharyya, and David I. pontin, “Generation and annihilation of three dimensional magnetic nulls in extrapolated solar coronal magnetic field: data-based Implicit Large Eddy simulation”, *Physica Scripta*, 2024, 99, 7, 075017, doi: <https://doi.org/10.1088/1402-4896/ad511e>
3. **Yogesh Kumar Maurya**, Ramit Bhattacharyya, David I. pontin, and Sanjay Kumar, “Exploring the generation and annihilation of three dimensional nulls through MHD simulations in initially chaotic magnetic field devoid of nulls”, *Physics of Plasmas*, 2024, 31, 7, doi: <https://doi.org/10.1063/5.0217951>